Melt flow singularity in linear polyethylene; Influence of molar mass, molar mass distribution and carbon-based fillers

By

Han Xu

A DOCTORAL THESIS

SUBMITTED IN PARTIAL FULFILMENT OF THE

REQUIRMENTS FOR THE AWARD OF DOCTOR OF

PHILOSOPHY OF LOUGHBOROUGH UNIVERSITY

Supervisors: Prof. Sanjay Rastogi

Prof. Mo Song

Department of Materials

Loughborough University

ABSTRACT

In the recent past it has been found that a considerable pressure drop occurred during the extrusion of linear polyethylene in the course of capillary flow. The pressure drop resides within a narrow temperature window of one to two degrees Celsius. In this research the hydrodynamic condition and molecular origin of the extrusion window of linear polymer were investigated further. The advantage of the extrusion window, viz. smooth extrudate with less die swell ratio attained at low extrusion pressure and temperature, has potential in industrial applications. However, the extrusion window, corresponding to linear polyethylene (PE) with relatively low polydispersity (<7), has a narrow window temperature interval, circa 1~2°C, thus it could not be applied to industrial scale processing at the industrial scale. To have a fundamental insight and make the process industrially viable, research in this thesis was devoted to broaden the extrusion window to tolerate the thermal fluctuations in conventional processing. To achieve this goal molecular weight dependence of window temperature and flow criticalities is revealed. The hydrodynamic conditions of the extrusion window observed in a rate-controlled rheometer and stick-slip flow studied in a stress-controlled rheometer could be traced back to the same origin, viz. slip flow arises due to the disentanglement of adsorbed chains on capillary wall from free chains in the bulk. Secondly, a dual window effect was uncovered in the course of capillary flow of a bimodal PE, which is consistent with the window temperature dependence on molecular weight. Moreover, it was found that flow induced orientation within the window effect is even less than that observed in steady state flow at a relatively low shear rate. This implies that in the window region only relaxed free chains are extruded through the capillary die and most of the adsorbed chains, which could be disengaged from the entangled melt, remain sticking to the inner capillary wall. This observation is consistent with the hydrodynamic origin of high-surface-energy-die slip flow. Finally, a unimodal linear PE with extremely broad molecular weight distribution, i.e. polydispersity (PDI) is 27, showed a broad window effect, circa 8°C, at an appropriate apparent shear rate. The molecular origin of such a broad window effect is due to its broad molecular weight distribution. These results have further implications for energy efficient processing.

Keywords: Polyethylene, extrusion, pressure-drop, molecular weight dependence, window effect, slip flow, helical distortion slip flow, broad extrusion window.

ACKNOWLEDGEMENTS

I would like to thank Professor Sanjay Rastogi and Professor Mo Song for their guidance and support. I would also like to thank Dr Lada Corbeij-Kurelec of SABIC - Europe for kindly providing the commercial polyethylenes.

I want to take this opportunity to thank all the staff in Department of Materials for their help, especially for Dr Jie Jin, Mr Andy Woolley, Mr Ray Owen, Mr John Bates and Dr David Ross. I also wish to thank the following people, Nilesh Patil, Kamal Yusoh, Anurag Pandey, Sara Ronca, Giuseppe Forte, Carmine Invigorito, Yohan Champouret and Maurizio Villani,.

I would also like to express my gratitude to EPSRC, ORSAS and ESRF for their financial support.

Finally, a personal thank is given to my family and friends for their love and encouragement.

LIST OF SYMBOLS

A	Surface area
$a_T \dot{\gamma}_c^{w}$	Rescaled critical apparent shear rate
b	Slip flow factor
D^*	Entanglement distance
D_e	Extrudate diameter
D_c	Capillary die diameter
D_e/D_c	Die swell ratio
d	Spacing between the planes in the lattice
E	Elastic modulus
E_a	Activation energy for chain relaxation
e	Extensional L/R
F_s	Shear force
F_T	Tensile force
f_c	Hermans Orientation factor
G	Shear modulus
$G(t)$	Relaxation shear modulus normalized by the plateau modulus
G_N^o	Plateau shear modulus
HBC	Hydrodynamic boundary condition
HSE	High surface energy
h	Thickness
$I(\beta)$	The diffracted intensity from the planes normal to the c-axis.
k_B	Boltzmann constant
L	Capillary length
ΔL	Elongational displacement
LSE	Low surface energy
L_0	Original length
L_1	Final length
dl	Incremental increase in length
l	Current length

M_c	Critical molecular weight
M_L	Low molecular weight component
M_H	High molecular weight component
M_w	Weight average molecular weight
MWD	Molecular weight distribution
M_Z	End tail molecular weight
M^*	Lower limit molecular weight for window effect
n	Power law index/ Rabinowitsch correction factor
ΔP	Pressure difference
P_L	Total pressure drop for capillary flow
P_0	Total pressure drop for pure convergent flow, 'zero die length' die
PDI	Polydispersity
Q	Volumetric output rate
Q_a	Applied flow rate
Q_C	Volumetric output rate corresponding to stick flow component in slip flow
Q_S	Volumetric output rate corresponding to slip flow component in slip flow
R	Die radius
R_g	Gas constant
r	Distance to the centre of capillary
SL	Slip flow
T	Temperature
T_{min}	Temperature corresponding to the pressure minimum in window effect.
T_{onset}	Onset temperature of window effect
T_s	Onset temperature of flow induced solidification
T_{ter}	Termination temperature of window effect
t	Time
V_s	Slip velocity
$w(M)$	Weight fraction of a given molecular weight component
2α	Die entry angle

β_c	The angle between the fibre or rod direction and the *c*-axis of orthorhombic PE crystal corresponding to the chain direction
$\dot{\gamma}$	Shear rate
$\dot{\gamma}_a$	Apparent wall shear rate
$\langle \dot{\gamma}_a \rangle$	Applied apparent shear rate
$\dot{\gamma}_{a,slip}$	Slip flow apparent wall shear rate
$\dot{\gamma}_{a,stick}$	Stick flow apparent wall shear rate
$\dot{\gamma}_c$	Critical apparent shear rate
$\dot{\gamma}_c^{\ h}$	Critical apparent shear rate corresponding to onset appearance of gross shape distortion
$\dot{\gamma}_c^{\ p}$	Critical apparent shear rate corresponding to onset appearance of periodic bulk distortion
$\dot{\gamma}_c^{\ w}$	Critical apparent shear rate corresponding to onset appearance of window effect
γ_s	Shear strain
$\dot{\gamma}_s$	Critical apparent shear rate corresponding to onset appearance of flow induced solidification at a given temperature.
$\dot{\gamma}_T$	True wall shear rate
$\dot{\gamma}_w$	Wall shear rate
ε	Tensile strain
$\dot{\varepsilon}$	Strain rate
η	Shear viscosity
η_a	Apparent shear viscosity
η_0	Zero shear viscosity
η^*	Complex viscosity
λ	Reptation time at shift temperature/window temperature
λ_0	Reptation time at reference temperature
λ_{rep}	Reptation time/relaxation time
μ	Coefficient of viscosity

σ	Shear stress
σ_c	Critical shear stress for stick-slip transition
σ_c^h	Critical wall shear stress corresponding to the onset appearance of helical
σ_E	Tensile stress
$\sigma_{\min}$	Wall shear stress at pressure minimum corrected by Cogswell correction
$\sigma_{\min} / T_{\min}$	Rescaled wall shear stress corresponding to the pressure minimum in window effect
σ_p	Wall shear stress corresponding to the onset appearance of pressure oscillation
σ_w	Wall shear stress
σ_w^u	Upper limit wall shear stress in pressure oscillation
σ_w^l	Lower limit wall shear stress in pressure oscillation distortion.
$\sigma_{w,c}$	Corrected wall shear stress
τ_y	Yield shear stress
ν	Adsorbed chain density
v_z	Linear flow velocity of a fluid at certain distance to the centre of capillary
x	Displacement under shear
ω	Rotational frequency

TABLE OF CONTENTS

Chapter 1 Introduction and objectives of project

1.1 Introduction

In the last five decades after the development of Ziegler-Natta heterogeneous catalysts polymer science and technology have grown hand in hand. The ease in processing of polymers and tailoring of the molecular architecture for the desired mechanical properties has been one of the main causes for this fast development. Impact of the revolution in this materials science is experienced in our daily life, for instance in packaging, building and construction, automotive, electrical and electronics, medical devices and others. Polymer applications can be divided into commodity plastics, engineering polymers and functional polymers. Among the commodity plastics, polyethylene (PE) is one of the highly dominating plastics in the market on account of its advantageous properties, such as its lightweight, high specific modulus, chemical resistance, recyclability etc. Considering the variation in available molecular architectures and thus the desired mechanical properties, polyethylene is a generic name for the polymer. For example, polymers such as polyethylene, having the same molecular configuration can be used for commodity purposes and also for the highly demanding applications such as prostheses, body implants, body armour etc. The vastly different final properties, from beverage containers to bulletproof armour, arises from the chemical structure controlled by polymer synthesis and molecular morphology achieved during processing.

Polymers are usually processed in the melt state, for semi-crystallised polymers, or in the rubbery state, for fully amorphous polymers. Among the conventional processing techniques, extrusion is one of the popular processes applied to manufacture polymer products since it is a continuous process capable of making products of any length. During extrusion polymer pellets are fed into the barrel from the hopper manually or vacuum fed automatically. The hopper often has a dryer on the top to remove moisture from the polymer pellets. When the resins enter the extrusion barrel, it is transported by the rotating screw which is powered by an electric motor. Since the rotating screw drags the resins and additives towards the die, the polymer molecules slide over each other, creating frictional heat which melts the material during drag flow. External heating devices provide additional heating. Once the polymer is melted,

it flows through a tailored die, which shapes it to a certain form. Then the plastic is cooled, and either cut into desired sections or rolled up.

With increasing awareness of reduction in the energy costs and greenhouse gas emissions it is getting essential to find energy efficient processing routes, which match the consensual request in most of the developed and developing countries. Conventional processing of polyethylene (PE) is usually performed at much higher temperatures, i.e. ≥ 160 °C, above its melting point. These high temperatures are prerequisite to avoid any interference of melt flow instabilities. However, there is a narrow 'extrusion window' situated in between the flow instability and flow induced solidification regions. The extrusion window is a specific melt flow singularity in extrusion, where polymer melts can be extruded smoothly without any distortion and the corresponding extrusion pressure shows a significant reduction. It implies that the extrusion window does offer potentially distinct advantages for energy-efficient processing. Therefore, numerous studies have been devoted to investigate the mechanism responsible for this window effect and flow criticalities of the extrusion window. However, the molecular origin of this window effect is still unrevealed. On the other hand, there is an apparent drawback of this window effect considering industrial applications since it is too narrow to be adopted in polymer processing. In industrial applications, the window effect should be at least several degrees in order to tolerate thermal fluctuations during processing. Considering the above unknown issues, this research is devoted to study the molecular origin of the window effect and to broaden the extrusion window with respect to the extrusion processing of polyethylene.

1.2 Objective of the dissertation

The prime objective of this research is to explore how to broaden the extrusion window of linear PE. To achieve the desired objective the reported study will consider:

1) The hydrodynamic condition of the window effect.
2) The molecular origin of the extrusion window.
3) The effect of nanofillers with distinct morphologies on the window effect of linear PE with a narrow molecular weight distribution.
4) The influence of molecular weight distribution on the extrusion window.

5) The hydrodynamic origin of stick-slip flow in the course of the rate-controlled capillary flow.
6) The influence of varying die geometries on flow criticalities.

1.3 Scope of the dissertation

Chapter 2 of the thesis gives brief overview of PE, from polymerisation to processing. The reviews in this chapter focus on flow behaviour and melt irregularities during capillary flow. Furthermore, research performed on the melt flow singularity of PE and the stick-slip transition is reviewed.

In Chapter 3, three different samples of high density polyethylene (HDPE) used in this study are characterised via Differential Scanning Calorimetry (DSC), Gel Permeation Chromatography (GPC) and Advanced Rheological Expansion System (ARES) to identify the molecular weight, polydispersity, melting point and crystallinity. The adopted methodology for the characterisation of the polymers is also introduced.

The molecular origin of the window effect is a matter of debate and is not well understood. Therefore a molecular weight dependence of flow criticalities will be introduced to elucidate the melt flow singularity of linear PE in chapter 4. In this work, the hydrodynamic origin of the window effect is elucidated and linked with stick-slip transition theory observed in a stress controlled rheometer. The molecular weight dependence of flow criticalities is quantitatively studied.

In Chapter 5, a bimodal PE having two distinct molar mass distributions is used to study the influence of molar mass and molar mass distribution on the window effect. The bimodal polymer shows an unexpected dual window effect. The nature of dual window effect is revealed and the influence of die geometries on the flow criticalities is investigated. A slip flow velocity test is performed to verify the appearance of slip flow in the extrusion window regime. Finally, the disentanglement mechanism of slip flow is verified with the help of ex-situ wide angle x-ray scattering (WAXS) experiments.

In Chapter 6, unimodal linear PE having broad molar mass distribution shows an intriguing broad extrusion window. The same rheological characterisations as mentioned in chapter 5 are performed to study the molecular origin and hydrodynamic conditions of the broad window effect.

From the reported studies it is apparent that the relaxation dynamics of a stretched chain has implications on the window effect. Thus, in Chapter 7, two carbon based nanoparticles with different particle morphologies are used to modify the relaxation dynamics of polymer chains. To have insight on the influence of the nano-fillers, different concentrations of the nano-particles are added to the polymer matrix. The linear PE chosen for the studies is the polymer having relatively narrow molecular weight distribution, used in chapter 4.

Finally, in Chapter 8 conclusions have been summarised and future work has been proposed.

Chapter 2 Literature review

2.1. Brief overview of polyethylene and processing

Polyethylene (PE) includes linear low density polyethylene (LLDPE), low density polyethylene (LDPE) and high density polyethylene (HDPE). It is the major member of the polymer family with 28 percent of total plastic demand in Europe in 2006, which is for the most widely used plastic, compared with the other four high-volume plastics including PP 19%, polyvinylchloride (PVC) 13%, polystyrene (PS) 7% and polyethylene terephthalate (PET) 7%[1].

With respect to the chemical structure of PE, such as the backbone length and branch density/length, the chemist can design the final polymer architecture by selecting distinct catalysts that include Ziegler Natta and metallocene/ post-metallocene catalysts etc. and choosing various polymerisation conditions including temperature, pressure and time.

PE was first synthesised by Fawcet and Gibson in laboratories of ICI in 1933 and ICI obtained the patent for its commercial production in 1937[2]. A waxy solid substance was formed in the reaction tube after polymerisation of ethylene and benzaldehyde in a high-pressure autoclave. The 'waxy solid' was termed as low density polyethylene (LDPE). The low density arises from the low crystallinity, resulting from high content of branches. During the free radical polymerisation, short and long branches are formed in transfer reactions. Therefore, polymer chains were difficult to pack into crystal. Although LDPE has poor mechanical properties due to the low crystallinity, it is still extensively used for packaging on account of its ease in processing.

The second breakthrough in polymerisation of ethylene occurred 20 years later. In 1950s[3] Ziegler synthesised high density polyethylene (HDPE) at low pressure and temperature using a heterogeneous titanium catalyst. Following that, Natta in 1954 applied this technology to synthesize polypropylene[4]. The heterogeneous catalyst system, today named after Ziegler-Natta, can yield linear PEs. The near absence of side branches enhances the crystallinity.

It is well known that the performance of a polymer product relies on molecular weight. Generally speaking, with increasing molecular weight, the final product properties such as modulus, abrasion and fatigue resistance are enhanced. Therefore, ultra high molecular weight polyethylene (UHMWPE) is selected as a material in prostheses applications, artificial knee and hip joints[5] and is also used for the development of high performance fibres[6]. However, the resulting problem with the higher molar mass polymer is difficulty in processing. PE is conventionally processed in the melt state by injection moulding, extrusion and film blowing or blow moulding[7], in which the processability is strongly dependent on melt viscosity. It is well known that the melt viscosity increases steeply with increasing molecular weight (M_w), obeying a power dependence of 3.4, when M_w is above a critical molar mass M_c[8], where the critical molar mass is dependent on the molar mass between entanglements. Owing to the high melt viscosity, UHMWPE is intractable in conventional processing route. In order to process UHMWPE, a more complicated route: solution-spinning[9], for instance, is adopted. However the final product profile is limited to fibre and tapes. Hence, there is a compromise between the ease of processing and the performance of product.

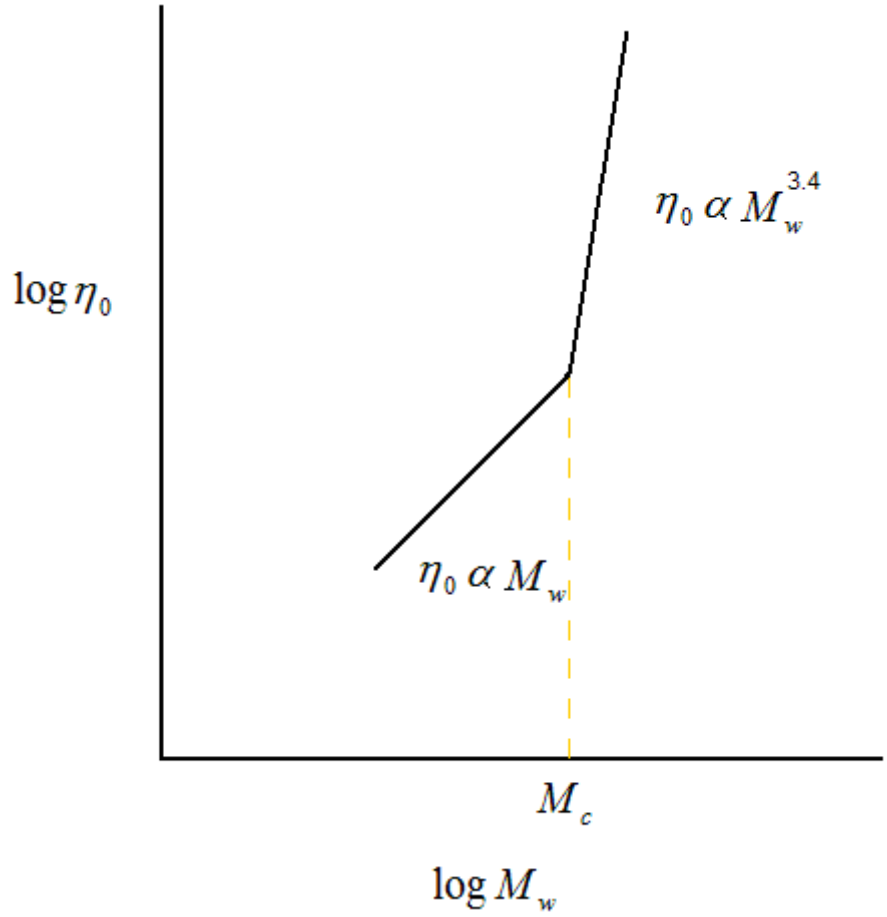

Figure 2.1: A plot of logarithmic zero shear viscosity vs. logarithmic weight average molecular weight[8].

On the other hand, the final product properties are also dependent on chain morphology developed during processing. One example is melt flow crystallisation behaviour, which can govern the final product properties and performance. Under flow conditions crystallisation behaviour exhibits significant differences compared with that under quiescent conditions. Firstly, flow induced crystallisation/ solidification causes a shift the melting point of the polymer to higher temperature compared to that at a quiescent state[10]. This means that under flow conditions nuclei and resulting crystalline phases can form above the thermodynamic melting point at the quiescent condition. Secondly, the crystallisation rate of the polymer melt can be enhanced during melt flow by promoting the formation of crystal nuclei[11]. Last but most important, it is observed and studied in detail that an interlocking crystal structure referred to as shish-kebab could develop under highly oriented melt flow conditions[12] . Particularly, in the early stages of crystallisation, precursors with a certain degree of order form under the melt flow condition. Once the size of a

growing precursor is beyond a critical dimension, it becomes a crystalline nucleus, inducing the formation of anisotropic crystallites. The relatively high molecular weight polymer chains possessing long relaxation time form a fibril core referred to as a shish and then short polymer chains crystallizes on it forming numerous stacks of lamellae named as a kebab. In summary, the final product properties such as mechanical and optical properties can be modified via various processing conditions.

2.2. Basic review of rheology

Rheological characterisation of thermoplastic materials can be performed in both solid state and molten state. Generally speaking, the final product performance is governed by solid rheology properties. On the other hand, the processability can be related to polymer melt properties. The rheological properties depend on material intrinsic nature and processing conditions. Viscoelastic polymer melt behaves neither as an elastic solid nor a Newtonian fluid.

2.2.1 The elastic solid (Hookean Solid)

An ideal elastic deformation obeys Hooke's law (i.e. the stress is linear with the strain) [13]. In simple tensile or compression deformation the imposed force is perpendicular to the surface of action.

$$\sigma_E = F_T / A \tag{2.1}$$

$$\varepsilon = \int_{L_0}^{L_1} \frac{dl}{l} = \ln \frac{L_1}{L_0} \tag{2.2}$$

$$\sigma_E = E\ \varepsilon \tag{2.3}$$

As a linear elastic material, the tensile stress σ_E is proportional to the strain ε.

2.2.2 The ideal fluid (Newtonian Fluid)

In shear deformation the imposed shear force is parallel to the surface.

$$\sigma = F_s / A \tag{2.4}$$

$$\gamma_S = x / h \tag{2.5}$$

$$\sigma = G\ \gamma_S \tag{2.6}$$

$$\dot{\gamma} = \frac{1}{h}\frac{dx}{dt} = \frac{v}{h} \tag{2.7}$$

$$\sigma = \eta\ \dot{\gamma} \tag{2.8}$$

The definition of variables is given in the list of symbols. An imposed shear stress causes deformation which increases steadily with time until the stress is released and the deformation is reversible and constant. σ is proportional to $\dot{\gamma}$ and the linear gradient is termed the coefficient of viscosity[13]. The coefficient of viscosity remains unaffected with imposed shear stress, and is independent of time.

2.2.3 Non-Newtonian fluids

Many materials in real life are non-Newtonian fluids, such as polymer melts, PVC pastes, ketchup, starch suspensions, paint, blood, shampoo etc. The σ - $\dot{\gamma}$ relationship of Newtonian fluids can be described by a single constant value, coefficient of viscosity. In non-Newtonian fluids, however, the relation between the shear stress and the strain rate is nonlinear, and can even be time-dependent. On the other hand, non-Newtonian fluids have visco-elastic properties, in which it behaves like a viscous liquid under certain conditions but it also shows partial elastic recovery after deformation[13]. There are three classes of non-Newtonian fluids:

1) Bingham body: this kind of material cannot be deformed until an internal structure collapses above a yield stress, following which $\dot{\gamma}$ increases linearly as the τ rises.
2) Pseudoplastic: Most polymer melt behave like a pseudoplastic. For this class of fluids, viscosity decreases as shear rate increases, referred to as a shear thinning effect.
3) Dilatancy: For this class of materials, μ (dynamic melt viscosity) increases with $\dot{\gamma}$, termed as shear thickening. A typical example is PVC plastisols over a limited range of shear rates[14].

In view of flow curve of pseudoplastic, it is apparent that the proportionality between shear stress and shear rate is not constant. Therefore the ratio of shear stress to shear rate is referred to as 'apparent viscosity' μ_a rather than coefficient of viscosity used for Newtonian liquids. It is to be pointed out that η_a at a given shear rate is the slope of secant drawn from the origin to the point of shear rather than the slope (tangent drawn) of the σ - $\dot{\gamma}$ curve. This is one of the reasons why it is termed as 'apparent viscosity'. One of the possible reasons to elucidate pseudoplastic behaviour is attributed to the reduction in entanglement points under orientation during the shear. For example, pseudoplastic, polymer melts, consists of extensively entangled and

randomly oriented molecular chains at quiescent conditions. Under shear the molecule chains tend to be aligned in the flow direction and become oriented. As a consequence, the reduced points of entanglements under shear give rise to the declining μ_a with increasing $\dot{\gamma}$ [13].

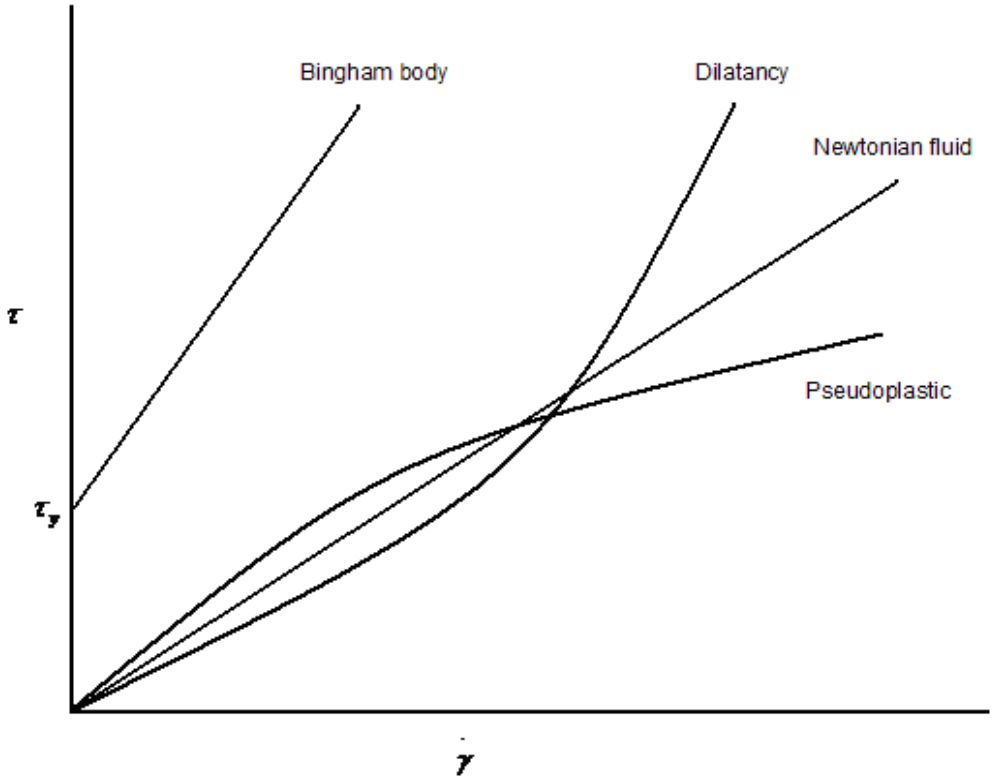

Figure 2.2: Shear stress vs. shear rate for Bingham bodies, Dilatant fluids and Pseudoplastic fluid compared with a Newtonian fluid. τ_y is the yield shear stress[13].

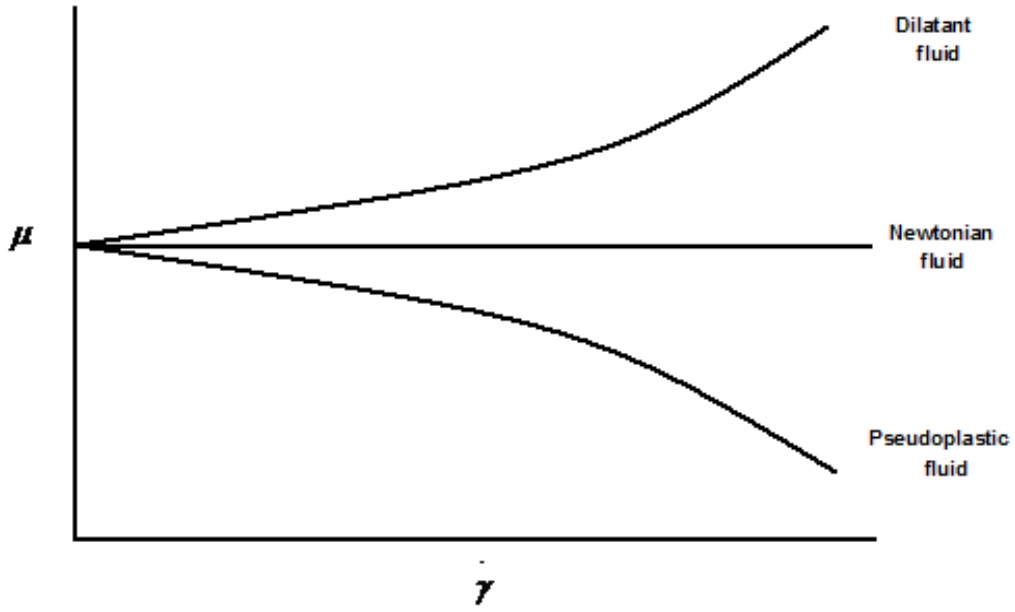

Figure 2.3: Viscosities as a function of shear rate for a dilatant fluid, a Newtonian fluid and a pseudoplastic fluid which possess the same zero shear viscosity at the intercept[13].

Many equations have been established to describe pseudoplastic behaviour [15]. However, only one of them which has been found to be used is Ostwald- de Waele equation:

$$\sigma = K(\dot{\gamma})^n \tag{2.9}$$

Non-Newtonian fluids have time-dependent flow behaviour, in which μ_a varies with time of shearing. Time-dependent flow behaviour arises from the disentanglement of molecules during the timescale of the applied shear. There are two basic time-dependent non-Newtonian pseudoplastic fluids:

1) Thixotropy: The longer the fluid undergoes shear stress, the lower the viscosity.
2) Rheopexy: The longer the fluid undergoes shear stress, the higher the viscosity.

Both thixotropy and rheopexy take a long time to recover to their initial state after cessation of shear. The viscosity of thixotropic or rheopectic material is dependent on the time of stirring compared to a pseudoplastic material which relies on the shear rate.

Polymer melts exhibit a viscoelastic response to stress or stain. The rheology of viscoelastic materials can be described by two components: one is dashpot representing the viscosity; the other is spring depicting the elastic modulus. There are two well-known models to simulate viscoelastic behaviour.

1) Maxwell model: a Newtonian viscous dashpot is placed in series with a Hookean elastic spring[16]. It can describe the stress relaxation at a constant strain. However, it fails to represent the creep behaviour at a given stress.
2) Kelvin-Voigt model: a Newtonian viscous dashpot is placed in parallel with a Hookean elastic spring. It can describe creep behaviour at a given stress. However, it fails to represent the stress relaxation at a constant strain

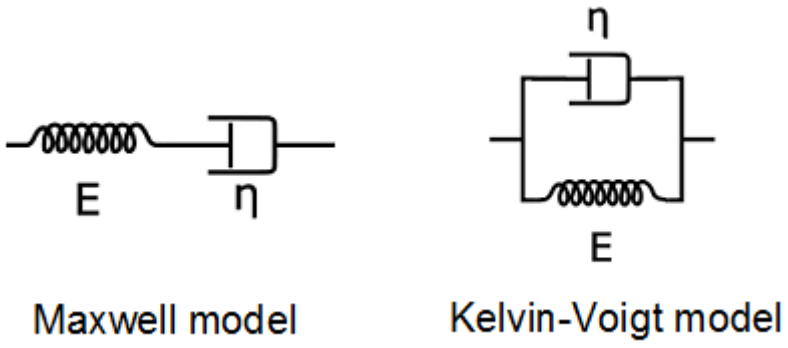

Figure 2.4: Schematic representations for Maxwell model and Kelvin-Voigt model.

2.2.4 Normal stress

The stress generated in flow conditions consists of two components: one is the shear stress, and the other is the normal stress. With respect to viscoelastic liquids such as polymer melts, the normal stress is apparent when a flow system undergoes a change in cross-section area. In the course of capillary flow polymer melt is forced to flow through a capillary or slit die to form a certain shape, where the change of cross-section area of polymer melt is significant. As a consequence, normal stress influences the flow behaviour during the entry of polymer melt into the die and dominates some features of polymer melt such as die swell.

2.3. Review of capillary rheology

Capillary rheometer is a widely used instrument to determine the rheological properties of polymer melts quantitatively. It covers the strain rate range of interest in practice processing from $1s^{-1}$ to $10{,}000s^{-1}$ and it can measure useful rheology properties which are essential for engineering purposes[20]. During capillary flow it is realised that the volumetric flow rate increases as the head pressure applied to a liquid at the other end of a pipe is increased. Based on a well-known Poiseuille law[17], the output rate-pressure difference relationship is postulated:

$$Q = \pi \Delta P R^4 / 8\eta L \qquad \textbf{(2.10)}$$

Where R is the radius of the capillary, L is the capillary length and η is the shear viscosity. Here η is assumed to be independent of $\dot{\gamma}$. However, in the real case of polymer melts, the melt viscosity is apparent shear viscosity rather than the coefficient of viscosity; hence it is referred to using the Greek symbol η rather than μ. For pseudoplastic η decreases as $\dot{\gamma}$ increases. There are several assumptions required to be considered to derive the quantitative relationship of rheological properties[13]:

1) The wall flow velocity of fluids is zero and there is no-slip at the capillary wall.
2) The fluid is time-independent.
3) The flow pattern is constant all along the capillary, i.e. laminar flow.
4) The flow is in the isothermal condition.
5) The volume of the polymer melt is incompressible.

2.3.1 Shear stress at wall

The shear stress at the capillary wall for a fully developed steady-state flow can be derived from the balance forces on a cylindrical element of fluid with length of dZ and radius r, in which the hydrostatic force in the flow direction F_1 should compensate the sum of hydrostatic force in the opposite of flow direction F_2 and drag force on the surface of the element F_3 [13]:

$$\sum F = 0 = F_1 + F_2 + F_3 \quad \textbf{(2.11)}$$

$$F_1 = P\ \pi r^2 \quad \textbf{(2.12)}$$

$$F_2 = -[P + (\partial P / \partial Z)dZ]\pi r^2 \quad \textbf{(2.13)}$$

$$F_3 = 2\pi r dZ \tau \quad \textbf{(2.14)}$$

On substituting equations **(2.12)-(2.14)** into equation **(2.11)**:

$$P\ \pi r^2 - [P + (\partial P / \partial Z)dZ]\pi r^2 + 2\pi r dZ \tau = 0$$

For a uniform pressured distributed capillary, $\partial P / \partial Z$ remains unaffected by Z. Therefore, the shear stress is obtained as:

$$\sigma_w = \frac{\Delta P}{2L / r} \quad \textbf{(2.15)}$$

The equation above applies to all time-dependent fluids and Newtonian or power law fluids. The shear stress can be determined if the pressure difference between the two ends of a capillary and the capillary geometries are known.

2.3.2 Shear rate at wall

The shear rate at wall can be calculated by the following assumptions. Considering the profile of flow velocity in a capillary, the linear velocity of the fluid at distance r from the centre is defined as v_z (when $r = R$, $v_z = 0$). Therefore, Q can be calculated by integrating the linear flow rate with respect to r between the limits 0 and R [20]:

$$Q = \int_0^R 2\pi r v_z dr = 2\pi \int_0^R r v_z dr \quad \textbf{(2.16)}$$

Considering the shear stress profile along the radius of capillary:

$$r = \frac{R}{\tau_w}\tau \quad \textbf{(2.17)}$$

Substituting equation **(2.15)** and **(2.17)** into equation **(2.16)** and rearranging the yield wall shear rate, $\dot{\gamma}_w$:

$$-\dot{\gamma}_w = \frac{1}{\pi R^3}(3Q + \Delta P \frac{dQ}{d\Delta P}) \quad \textbf{(2.18)}$$

Simplify the equation by assuming Q is linear with ΔP can give a convenient equation to determine the apparent shear rate, $\dot{\gamma}_a$:

$$\dot{\gamma}_a = \frac{4Q}{\pi R^3} \quad \textbf{(2.19)}$$

The above equation fails to represent the rheological properties of time-dependent polymer melt during shear flow. Hence the wall shear rate calculated from this equation is referred as apparent wall shear rate. In order to determine the true wall shear rate, $\dot{\gamma}_T$, the Rabinowitsch correction is used to justify the simple equation **(2.19)**:

$$\dot{\gamma}_T = (\frac{3n+1}{4n})\frac{4Q}{\pi R^3} \quad \textbf{(2.20)}$$

Where n is the power law index in equation **(2.9)**.

2.3.3 Corrections for capillary rheometer

2.3.3.1 Bagley correction

When measuring rheological properties during capillary flow of a high viscous polymer melt in capillary flow, there are three main sources of errors including reservoir and friction losses, ends pressure drop (Bagley correction) and non-parabolic velocity profile (Rabinowitsch correction)[18]. Regarding the end pressure drop, a total pressure drop measured by pressure transducer will involve some pressure contribution from extensional properties, such as entry pressure drop and exit pressure drop. The former is attributed to the convergent flow, referred to as elongational flow, occurring at the entrance of die, and the latter arises from elastic relaxation/ elastic recovery when the deformed pseudoplastic melt leaves the die. Hence, in order to attain the true capillary pressure drop, the effect of extensional properties should be extrapolated and deducted from the total pressure drop.

An end correction is recommended to derive the true wall shear stress τ_T. Historical method, Bagley correction[19], is used to deduct the end pressure drop, owing to extensional properties, from the total pressure drop. A plot of pressure drop versus die *L/R* ratio at varying fixed $\dot{\gamma}_a$ gives a series of straight lines and can extrapolated back to zero pressure. The intercept of straight line on zero pressure gives a correction on

capillary die length, referred to as effective die length. If the material only undergoes shear flow, the graph would have an intercept at the origin. If there is a degree of extensional flow including any elastic response and vortex flow, the intercept at ΔP =0 is at a negative L/R value, e. This value can then be used to calculate the true shear stress, τ_T, at the wall by the formula shown below[13]:

$$\tau_T = \frac{\Delta P}{2(L/R + e)} \quad \textbf{(2.21)}$$

However the Bagley correction requires extensive experimentation using at least three or preferably more capillary dies with large L/D ratio in order to achieve accurate results; on the other hand, if the data is non-linear due to melt compressibility or some wall slip, complex extrapolated method such as cubic or quadratic fit must be required to analyse the results. Therefore, it may not be accurate because of the non-linearity problems.

2.3.3.2 Cogswell correction

The Cogswell method was adopted to resolve the aforementioned problems in which the end pressure drop can be deducted from total pressure drop using an orifice die considered as 'zero length' die. The advantage of this method is its independence on extrapolation, resulting in the most accurate determination of extensional properties under various processing conditions. In case of the twin-bore rheometer, the extensional data such as extensional pressure drop are obtainable. On the other hand, the same conditions are used for both parts of the test (capillary and orifice die). Therefore, the experimental errors (due to operator, temperature etc) can be eliminated.

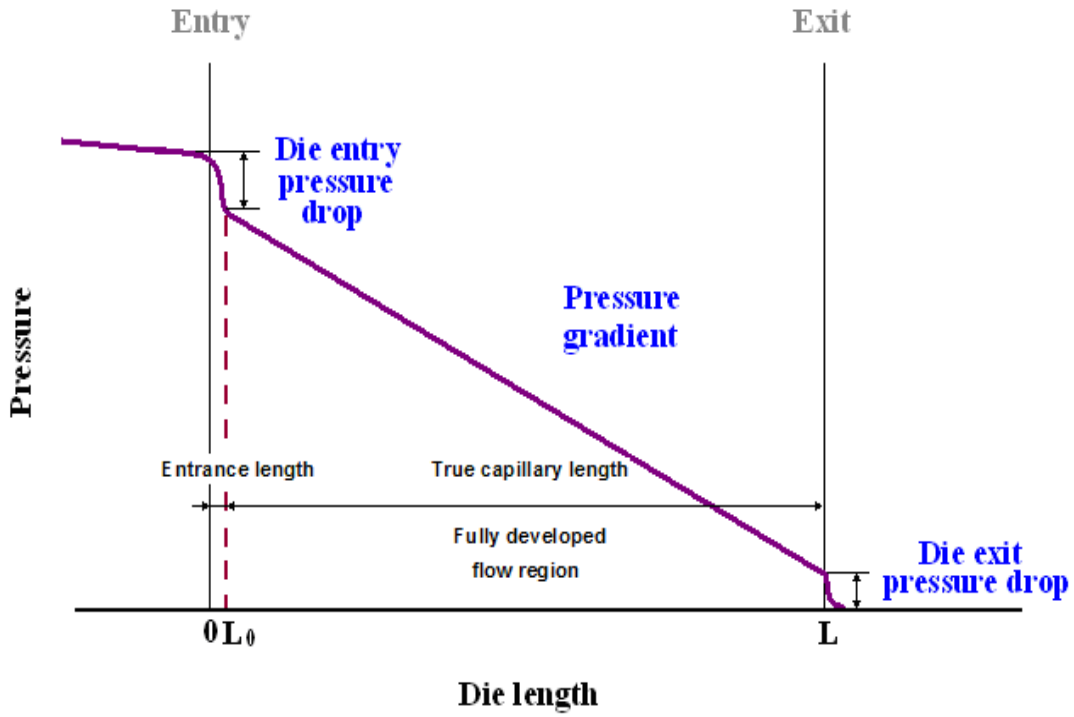

Figure 2.5(a): A schematic diagram of pressure drop distribution of capillary flow, showing the end correction including the entry and exit pressure drops.

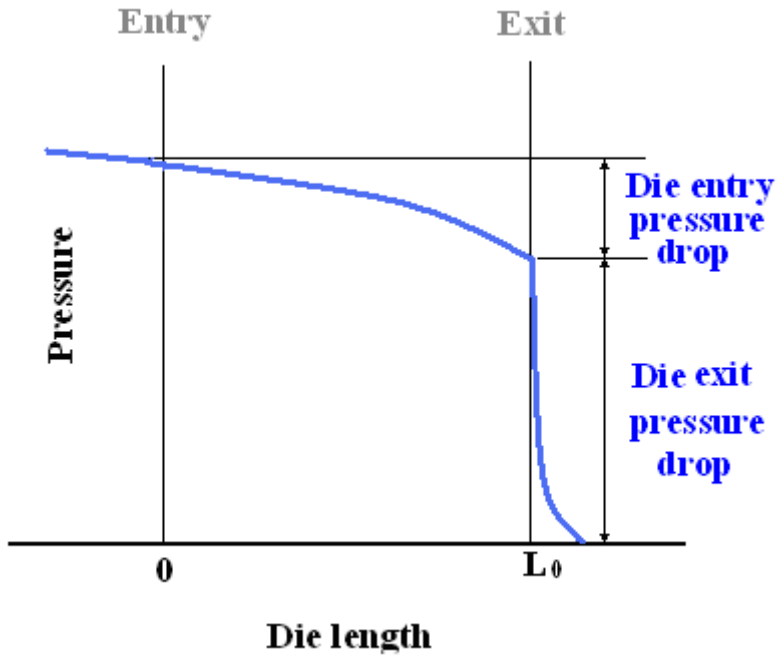

Figure 2.5(b): An enlarged schematic diagram of pressure drop distribution of capillary free flow (L_0=0.25mm).

In the Cogswell method, the corrected shear pressure corresponding to the capillary flow, P_C, can be attained by deducting the end pressure drop of orifice flow from the

total pressure drop of capillary flow, $P_C = P_L - P_0$. Therefore, the corrected wall shear stress resulting from Cogswell method is as following:

$$\tau_w = \frac{(P_L - P_o)}{2L/R} \quad \textbf{(2.22)}$$

Where: P_L is total pressure drop for capillary flow, including entry pressure drop, capillary pressure drop and exit pressure drop,

P_0 is total pressure drop for orifice die, 'zero die length' die, including entry pressure drop and exit pressure drop.

In practice, great accuracy is attained by combining a long die with an orifice die[20] as the difference between the L and the L_t, true capillary length, is negligible when L/R ≥32.

2.3.4 Die swell

Die swell is a common effect occurring in polymer extrusion. It is described that the extrudate cross-section area is greater than the cross-section area of die. Numerous studies have been devoted to study die swell and the molecular origin of it[21].The consensus is that die swell arises from elastic recovery[22]. In quiescent conditions polymer chains are coiled up in an almost random status. During the convergent flow at the die entry, the molecular chains are orientated and tend to align in the flow direction. The stretched chain conformation resulting from chain orientation can be maintained during capillary flow under a certain shear. However, once the polymer melt is extruded out of the die, the orientated chains begin to coil back due to the elastic recovery, resulting in longitudinal shrinkage and lateral expansion. It is also found that the leading ends of the extrudate have a convex shape after shrinkage[13] . It supports the fact that higher shear rate occurs close to the die wall leading to higher shrinkage on the outside surface of the extrudate.

The following effects of various flow conditions on die swell are reported in literature:

1) Die swell increases with apparent shear rate up to a limit rate which is near to but below the critical shear rate of melt fracture. Beyond this point, die swell declines until the melt fracture occurs[21(d)].
2) Die swell decreases with increasing temperature at a fixed shear rate[21(d)].

3) Die swell decreases with the length of the die at a fixed shear rate[21(a)(c)]. This effect is consistent with the fact that greater residence time in the capillary reduces the die swell[21(g)].
4) Die swell enhances with reservoir-to-capillary diameter ratio below a certain value[21(e)].

Regarding the influence of molecular characteristics on die swell, there are many contradictory results. Beynon *et al.* [21(d)] studied the effect of molecular weight on die swell using LDPE. They found that the die swell increases with M_w. However, Metzger and Matlack reported the opposite results using HDPE[21(g)]. With respect to the impact of molecular weight distribution, it is found that die swell increases with the ratio of M_w / M_n [21(j)]. The reported contradictions in the results can be attributed to distinct molecular characteristics of the synthesised polymer such as M_w, M_w / M_n and branch density.

2.3.5 Melt irregularities

According to the pioneering studies performed by Nason[23], Tordella[24], Bagley[25] and others[26], it has been observed that melt irregularities, also termed as 'melt fracture', emerge when $\dot{\gamma}_a$ reaches or goes beyond the critical value. The melt irregularities are classified into two classes: one is melt instabilities and the other is extrudate distortions. Based on numerous experimental observations of melt fracture, it is found that melt instabilities and extrudate distortion often take place simultaneously. However, the extrudate distortion can occur without any sign of melt instabilities, on the other hand, the melt instabilities always give rise to the extrudate distortion.

The melt irregularities of PE have been widely studied including low density polyethylene (LDPE) and high density polyethylene (HDPE). HDPE is the polymer studied in this thesis. At the lowest shear rate, both classes of materials show a smooth and glossy extrudate. With increasing $\dot{\gamma}_a$, distinct melt irregularities emerge at varying flow criticalities.

The first emergence of extrudate distortions, surface irregularity, is situated at the upstream flow pattern. The surface irregularity, also referred to as surface melt fracture, loss of gloss, surface roughness or 'sharkskin', is characterised by a series of

ridges perpendicular to the flow direction. The effect of molecular characteristics on sharkskin has been studied by Howells and Benbow[26(c)]. It was found that molecular weight has little effect on sharkskin whereas molecular weight distribution appears to play an important role in surface irregularity. It has been known that:
(i) Broad molecular weight distribution lowers the susceptibility to sharkskin.
(ii) Low swelling ratio and higher the value of power law index n (in equation 2.9) enhance the degree of sharkskin.

The mechanism involved in the development of sharkskin is based on experimental observations. Sharkskin is dependent on the extrudate velocity (shear rate) and temperature. One of the possible reasons for sharkskin is attributed to the elastic energy released at the exit of the die. Once the polymer melt is extruded out of the die, the huge pressure differences give rise to a drop in the flow velocity. As a consequence, the tensile forces build up at or near the extrudate surface exceeding the tensile strength of the melt, this results into tearing of the surface followed by stress release. With further extrusion the sharkskin repeats when tensile force goes beyond the surface tensile strength.

There is a unique flow behaviour, known as flow discontinuity, occurring when $\dot{\gamma}_c^{\,p}$ or $\sigma_c^{\,p}$, the critical shear rate/shear stress corresponding to the onset of pressure oscillation, is attained. This anomalous pulsing flow, notably with HDPE, was first studied using a stress-controlled rheometer by Bagley[25]. In Figure 2.7 it was found that there was a sudden jump in Q when ΔP attains a critical value at steadily increasing pressure. In reverse the onset appearance of discontinuity is at a lower pressure C. A consistent result is obtained with a rate-controlled rheometer. When the critical apparent shear rate is attained, a stick-slip flow is observed during the melt flow. It is characterised by periodic bulk distortion accompanied with pressure oscillation, where the relationship between shear rate and shear stress breaks down. It is observed that the extrudate shows a spiral thread and a straight rod-like thread alternatively. The mechanism responsible of periodic bulk distortion is widely accepted to arise from capillary flow since this effect is not observed in capillary free flow with a zero-length die[21(i)]. The periodic bulk distortion appears to be related to slip flow effect and melt compressibility. Regarding the role of molecular weight and

molecular weight distribution on flow criticalities, it is found that the onset of oscillatory flow decreases with increasing weight average molecular weight and the broader the molecular weight distribution the higher $\dot{\gamma}_c^{\,p}$.

Since flow instabilities set up the boundary condition of polymer processing, numerous studies have been devoted to investigate the nature of flow instabilities by adjustment of either processing conditions or polymer parameters in order to minimise flow instabilities and broaden the conventional processing window. Two molecular origins are suggested to elucidate the appearance of flow discontinuities. The first possible reason is stick-slip flow owing to the polymer desorption from the melt–wall interface[27]. The polymer chains closest to the capillary wall fail to adsorb on the capillary wall and, as a consequence, a slip flow occurs. Another approach is suggested that the stick-slip transition arises from the disentanglement of the adsorbed chains from the bulk at the melt-wall interface[28]. It has been widely accepted that the first mechanism responsible is related to a low surface energy die, viz. a die coated by processing aid to reduce surface energy of capillary wall. By contrast the disentanglement of the adsorbed chains from the bulk free chains is likely to occur within the capillary flow of a high surface energy die, viz. no-coating metal die.

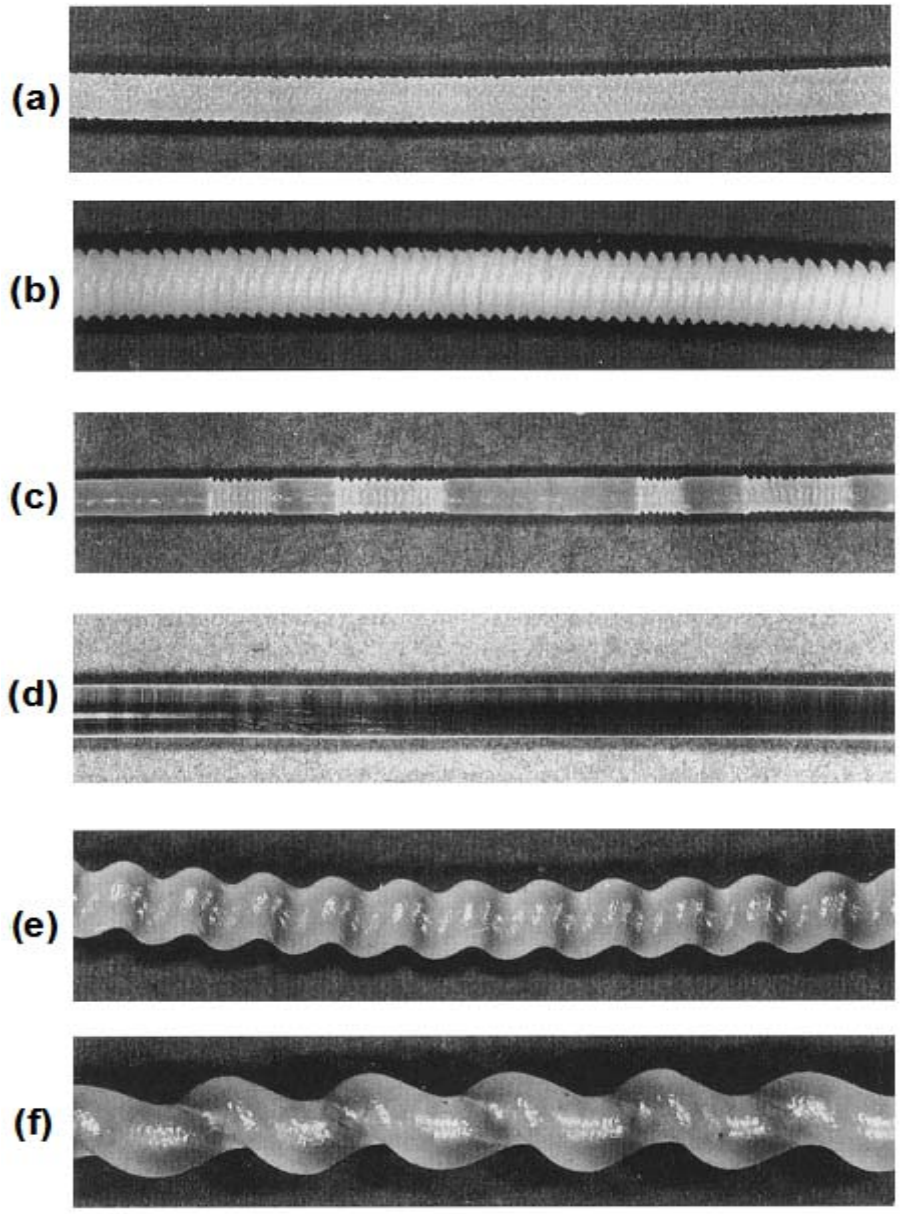

Figure 2.6: Various extrudate distortions under melt fracture (a-b) shark-skin of LLDPE and HDPE extrudates,(c) the extrudate of HDPE shows periodic distortions (d) smooth extrudate of PS in slip flow (e-f) Helical distortion observed in extrusion of PS and PP at high shear rate (From Agassant *et al.*, 1991[29]).

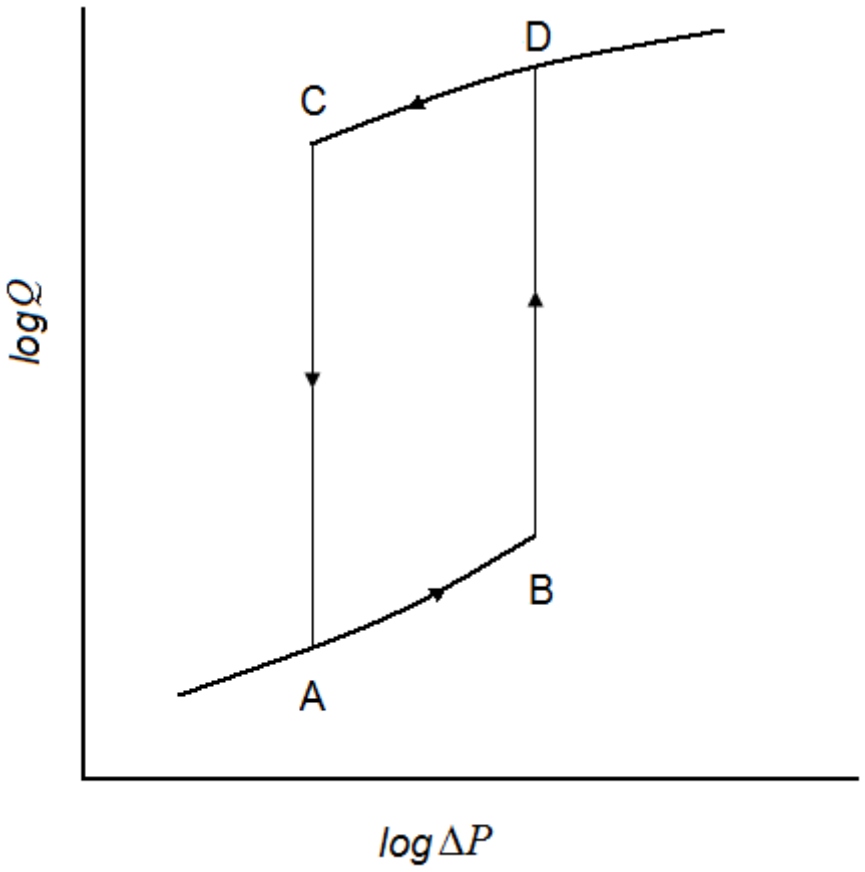

Figure 2.7: A schematic diagram of dual output flow curve during pulsing flow of HDPE at varying imposed pressure using a stress-controlled rheometer (after Bagley *et al.*, 1958[25(a)])

There is no periodic bulk distortion occurring in the melt flow behaviour of LDPE. Nevertheless, both LDPE and HDPE display gross shape distortions, known as 'melt fracture', when the shear rate reaches a critical value. The gross shape distortion starts from helical distortion initially and becomes chaotic and uneven with a further increase in the apparent shear rate. It is to be noted that the critical shear rate is usually related to the apparent wall shear rate corresponding to the onset appearance of distortion, rather than the strictly corrected true shear rate at the wall. It seems to reach an agreement in literature that the gross shape distortion arises from the entry orifice. The critical apparent shear rate for the onset of helical distortion, $\dot{\gamma}_c^{\,h}$, increases with temperature significantly. However, there is less impact of temperature on the critical shear stress[26(j)].

2.4 Extrusion window of linear polyethylene

There is an unusual melt flow effect observed in the course of capillary extrusion of linear polyethylene (PE) as depicted in Figure 2.8. It was found that a significant

pressure drop occurs in a narrow temperature window, referred to as an 'extrusion window' at or around 150°C[30]. Within this extrusion window, a reduced flow resistance was accompanied with smooth extrudate and comparatively little die swell. The observed specific melt flow singularity during extrusion of linear polyethylene is not predictable and explainable from conventional rheology. Besides the intrinsic scientific interest, this extrusion window is also a subject for the development of energy-efficient processing, since it has an indisputable advantage in practical processing on account of the low temperature and pressure processing condition, combined with the absence of extrudate distortions.

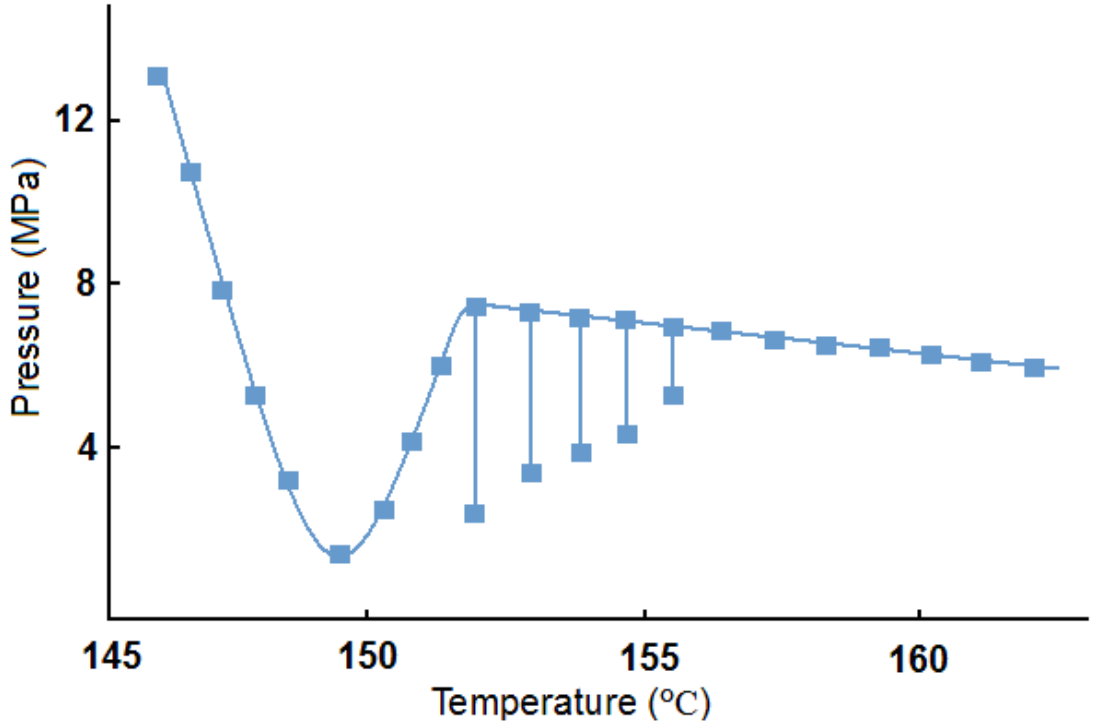

Figure 2.8: A plot of pressure vs. temperature showing the window effect. The vertical lines symbolize oscillations in pressure[31].

Since the first discovery of melt flow singularity of linear polyethylene, numerous studies have been devoted to explore the hydrodynamic origin of the extrusion window[31]. However, the molecular origin of the melt flow singularity is still not clearly elucidated[31]. Keller *et al.*[30] suggested that such a sudden pressure drop in extrusion window would not arise from rheological considerations alone and must result to the formation of a high entropy symmetric phase, such as the possible hexagonal packing of chains. It is also known that high chain mobility along the c-axis exists in the hexagonal phase of linear polyethylene due to weak Van der Waals

interaction between the intermolecular chains. If it is possible to attain this kind of mobile mesophase in a flexible polymer, typically polyethylene during extrusion window, the molecular origin of extrusion window could arise from elongation-flow-induced orientation inducing the liquid to mesophase transition[30]. Figure 2.9 shows the schematic plot of free energy versus temperature in which the G_h represents the mobile hexagonal phase lying between G_L (liquid) and G_o (orthorhombic) having a negative slope. According to thermodynamics, the hexagonal phase cannot appear in quiescent condition since G_h is always situated above G_o or G_L. However, under flow condition all the Gibbs free energies shift to high value. However the effects of flow rate on G_h.and G_L are more pronounced compared with G_o, causing the greater shift in the free energy curves of G_L and G_h compared to G_o. Such a shift causes appearance of the thermodynamically stable hexagonal phase.

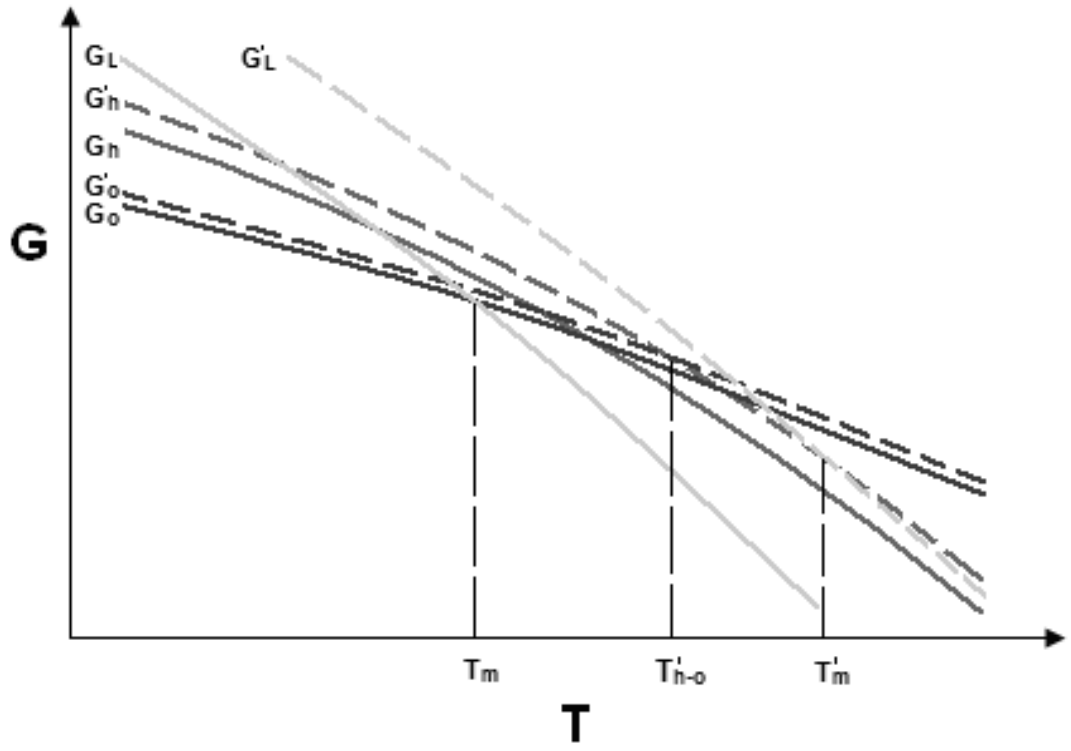

Figure 2.9: Schematic plot of Gibbs free energy, G, versus temperature, T. At quiescent condition the free energy for liquid phase, G_L, orthorhombic phase G_o and hexagonal phase G_h are shown by solid lines. Under flow condition the constrained liquid phase G_L', orthorhombic phase G_o' and hexagonal phase G_h' shift to high value as shown by dash lines. In flow conditions the melting temperature increases from T_m to T_m'. And a narrow temperature interval in between T'_{h-o} and T_m' corresponds to a thermal dynamic stable hexagonal phase[30].

Following this line of research, Kolnaar together with Keller[31] dedicated a part of his research to study the possibility to attain such a mobile hexagonal phase in the course

of capillary flow. However, his results were in disagreement with the Keller's earlier hypothesis. In capillary flow, the elongational flow induced orientation strongly relies on the convergent flow at the die entrance. Smit and Van der Vegt[32] studied the quantitative relationship between die entrance angle (2α) and the critical apparent elongational flow rate, defined as the onset of sharp pressure upswing during extrusion, leading to blockage of the flow.

$$\dot{\varepsilon}_c = K\,\dot{\gamma}_c \tan 2\alpha \qquad \textbf{(2.23)}$$

Where K is a constant;

$\dot{\varepsilon}_c$ is critical elongational flow rate corresponding to the onset appearance of flow induced solidification.

$\dot{\gamma}_c$ is critical apparent shear rate associated with the first appearance of the flow induced solidification.

2α is the die entrance angle.

According to the equation (2.23) proposed by Smit and van der Vegt, it can be concluded that the 'strength' of the elongational flow increases with the die entrance angle (2α). If Keller's hypothesis is correct, critical apparent shear rate, $\dot{\gamma}_c^{\,w}$, corresponding to the onset appearance of extrusion window should decrease with die entrance angle. However, Kolnaar found that $\dot{\gamma}_c^{\,w}$ remains unaffected by varying die entrance angles. Moreover, it was also observed that the extrusion window also emerges in the constriction-free pure tube flow (polymer extruded through a rheometer barrel). These systematic studies lead Kolnaar and Keller to conclude that the 'window' effect does not rely on convergent flow. Therefore elongation-flow-induced orientation fails to explain the mechanism of melt flow singularity of linear polyethylene.

Following this observation, Kolnaar conducted his further research to study the effect of die length and die diameter on flow criticalities of the extrusion window. The observations were that change in die geometry had less or no effect on the existence and appearance of the extrusion window. On the other hand, capillary flow is a prerequisite for the existence of the window effect since the melt flow singularity vanishes on capillary free flow using an orifice die (orifice alone without a capillary).

The next question is whether or not shear flow can induce the phase transition from orthorhombic to hexagonal phase/mesophase. Therefore, Kolnaar et al[33] performed real-time wide angle X-ray scattering (WAXS) experiments using a high intensity X-ray beam to explore the molecular origin of the extrusion window of linear polyethylene. According to the plot of intensity versus double Bragg reflection angle (*2q*) at an extrusion window temperature, viz. 149°C, a single weak reflection (*inter-spacing d = 0.220±0.003*) arises from crystalline phase located at the shoulder of broad peak corresponding to the melt amorphous phase. On subtraction of the observed diffraction pattern with the X-ray diffraction pattern obtained in the quiescent condition, a clear peak was observed. The emergence of the single reflection leads to the conclusion that the presence of high-temperature crystalline phase arises under the applied flow conditions. The incoming question was to address the nature of this crystalline phase. The authors attributed the single reflection to the high symmetry hexagonal phase, emerging during the capillary flow.

Meanwhile van Bilsen[34] also studied the phase transition occurring in the window effect via the same technique (i.e. in-situ X-ray scattering (WAXS) experiments). He also found that there was only one weak reflection besides the amorphous scattering at 150±1°C. Moreover, according to his results, all the characteristic reflections from the orthorhombic phase vanished instantaneously at 150±1°C. The reasons why the unique single reflection observed at 150±1°C cannot arise from the orthorhombic phase, are not only because the single reflection is located at $2\theta_{hkl}$=20.9° which is 0.8° below the Bragg reflection angle of $(110)_{Orth}$ at 149±1°C, but also because the intensity of the single reflection at 150°C was stronger than the $(110)_{Orth}$ reflection at 149°C.

In accordance with the preliminary experiments, a single reflection was also observed from constrained melting experiments of ultra-oriented ultra-high molecular weight PE fibres[35] (e.g. $2\theta_{hkl}$=20.42°/ d=0.221nm at 152°C) and slightly crosslinked polyethylene fibre[36] (e.g. $2\theta_{hkl}$=20.3±0.3°/ d=0.222±0.003nm at 150°C [36(b)]). The observed single reflections from the above studies reveal the existence of hexagonal phase. With respect to the Bragg reflection angle ($2\theta q_{hkl}$=20.9°/d=0.216) at 150±1°C observed in Bilsen's experiments, it is in between the $2\theta_{110}^{Orth}$ and $2\theta_{100}^{hex}$. Considering that the shear flow in capillary is not strong enough to constrain the

polymer chains, the single reflection at $2\theta_{hkl}$=20.9°/d=0.216 was attributed to the shear induced mesophase with symmetrical hexagonal packing rather than a hexagonal phase.

After numerous experiments, including rate-controlled rheology and stress-controlled rheology, a consensus has been reached that the extrusion window of linear polyethylene arises from slip flow. Kolnaar[37] illustrated the window effect arising from the slip flow and attributed it to either 'pure wall slip' or 'slip film flow'. In the pure wall slip, the polymer chains close to the capillary wall are fully desorbed from the capillary wall and they simply flow along the wall. Whereas in the slip film flow a thin layer of interface is formed close to the wall favouring a much reduced viscosity compared to the bulk. However, Kolnaar did not give a clear elucidation regarding the molecular origin and hydrodynamic origin of the window effect.

In addition, Kolnaar pointed out that the hydrodynamic boundary conditions of the window effect were governed by two critical shear rates corresponding to the onset of window effect and helical distortion, $\dot{\gamma}_c^{\,w}$ and $\dot{\gamma}_c^{\,h}$ respectively. In detail, $\dot{\gamma}_c^{\,w}$ gives the lower limit hydrodynamic boundary condition and the upper limit is dependent on $\dot{\gamma}_c^{\,h}$. Within the extrusion window regime of HDPE (148~152°C) it was found that both surface distortions and periodic bulk distortions were absent. Whereas, gross shape distortions can emerge in the extrusion window regime. Regarding the molecular weight dependence on flow criticalities, Kolnaar pointed out that $\dot{\gamma}_c^{\,w}$ scaled as a -4.0 power of the molecular weight. On the other hand, $\dot{\gamma}_c^{\,h}$ also showed a power law dependence on the molecular weight which scaled as -1.5. Two characteristic boundary conditions had an intersection in the plot of upper limit $\dot{\gamma}_c^{\,h}$ and lower limit $\dot{\gamma}_c^{\,w}$ against M_w. The M_w corresponding to this intersection point was referred to the lower limit molecular weight (M^*). Kolnaar estimated the critical molecular weight to be 10^5 g mol^{-1}, i.e. Kolnaar argued that no window effect will be anticipated if the selected HDPE has molecular weight below M^*.

2.5 Stick-slip transition

It is observed that linear PE might undergo a superfluid-like stick-slip transition in the course of stress-controlled capillary flow. The transition was described by a considerable discontinuity in the flow rate, occurring when the shear stress reaches a critical value[38]

It was found that the critical wall shear stress σ_C corresponding to the onset of superfluid like stick-slip transition was linear with temperature. In addition, the rescaled stress σ_C / T remained constant, suggesting that the stick-slip transition occurred at a critical chain deformation. The critical wall shear stress σ_C was found to scale with the -0.5 power of the molecular weight and scaled linearly with temperature ranging from 200 to 260°C.

Wang[39] first quantitatively characterised the superfluid like stick-slip transition. These studies were in contrast with a spurt flow phenomenon observed in rate-controlled rheometer. An extrapolation length b was first addressed by Wang to quantify the magnitude of a large discontinuity of flow rate occurring during the slip-stick transition at a critical stress. b was defined as:

$$b = V_s / \dot{\gamma}_T \tag{2.24}$$

Where V_s is slip velocity; $\dot{\gamma}_T$ is the true wall shear rate.

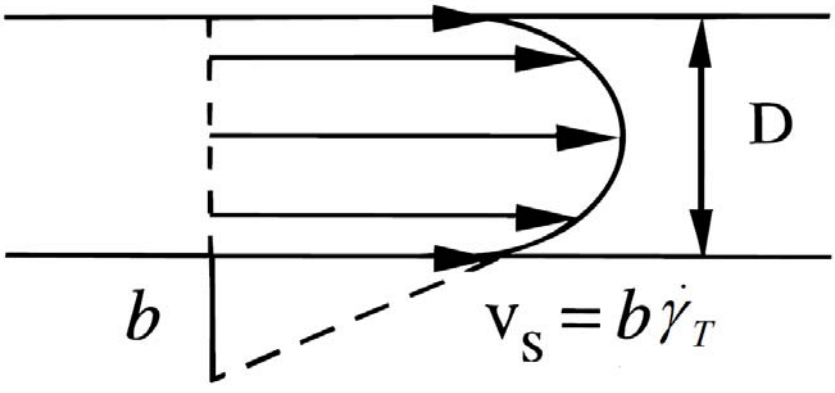

Figure 2.10: a schematic diagram of slip flow occurring in a capillary die. Where D is the die diameter and the extrapolation length *b* is related to the true shear rate at the wall and apparent slip velocity, *Vs*[39].

The volumetric output rate during slip flow consists of slip flow component and stick flow component:

$$Q_S = Q_C + \pi R^2 V_s \quad \textbf{(2.25)}$$

Where Q_S is the entire slip flow volumetric output rate; Q_C is volumetric output rate corresponding to stick flow component in slip flow; R is die diameter.

Substituting equation (2.19), here $\dot{\gamma}_a = \frac{4Q_s}{\pi R^3}$ and $\dot{\gamma}_T = \frac{4Q_c}{\pi R^3}$, and equation (2.24) into equation (2.25) yield:

$$b = \frac{R}{4}(\dot{\gamma}_a / \dot{\gamma}_T - 1) \quad \textbf{(2.26)}$$

According to extensive study of stick-slip transition at varying temperature, it was found that b scaled as a 3.4 power of the molecular weight and was linear with apparent shear viscosity, η_a, but was independent of temperature. It implies that b is an intrinsic material property.

The molecular weight dependence of critical wall shear stress σ_C and extrapolation length b implies the molecular origin of stick-slip transition and slip flow may be due to the disentanglement mechanism. When the critical wall shear stress σ_C is attained, a sudden slip flow emerges as the adsorbed chains disentangle from the surrounding free chains. As a consequence, the materials of die construction may not have any impact to the appearance of stick-slip transitions, as long as the melt/wall interfacial interactions can be sustained during the disentanglement of adsorbed chains from free chains. According to disentanglement mechanism, the adsorbed chains at melt/wall interfaces after disentanglement from bulk free chains should remain attaching on the metal surfaces of inner capillary wall rather than being extruded out through the die. It coincides with a spectroscopic study of polyethylene-metal interface after peeling[40].

An anomalous stick-slip transition occurred when the temperature was below 200°C, in which the rescaled critical shear stress σ_c / T decreased with lowering temperature and the extrapolation length b increased as the temperature declined. This anomalous effect at lower temperature was attributed to the effect of flow-induced mesophase on disentanglement mechanism. According to Brochard and de Gennes' theory[41], Wang derived an expression to quantify the critical shear stress (σ_c) for the stick-slip transition.

$$\sigma_c = \frac{\nu k_B T}{D^*} \tag{1.26}$$

Where σ_c is the critical shear stress for the stick-slip transition,

ν is the adsorbed chain density ,

k_B is Boltzmann constant ,

T is temperature,

D^* is the entanglement distance.

It was found that σ_c / T remains unaffected at high temperature, from 200°C to 260°C. However, σ_c / T decreases with lowering the temperature (<200°C) based on experimental results. Considering the increase in adsorbed chain density as the temperature decreases, it appears that entanglement distance should increase further with lowering temperature. Such a possibility leads Wang to suggest that flow-induced mesophase should appear at lower temperatures. Moreover, such an oriented structure at the melt-wall interface eases the disentanglement of tethered chains from the free chains at or beyond the critical shear stress.

2.6 Reptation time

A well-established reptation model[42] has been used to represent constrained chain dynamics. In this model, a polymer chain is surrounded by or entangled with neighbouring chains. On account of this topological constraint, long range displacements are only possible by snake-like motion along the imaginary tube axis. The relaxation time λ_{rep} for a constrained chain to vacate the original tube, viz. reptation time, is proportional to the square of the contour length L divided by the reptation velocity ν ($\lambda_{rep} = L/\nu$), in which the contour length is linear with the molecular weight and the reptation velocity is proportional to the reciprocal of molecular weight. Hence, the reptation time can be quantified in terms of molecular weight:

$$\lambda_{rep} \sim \frac{M_w^2}{M_w^{-1}} \sim M_w^3 \tag{2.27}$$

2.7 Molecular characterisation of linear polyethylene via rheology route

Mechanical and physical properties of polymer depend on molecular weight, M_w, and molecular weight distribution, MWD. In principle it is possible to invert this relationship so the molecular characteristics from rheology data could be determined.

In the recent two decades numerous methods were developed to determine M_w and MWD from the melt rheology data of polymer. To classify, there are two types of model, viz. 'Viscosity Model' and 'Modulus Model'.

The viscosity model is based on the relationship of M_w and MWD with the viscosity of polymer melt at a certain shear rate. It has been reported that M_w of a given polymer can be estimated from zero shear viscosity, η_0. For a linear polymer, η_0 is linear with M_w[43]. With increasing the molecular weight beyond a critical value, M_c, there is a power law relationship between η_0 and M_w, viz. $\eta_0 = M_w^{3.4}$ [44]. On the other hand, many analytical viscosity models have been developed to predict the MWD from a rheological flow curve of melt viscosity, η, vs. shear rate, $\dot{\gamma}$[45].

The modulus model presents viscoelastic properties of a polymer. In the modulus model the relaxation spectrum can be converted from the time domain to the molecular weight domain, followed by a regularized integral inversion to recover the MWD curve[48].

$$\frac{G(t)}{G_N^o} = \left(\int_{\ln(M_e)}^{\infty} F^{1/\beta}(t,M) w(M) d(\ln M) \right)^{\beta} \qquad \textbf{(2.28)}$$

Where *G(t)* is relaxation modulus normalized by the plateau modulus, G_N^o, *F(t,M)* is a kernel function describing the relaxation behaviour of a monodisperse component of molecular weight M_w. The weight fraction of the MWD function is represented by *w(M)*. The exponent, β, is a parameter associated with the mixing behaviour of the chains. For instance, β is 1 for simple reptation and 2 for double reptation theory. M_e is the average molecular weight between entanglements.

In this thesis double reptation theory was applied in modulus model[46]. Compared with the single reptation model proposed by de Gennes[42], double reptation theory takes account of the contribution of higher-order entanglements and the effect of the tube dilation. The β imposed from the double reptation theory is a value of circa 2, in fact slightly higher than 2[47]. One of the successful algorithms is developed by Mead[48]. It is

commercialised by TA instruments in their Orchestrator software and is adopted to predict the M_w and MWD as described in chapter 3 of this thesis.

2.8 Summary

In this chapter a brief overview of polyethylene and the fundamental theory of rheology were reviewed. Regarding the extrusion window, the specific singularity in extrusion behaviour of linear polyethylene does have potential to enhance energy efficient processing on account of the significant reduction in extrusion pressure and lower extrusion temperature. Whereas the extrusion window reported in the early publications is too narrow to be adopted in commercial polymer processing, it has been revealed that the molecular origin of stick-slip transition emerging at a critical shear stress is attributed to the disentanglement of the adsorbed chains on the capillary wall from the free chains in the bulk. If the stick-slip transition and the extrusion window can be linked together by a quantitative molecular weight dependence of flow criticalities, the nature of two effects can be attributed to the same mechanism. If the extrusion window arises from the disentanglement mechanism, it is a key to broaden the extrusion window, which will be addressed in the research study.

Chapter 3 Experimental

The materials used in this study and the methodology applied to study the extrusion window will be stated in this chapter. Three linear polyethylenes with distinct molecular characteristics were selected to study the effect of molar mass distribution on the window effect. Following that two nano-sized fillers, viz. carbon nanotubes and carbon black, were added into one of the linear polyethylenes to investigate the influence of nanofillers on the window effect. Regarding the experimental methodology, three neat polymers were characterised via gel permeation chromatography (GPC) and advanced rheological expansion system. With regard to the nanocomposites, scanning electron microscopy (SEM) was applied to observe the filler morphologies and filler distribution/dispersion in the polyethylene matrix. The main experimental work was carried out via a twin-bore capillary rheometer. Here the window effect, flow behaviour and extrudate profiles were studied and recorded. Finally the extrudate surface orientation corresponding to the window condition was studied via micro-beam wide angle X-ray scattering in ESRF.

3.1 Materials

The polymers under investigation were grades of high density polyethylene (HDPE) supplied by Borealis and SABIC Europe respectively and referred to as PE-A, PE-B and PE-C.

Table 3.1: Polymer characteristics results from GPC[a]

Sample	Supplier	Modality	M_w (g mol^{-1})	M_n (g mol^{-1})	M_w/M_n	M_z (g mol^{-1})
PE-A	SABIC	unimodal	89,750	24,500	3.7	255,00
PE-B	Borealis	bimodal	170,500	12,200	14.0	825,000
PE-C	SABIC	unimodal	303,000	17,450	17.4	1,785,000

Multi-walled carbon nanotubes (MWCNTs), characterised with 50μm length and 20nm diameter, were supplied by Chendu Institute of Organic Chemistry, Chinese Academy of Sciences. Nano-sized Carbon black (CB) with 28nm diameter was supplied by CABOT. Two carbon-based nanofillers, MWCNTs and CB, were homogeneously distributed into PE-A using a physical route. The loading of MWCNTs and CB in PE-A are 0.2wt% and 0.6wt% respectively. PE-A

[a] Refer to the molar weight distribution curves, figure 4.1 and 4.2, in chapter 4, and the material data sheets are included in Appendix A.

nanocomposites were kindly prepared by Dr Jie Jin via a confidential physical router in the Department of Materials, Loughborough University.

3.2 Methodology

3.2.1 Differential Scanning Calorimetry (DSC)

A standard TA DSC Q200 was adopted to perform thermal analysis. Each sample was weighed by a precise balance and encapsulated in a standard aluminium pans and lids. An identical empty pan with lid was used as a reference. Nitrogen flow rate into the thermal cell was set-up at 50cm^3 min^{-1}. DSC was calibrated using indium and tin.

Thermal analysis was performed to determine the melting temperature and fusion enthalpy of nascent and melt crystallised polymer. The method is used to investigate the crystallization temperature and crystallization enthalpy. An identical thermal programme adopted for each sample is as follows:

1. Isothermal at 25°C for 5mins
2. Ramp to 160°C at 10°C min^{-1} (The first heating run)
3. Isothermal at 160°C for 5 min (To remove the entire thermal history)
4. Ramp to 25°C at 10°C min^{-1}
5. Isothermal at 25°C for 5min
6. Ramp to 160°C at 10°C min^{-1}

3.2.2 Gel Permeation Chromatography (GPC)

GPC was used for molecular characterisation of the investigated polymers. High temperature GPC was performed in Polymer Laboratories of Rapra, using GPC220 under the supervision of Dr Steve Holding. A single solution of each polyethylene specimen was prepared by dissolving 15.0 mg of sample into 15cm^3 solvent, 1,2,4-trichlorobenzene with anti-oxidant and heating at 190°C for 20 minutes on shaker. Each sample solution was filtered through a glass fibre filter and a part of solution was moved into a glass sample vial. In order to attain thermal equilibrium condition of each sample, there was a thirty minutes delay in a heated sample compartment. After that, part of the contents was injected in each vial automatically. The Chromatographic conditions were:

(1) Columns: PLgel guard plus 2 x mixed bed-B, 30 cm, 10 μm;

(2) Solvent: 1,2,4-trichlorobenzene with anti-oxidant;

(3) Flow-rate: 1.0 cm^3 min^{-1} (nominal),

(4) Temperature: 160°C (nominal),

(5) Detector: refractive index (& Viscotek differential pressure).

Finally, the data was collected and analysed using Polymer Laboratories "Cirrus 3.0" software.

3.2.3 Field Emission Gun Scanning Electron Microscopy (FEGSEM)

A high resolution FEGSEM with 5kV acceleration voltage was used to observe morphology of the nanofillers, and the dispersion and distribution of nanofillers, MWCNTs and CB, in PE-A matrix. The signal was collected by InLens detector. As MWCNTs and CB are electrically conductive, FEGSEM experiment of each nanocomposite was carried out without gold coating.

3.2.4 Advanced Rheological Expansion System plate-plate rheometer(ARES)

Dynamic frequency sweep (DFS) measurements were performed on an ARES strain controlled rheometer with oscillatory shear in the linear viscoelastic regime at temperature of 160°C with angular frequencies (ω) ranging from 0.001 to 500 rad s^{-1} and a constant strain of 5%. Prior to the DFS measurements, dynamic strain sweep (DSS) measurements were performed to investigate the linear viscoelastic regime of each polymer within broad strain region from 0.01% to 100% at a frequency of 500rad s^{-1} or 100rad s^{-1}. Each sample was first hot-compressed at 160°C in a steel mould 1mm thick and 25mm inner diameter. The compressed sample was used for the plate-plate rheology measurements. Finally the crossover point of storage modulus (G') and loss modulus (G'') and molecular weight characteristics (M_w, M_n, M_w/M_n and M_z) were determined and calculated via the Orchestrator software provided by TA Instruments.

3.2.5 Capillary Rheometry

A Rosand twin-bore rheometer was used to study the melt flow behaviour of three polymers, in which the extrusion pressure was measured via a built-in pressure transducer situated at upstream of the die, as shown schematically in Figure 3.1. Three thermocouples were fitted within the reservoir wall at three different locations: top barrel, middle barrel and die. Flowmaster software was used to control the rheometer, then collect and analyse the rheological data. The rheometer barrel diameter is 15mm and a series of dies with varying die geometry shown in Figure 3.2 were used.

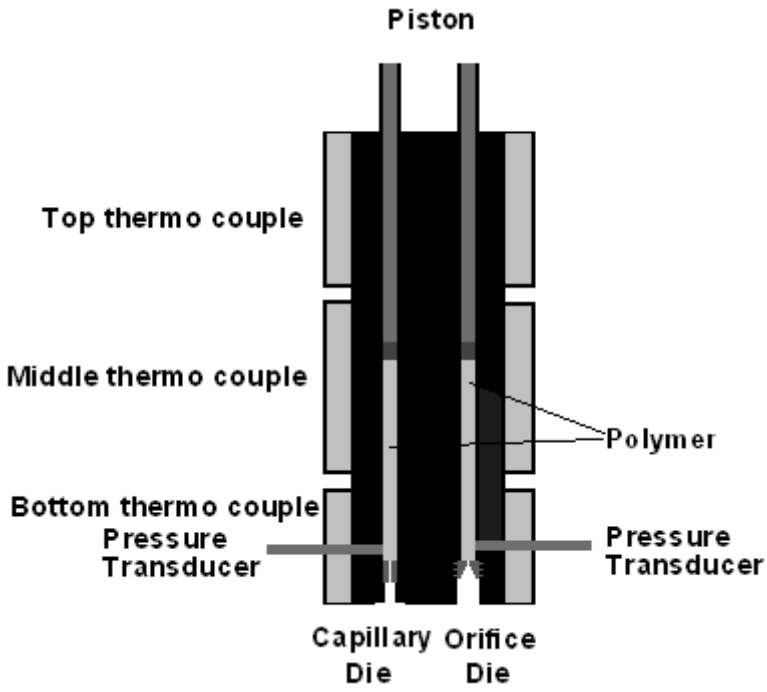

Figure 3.1: Schematic representation of the twin bore rheometer used in extrusion experiments.

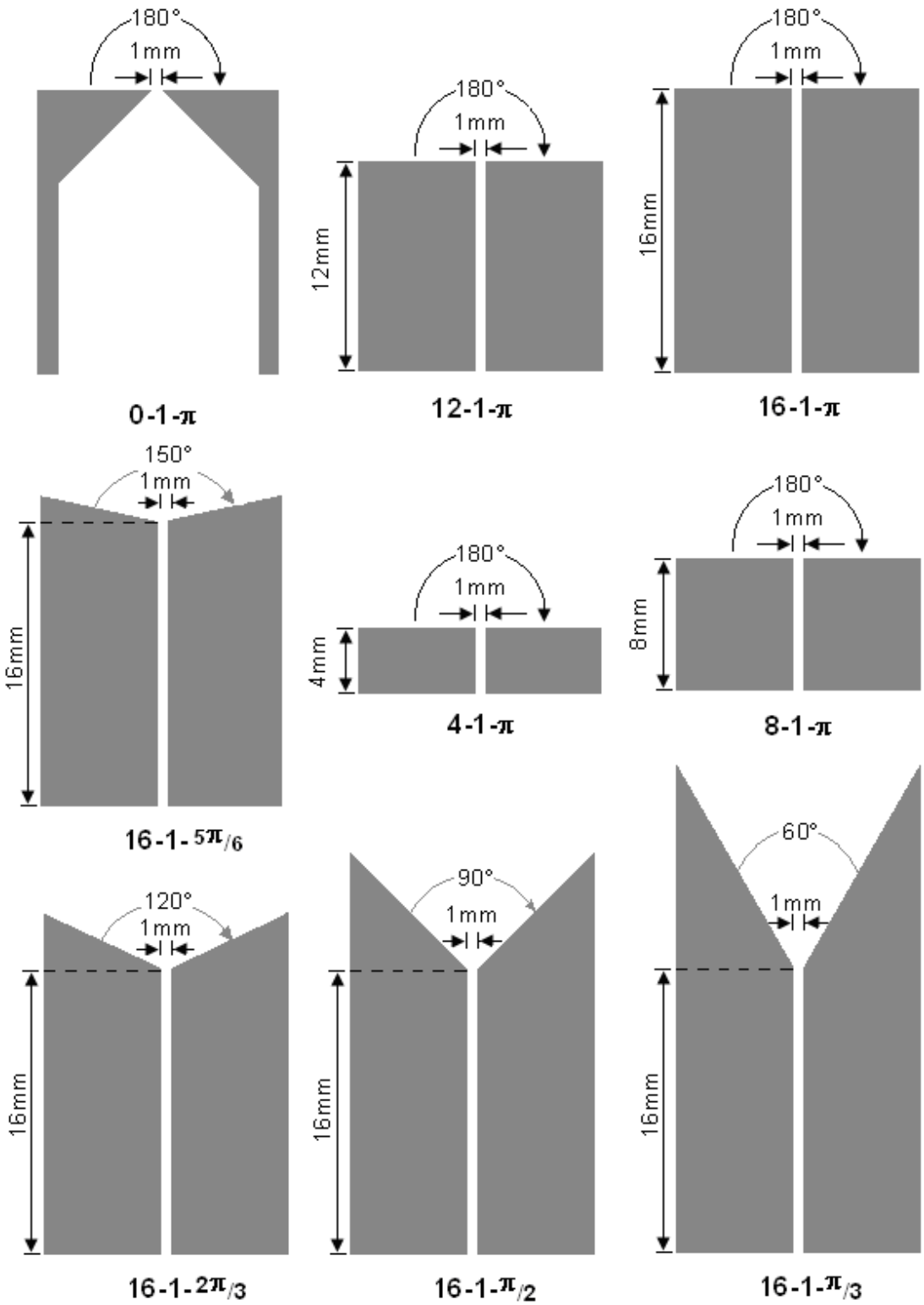

Figure 3.2: Schematic diagrams of axial cross sections of orifice die and capillary dies showing the differences in die geometries including capillary length (L/mm),capillary diameter (D/mm) and die entrance angle (2α/rad). L-D- 2α values corresponding to each die are shown at the bottom of each Figure. The die entry angle is represented by a radian number(Radian= (degree×π)/180°).

3.2.5.1 Specimen preparation for capillary rheological characterisation

Prior to rheological characterisation, polymer pellets or powders were compacted at ambient temperature and then heated up to a pre-heating temperature, far above the melting point. This step was required to erase the grain boundary and remove the air traps, and eventually to gain a homogenous melt which is prerequisite for capillary rheology measurements. The pre-heating temperature and time are dependent on molecular characteristics (M_w) and melt flow behaviour. For example high molecular weight PE required more time to attain the homogenous melt compared to the low molecular weight PE. On the other hand, different molecular weight PEs possess various window temperatures and distinct melt instability regime; hence, varying pre-heating temperatures were selected in pre-test setting.

Table 3.2: Pre-heating setting for sample preparation prior to the rheological characterisation.

Sample	Pre-heating temperature (°C)	Pre-heating time(min)
PE-A	160	10
PE-B	170	20
PE-C	200	20

3.2.5.2 Dynamic temperature sweep (DTS)

A DTS was performed to probe the window location while cooling melt at a constant rate, circa 1.5°C min^{-1} and at a constant shear rate. At a given piston velocity at fixed barrel and capillary dimensions the shear rate remained constant. DTS only consists of cooling run to avoid any interference of residual solid phase on melt flow behaviour. Aims of DTS experiments were as follows:

1. To determine the critical apparent shear rate, $\dot{\gamma}_c^{\,w}$, corresponding to the onset of the window effect.
2. To determine the window location and temperature interval. Since DTS is non-isothermal rheological characterisation, it can merely give general information on window location. In order to locate the real window temperature, isothermal step rate tests were performed.
3. To investigate the impact of the shear rate on the window effect.

3.2.5.3 Isothermal step rate test (ISR)

In contrast to the DTS a 'static' experiment was conducted to study the melt flow behaviour at the isothermal conditions in which the extrusion pressures were recorded at different shear rates with time. After pre-heating was completed, the barrel and

capillary die were cooled to pre-selected temperature for 15mins to attain equilibrium thermal condition prior to the ISR. The objectives of ISR were as follows:

1. To investigate the melt flow behaviour at isothermal conditions with varying step changes in shear rate.
2. To justify the existence and appearance of window effects under isothermal conditions.
3. To study the hydrodynamic origin of the window effect.

3.2.5.4 Isothermal mono-rate time sweep (IMTS)

Melt flow instabilities were studied in IMTS in which the extrusion pressures were recorded as a function of time, at a fixed apparent shear rate, while the barrel temperature was kept constant. IMTS was also adopted to determine the flow criticalities including the onset apparent shear rates corresponding to periodical bulk distortion, window effect and helical distortion/ gross shape distortion, referred to as $\dot{\gamma}_c{}^p$, $\dot{\gamma}_c{}^w$ and $\dot{\gamma}_c{}^h$. On the other hand, the slip flow velocities were also determined in *IMTS.* The apparent shear rates corresponding to a given shear stress were recorded in the capillary flow using different dies with constant L/R ratio. (Die geometries L(mm)-D(mm)-2α (rad) of capillary dies used in slip flow velocity measurement were as follows: 24-1.5-π, 20.8-1.3-π, 18.4-1.15-π and 16-1-π). The thermal history in IMTS was identical with ISR. The objectives of IMTS were to:

1. To determine the critical apparent shear rates associated with the onset of pressure oscillation, window effect and helical distortion.
2. To study the melt irregularities at varying shear rates and distinct temperatures.
3. To determine the slip flow velocity.

3.2.5.5 Die swell measurement

The die swell was measured by an in-situ laser detector situated at 2cm under the capillary die. During the measurement, the extrudates were continuously cut off manually to maintain the measuring length no more than 15cm in order to avoid the sagging effect.

3.2.6 MeF3 Microscope

Photographs of PE extrudate were taken via Reichert-Jung MeF3 microscope with a macro unit using a reflective light. The exposure time was fixed at 3.11ms.

3.2.7 Ex-situ Wide Angle X-ray Scattering (WAXS)

Flow induced orientation was studied by ex-situ WAXS experiments performed on the beam line ID11 of the European Synchrotron Radiation Facility (ESRF) in Grenoble. Each sample, PE-B, was extruded through a capillary die(16-1-π) followed by quenching in ice water to 0°C in order to minimise the influence of chain relaxation on flow induced orientation. Consequently, more flow induced orientation was maintained on the surface layer of extrudate compared with self-cooling in the atmosphere. After extrudate melts were fully solidified, each extrudate was sliced along the longitudinal direction from both sides to achieve a proximate orthorhombic section with thickness of 250 μm depicted in Figure 3.3. An elliptical micro beam with 15 μm major axis and 5 μm minor axis scanned the pre-sectioned extrudate mounted perpendicularly on a 3.17mm wide slot on a copper plate. The monochromatic X-ray with a wavelength =0.417nm probed the pre-sectioned extrudate along the transverse direction of extrudate. Two-dimensional X-ray diffraction patterns were recorded on ESPIA Frelon detector and corrected for spatial distortion. Prior to the data analysis the scattering of air and sample free holder was subtracted from the scattering of each sample. Finally the data were analysed via FIT2D software provided by ESRF.

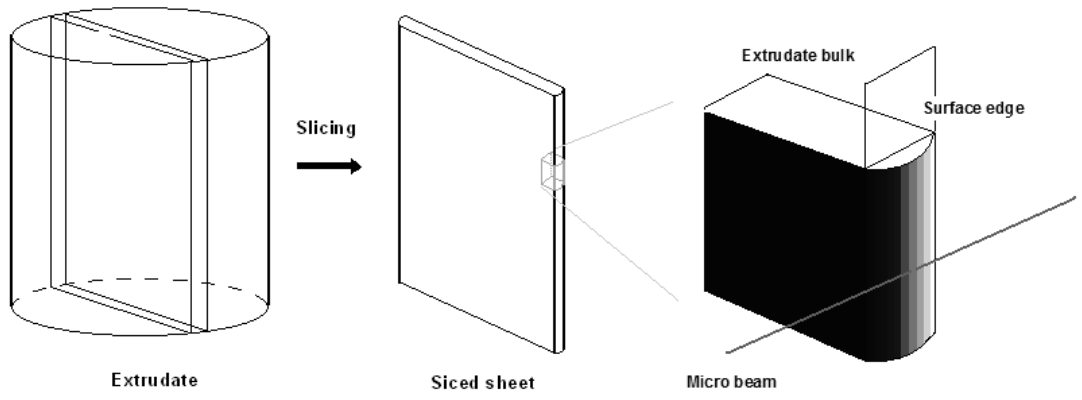

Figure 3.3: Schematic diagram of a pre-sectioned extrudate on left. The enlarged diagram with gradual discolouring effect on right represents for surface edge of pre-sectioned extrudate.

Chapter 4 Material characterisation

4.1 Polymer characteristics

4.1.1 DSC

Table 4.1 summarizes DSC data of each sample. The melting temperature is broadly consistent with expectations from thermal analysis of PE.

Table 4.1: Thermal analysis of three different polyethylenes (Appendix E)

Sample	$T_{m\ onset}$ (°C)	$T_{m\ peak}$ (°C)	ΔH_m (J g^{-1})	X_c (%)
PE-A	125.13	131.75	182.8	62
PE-B	122.01	129.30	174.6	59
PE-C	122.23	129.60	171.3	58

4.1.2 GPC

PE-A and PE-C are unimodal linear polyethylenes supplied by SABIC Europe. The molecular characteristics of each sample were determined by GPC as shown in Table 3.1 and Figure 4.1. One symmetric distribution peak for the two samples confirms unimodal nature of PE-A and PE-C respectively. According to GPC data depicted in Figure 4.1, it is apparent that PE-A and PE-C have different M_w and MWD. Compared to PE-C, PE-A is low molar mass linear polyethylene with comparatively narrow molar mass distribution. The polydispersity of PE-A is analogous to Kolnaar's samples[31]. However, M_w of PE-A is lower than all the Kolnaar's linear PEs.

The sample, PE-B, was supplied by Borealis. According to the molecular weight distribution curve shown in Figure 4.2, it can be observed that PE-B shows bimodal molar mass distribution.

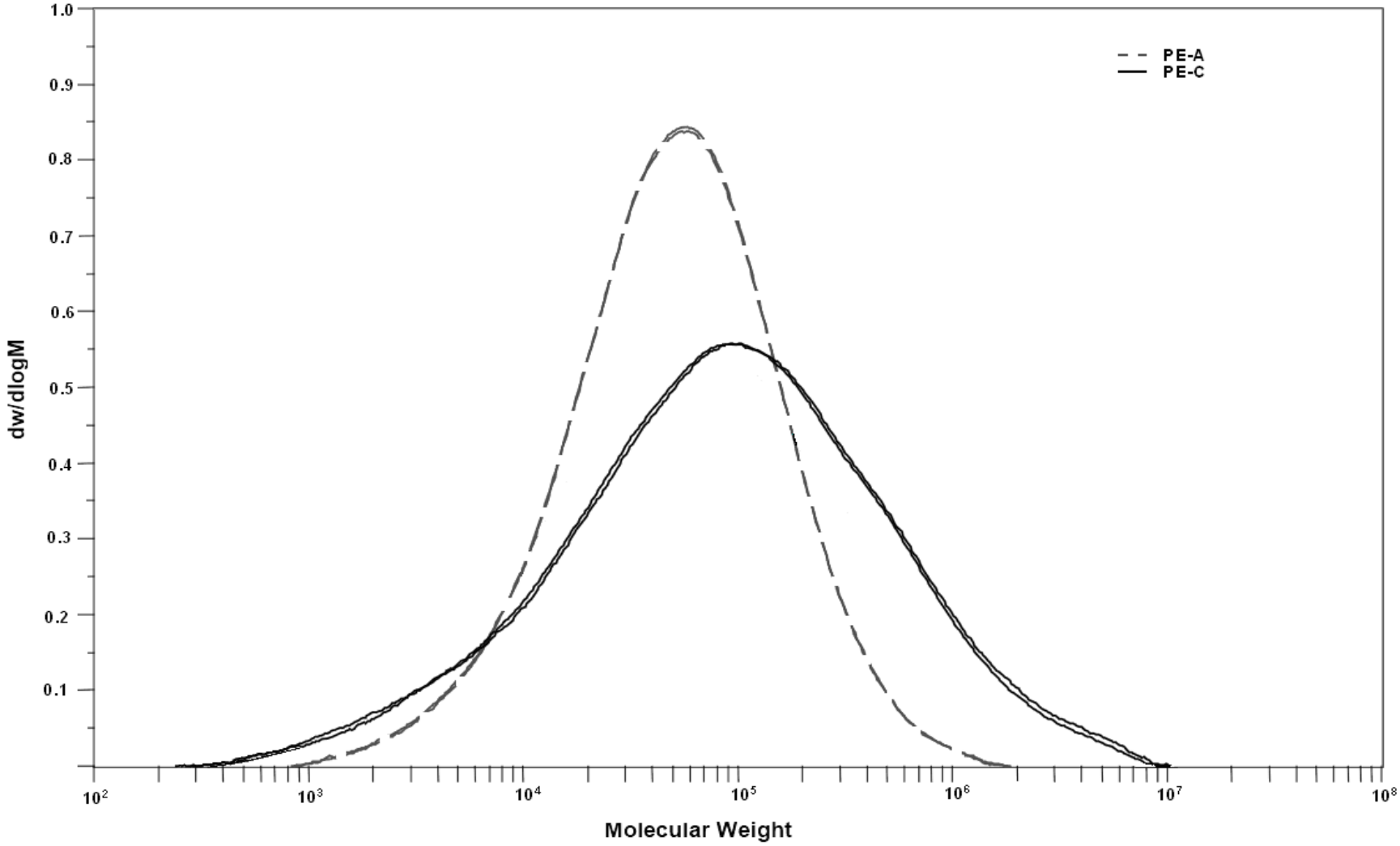

Figure 4.1: Molecular weight distributions of PE-A and PE-C. GPC measurements of each sample have been done twice.

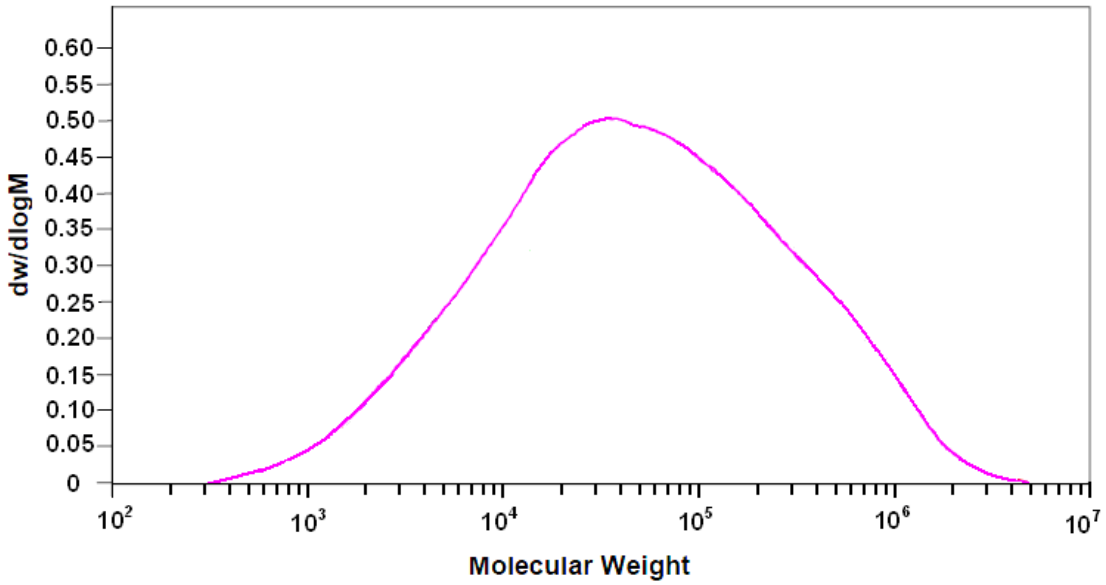

Figure 4.2: Molecular weight distribution of bimodal polyethylene PE-B.

4.1.3 ARES – plate to plate rheometry

Molecular characteristics can also be determined via rheology route. First step is to determine a linear viscoelastic regime for a given polymer via the dynamic strain sweep (DSS) experiment, in which storage modulus, G', and loss modulus, G'', are recorded and plotted against strain rate as shown in Figure 4.3. It can be seen that G' and G'' remain unaffected within a strain region from 0.1% to 10%. Therefore, this region is referred to as linear viscoelastic regime. Following DSS a dynamic frequency sweep (DFS) was performed to measure the rheological properties at different frequencies with a fixed strain selected in the linear viscoelastic regime. As shown in Figure 4.4, there is a crossover point of G' and G'' for PE-A and PE-C respectively. It is well-known that a low molecular weight linear polymer with narrow molar mass distribution shows a crossover point (G'/G'') located at higher angular frequency and higher modulus compared with a high molecular weight linear polyethylene characterised with a broader molecular weight distribution. Therefore, it is possible to achieve qualitative information about M_w and M_w / M_n in comparison of the crossover points obtained in DFS. According to Figure 4.5, the G'/G'' crossover point of PE-C situated at low frequency and the low modulus compared with PE-A, suggests that the polymer PE-C is a high molecular weight polymer with broad molar mass distribution. These results are in agreement with the quantitative results obtained in GPC.

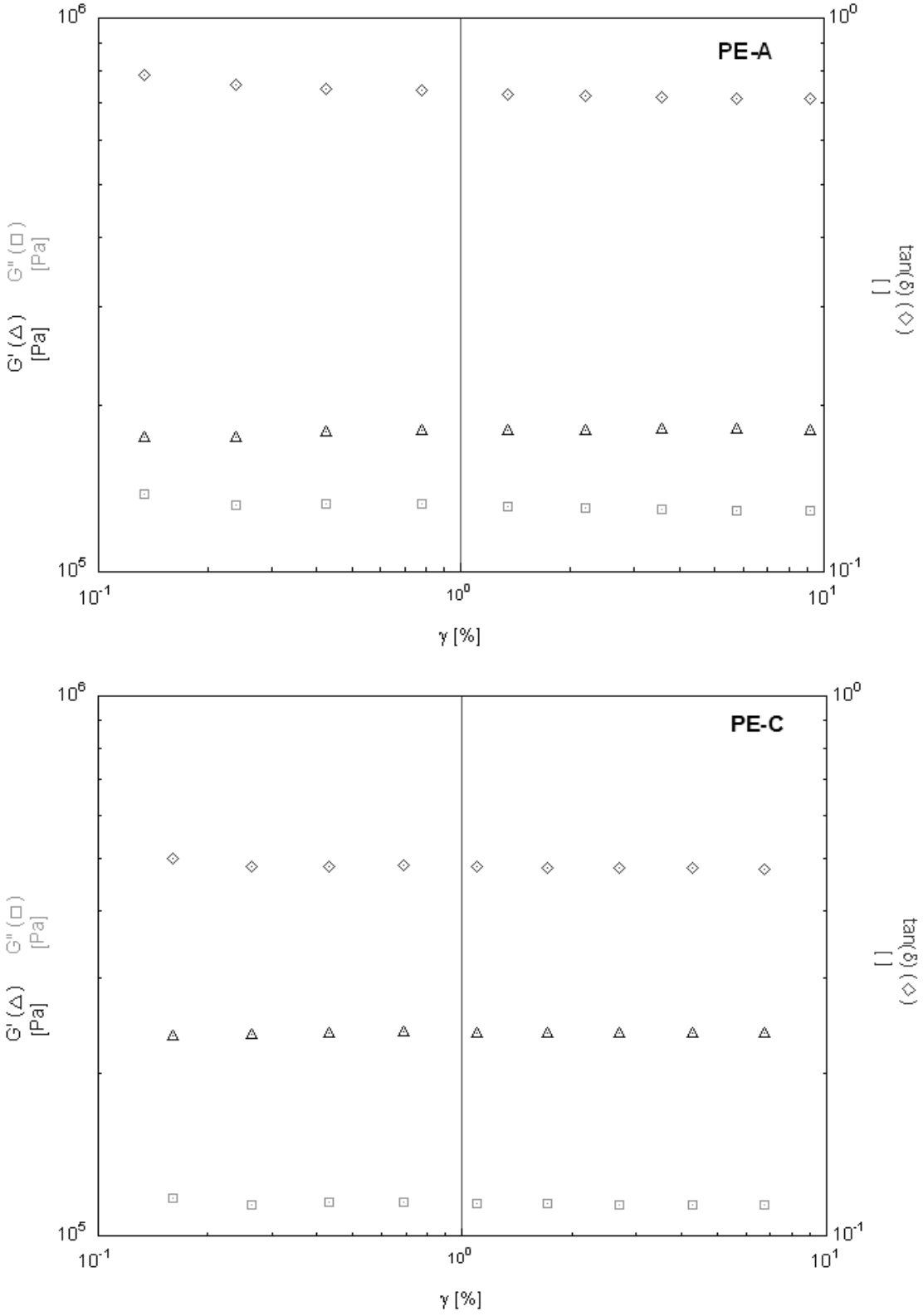

Figure 4.3: Dynamic strain sweep results of logarithmic storage modulus G', loss modulus G''(Pa) vs. shear strain γ_s (%) showing the linear viscoelasticity regime under oscillatory shear, while holding a fixed frequency at 500rad s^{-1} for PE-A and 100rad $s^{-1}$for PE-C at a constant temperature of 160°C.

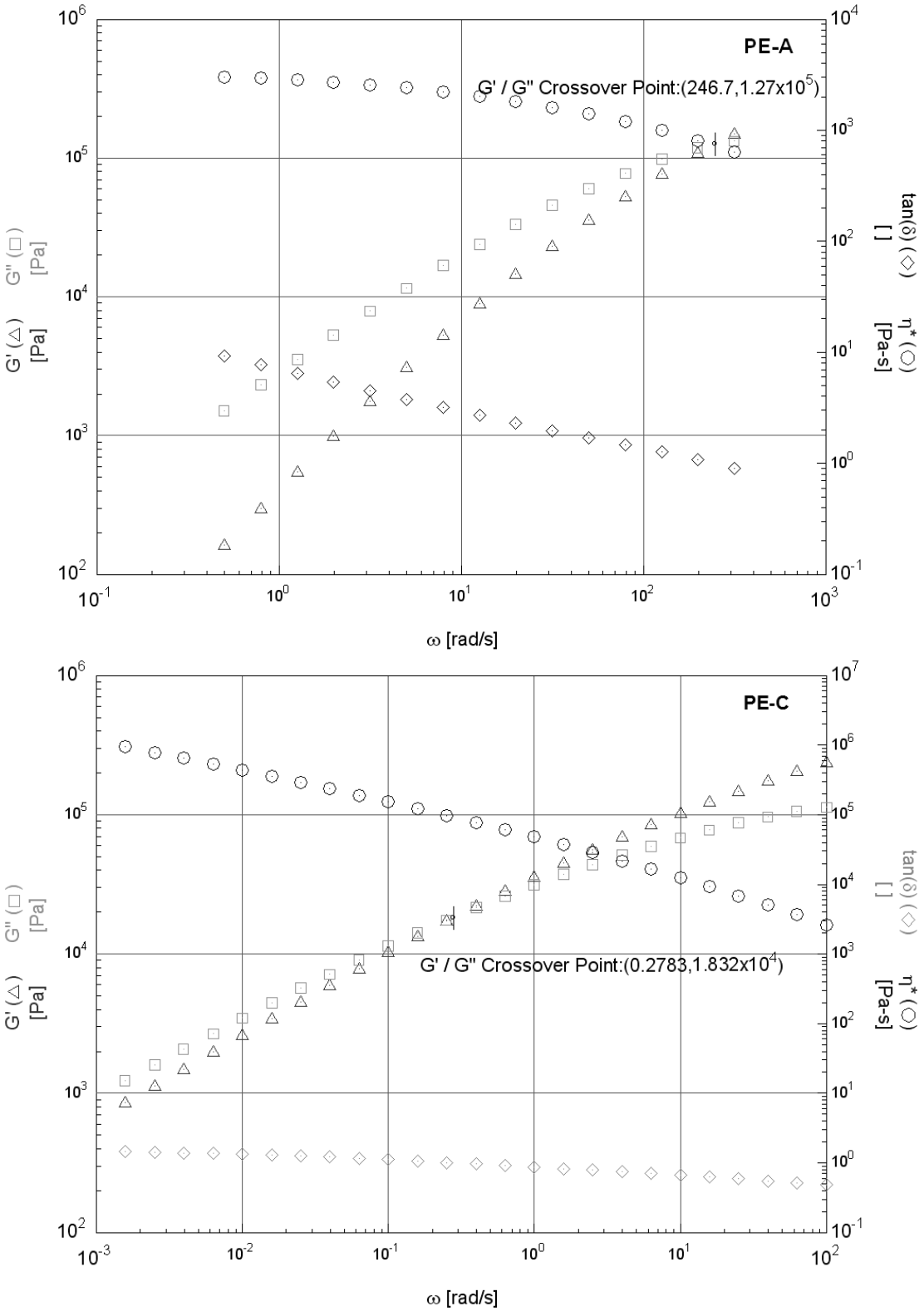

Figure 4.4: A logarithmic plot of storage modulus G' (Pa), loss modulus G'' (Pa), loss angle/phase shift δ and complex viscosity η*(Pas) against frequency ω (rad s^{-1}). The dynamic frequency sweep performed at 5% strain.

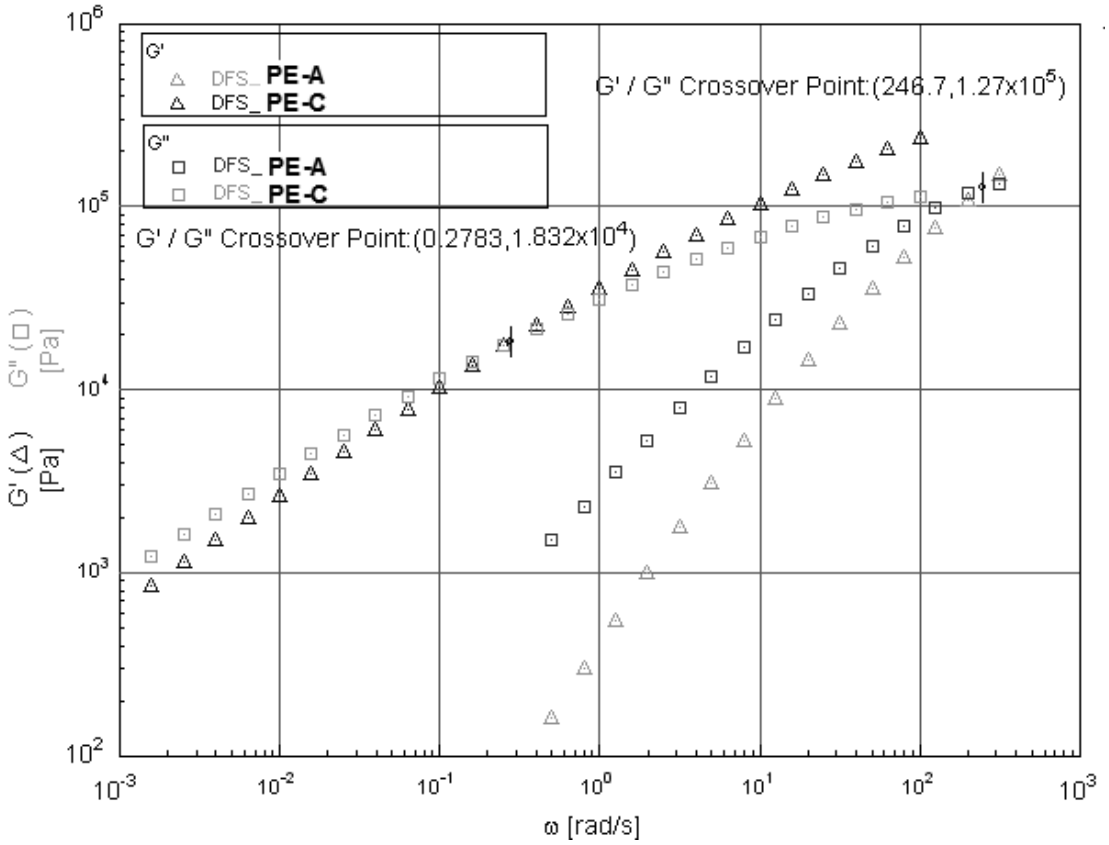

Figure 4.5: Two unimodal linear polyethylenes possessing distinct molecular weight and polydispersity show different crossover point of storage modulus and loss modulus in the logarithmic plot of storage modulus and loss modulus against frequency. The positions of respective crossover points indicate the relative molecular weight and molar mass distribution.

To quantitatively study the molecular characteristics through the use of rheological measurements, numerous studies have been devoted to establish the relationship of measured rheology properties with the known values for M_w and M_w / M_n based on the predictions of linear viscoelastic models[46]. According to double-reptation model[48], the polymer characteristics were calculated by TA Orchestrator software and the results are shown in Table 4.2 and synthesised MWD traces are exhibited in Figure 4.6. As a benchmark, results from GPC are compared with the modelling results in order to predict the capability of the double-reptation model for determination of polymer characteristics. It is found that M_w and M_w / M_n calculated based on double–reptation model are in good agreement with the GPC results except an apparent difference of M_w / M_n between them for PE-C. One of the possible reasons is that the rheology route is more sensitive to small amounts of high molecular weight polymer. In other words, GPC is not a reliable technique to determine the molecular

weight beyond circa 10^6 g mol^{-1}or a broad molecular weight distributed polymer with a high molecular weight fraction above approx. 10^6 g mol^{-1}.

Table 4.2: Polymer characteristics results of PE-A and PE-C from ARES plate-plate rheometer compared with GPC results

Technique	Sample	M_w (g mol^{-1})	M_n (g mol^{-1})	M_w/M_n
ARES	PE-A	74,200	28,871	2.6
GPC	PE-A	89,750	24,500	3.7

Technique	Sample	M_w (g mol^{-1})	M_n (g mol^{-1})	M_w/M_n
ARES	PE-C	349,100	12,553	27.8
GPC	PE-C	303,000	17,450	17.4

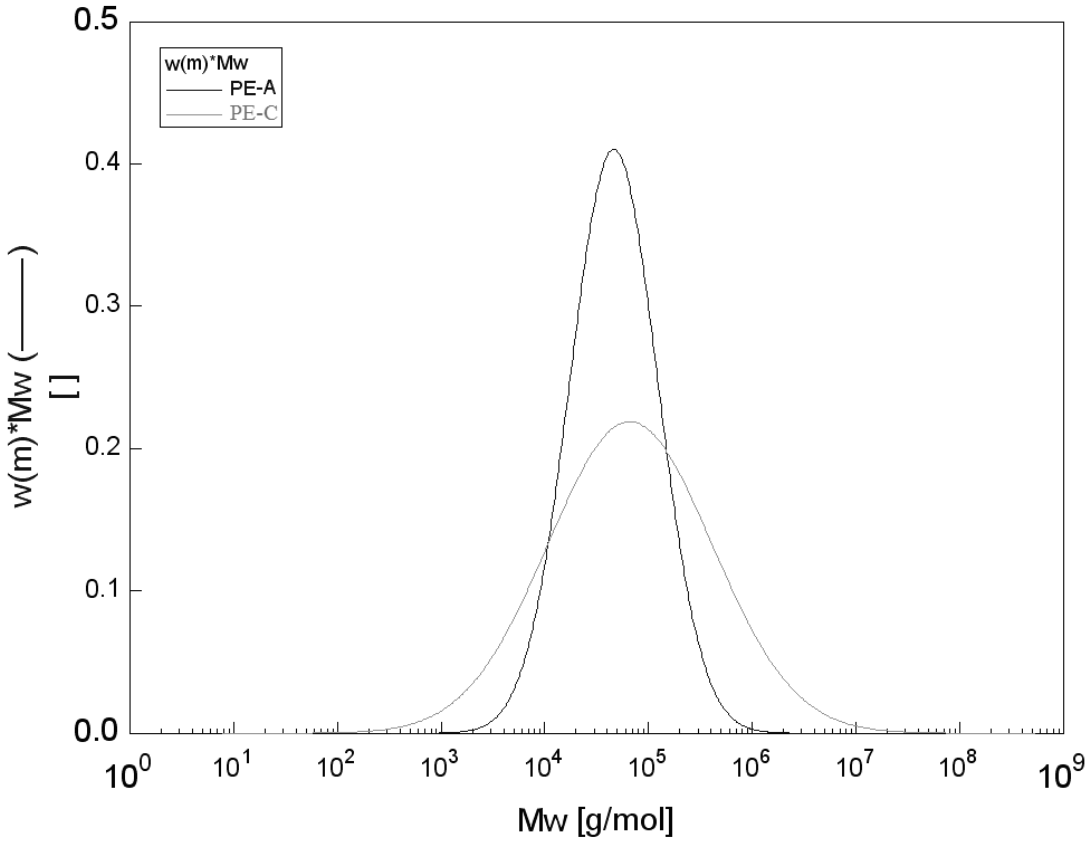

Figure 4.6: Synthesised molecular weight distribution traces for PE-A and PE-C based on the double reptation model, resulting from the dynamic frequency sweep in the linear viscoelasticity regime of each polymer. The entanglement molecular weight 1900g mol^{-1} and minimum reptation molecular weight 4000g mol^{-1} were the input parameters for calculation.

4.2 Nanocomposites characterisations-FEGSEM

Figures 4.7 and 4.8 show particle morphologies of CB and MWCNTs. It can be seen that CB are spherical nano-particles with aspect ratio of one. In contrary to CB, rod-like MWCNTs possess high aspect ratio. From figures 4.9 and 4.10 it may be stated that both CB and MWCNTs are finely distributed on the surface of PE-A powder.

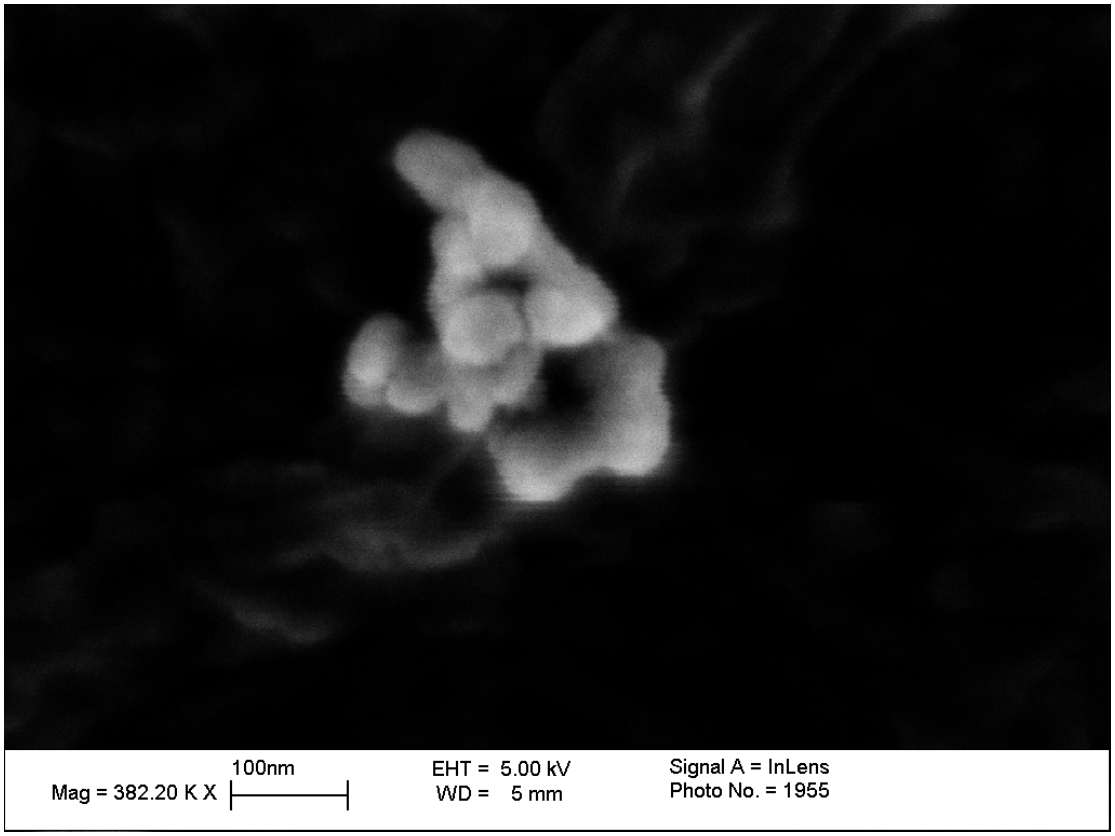

Figure 4.7: FEGSEM image showing the morphology and particle size of CB

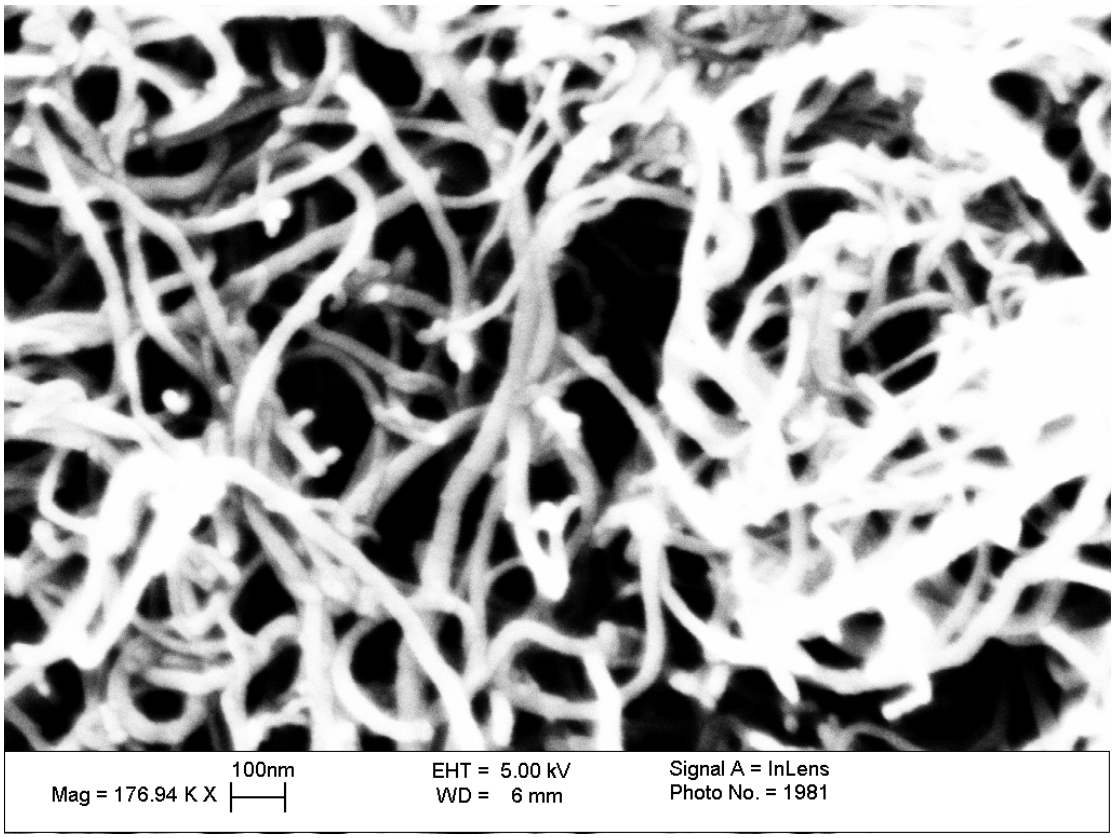

Figure 4.8: FEGSEM image showing the morphology and particle size of MWCNTs

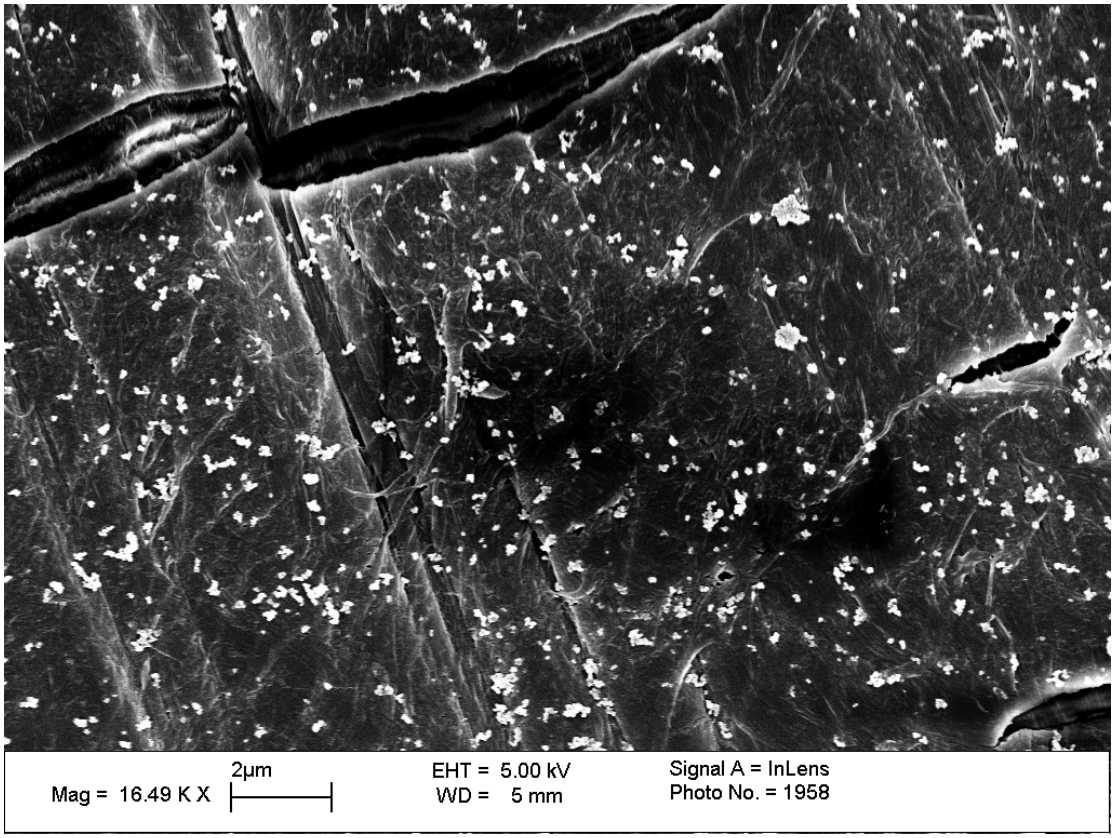

Figure 4.9: FEGSEM image of 0.2wt%CB-PE-A

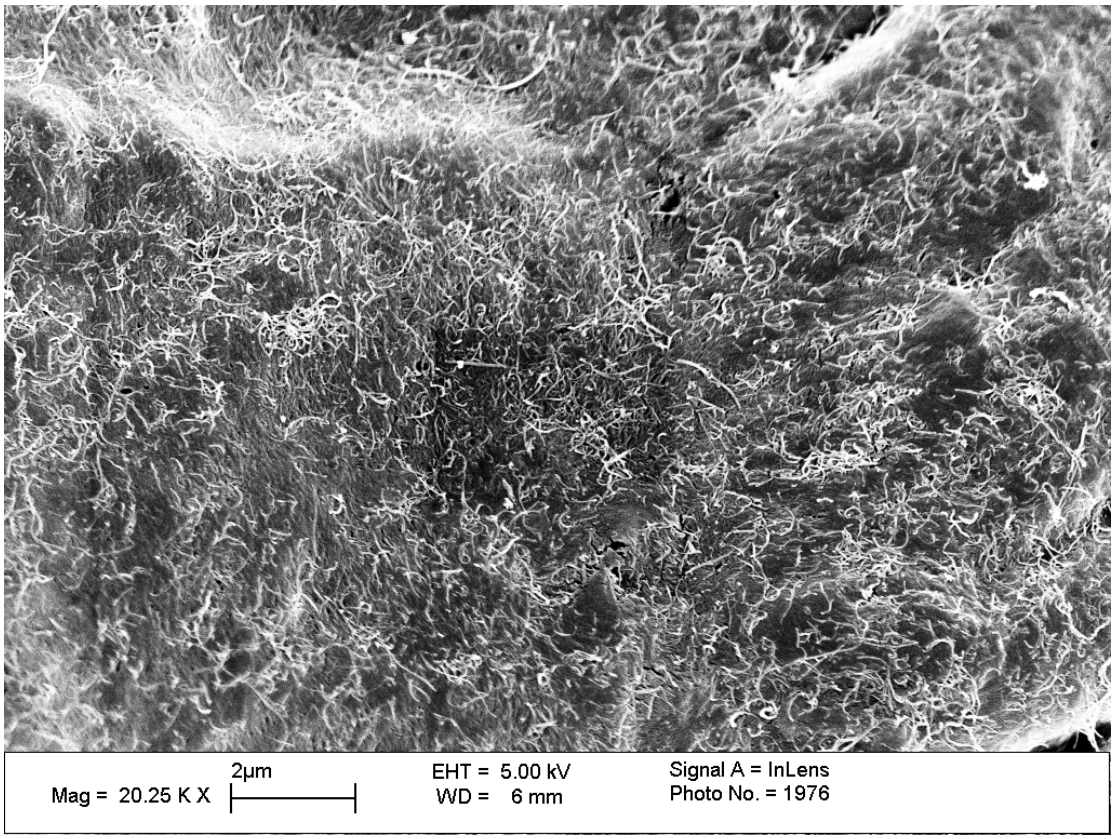

Figure 4.10: FEGSEM image of 0.2wt%MWCNTs-PE-A.

Chapter 5: Molecular origin of window effect

5.1 Introduction

The extrusion window of linear polyethylene (PE) was first addressed by Keller *et al.*[30]. The weight average molar mass of those PEs under Keller's study are in between 10^5 g mol^{-1} and 10^6g mol^{-1} The window effect was described by a pressure drop occurring at and around 150°C for a constant material throughput rate without any distortion. The advantages of the window effect are less processing energy for continuous flow without flow instabilities and uniform smooth extrudate with less die swell. Therefore the extrusion window can offer an energy efficient processing route to process linear PE without extrudate distortion at a given volumetric flow rate. However, the narrow temperature window cannot be adopted for industrial applications. Therefore, to make the process applicable, broadening of the window effect is a requisite. To achieve the goal it is also essential to understand hydrodynamic origin of the window effect. As stated in the earlier chapter, one of the possible reasons for the appearance of the window is slip flow. However, there is no clear elucidation regarding the hydrodynamic origin of the effect of slip flow on the window. One of the possible slip flow mechanisms is related to the disentanglement of adsorbed chains from free chains. In detail, the oriented tethered chains are likely to act as a lubricant and provide smooth flow. Such a general possibility of disentanglement of tethered chains from free chain in bulk melt at or above a critical flow rate has been addressed by Brochard and de Gennes[41]. These concepts have been further strengthened by the systematic studies performed by Wang[39]. However, there is a lack of quantitative study on the flow criticalities of extrusion window in order to link that with stick-slip theory.

5.2 Results

5.2.1 Melt flow singularity of PE-A

The polymer used for studies in this chapter is PE-A, molecular characteristics of which are shown in Chapter 3 (Table 3.1) of this thesis. To recall, molar mass and molar mass distribution of PE-A are 89,750g mol^{-1} and 3.7 respectively as determined by GPC. Kolnaar *et al.* estimated that linear PE with M_w <10^5g mol^{-1} has no window effect. However no experimental data for the molar masses lower than the critical molar mass is provided in the literature. In this respect the present study is likely to

be the first on the melt flow singularity of the linear PE with M_w lower than the Keller's 'critical' molecular weight (M^* ~10^5 g mol^{-1}).

Figure 5.1 depicts the basic melt flow behaviour of PE-A. During the dynamic temperature sweep experiments (DTS) at shear rate of 225s^{-1} starting from 160°C, three types of characteristic flow behaviour, viz. stick flow, window effect and flow induced solidification, are observed in four temperature regions:

(a) At higher temperature (>144°C) corresponding to the stick flow region, no melt fracture or extrudate distortion appears and the extrusion pressure steadily increases with decreasing temperature.

(b) Within the extrusion window (144°C~142°C), a considerable pressure drop emerges and a smooth extrudate with no melt irregularities are observed.

(c) In between 142°C~139°C, the flow behaviour is situated in the stick flow region again after the termination of window effect terminates at 142°C.

(d) At lower temperature (<139°C), extrusion pressure increases significantly and eventually swings up towards the upper limit pressure of rheometer. These flow behaviours were first addressed by Odell *et al*[50] and are referred to as flow induced solidification, at the end no flow through the die is observed.

To investigate the molecular origin of the window effect the polymer PE-A has been selected as a reference sample. The influence of carbon-based nanofillers on extrusion window is addressed in chapter 7.

Figure 5.1 shows distinct flow behaviour corresponding to capillary flow and capillary free flow. During DTS experiment at a shear rate of 225s^{-1}, a capillary die (L-D-2α:16-1-π)[b] and an orifice die (L-D-2α:0-1-π) were attached at the bottom of barrels on left and right side of the capillary rheometer. Hence, both the capillary flow and the capillary free flow can be compared in the same flow condition simultaneously. It is found that there is no existence of extrusion window when the polymer melt is extruded through the orifice die. However, in capillary flow, an apparent pressure drop complemented with uniform flow of the extrudate without any melt fracture and extrudate distortion, occurs in a narrow temperature window,

[b] L-D-2α: L is capillary length, D is capillary inner diameter and 2α radian of capillary die entry angle.

residing between 144°C~142°C. The characteristics of the window effect observed in this low molar mass PE are similar to the earlier findings, where high molar mass was used.

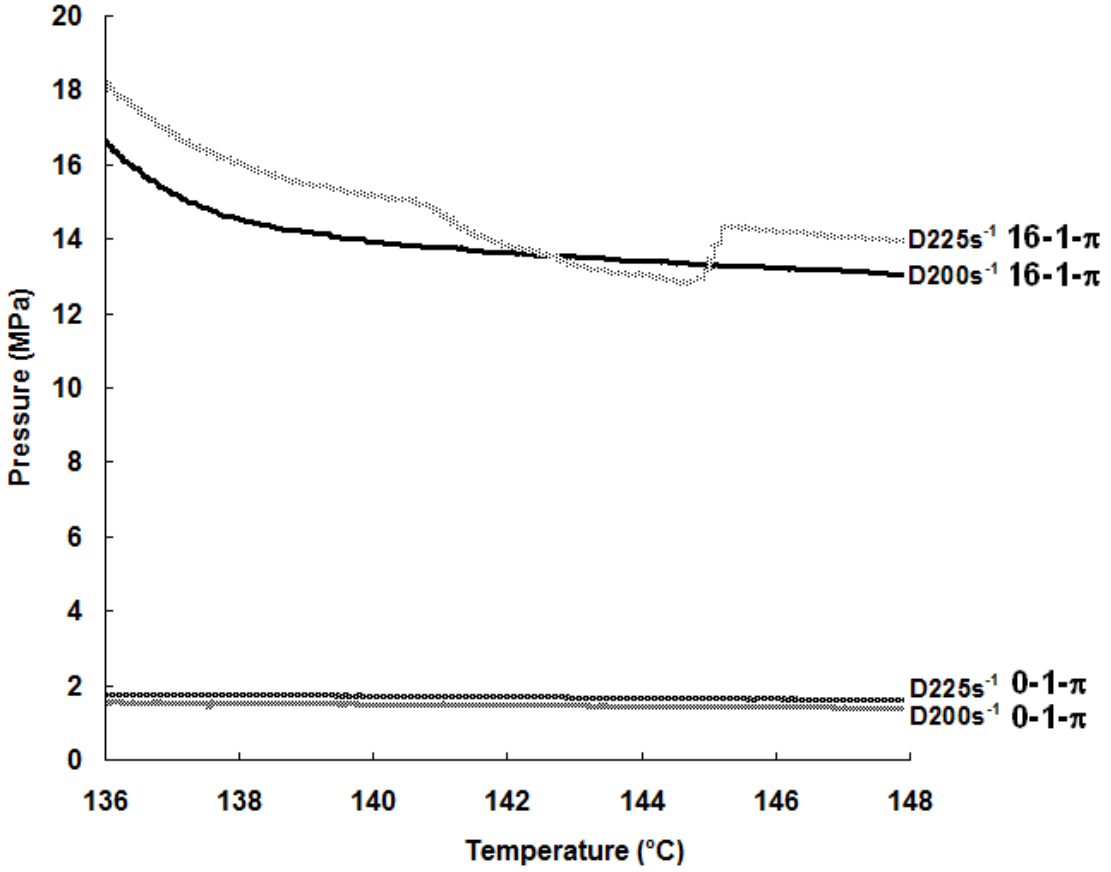

Figure 5.1: A plot of extrusion pressure against temperature for orifice die(L-D-2: 0-1-π) and capillary die (L-D-2*α*: 16-1-π). D225s^{-1} is an abbreviation for dynamic temperature sweep with a fixed apparent shear rate at 225s^{-1}.

5.2.2 The effect of shear rate on window effect

The effect of apparent shear rate on the extrusion window is studied further in the dynamic cooling experiments, as depicted in Figure 5.2.

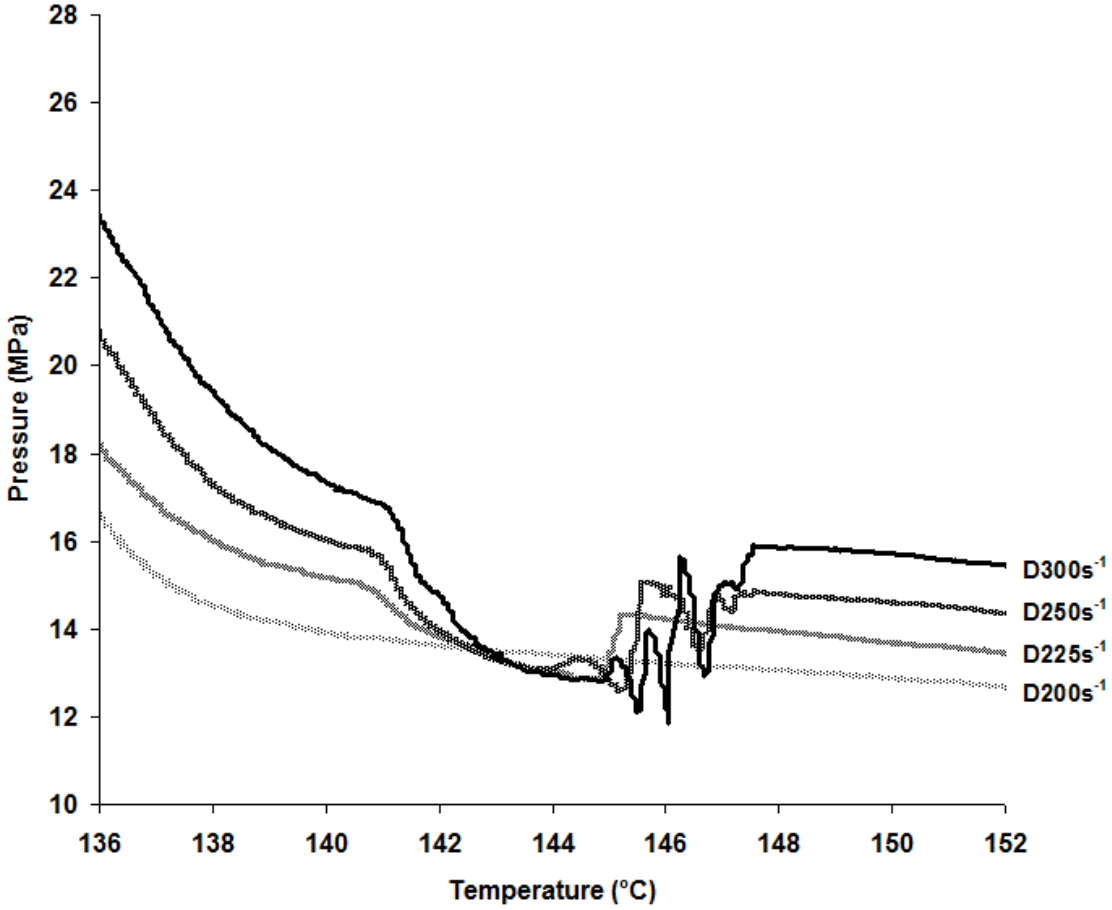

Figure 5.2: Extrusion pressure against temperature traces for different shear rates indicating the critical shear rate corresponding to the onset of extrusion window (L-D-2*α*: 16-1-π)

The critical apparent shear rate, $\dot{\gamma}_c^{\,w}$, corresponding to the onset of the window effect, is $225s^{-1}$. Below this shear rate no extrusion window is observed. With increasing apparent shear rate ($>225s^{-1}$), the extrusion window and pressure oscillation region shifts to high temperature, Figure 5.2, suggesting shear rate dependence of the onset of the window temperature. Finally, it is worth noting that the pressure minima observed in the window region is lower than the extrusion pressure observed below the critical shear rate, such as ($200s^{-1}$). This suggests that distinction in the hydrodynamic condition exists in the window and non-window regions.

5.3 Discussion

One of the requirements of the performed rheological studies is the isothermal condition. It is desired that the system attains the thermal equilibrium state. Though in dynamic temperature sweep (DTS) the set cooling rate of 1.5°C min^{-1} cannot completely fulfil the static isothermal requirement, it had been shown in Kolnaar's

study that the window temperature only shifts by less than 1°C on varying the cooling rate including isothermal experiments[31(a)].

Before discovering the molecular origin of window effect here we reconcile the existing concepts on flow behaviour as depicted schematically in the Figure 5.3. The schematic plot of pressure trace recorded in DTS test of PE-A can be classified into four regions:

Region I (as shown in Figure 5.3): *stick flow region* observed at high temperatures where the extrudate flows smoothly through the capillary die without distortion. In such a stable melt flow extrusion pressure continuously increases as the temperature diminishes, thus the apparent shear viscosity is proportional to the reciprocal temperature, obeying an Arrhenius type relationship:

$$\eta_a = Ae^{E_a / RT} \qquad \textbf{(5.1)}$$

Where η_a is the apparent shear viscosity,

E_a is the melt/ solid state flow activation energy ,

R is the universal gas constant.

It is to be noted that during conventional processing PE falls in this region.

Region II: *stick-slip flow region* shows pressure oscillation and it is also referred to as periodic distortion.

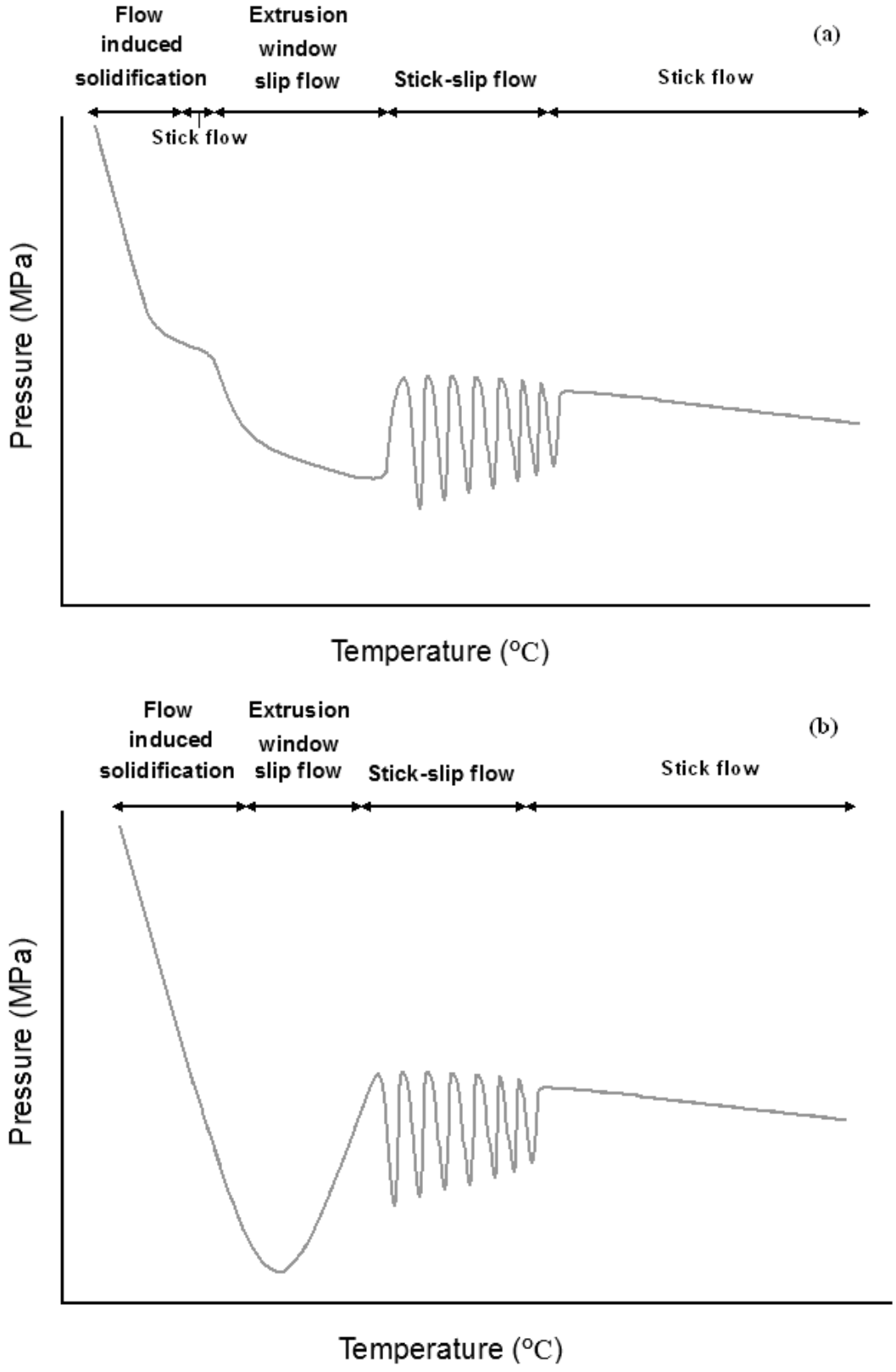

Figure 5.3: Two schematic plots of extrusion pressure vs. temperature, showing four distinct flow regions: (I) stable flow, (II) stick-slip flow, (III) extrusion window and (IV) flow induced solidification. (a) Flow behaviour of PE-A with weight average molecular weight below 10^5g mol^{-1}; (b) Flow behaviour of PE with weight average molecular weight above 10^5g mol^{-1} (Kolnaar and Keller, 1994, 1995, 1997 [30])

Region III: A *melt flow singularity* in a narrow temperature interval occurs in this region. Compared with the flow conditions in Region I, melt flows continuously through the capillary die, but at lower pressures and temperatures.

Region IV: A sudden upswing in the extrusion pressure is observed when the temperature decreases below a certain critical value during the DTS test. The reason could be attributed to the crystallisation of polymer melt under the flow conditions. Therefore, it is termed as *flow induced solidification*.

It is worth highlighting that PE-A with molecular weight below the suggested critical value ($M_w < M^*$) shows an isolated window effect without inference of flow induced solidification. However, in contrast, other linear PEs with relatively high molecular weight ($M_w > M^*$) exhibit extrusion windows accompanied by flow induced solidification.

5.3.1 Molecular origin of narrow extrusion window (Region III)

In Region III, the neat polymer, PE-A, showed a considerable pressure drop over a narrow temperature interval, referred to as the extrusion window. Although many researches[30,31] have been devoted to study the extrusion window, the molecular origin of the window effect is still unrevealed. Regarding the mechanism responsible, it is found that capillary flow gives rise to the extrusion window, rather than elongational flow[31]. On the other hand, it has been reported that the critical apparent shear rate follows a power law dependence on molecular weight which scales with -4.0±0.1[31(c)] .These findings reveal that the window effect arises when a certain stretched chain conformation can be maintained at or near the flow criticalities during capillary flow. Moreover, it was also observed that window temperatures were dependent on molecular weight[31(a)]. Therefore, it is impossible to compare the critical apparent shear rates for different molar mass PE at different temperatures. In order to compare flow criticalities at the same temperature, it is essential to introduce a shift factor a_T (in Table 5.1) to reflect the temperature dependence of the chain relaxation time, λ_{rep}. Figure 5.4 shows the superposition of critical apparent shear rate, $\dot{\gamma}_c^{\,w}$, for different molar masses of linear PEs. It is found that the rescaled critical apparent shear rate, $a_T\,\dot{\gamma}_c^{\,w}$, scales with -3.7±0.2 power of the molecular weight. where a_T is

obtained from an Arrhenius equation, Eq 4.6, here the activation energy is 29.057KJ mol^{-1}[157]. This power law relationship offers the internal link between molecular origin of the extrusion window and stick-slip flow theory. In detail, Wang studied a superfluid-like stick-slip transition[5] using a stress-controlled rheometer. He pointed out that the critical shear stress, σ_c, scales with -0.5 power of the M_w at different temperatures, 160°C and 200°C. It is apparent that two flow criticalities, $\dot{\gamma}_c^{\,w}$ and σ_c can be connected by a universal power law relationship between M_w and shear viscosity, η. (i.e. $\dot{\gamma}_c^{w} \sum M_w^{-3.75\pm0.2}$, $\sigma_c \sum M_w^{-0.5}$ and $\eta \sum M_w^{\,3.4} \Leftrightarrow \sigma = \eta\gamma$). Therefore, the slip flow emerging within the extrusion window at the critical shear rate may arise from an identical hydrodynamic origin of slip flow observed in stress-controlled rheometer, based on molecular weight dependence of flow criticalities. Even though the two experiments were performed using different capillary dies, it has been reported by Keller and Kolnaar[31(b)] that the flow criticalities remain less affected with different capillary die geometries.

Table 5.1: The rescaled critical shear rates of PE-A and the other three samples used in Kolnaar's research[31] (reference temperature is 160°C).

Sample	M_w (g mol^{-1})	PDI	$\dot{\gamma}_c^{\,w}$ (s^{-1})	T_{min} (°C)	a_T	$a_T\dot{\gamma}_c^{\,w}$ (s^{-1})
PE-A	89,750	3.7	225.00	144.0	1.36	306.00
PE-KA	262,000	3.1	7.00	149.5	1.22	8.54
PE-KB	381,000	5.1	1.70	149.9	1.21	2.06
PE-KC	708,000	6.5	0.13	151.8	1.17	0.15

Another internal link between the stick-slip theory and the extrusion window effect needs to be highlighted. Wang reported a low-temperature anomaly, viz. the rescaled critical shear stress σ_c / T decreases with decreasing temperature T (<200°C). Wang suggested that a flow-induced ordered phase may occur and ease the disentanglement of adsorbed chains from free chains at low temperature. In fact, such a flow-induced ordering has been detected by in-situ WAXS experiments[33-34] in rate-controlled capillary flow within the extrusion window. A single reflection corresponding to d=0.216nm at $2\theta_{hkl}$=20.9° (for CuKα radiation with wavelength of 0.154nm) was observed during extrusion of HDPE at the window temperature. Such a flow induced mesophase emerging at the PE/wall interface can assist the disentanglement of tethered chains adhered to the capillary wall from the chains in the bulk (free chains).

Therefore, the molecular mechanism of both the extrusion window and superfluid-like stick-slip transition, at low temperature <160°C, may be attributed to the same origin. In detail polymer chains are adsorbed on the inner capillary wall and then those adsorbed chains are oriented along the flow direction. At an appropriate flow conditions, viz. shear rate and temperature, the stretched chain conformation of adsorbed chains can be maintained and disentangled from the free chains.

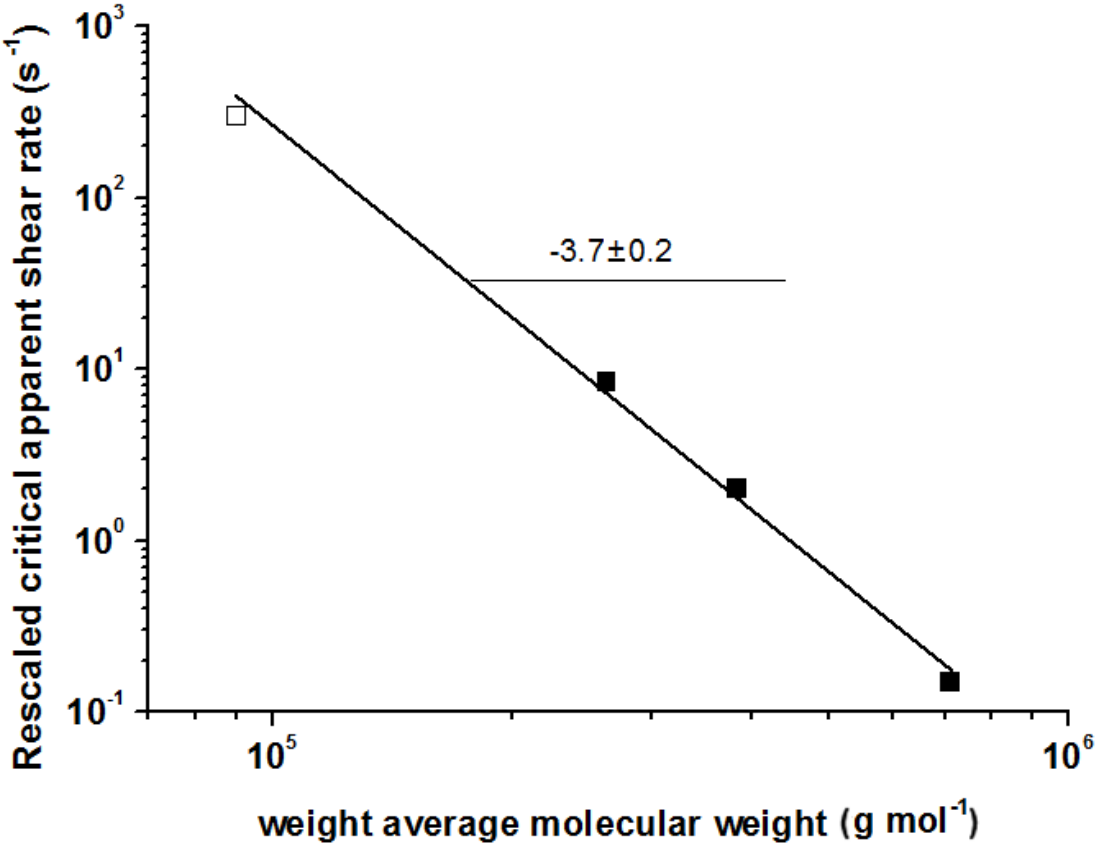

Figure 5.4: Rescaled critical apparent shear rate as a function of weight average molecular weight. The unfilled symbol represents the rescaled critical shear rate of PE-A, the M_w of which is below the suggested critical molecular weight (M^* =10^{5}g mol^{-1}) and the rest of filled symbols are taken from literature (PE-KA: 2.62×10^5 PDI=3.1, PE-KB: 3.81×10^5 PDI=5.1, and PE-KC: 7.08×10^5 PDI=6.5 [31(a)]).

According to the molecular origin of the window effect, the appearance of the extrusion window is correlated with a certain stretched chain conformation. Such a stretched chain conformation is dependent on relaxation time of polymer chains and the imposed shear rate. Polymers exhibit time-dependent viscoelastic behaviour[49]. In order to attain and maintain the stretched chain conformation for slip flow, the applied strain rate, viz. shear rate, should be greater than the inverse of the characteristic relaxation time. As a consequence the internal relaxation, viz. coiling back, cannot occur prior to the disentanglement of the adsorbed chains from the free chains. The

Weissenberg number indicates the boundary condition for the coil-stretch transition andis defined by[51]:

$$W_i = \frac{\lambda_{rep}}{t} \tag{5.2}$$

Where λ_{rep} is the characteristic relaxation time of a polymer chain and t is the characteristic time of the fluid deformation rate. On substitution of the wall shear rate $\dot{\gamma}_w$ for $1/t$, the Weissenberg number can be expressed as:

$$W_i = \lambda_{rep} \dot{\gamma}_w \tag{5.3}$$

When W_i <1, polymer chains can reach internal equilibrium (i.e. coil state) faster than changes arising from the externally imposed strain. Therefore in such a situation, slip flow cannot occur. A coil-stretch transition occurs when W_i =1. In order to attain hydrodynamic boundary condition of continuous slip flow corresponding to high surface energy die, W_i should be above 1.

According to reptation model[42], the relaxation time λ_{rep} is proportional to the square of the contour length divided by the tube diffusion coefficient. The contour length is linear with molecular weight, and the tube diffusion coefficient is inversely proportional to the molecular weight. Hence, the reptation time is

$$\lambda_{rep} \sim M_w^3 \tag{5.4}$$

Therefore, if the two PEs with distinct M_w have respective window effects at a given temperature, the higher molecular weight PE with a longer relaxation time should exhibit the window effect at a lower shear rate compared to the low molecular weight PE. It coincides with the steep inverse power law relationship between the $a_T \ \dot{\gamma}_c^{\ w}$ and M_w.

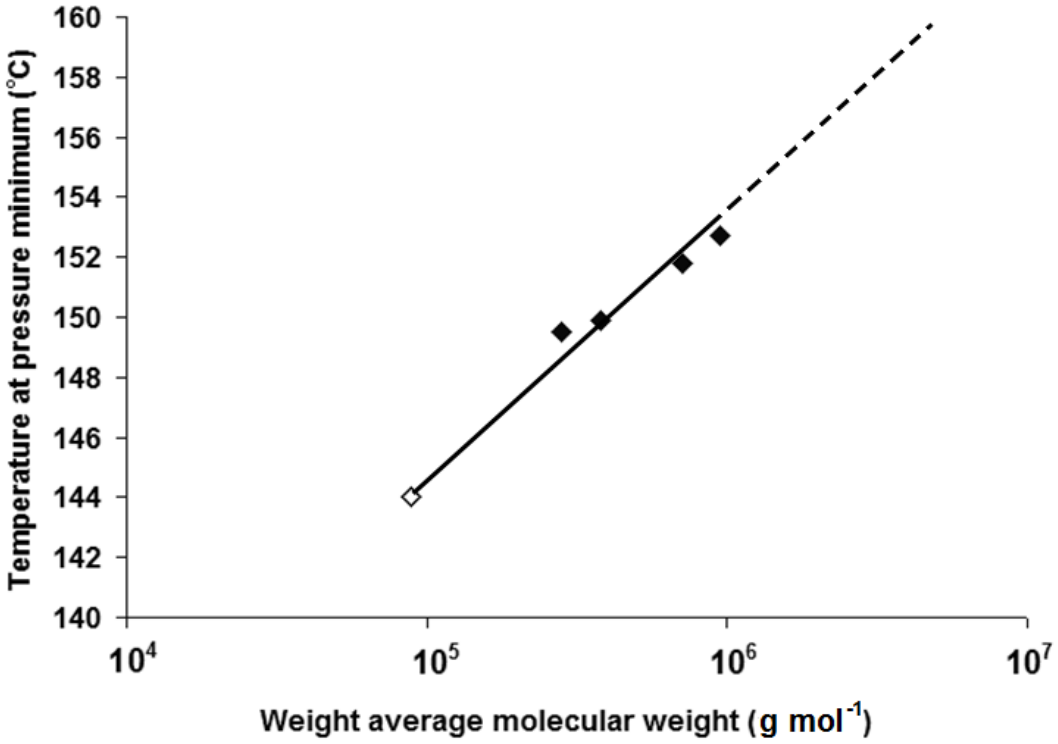

Figure 5.5: Temperature at pressure minimum (in the window region) as a function of logarithmic M_w. Filled data points are from the experiments reported in Kolnaar's paper (PE-KM: 2.8×10^5 PDI=7.5, PE-KB: 3.81×10^5 PDI=5.1, PE-KC: 7.08×10^5 PDI=6.5 and PE-KD: 9.5×10^5 PDI=4.2[31(a)]). The unfilled symbol is from the polymer used in this thesis (PE-A). The extrapolated dash line refers to the possibility of the window temperature anticipated in the high molecular weight PE (>10^6) having molar mass distribution below 7.0.

On the other hand, the characteristic relaxation time is also dependent on T. It can be estimated by the Arrhenius type equation:

$$\frac{1}{\lambda} = \frac{1}{\lambda_0} e^{-\frac{E_a}{R_g T}} \tag{5.5}$$

$$a_T = \exp\left[\frac{E_a}{R_g}\left(\frac{1}{T} - \frac{1}{T_0}\right)\right] \tag{5.6}$$

Where λ is relaxation time at shift temperature/window temperature, λ_0 is the relaxation time at reference temperature. E_a *is* the activation energy for chain relaxation, R_g is gas constant, and T is window temperature. According to equation 4.5, the relaxation time decreases dramatically with increasing temperature. For a given linear PE with a certain M_w, there is a critical temperature T_c^{onset} corresponding to the onset of the stationary stretched chain conformation at a given apparent shear rate ($\dot{\gamma}_a \geq \dot{\gamma}_c^{\,w}$). Above this temperature, the stretched chain conformation of the adsorbed

chain cannot be maintained within the time scale for the entire disentanglement of the adsorbed chains from free chains. For the narrow extrusion window the T_c^{onset} is circa 1°C above $T_{\min}$ (a temperature corresponding to the pressure minimum within the extrusion window). According to the temperature dependence of the window effect on the molar mass, if two PEs with distinct M_w show window effects at a given apparent shear rate, the higher molecular weight PE is expected to exhibit window effect at the higher temperature and the lower molecular weight PE is likely to have the window effect at the lower temperature.

However, the critical apparent shear rates for the onset of window effects, $\dot{\gamma}_c^{\ w}$, are different between high M_w and low M_w PEs. It is to be realised that the extrusion window in the high M_w PE arises at the low $\dot{\gamma}_c^{\ w}$; whereas in the low M_w PE the window effect is observed at high $\dot{\gamma}_c^{\ w}$. In order to compare the window temperatures of different M_w PEs at the same apparent shear rate, the influence of shear rate on window temperature need to be taken into account. It is found that the extrusion window can shift to higher temperature with increasing apparent shear rate. For an example, as shown in Figure 5.6, a high M_w PE referred as 2 shows an onset window effect, b, at $\dot{\gamma}_c^{\ w}$, here referred to be as $\dot{\gamma}_c^2$, which is lower than that , $\dot{\gamma}_c^1$, of low M_w PE. To have a proper comparison for the window temperature in the two molar masses the applied shear rate in the high molar mass PE should be set at an apparent shear rate required for the low molar mass (i.e. $\dot{\gamma}_c^1 = (\dot{\gamma}_c^2 + \dot{\gamma})$). On increasing the shear rate from $\dot{\gamma}_c^2$ to $(\dot{\gamma}_c^2 + \dot{\gamma})$ the extrusion window *b* will shift to a higher temperature, *b'*, from $T_{\min}^2$ to $T_{\min}^2 + T$.

Consequently, two extrusion windows for two different molar masses (high and low) can be compared at the same apparent shear rate as shown in Figure 5.6. At the identical apparent shear rate, $\dot{\gamma}_c^1$, the window temperature, $T_{\min}^2 + T$, of high M_w PE is apparently higher than that, $T_{\min}^1$, of the low M_w PE, since $T_{\min}^1$ is lower than $T_{\min}^2$ as shown in Figure 5.5.

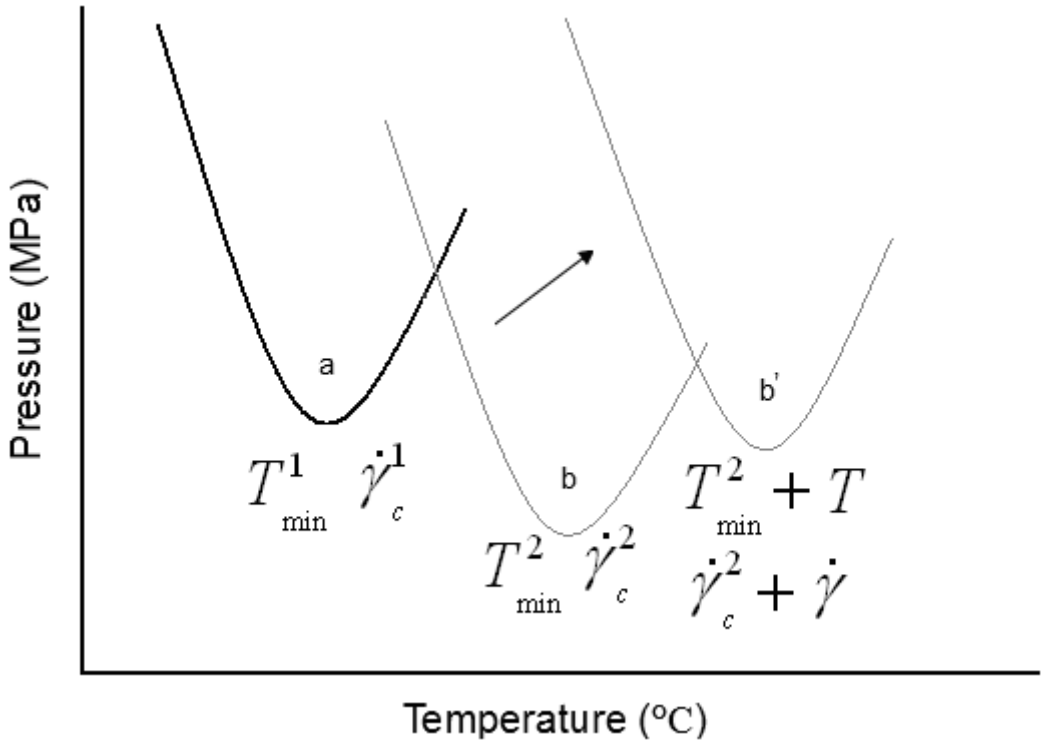

Figure 5.6: A schematic diagram of window effect corresponding to two distinct molecular weight PEs. The black curve represents the extrusion window of low molecular weight PE. On the other hand, the grey curves represent extrusion window of high molecular weight PE occurring at T^2_{min} and $T^2_{min}+T$ at different shear rates. With increasing apparent shear rate from $\dot{\gamma}^2_c$ to $(\dot{\gamma}^2_c+\dot{\gamma}=)\,\dot{\gamma}^1_c$, the extrusion window corresponding to the high molecular weight PE shifts from T^2_{min} to the high temperature $T^2_{min}+T$.

The onset temperature of the window effect, T_{onset}, is dependent on the relaxation time and the imposed shear rate, whereas the molecular origin of the termination temperature of the window effect is still unrevealed. Keller suggested that the window effect ceases when flow induced solidification occurs[30]. However, it is found that the window effect of PE-A terminates prior to the appearance of flow induced solidification, see Figure 5.1. Therefore, it implies that window termination cannot be simply explained by the solidification of the melt.

One of possible reasons for the window termination of PE-A can be related to the slip flow-hydrodynamic boundary condition (*SL - HBC*). With decreasing temperature the frequency of adsorption and desorption process of chains on the capillary wall is likely to decrease. This would result into the increase in density of the adsorbed chain segments on the capillary wall, ν. Below the window temperature, with decreasing temperature as the free volume also decreases, see Figure 5.7 at 142°C, it is less likely

for chains in the bulk to disengage from the adsorbed chain segments on the capillary wall. Thus once the disengagement process of chains in the bulk from the adsorbed chains is suppressed, the ease in flowability will be hindered causing the increase in pressure ultimately leading to window termination. The overall molecular effect will cause re-appearance of stick flow region at low temperatures in the intermediate prior to the sudden decrease in the free volume due to crystallisation and after the termination of the window effect. Such a possibility is further strengthened by considering that the critical shear rate for disentanglement of adsorbed chains increases with increase in surface coverage. Thus at a given shear rate as the density of adsorbed segments increases the tendency to slip will decrease. This would be the origin for decrease in distance between entanglements. On decreasing temperature further, the increased bulk density and the arising constraints due to flow will induce solid state solidification due to crystallisation.

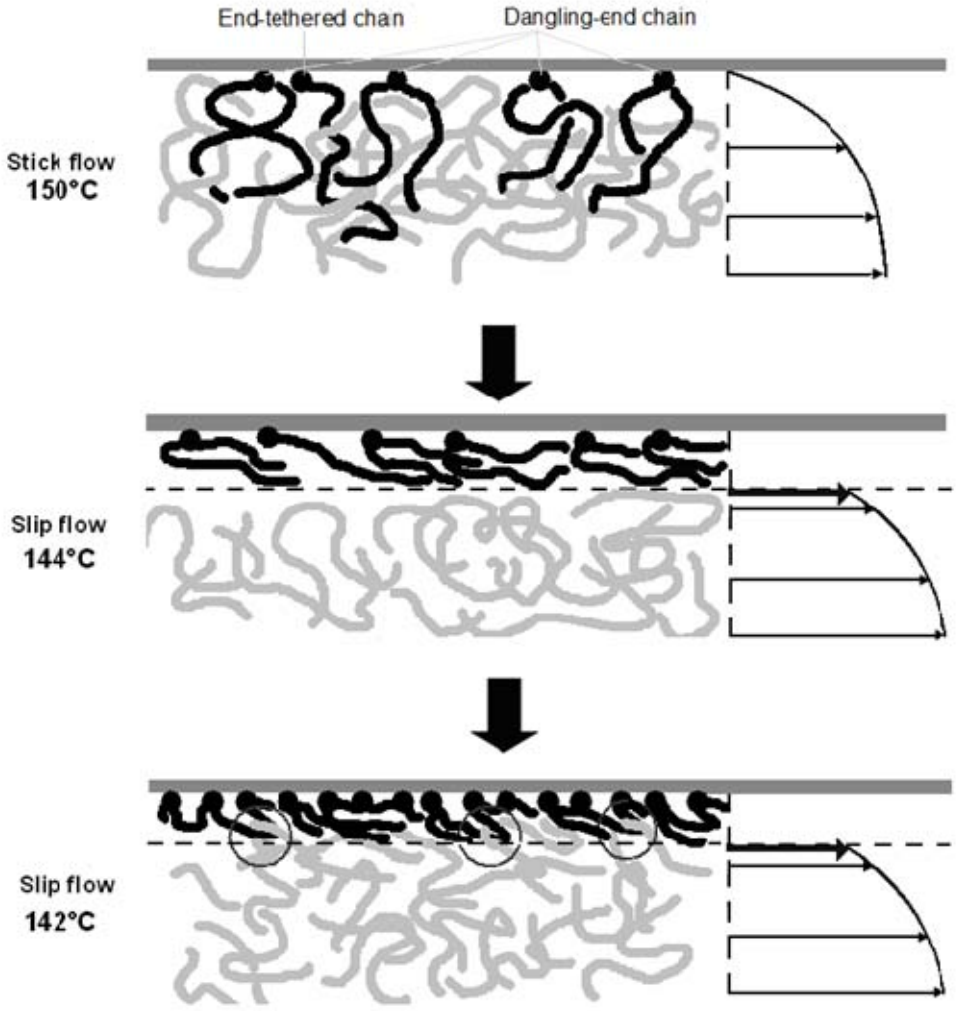

Figure 5.7: Schematic view of hydrodynamic conditions arising from stick flow and slip flow corresponding to the flow behaviours observed in DTS at shear rate, 250s-1. At high temperature,

e.g. 150°C, stick flow is likely to occur, as shown on top, where adsorbed chains cannot maintain the stretched chain conformation. As the temperature reduces to the extrusion window temperature, 144°C, slip flow mainly occurs due to the disentanglement of the adsorbed chains from free chains since the stretched chain conformation of the adsorbed chain can be retained at the window temperature in the time scale of the entire disengagement. With further decreasing temperature to 142°C, more chains or chain segments from the same chain can adsorb on the inner capillary wall, thus decreasing the entanglement distance and suppressing the disengagement of free chains from the adsorbed chains.

5.3.2 Flow induced solidification (Region IV)

Below a certain temperature the apparent viscosity increases dramatically and eventually the capillary is blocked. The reason for that has been interpreted by flow-induced crystallisation/solidification [50]. The onset temperature of flow induced solidification, T_s, is defined as a temperature corresponding to the sudden upswing in apparent shear viscosity as shown in Figure 5.8. From Table 5.2, it is found that the T_s increases with apparent shear rate. Regarding molecular origin of the flow induced solidification, randomly coiled polymer chains are first oriented during convergent flow. If such stretched chain conformation can be maintained in capillary flow, the oriented chains can act as precursor for further crystallisation. However, the flow induced ordered phase is unstable under Brownian motion at elevated temperature. In order to maintain such a stretched chain conformation, the Weissenberg number must reach or go beyond a critical value. According to coil-stretch theory, the stretched chain conformation can be maintained when $\dot{\varepsilon}\,\lambda_{rep} >> 1$ where $\dot{\varepsilon}$ is strain rate, here is related to apparent shear rate, and λ_{rep} is relaxation time of agile polymer chain. It is well known that the λ_{rep} decreases with temperature. Therefore, a higher shear rate is required to maintain such a stretched chain conformation at higher temperature, resulting in a higher T_s.

It is important to note that flow induced solidification and window effect are both time dependent effects and are related to the stretched chain conformation. However, the appearance of flow induced solidification requires a high Weissenberg number compared to the window effect. In other words, molecular chains need to be more highly oriented and aligned in flow direction to form a precursor for further crystallisation/solidification. On the other hand, in order to induce crystallisation, the size of the precursor must reach a critical value. Therefore, considering flow induced crystallisation such a stretched chain conformation needs to be maintained at high

temperature longer than that for the window effect, so that the precursor can grow and reach the critical particle size for further crystallisation. Therefore, the window effect can occur at high temperature, due to the lower Weissenberg number, compared to flow induced solidification.

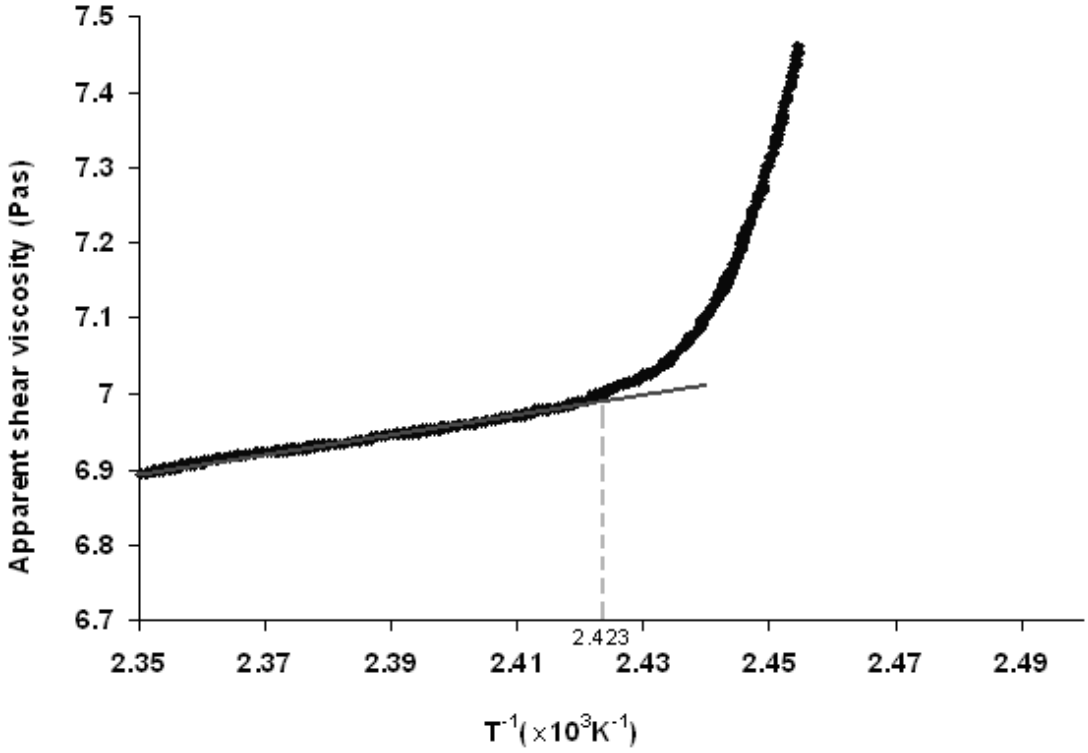

Figure 5.8: Logarithmic plot of apparent shear viscosity as a function of reciprocal temperature indicating the flow induced solidification effects emerging at 139.56°C , i.e. $1 \times 10^3/(T_{onset}+273.15)=2.423$. Results from dynamic temperature sweep of PE-A at shear rate of $200s^{-1}$ in Figure 5.2.

Table 5.2 The onset temperature of flow induced solidification of PE-A at different apparent shear rate.

Apparent shear rate (s^{-1})	T_s (°C)
200	139.5
225	139.6
250	139.6
300	140.0

5.4 Conclusion

The appearance of extrusion window of PE-A implies that the critical molecular weight, M^* , for the window effect is below 10^5 g mol^{-1}, an observation in contradiction to the suggested value given by Keller and Kolnaar.

With regards to the effect of shear rate on extrusion window, it was found that the window effect shifted to high temperature with increasing apparent shear rate. On the other hand, T_s increased with the apparent shear rate since flow induced ordered phase can only be maintained at higher strain rate with increasing the temperature.

The molecular weight dependence is an exquisite feature of the window effect and reveals the molecular origin of extrusion window. The rescaled critical apparent shear rate, $a_T \dot{\gamma}_c^{\ w}$, showed a power law dependence on M_w that scales with -3.7±0.2. This M_w dependence gives a quantitative relationship between stick-slip theory and extrusion window. Therefore, molecular origin of melt flow singularity of linear PE is concluded to arise from slip flow due to the disengagement of tethered chains on capillary wall surface from the free chains, where the aligned tethered chains may give rise to the formation of columnar like mesophase and finally ease the disengagement process.

Chapter 6: Melt flow singularity of bimodal polyethylene

6.1 Introduction

In the previous chapters it is conclusively shown that molecular origin of the extrusion window arises from the disengagement of tethered chains adhered to the capillary wall from the free chains (chains residing in the bulk), with assistance of a possible appearance of the columnar mesophase. According to the disentanglement mechanism[39], high molecular weight linear PE has the potential to possess a higher temperature window due to the relatively longer relaxation time[51]. In this chapter, a bimodal PE, referred to as PE-B, is selected to investigate the effect of bimodal molecular weight distribution on the melt flow singularity. The material used in this chapter, coded as PE-B, is synthesised by two different Ziegler Natta catalysts, where one catalyst synthesises the high molar mass and the other catalyst is for the low molar mass. Hence, PE-B can be considered as a molecular blend of two different molecular weight components mixed. For these fundamental studies, the synthesised sample PE-B is kindly provided by Borealis.

6.2 Results

6.2.1 The basic effect of melt flow singularity of PE-B

The bimodal PE, PE-B, shows an analogous melt flow singularity, depicted in Figure 6.1, in DTS as unimodal linear PE. The pressure drop occurs within a temperature interval, 144~147 °C, in which polymer melts are extruded smoothly without any distortion. In view of flow behaviour, stick flow starts from a high temperature, where the extrusion pressure gradually increases with decreasing temperature. Below 156°C, the flow behaviour of PE-B is situated in the pressure oscillation regime, in which the extrudate shows periodic bulk distortion. Once the temperature reduces to 147°C, a smooth extrudate with minimum die swell is observed. With a further decrease in the temperature, following the 'extrusion window' regime (<144°C), the extrusion pressure jumps up dramatically and a considerable increase in die swell occurs. Figure 6.2 shows four typical extrudate profiles at 140°C, 146°C, 152°C and 160°C, corresponding to four distinct flow regimes: flow induced solidification, extrusion window, melt instabilities and stable melt flow respectively. The die swell ratios show a minimum value in the extrusion window temperature as shown in Figure 6.3.

It is worth noting that the observed extrudate profiles in Figure 6.2 at 152°C consist of three classes. Starting from right hand side a helical distortion occurs in slip flow, just after the extrusion pressure reaches the maximum value. Following that, fairly smooth extrudate is observed in the slip flow regime at relatively low apparent shear rate compared to the helical distortion slip flow. Finally, very smooth extrudate shown on the left hand side emerges in the stick flow regime. It is apparent that the die swell ratio of smooth extrudate yielded in the slip flow is higher than that in the stick flow.

The effect of capillary flow on extrusion window is studied using a twin-bore rheometer, and compared with capillary free flow. Besides the end pressure correction, twin bore rheometer can offer a route to perform twin rheological characterisation simultaneously in the same condition. Prior to rheological measurements, the sample PE-B was filled into each barrel and was subjected to identical thermal history. Following the pre-heating the same piston velocity was applied in DTS (Dynamic Temperature Sweep), resulting in an identical apparent shear rate. Capillary die attached on the left barrel led to capillary flow, whereas orifice die on the right side resulted in a capillary free flow. It is apparent that a considerable pressure drop emerges at the window temperature in the capillary flow as shown in Figure 6.1, whereas no window effect is observed within pure convergent flow. These findings are in agreement with the earlier studies[31] and confirm that the convergent flow is not the origin of the window effect, while capillary flow facilitates the appearance of the window effect.

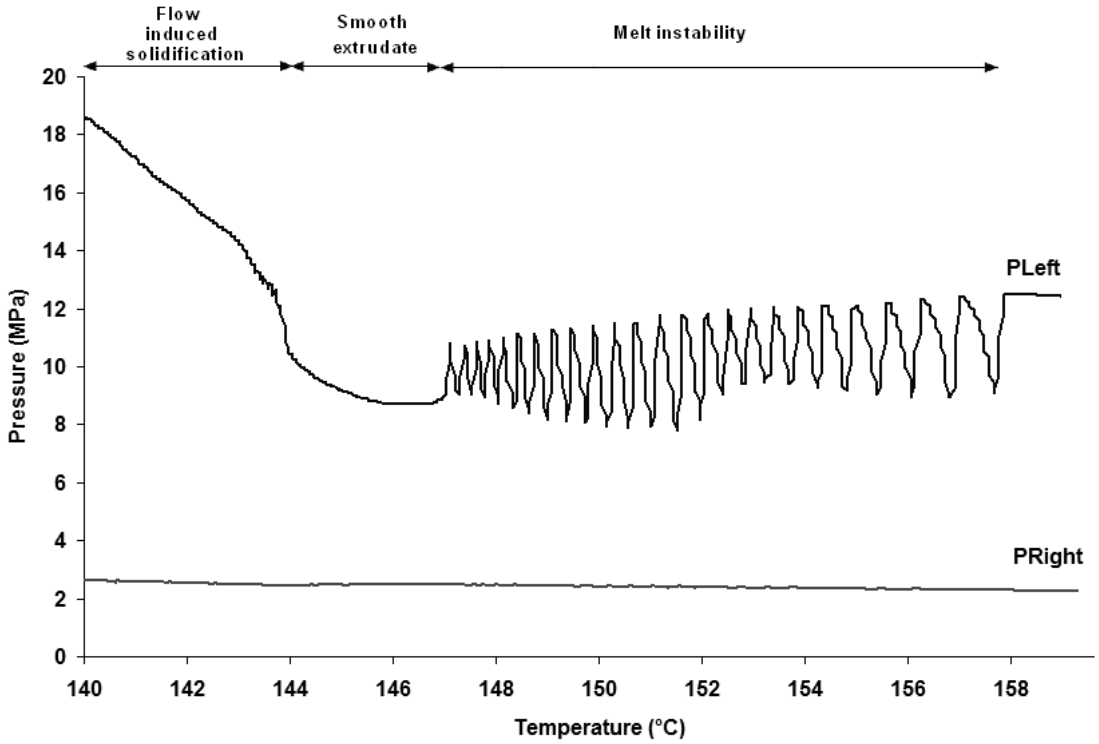

Figure 6.1: A plot of extrusion pressure vs. temperature recorded during dynamic cooling run at a given apparent shear rate of 150s^{-1}, showing the pressure minimum at 146°C (Cooling rate 1.50°C min^{-1}, M_w=1.7×10^5, capillary die geometry L-D-A: 16-1-π, Orifice die geometry: 0-1-π). PLeft corresponds to extrusion pressure drop in capillary flow and PRight is associated with extrusion pressure drop in capillary free flow.

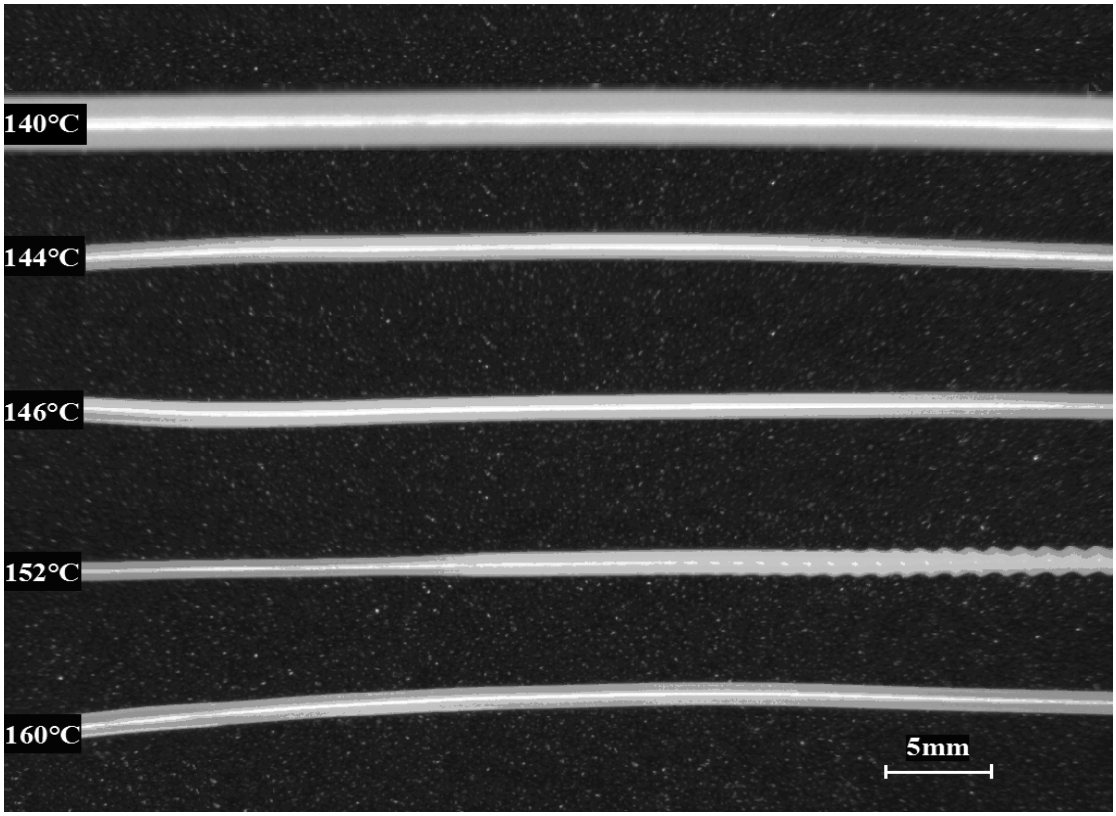

Figure 6.2: Photographs of extrudates obtained in DTS at different temperature at a fixed shear rate of 150s^{-1}

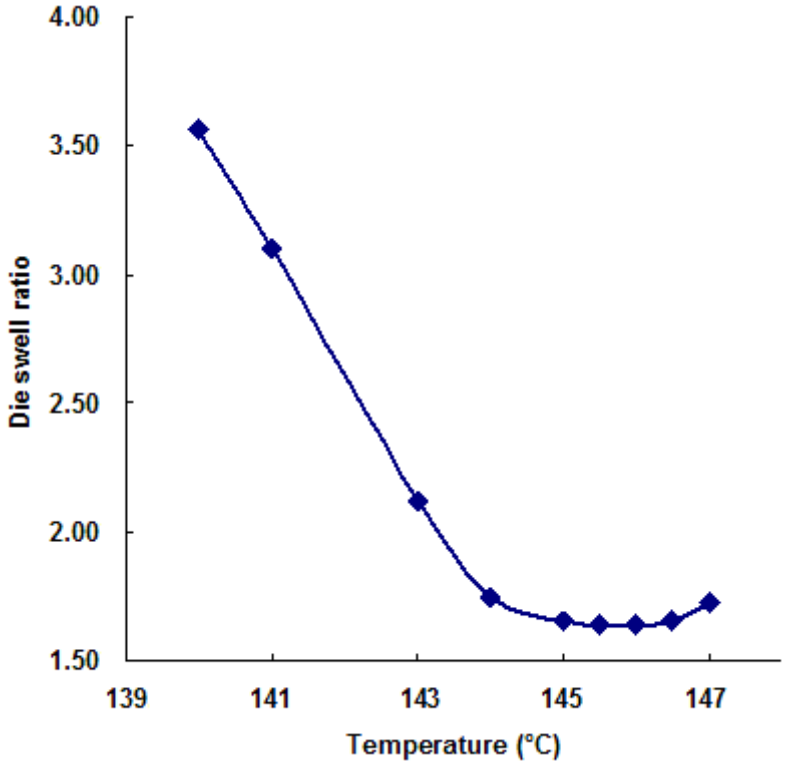

Figure 6.3: Die swell ratio as a function of temperature recorded in ISR at a fixed shear rate, 150s^{-1}.

6.2.2 The effect of apparent shear rate on the melt flow singularity of PE-B

The influence of apparent shear rate on the melt flow behaviour of PE-B is shown in Figure 6.4. The critical shear rate corresponding to the onset of the window effect is determined in DTS. The extrusion window appears at a minimum shear rate of 108s^{-1}, referred to as a critical shear rate $\dot{\gamma}_c^{\,w}$ for PE-B. Below this critical value, no window effect is observed in the extrusion of PE-B, where the extrusion pressure gradually increases with the decreasing temperature throughout the entire experimental temperature scale. The gradual increase in pressure is attributed to the increase in melt viscosity (η), which obeys a familiar Arrhenius type of relationship between η and T.

Above the critical shear rate $\dot{\gamma}_c^{\,w}$ for PE-B, a single pressure drop occurs in the window temperature interval. In addition, it is observed that there is an inverted saddle shaped pressure oscillation pattern occurring at a shear rate of 150s^{-1}. With a further increase in the apparent shear rate, at 300s^{-1}, three pressure drops emerge instead of one. One pressure drop located at the low temperature regime 146~148°C is named as low temperature window, where the smooth extrudate without any distortion is observed. If this low temperature window has the same molecular origin

as single extrusion window observed at low shear rate, such as at a shear rate of $108s^{-1}$, it is apparent that with the increase in the shear rate the window effect shifts to high temperature and pressure minimum shifts to high value. Regarding the middle temperature pressure drop, hereafter referred to as the middle temperature window, it possesses lowest pressure minimum located at 151.5°C in comparison with the other pressure drops. On the other hand, the middle temperature window is located at a broad temperature regime from 148°C to 154°C. The extrudate obtained in this regime is smooth and glossy with no distortions. Besides the two pressure drops, the third pressure drop is observed at the highest temperature, between 154°C to 158°C. Although there is no pressure oscillation occurring in the high temperature pressure drop, the extrudate in this regime exhibits fine scale surface distortion as shown in Figure 6.5 at 155°C. From these observations it is apparent that the extrusion window of the bimodal PEs is relatively complicated at high shear rates and opens a possibility to widen the narrow pressure drop in linear PEs.

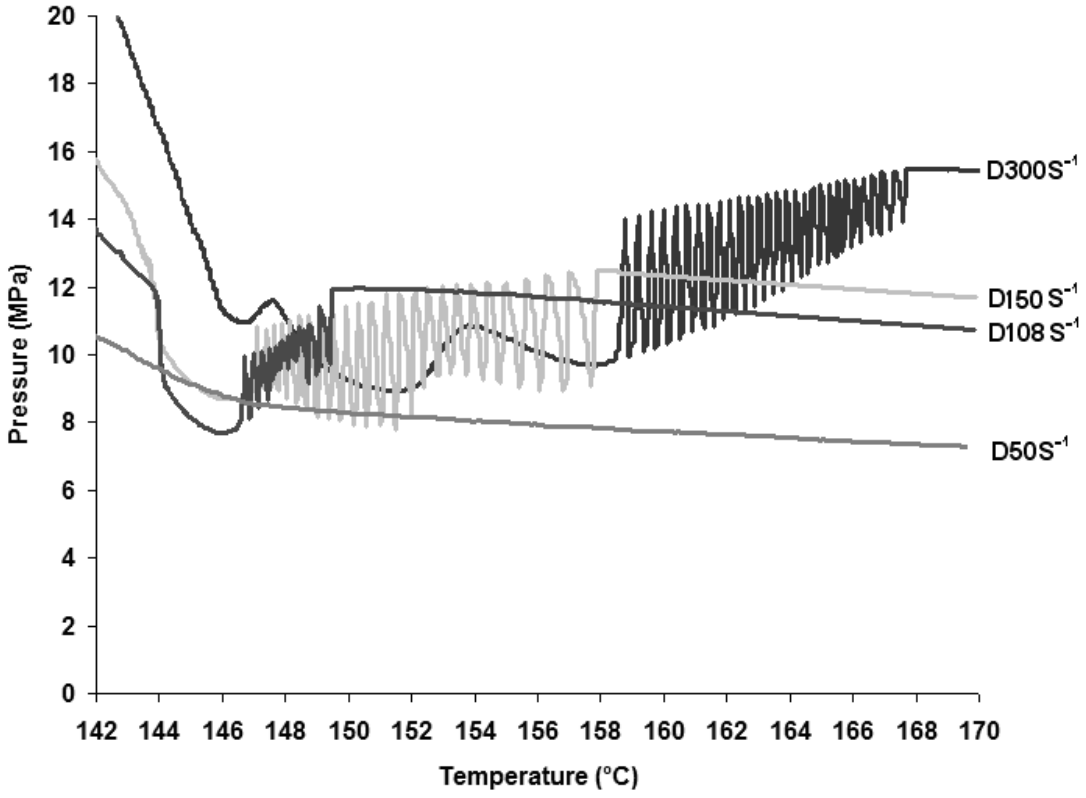

Figure 6.4: A plot of extrusion pressure vs. temperature recorded during DTS of PE-B at different apparent shear rate, $50s^{-1}$, $108s^{-1}$, $150s^{-1}$ and $300s^{-1}$ with a constant cooling rate 1.50°C min^{-1} (capillary die geometry: L-D-A: 16-1-π).

Figure 6.5 shows different extrudate profiles obtained at various temperatures in DTS at the shear rate of $300s^{-1}$. It is to be realised that the periodic bulk distortion occurs

above 158°C. This temperature is much higher than that observed at the lower shear rate of $150s^{-1}$.

The die swell ratios recorded in ISR experiments are plotted against temperature in Figure 6.6. From this Figure it is apparent that die swell ratio has two minima, at 146.5°C and 152°C, which coincide with window location, viz. window temperatures occurring in DTS at a shear rate of $300s^{-1}$, depicted in Figure 6.4. In addition the die swell ratio at 152°C is lower than at 146.5°C.

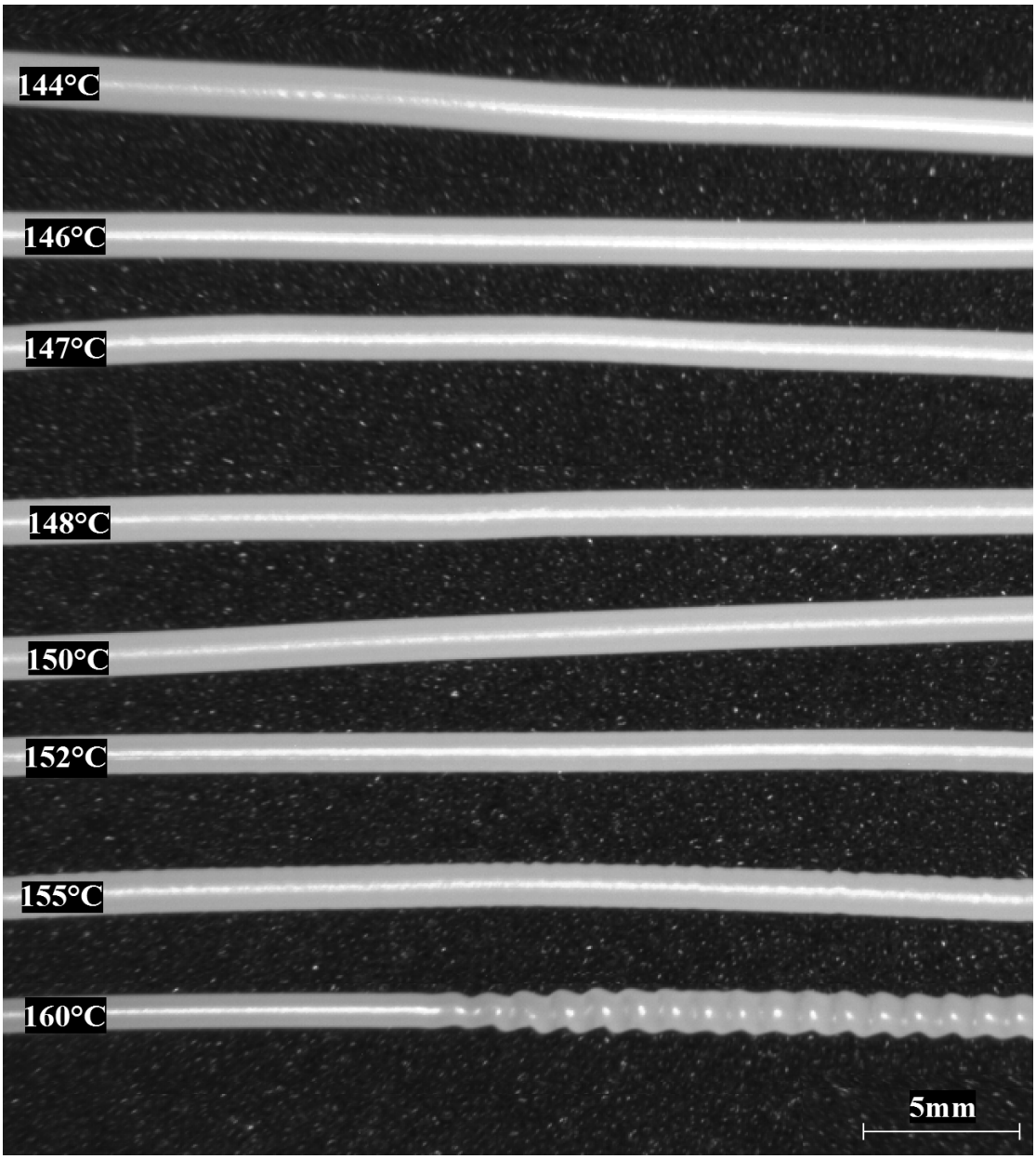

Figure 6.5: Photographs of extrudate obtained in DTS at different temperatures at a fixed shear rate, $300s^{-1}$.

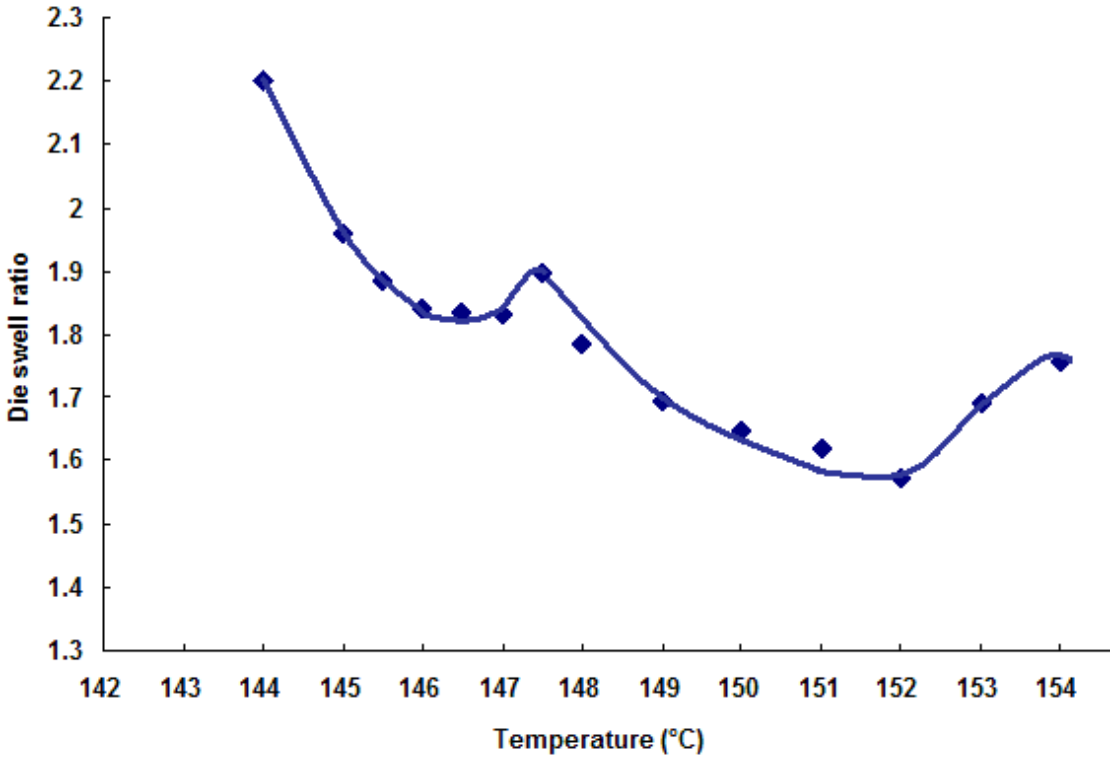

Figure 6.6: The die swell ratio as a function of temperature recorded in ISR at a fixed shear rate, 300s^{-1}.

6.2.3 Window effect at isothermal conditions

In dynamic experiments, extrusion pressures are recorded with decreasing temperature at a cooling rate of 1.50°Cmin^{-1}. In spite of the slow cooling rate, thermal equilibrium cannot be attained on account of thermal lag in between the capillary wall and polymer melt. To verify the existence and appearance of the window effect in isothermal flow conditions a series of isothermal step rate (ISR) rheological characterisations were performed at various temperatures.

Figure 6.7 depicts a series of plots of extrusion pressure vs. time at different shear rates recorded at isothermal conditions. In these set of experiments while the temperature is kept constant, shear rate is varied with time. The resultant changes in pressure corresponding to capillary flow (Pleft) and capillary free flow (Pright) are recorded. From Figures 5.7(a-c), it is apparent that extrusion pressure at 150s^{-1} is less than that at 50s^{-1}. These high shear rate anomalies can only be interpreted by distinct hydrodynamic conditions between stick flow and slip flow. Further evidence to verify the appearance of slip flow in extrusion window flow conditions will be shown in slip flow velocity measurements. A comparison of pressure at a specific shear rate can be made by compiling the experimental data at different temperatures. For instance,

shaded regions in Figure 6.7 correspond to extrusion pressures recorded during the isothermal capillary flows at a specific shear rate of $150s^{-1}$. Compiling all the isothermal results together, a panorama plot of extrusion pressure vs. temperature at a shear rate of $150s^{-1}$ is shown in Figure 6.8(a). It depicts change in extrusion pressure with temperature at a fixed shear rate of $150s^{-1}$ in which a pressure minimum observed at 146°C is consistent with window temperature location found in DTS shear rate of $150s^{-1}$. Figure 6.8(b) depicts extrusion pressures recorded in ISR at a shear rate of $300s^{-1}$, in which triple pressure drops coincide with the high shear rate window effect observed in DTS at $300s^{-1}$ as well. These isothermal studies complement the existence of extrusion window and window temperature location determined by DTS experiments. However, the pressure minima recorded in ISR is higher than those measured in DTS, which may arise from thermal lag in DTS.

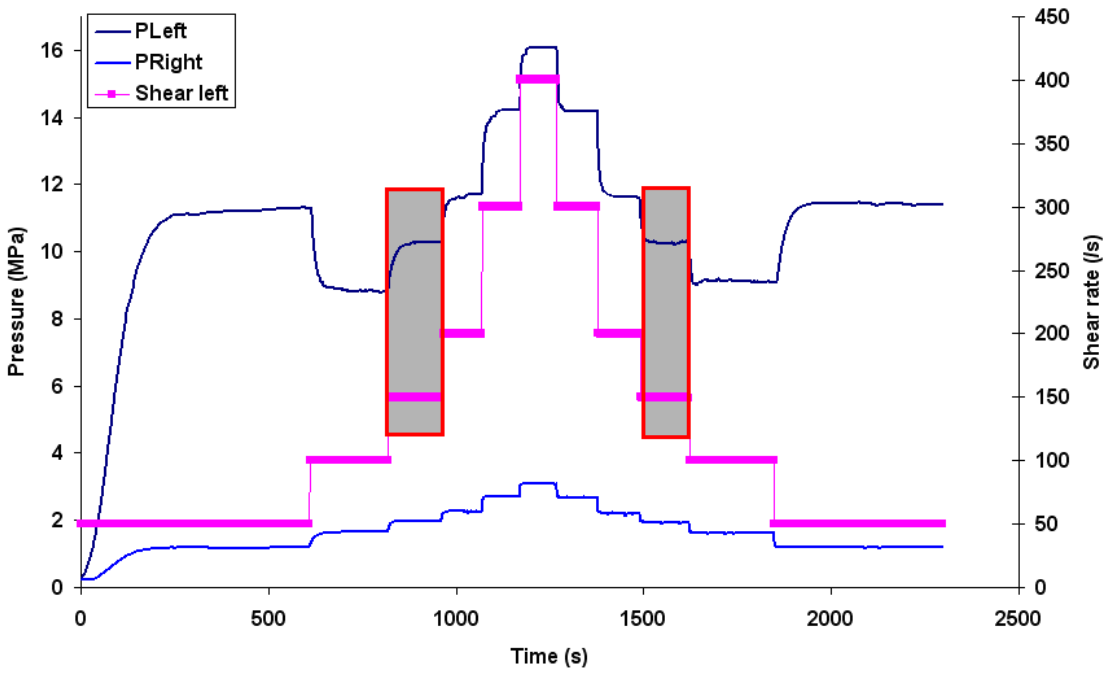

Figure 6.7(a): ISR results at 144°C show the extrusion pressure vs. time at different shear rate. Pressure profiles at $150s^{-1}$ are highlighted and compared with others at different isothermal conditions.

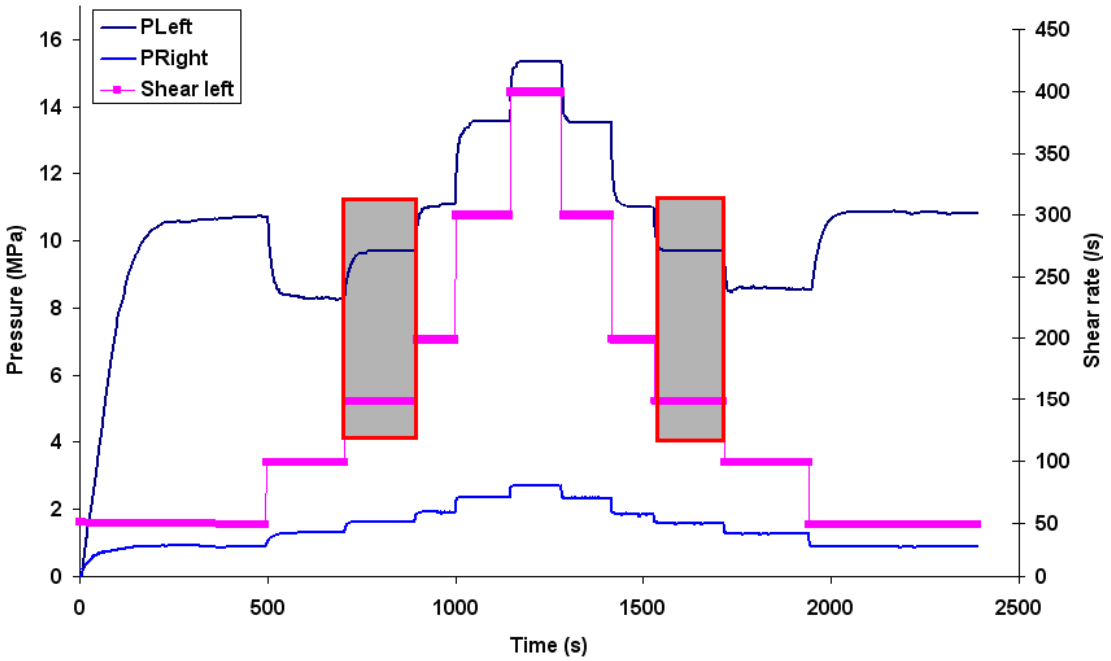

Figure 6.7(b): ISR results at 145°C show the extrusion pressure vs. time at different shear rate. Pressure profiles at 150s^{-1} are highlighted and compared with others at different isothermal conditions.

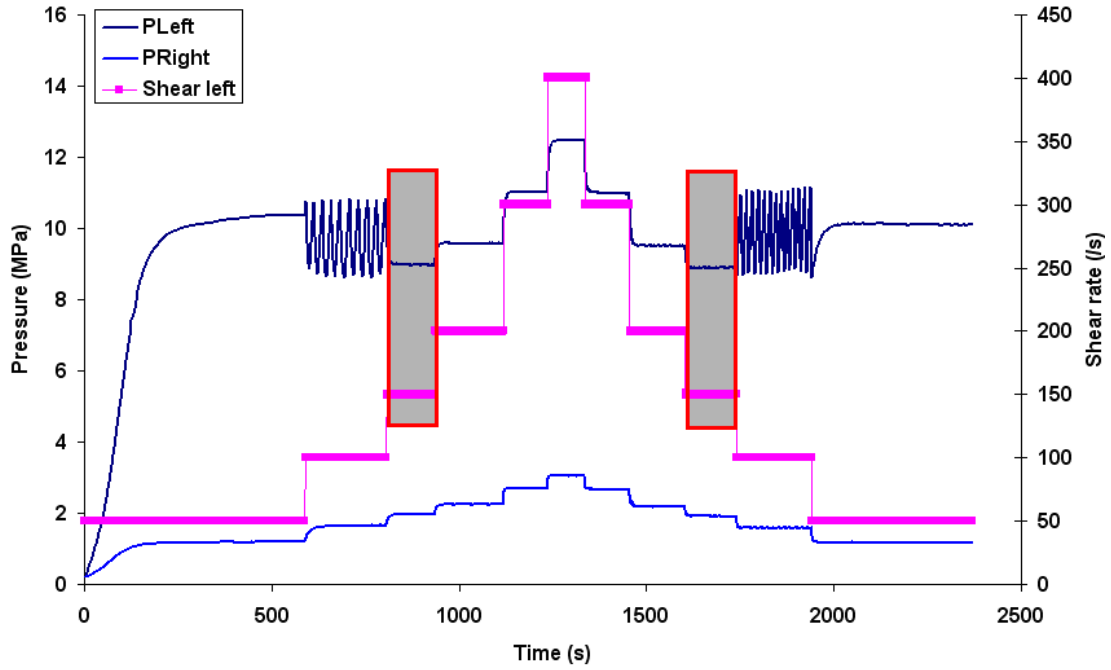

Figure 6.7(c): ISR results at 146°C show the extrusion pressure vs. time at different shear rate. Pressure profile at 150s^{-1} are highlighted and compared with others at different isothermal conditions.

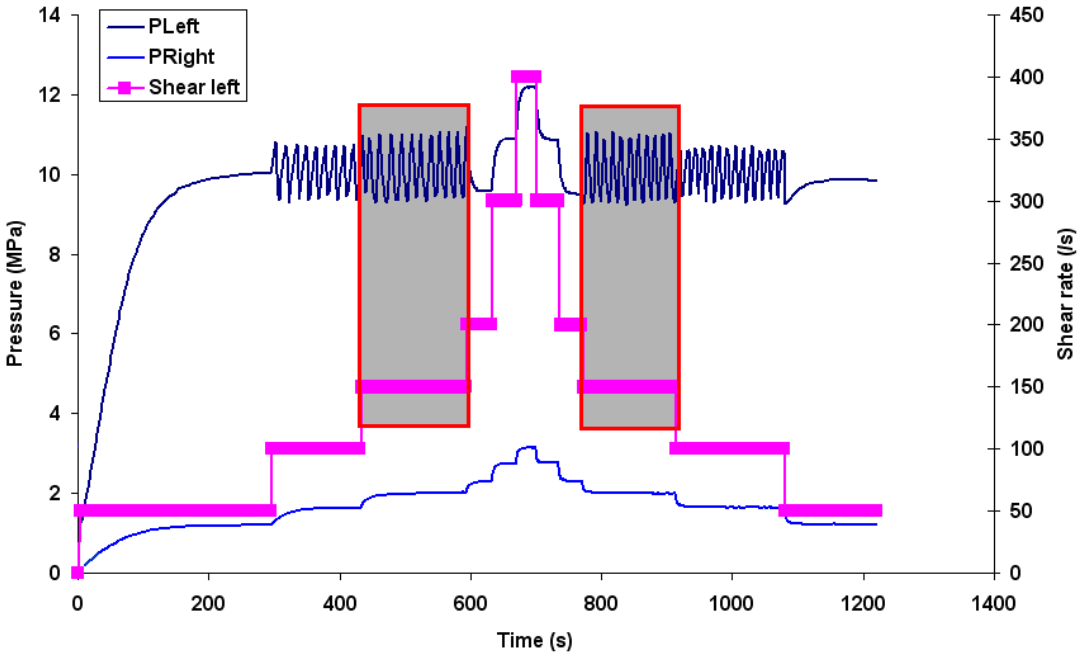

Figure 6.7(d): ISR results at 147°C show the extrusion pressure vs. time at different shear rate. Pressure profiles at 150s^{-1} are highlighted and compared with others at different isothermal conditions.

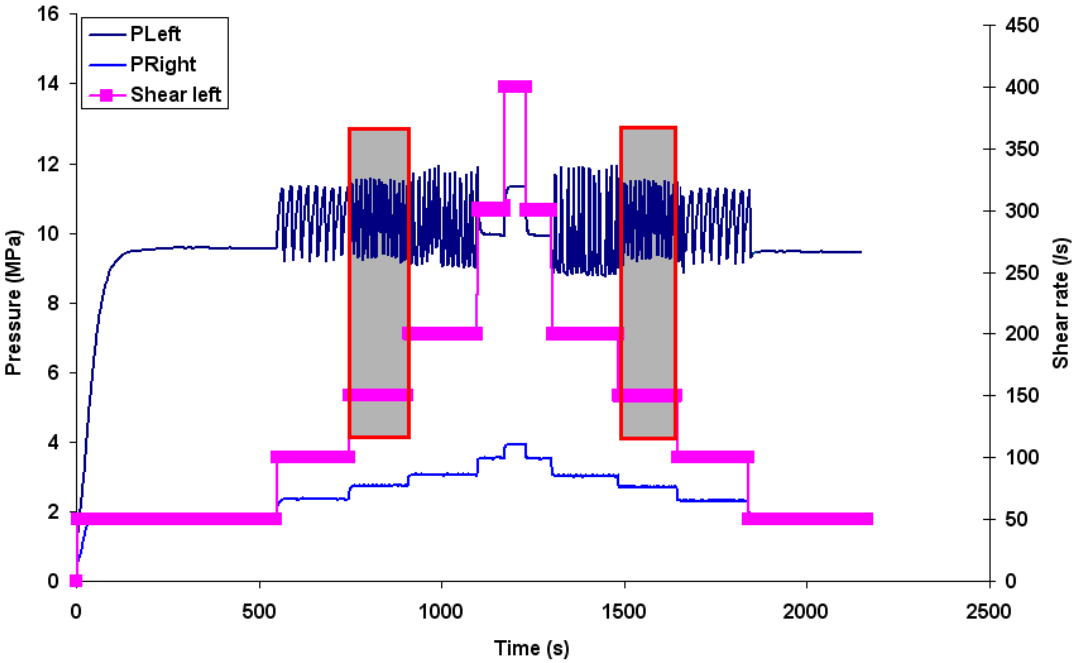

Figure 6.7(e): ISR results at 148°C show the extrusion pressure vs. time at different shear rate. Pressure profiles at 150s^{-1} are highlighted and compared with others at different isothermal conditions.

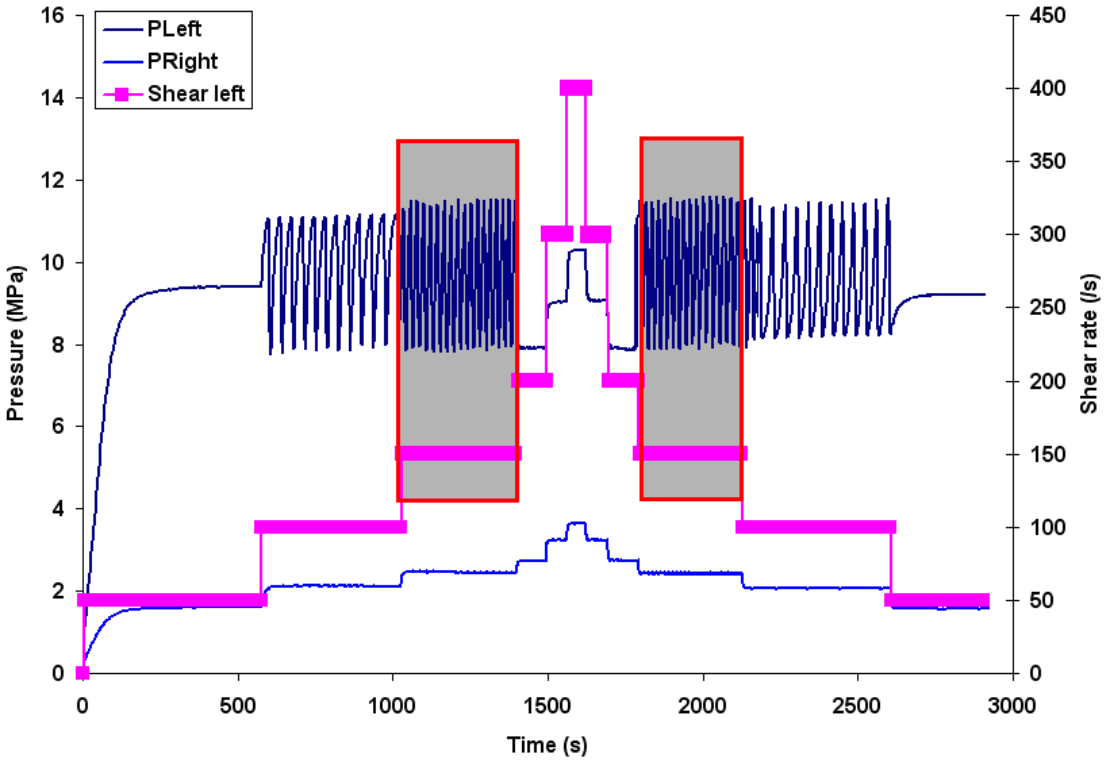

Figure 6.7(f): ISR results at 150°C shows the extrusion pressure vs. time at different shear rate. Pressure profiles at 150s^{-1} are highlighted and compared with others at different isothermal conditions.

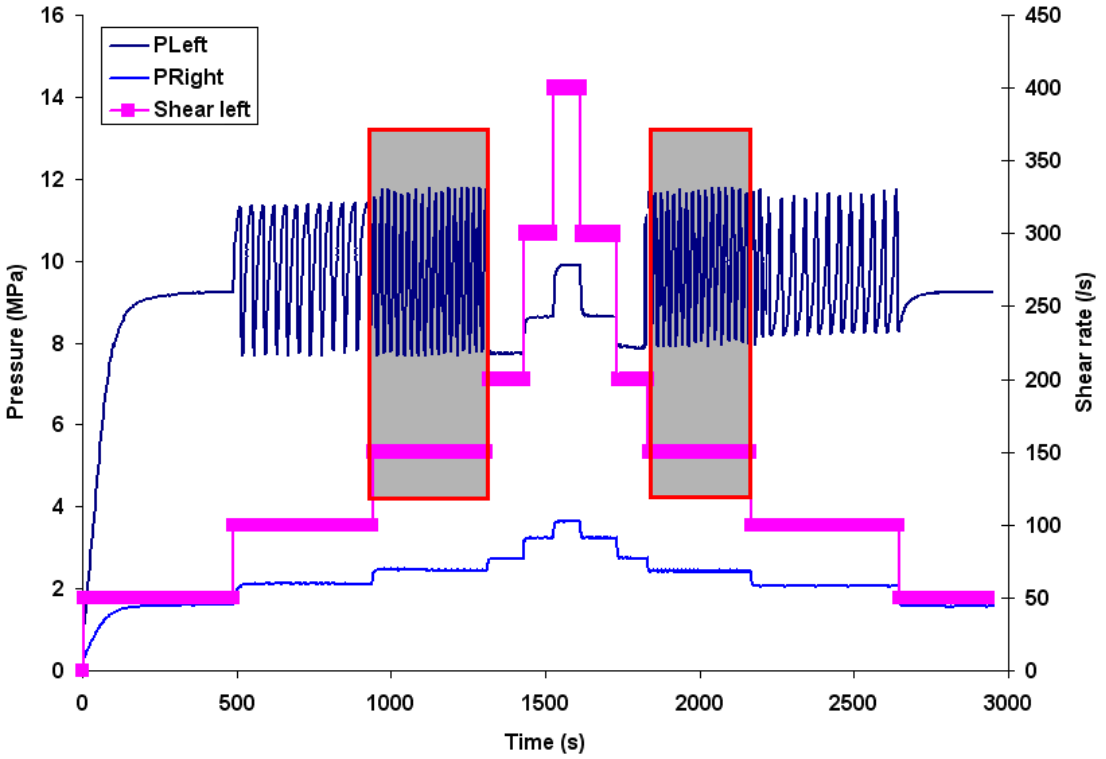

Figure 6.7(g): ISR results at 152°C shows the extrusion pressure vs. time at different shear rate. Pressure profiles at 150s^{-1} are highlighted and compared with others at different isothermal conditions.

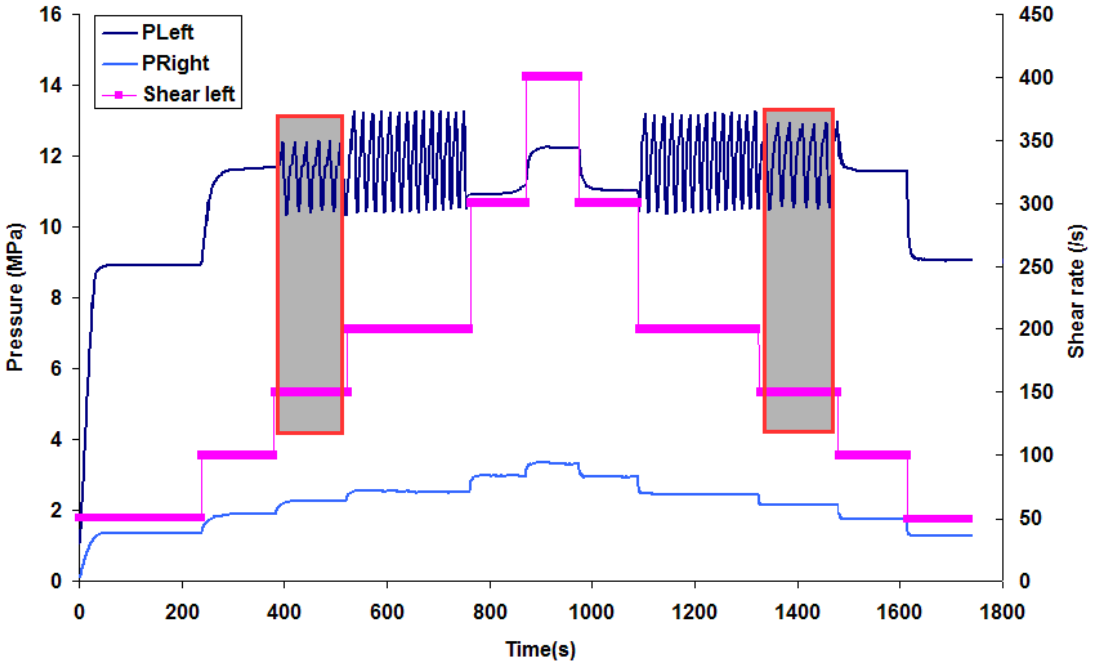

Figure 6.7(h): ISR results at 154°C show the extrusion pressure vs. time at different shear rate. Pressure profiles at 150s^{-1} are highlighted and compared with others at different isothermal conditions.

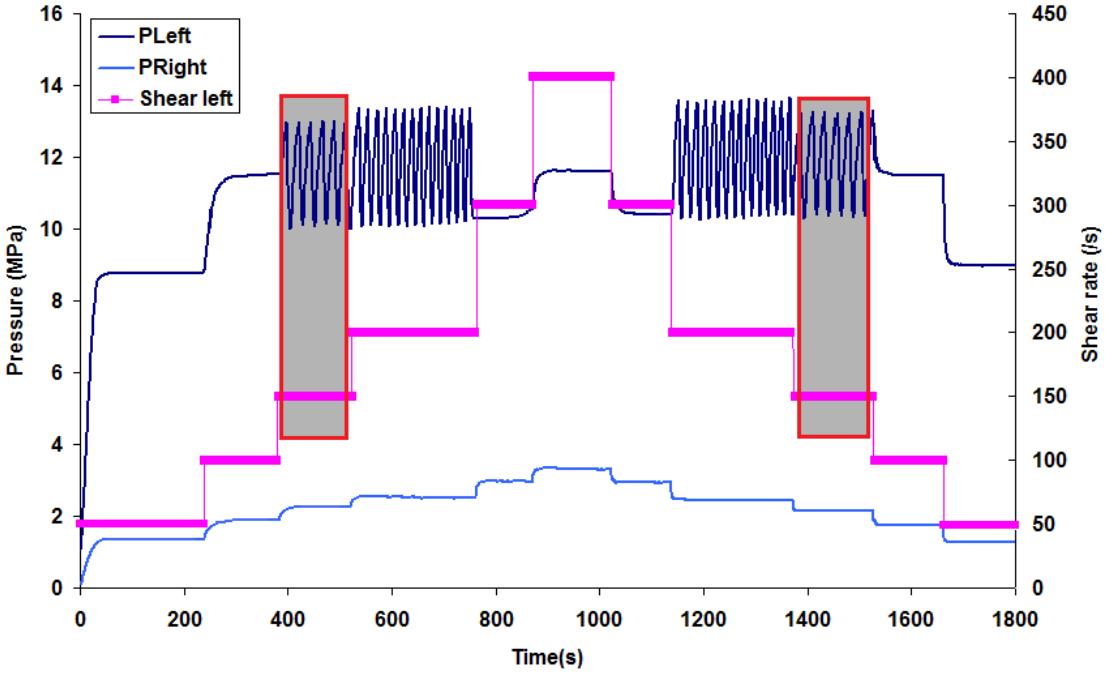

Figure 6.7 (i): ISR results at 155°C show the extrusion pressure vs. time at different shear rate. Pressure profiles at 150s^{-1} are highlighted and compared with others at different isothermal conditions.

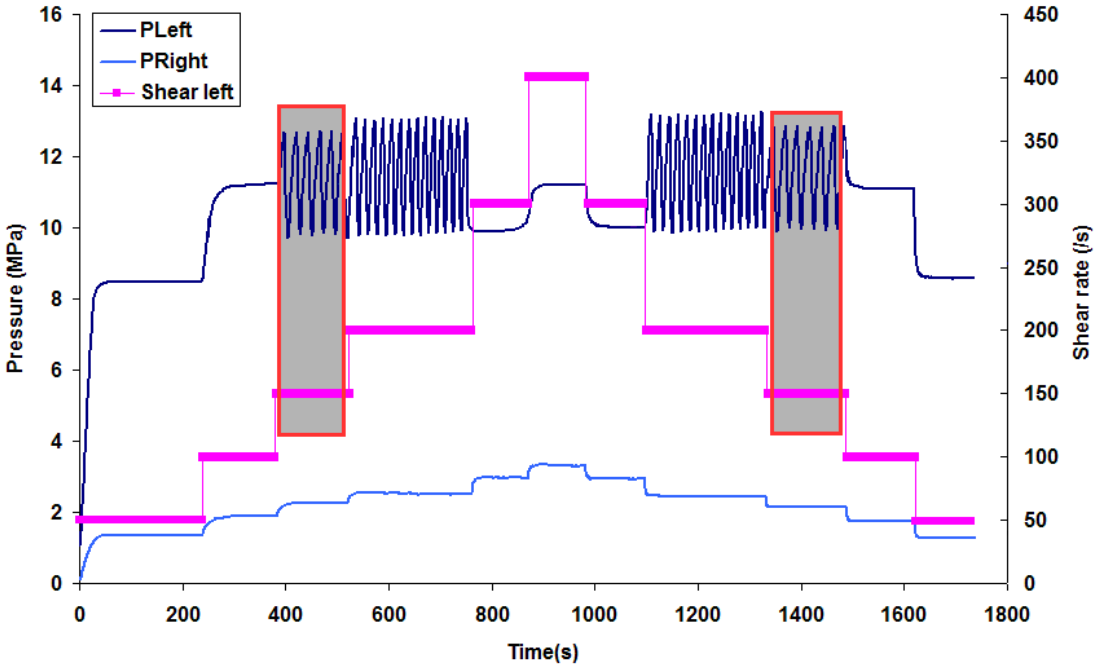

Figure 6.7 (j): ISR results at 158°C show the extrusion pressure vs. time at different shear rate. Pressure profiles at 150s^{-1} are highlighted and compared with others at different isothermal conditions.

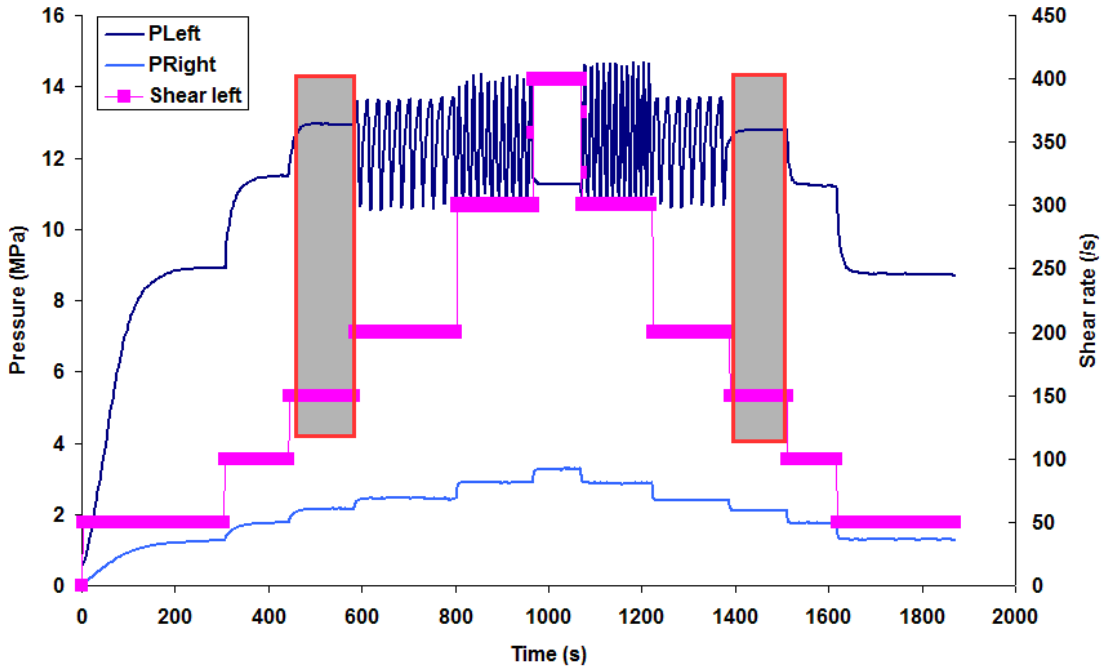

Figure 6.7(k): ISR results at 160°C show the extrusion pressure vs. time at different shear rate. Pressure profiles at 150s^{-1} are highlighted and compared with others at different isothermal conditions.

In addition, at all temperatures periodic bulk distortion and pressure oscillation are not observed in capillary free flow. These findings further confirm that periodic bulk distortion arises from capillary flow. Secondly, it is found that the extrusion pressure

increases with the imposed shear rate in the stick flow regime. Finally, it is worth pointing out that there is no slip flow occurring in the course of capillary free flow (flow of the extrudate through the orifice alone), which is in the agreement of that the capillary flow gives rise to the window effect.

The ISR results fully complement the existence of window effect observed in DTS. From the comparison it could be stated that the window location and pressures minimum from DTS coincides with the results obtained from the isothermal experiments, even though the thermal equilibrium cannot be attained in DTS. Therefore, DTS could be suggested to investigate the window effect since ISR experiments are more time-consuming technique. Parameters that could be determined in DTS at the cooling rate of 1.50°C min^{-1} are the critical apparent shear rate for the onset of the window, $\dot{\gamma}_c^{\,w}$, window temperature intervals, and window temperature location.

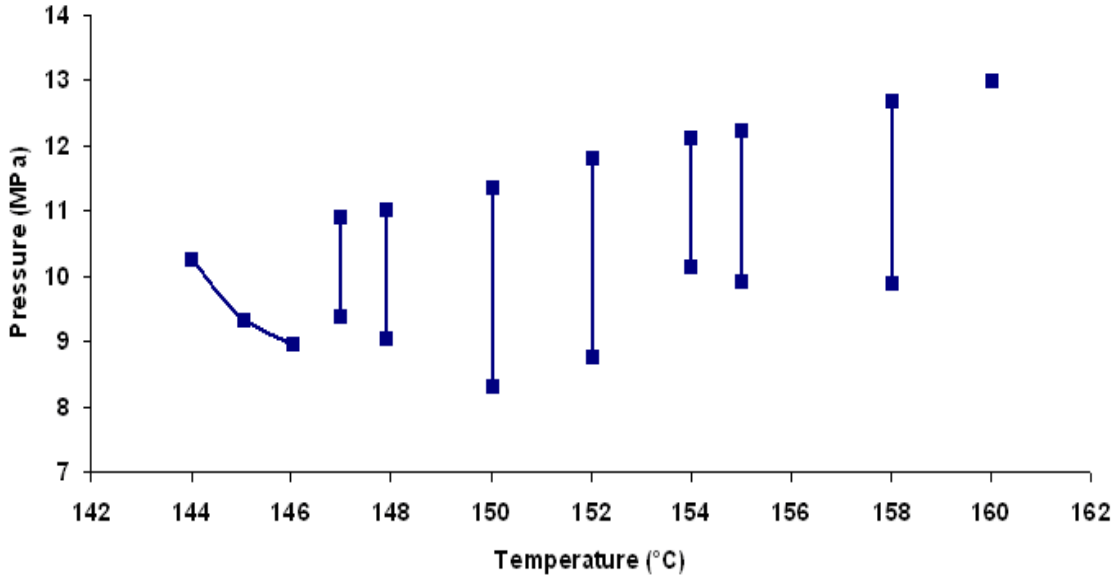

Figure 6.8(a): A plot of extrusion pressures vs. temperature at a shear rate of 150s^{-1}recorded in ISR for the bimodal sample PE-B. The vertical lines represent oscillations in the pressure (Die geometry: L-D-2α: 16-1-π).

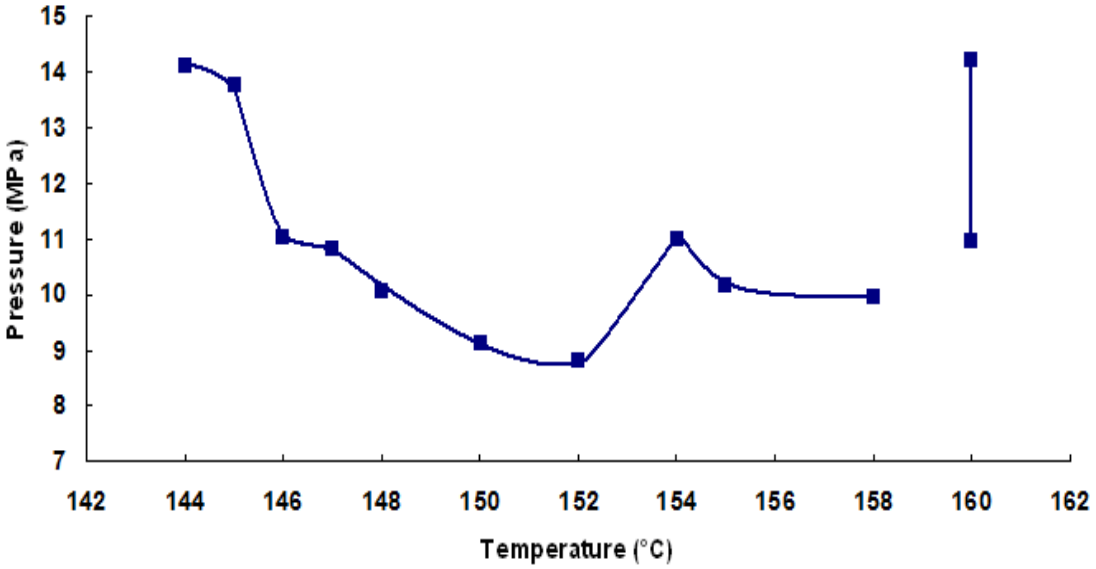

Figure 6.8(b): A plot of extrusion pressure vs. temperature at a shear rate of 300s^{-1} recorded in the ISR experiment. The Figure shows three pressure drops located at 146°C, 152°C and 158°C. These observations are in accordance with DTS results for the sample PE-B, see Figure 6.4. The vertical line at 160°C represents oscillations in the pressure (Die geometry: L-D-2α: 16-1-π).

6.2.4 Isothermal mono-rate time sweep characterisation

'Melt fracture' is a common problem encountered in plastic extrusion. The onset of melt irregularities indicates boundary conditions for polymer processing. Considering the window effect, two flow criticalities indicate the boundary condition of the extrusion window. Therefore, an isothermal mono-rate time sweep (IMTS) characterisation was adopted to determine the flow criticalities, in which the critical apparent shear rates including $\dot{\gamma}_c^{\,p}$, $\dot{\gamma}_c^{\,w}$ and $\dot{\gamma}_c^{\,h}$, corresponding to onset of periodic bulk distortion, window effect slip flow and helical distortion respectively, are determined at a given temperature. In addition, melt instabilities and extrudate distortions are also studied in IMTS at different temperatures and apparent shear rates. Since polymer melts have 'memory effect', the flow history does influence the rheological behaviour. Therefore, IMTS is adopted to determine the extrusion pressure at a single shear rate (mono-rate) without any interference of pre-flow history. In this respect compared to ISR experiments, IMTS is more accurate.

The melt fracture observed in the course of capillary flow of PE-B falls into two categories, namely *periodic bulk distortion*, associated with pressure oscillations, and *helical distortion*. However, surface melt fracture, referred to as 'shark-skin', does not emerge during the capillary flow of PE-B at varying flow conditions. Figure 6.9 shows extrusion pressure at different shear rates recorded in IMTS test at 170°C. The

extrudate profiles and flow behaviour are described as follows with the increasing shear rate:

(1) The extrudate is smooth and glossy when the shear rate is below $\dot{\gamma}_c^{\,p}$. In addition, surface distortion is not observed in the high-shear-rate stick flow of the bimodal polymer, PE-B; before the appearance of the pressure oscillation. However, such a shark-skin effect usually occurs at high-shear-rate stick flow of unimodal polyethylene with relatively low polydispersity,

(2) At and above the $\dot{\gamma}_c^{\,p}$ ($346s^{-1}$), pressure oscillations are observed and are accompanied with periodic bulk distortion. The pressure oscillation possesses a regular pattern of increasing and decreasing pressures as a function of time, shown in Figure 6.13. Combining the recorded pressure oscillations in Figure 6.13 and the corresponding extrudate profile shown in Figure 6.9(b), it is found that each 'cycle' of pressure oscillation observed at 170°C consists of two steps. In the first step, the extrusion pressure increases gradually during stick flow, yielding a smooth and glossy extrudate. With increasing extrusion pressure, before attaining the maximum value, the efflux rate drops to the minimum. Once the pressure reaches the maximum value, extrusion pressure decreases dramatically in a short time and the resultant extrudate shows helical distortion.

(3) With increasing the apparent shear rate further, at or above $\dot{\gamma}_c^{\,h}$ ($510\ s^{-1}$), helical distortion occurs during slip flow without any trace of pressure oscillation. The extrusion pressure corresponding to the onset occurrence of helical distortion succeeds the minimum pressure of pressure oscillation at the highest apparent shear rate. In addition, the extrusion pressure in this regime increases with the imposed apparent shear rate.

With respect to the flow behaviour and extrudate profiles observed at relatively low temperature at 158°C and 152°C, it is found that the slip flow falls into two categories in both the stick-slip flow and the stationary slip flow. One is helical distortion slip flow as aforementioned at 170°C, the other is termed as window effect slip flow since the flow conditions and extrudate profile are identical to the window effect. Regarding the stick-slip flow observed at 158°C and 152°C, pressure oscillation occurs when the $\dot{\gamma}_a \geq \dot{\gamma}_c^{\,p}$ and the resultant extrudate profiles are shown in Figure 6.10(b) at $220s^{-1}$ and Figure 6.11(b) at $110s^{-1}$. It can be observed that there are three types of extrudate

profiles emerging in the pressure oscillation regime rather than two at 170°C with the shear rate of 370s^{-1}. The only difference is the emergence of discrete window effect slip flow. It occurs after extrusion pressure reaches a critical value during the pressure oscillation. The resultant extrudate is smooth but with higher die swell ratio compared with smooth extrudate yielded in the discrete stick flow at the same shear rate. With regards to stationary slip flow, window effect slip flows occur first when the $\dot{\gamma}_a$ reaches or exceeds the corresponding $\dot{\gamma}_c^{\,w}$, as shown in Figure 6.10(b) at 260s^{-1} and 6.11(b) at 240s^{-1}. When $\dot{\gamma}_a \geq \dot{\gamma}_c^{\,h}$, helical distortion slip flow occurs.

As the temperature declines further, at 146°C as depicted in Figure 6.12, the helical distortion slip flow does not appear in the periodic distortion regime as shown in Figure 6.12(b).

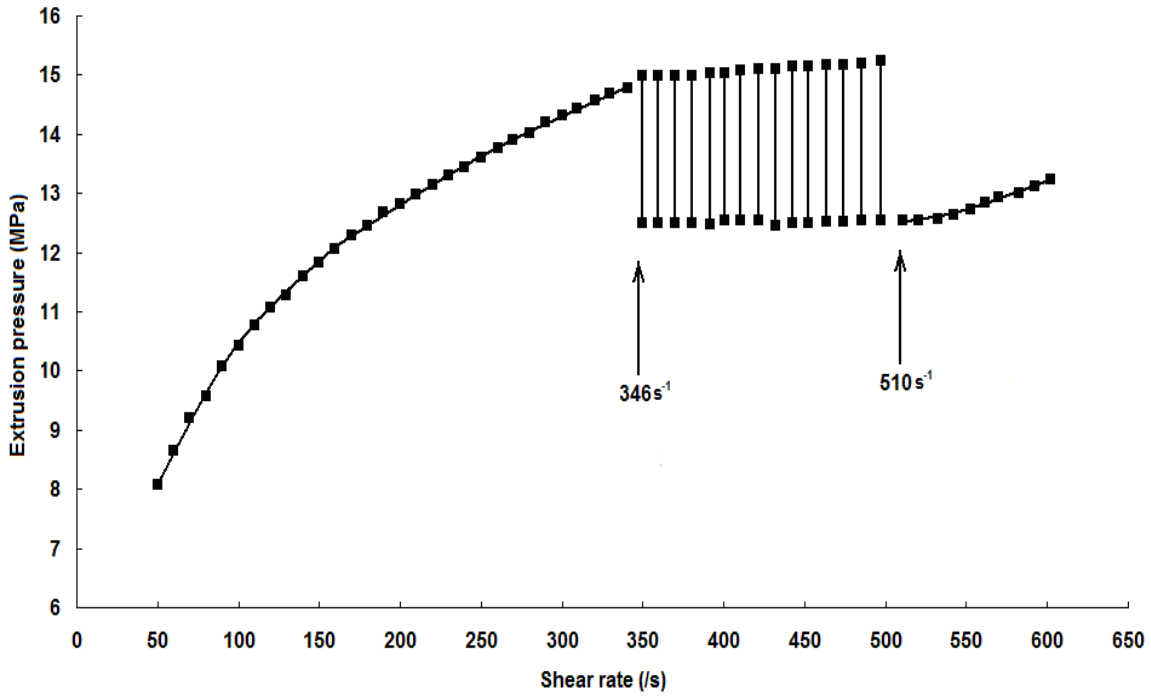

Figure 6.9(a): Flow curve for PE-B recorded at 170°C. The vertical lines represent the pressure oscillations. The arrows indicate the $\dot{\gamma}_c^{\,p}$ at 346s^{-1} and $\dot{\gamma}_c^{\,h}$ at 510 s^{-1}.

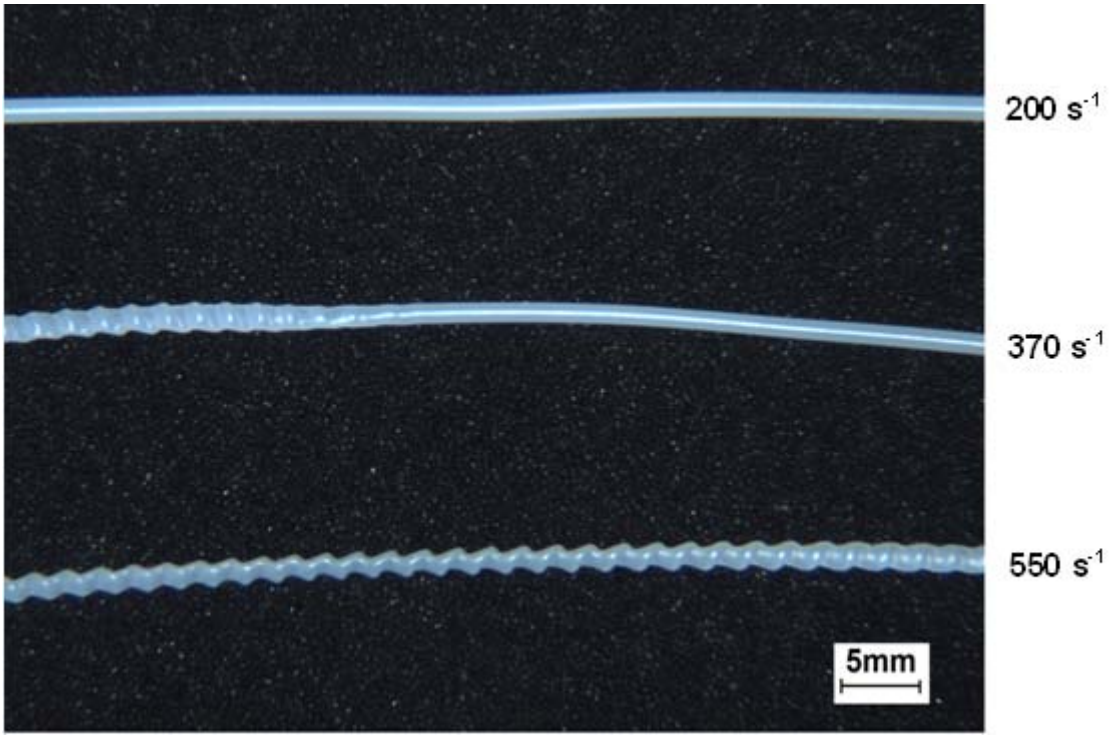

Figure 6.9(b): Typical extrudate profiles at 170°C, showing smooth extrudate in the stick flow regime at 200s^{-1}, periodic bulk distortion at 370s^{-1} in the stick-slip flow regime and helical distortion at 550s^{-1}.

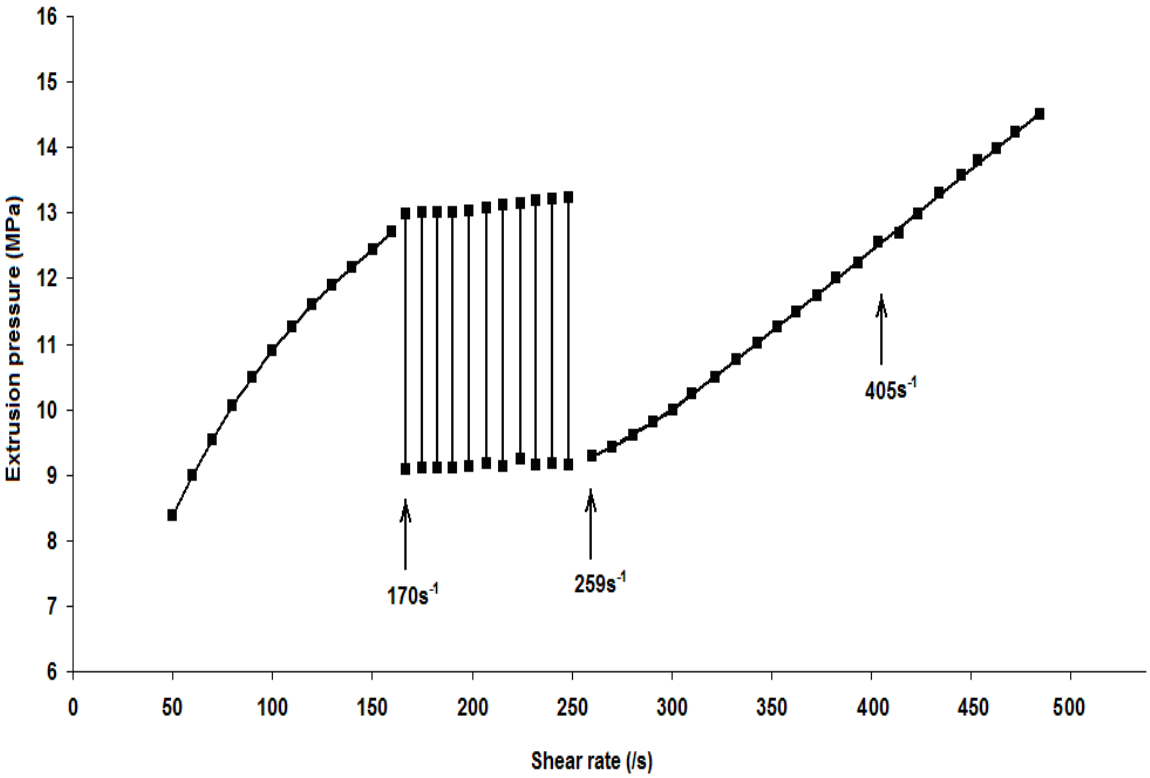

Figure 6.10(a): Flow curve for PE-B recorded at 158°C. The vertical lines represent the pressure oscillations. The arrows indicate the $\dot{\gamma}_c^{\,p}$ at 170s^{-1}, $\dot{\gamma}_c^{\,w}$ at 259s^{-1} and $\dot{\gamma}_c^{\,h}$ at 405s^{-1}.

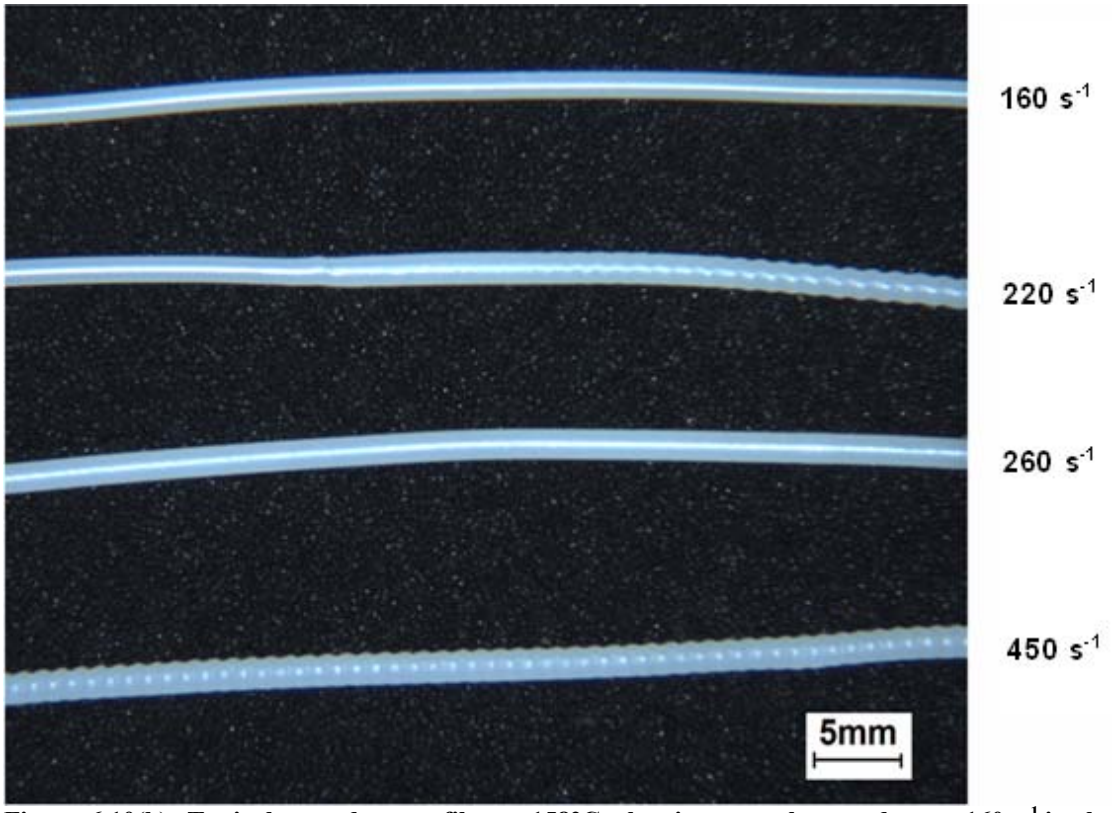

Figure 6.10(b): Typical extrudate profiles at 158°C, showing smooth extrudate at 160 s^{-1} in the stick flow regime, periodic bulk distortion at 220s^{-1} in the stick-slip flow regime, and smooth extrudate again at 260 s^{-1} in the window effect slip flow regime and helical distortion at 450 s^{-1}.

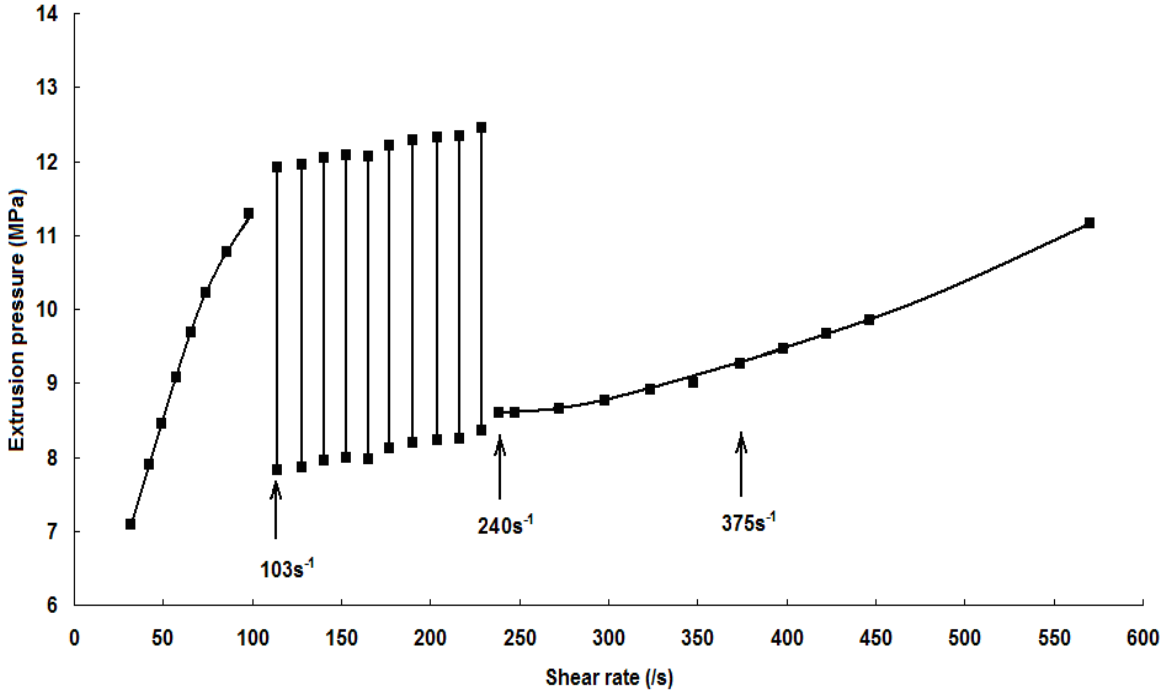

Figure 6.11(a): Flow curve for PE-B recorded at 152°C. The vertical lines represent the pressure oscillations. The arrows indicate the $\dot{\gamma}_c^{\,p}$ at 103s^{-1}, $\dot{\gamma}_c^{\,w}$ at 240 s^{-1} and $\dot{\gamma}_c^{\,h}$ at 375 s^{-1}.

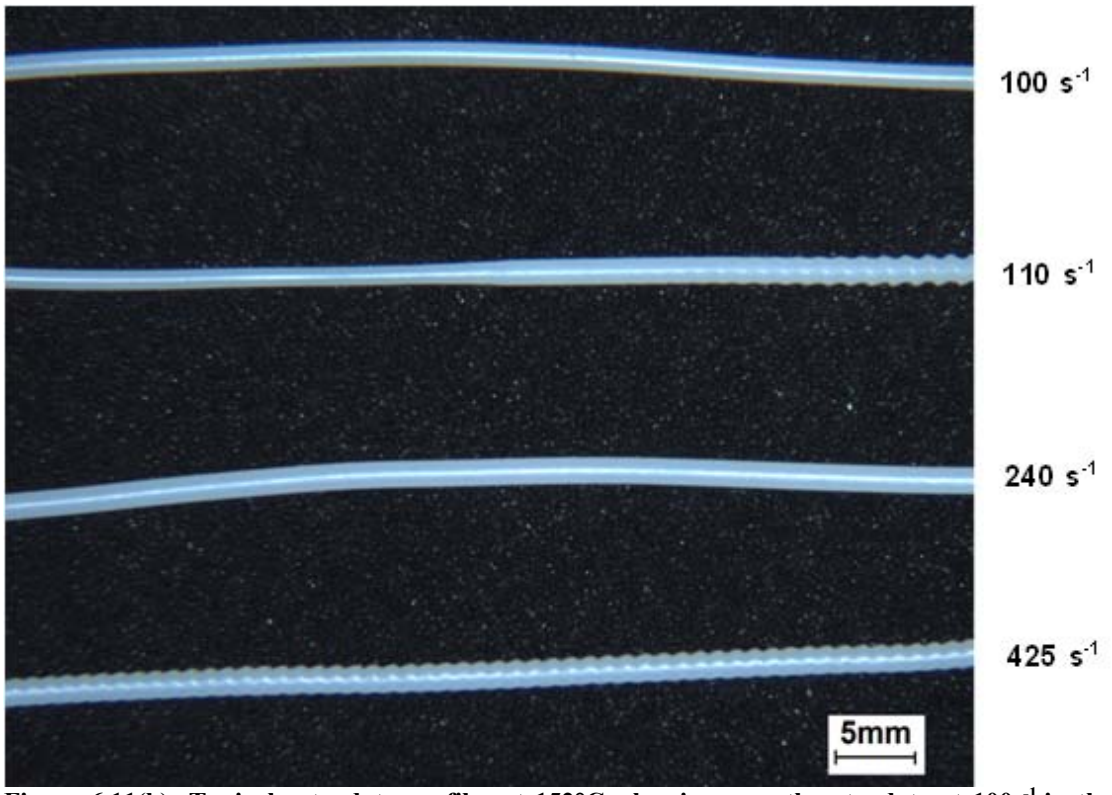

Figure 6.11(b): Typical extrudate profiles at 152°C, showing smooth extrudate at 100s^{-1} in the stick flow regime, periodic bulk distortion at 110s^{-1} in the stick-slip flow regime, smooth extrudate again at 240s^{-1} in the window effect slip flow regime and helical distortion at 425s^{-1}.

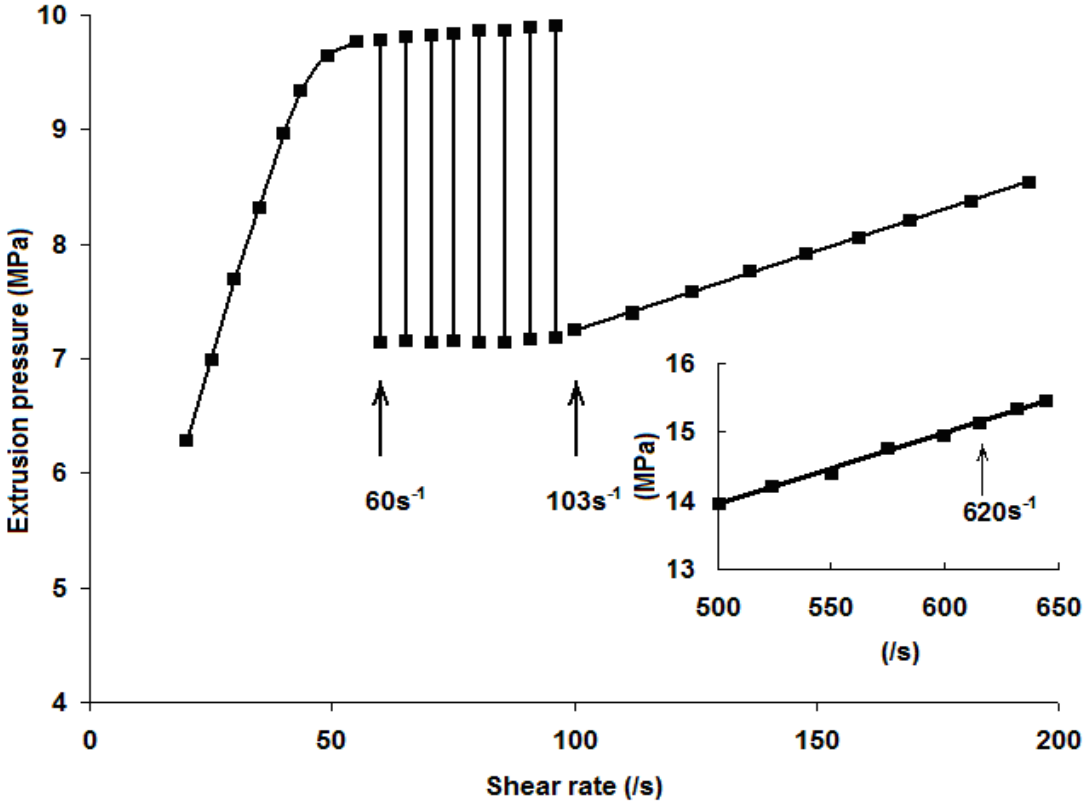

Figure 6.12(a): Flow curve for PE-B recorded at 146°C. The vertical lines represent the pressure oscillations. The arrows indicate the $\dot{\gamma}_c^{\,p}$ at 60s^{-1}, $\dot{\gamma}_c^{\,w}$ at 103s^{-1}. The insert shows there is no helical distortion occurring at 620s^{-1}.

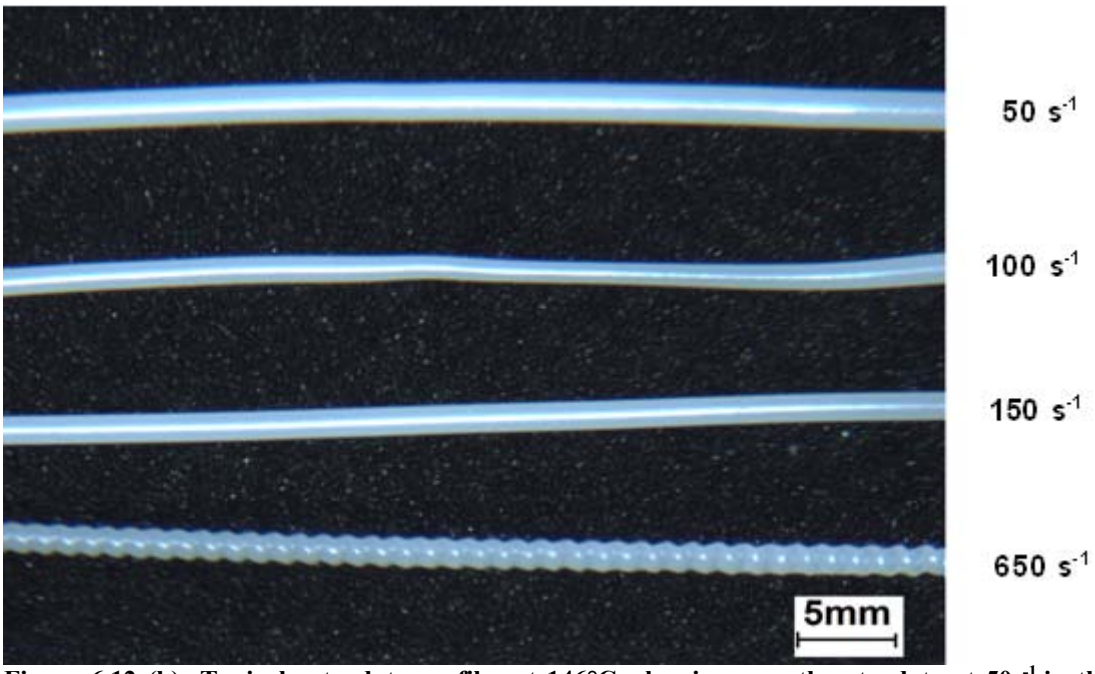

Figure 6.12 (b): Typical extrudate profiles at 146°C, showing smooth extrudate at 50s^{-1} in the stick flow regime, periodic bulk distortion at 100s^{-1} in the stick-slip flow, smooth extrudate again at 150 s^{-1} in the window effect slip flow regime and helical distortion at 650s^{-1}.

In comparison with the hydrodynamic boundary conditions at varying temperatures, it is found that the flow criticalities of $\dot{\gamma}_c{}^p$ and $\dot{\gamma}_c{}^w$ shift to higher values with increasing temperature. In addition, the pressure minima and maxima of pressure oscillation increase with temperature. With respect to the helical distortion, at high temperatures (≥158°C), it is found that the distortion occurs when the resultant wall shear stress attains a critical value, σ_c^h , at and around 0.194~0.195MPa, which remains independent of temperature. However, there is low-temperature anomalies of σ_c^h . As shown in Figure 6.11(a), the σ_c^h reduces to 0.145MPa at 152°C which temperature is situated in the temperature interval of the middle temperature extrusion window observed in DTS and ISR experiments. Whereas, the σ_c^h increases to 0.235MPa at 146°C corresponding to the low temperature window location. These findings suggest that the existence of extrusion window at 152°C or flow induced solidification at 146°C is likely to have impacts on the σ_c^h .

It is worth highlighting the σ_c^h dependence of the extrudate profile in periodic distortion. In pressure oscillation, the upper limit wall shear stress, here referred to

as σ_w^u; corresponds to the pressure maximum in the spurt flow; on the other hand, lower limit wall shear stress, σ_w^l, is associated with the minimum pressure.

a) As shown in Figure 6.13, at high temperature 170°C, σ_c^h is equal to σ_w^l. Therefore, only helical distortion slip flow occurs in the discrete slip flow.

b) At middle window temperature, 152°C, σ_c^h lies between σ_w^u and σ_w^l as shown in Figure 6.14. It is found that σ_c^h indicates boundary condition between the discrete helical distortion slip flow and the discrete window effect slip flow. In each pressure oscillation cycle, once the extrusion pressure reaches the upper limit, polymer melt accumulated in the discrete stick flow spurts out and shows helical distortion until σ_w reaches σ_c^h. Following that the flow behaviour is located in the discrete window effect slip flow regime when $\sigma_w < \sigma_c^h$.

c) At low temperature, 146°C, σ_c^h is greater than σ_w^u, only the discrete window effect slip flow occurs in the periodic distortion regime.

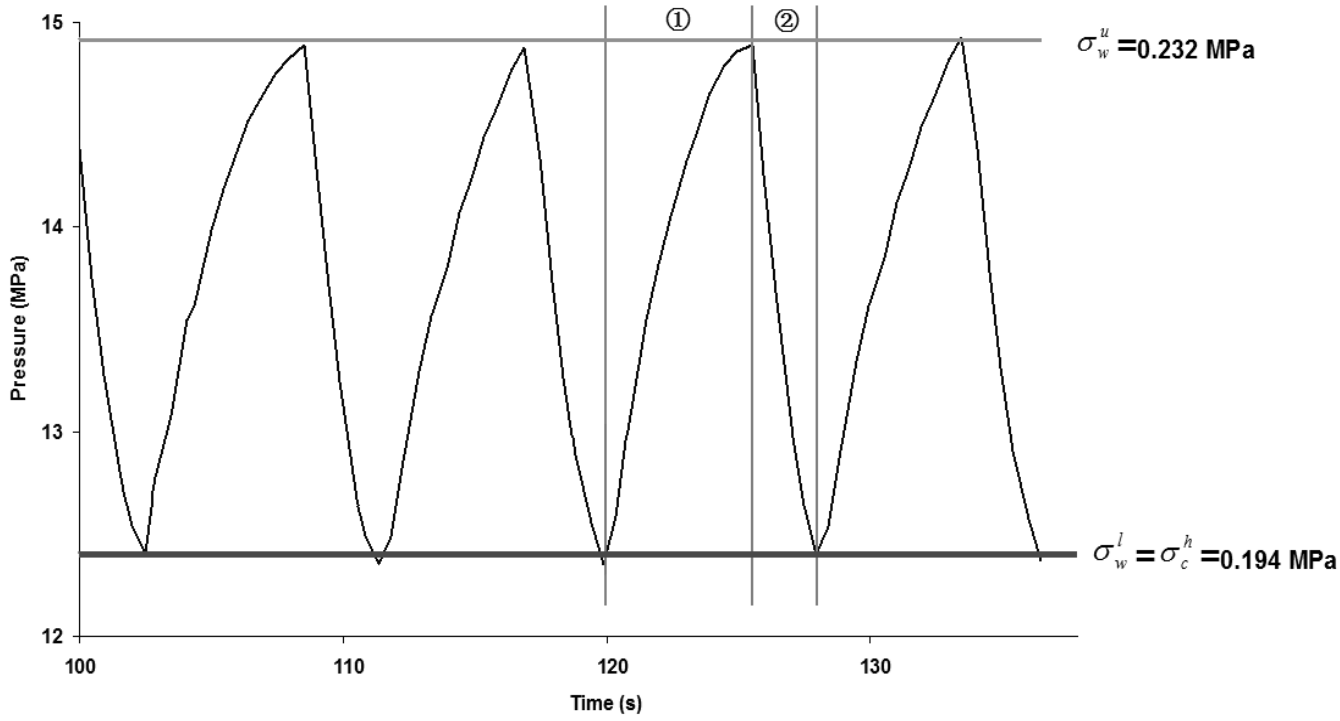

Figure 6.13: Pressure oscillation recorded in IMTS test at 170°C at an apparent shear rate of 370s^{-1}, showing each cycle of pressure oscillation consists of two steps: ① is the discrete stick flow; ② is the discrete helical distortion slip flow.

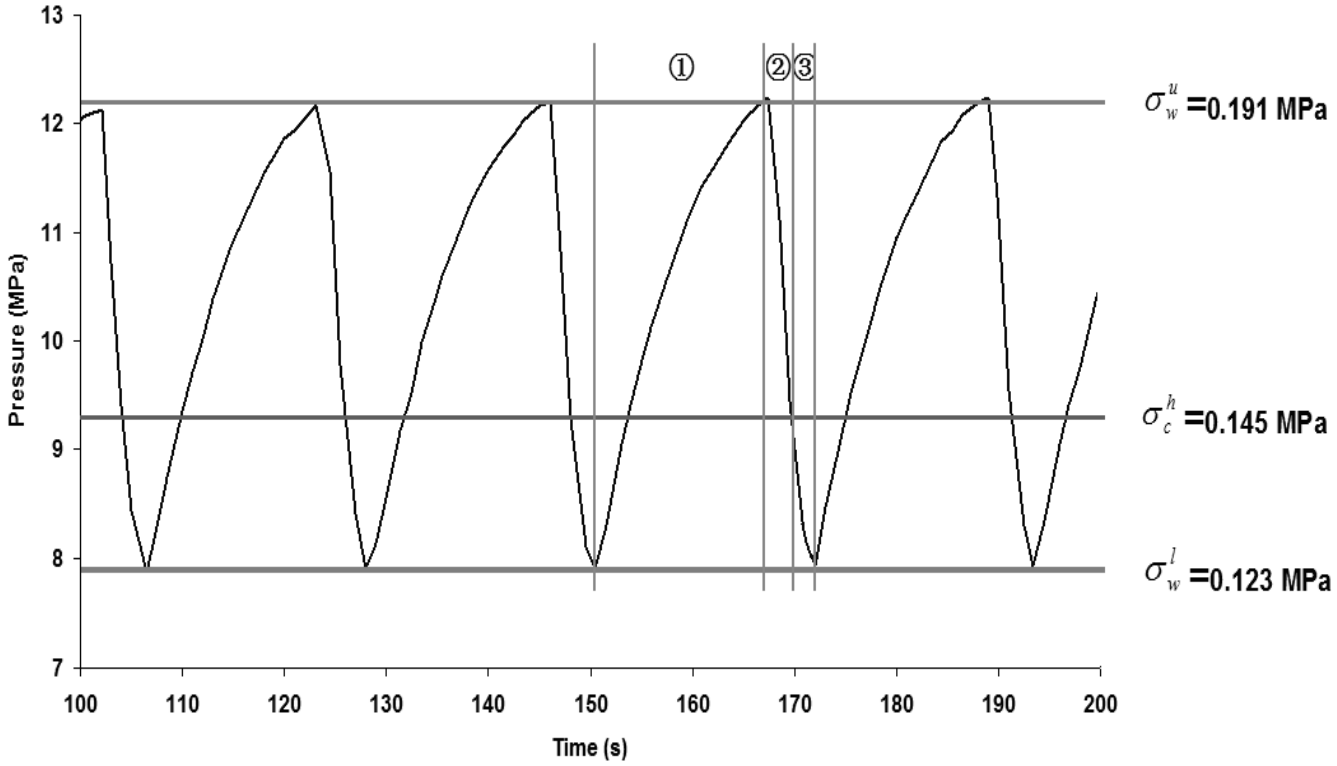

Figure 6.14: Pressure oscillation recorded in IMTS test at 152°C at an imposed apparent shear rate of 150s^{-1}, showing each cycle of pressure oscillation consists of three steps: ① is the discrete stick flow; ② is the discrete helical distortion slip flow and ③ is the discrete window effect slip flow.

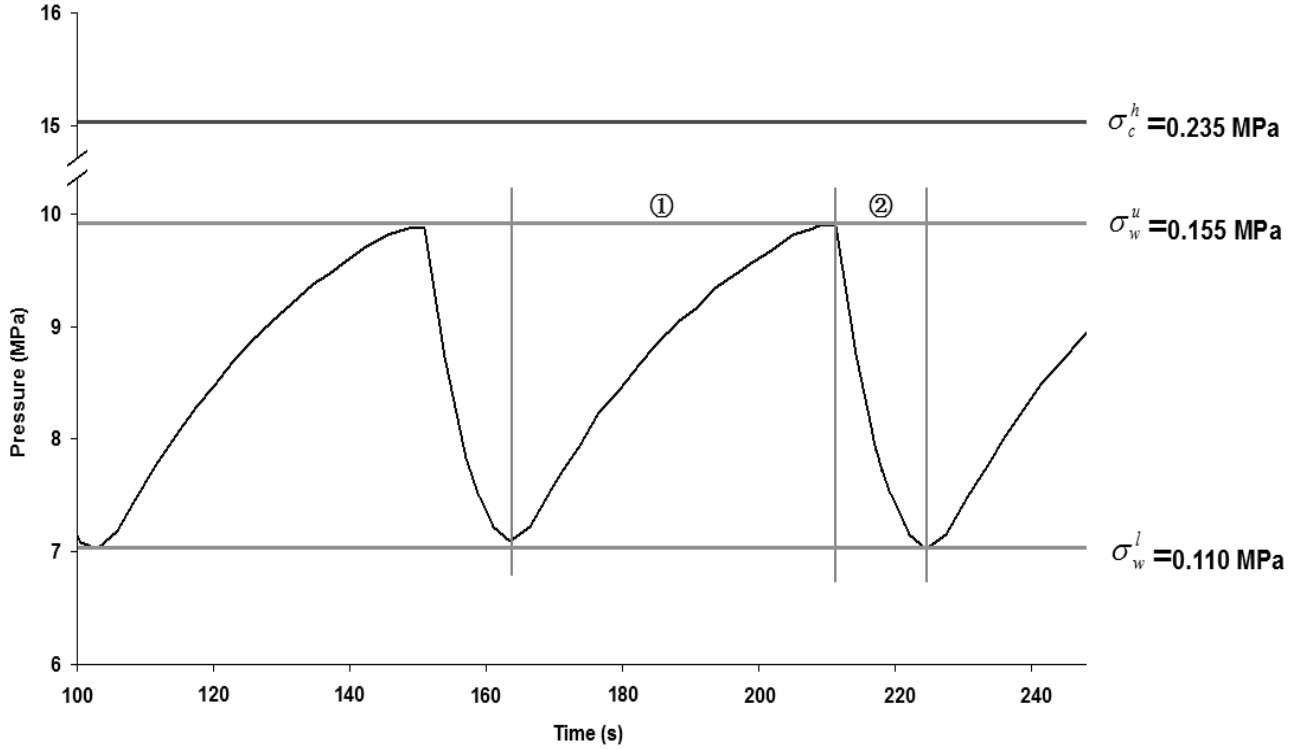

Figure 6.15: Pressure oscillation recorded in IMTS test at 146°C at an imposed apparent shear rate of 60s^{-1}, showing each cycle of pressure oscillation consists of two steps: ① is the discrete stick flow; ② is the discrete window effect slip flow.

6.2.5 The effects of die geometry on extrusion window

6.2.5.1 Variation of capillary length:

The role of capillary flow in the melt flow singularity of PE-B was investigated and compared with capillary free flow using an orifice die. It was found that the extrusion window vanished in capillary free flow as shown in Figure 6.16 and 6.17, since no pressure drop occurs when the polymer melt flows through an orifice die. From here it is apparent that the existence and appearance of the window effect is strongly dependent on capillary flow. In other words, elongational flow is not mechanism responsible for the melt flow singularity of polyethylene since no window effect is observed from the convergent flow alone. On the other hand, it is found that the appearance of the window effect is independent of capillary length. Finally it is also found that $\dot{\gamma}_c^{\,w}$ remains unaffected with varying capillary length, viz.108±5s^{-1}.

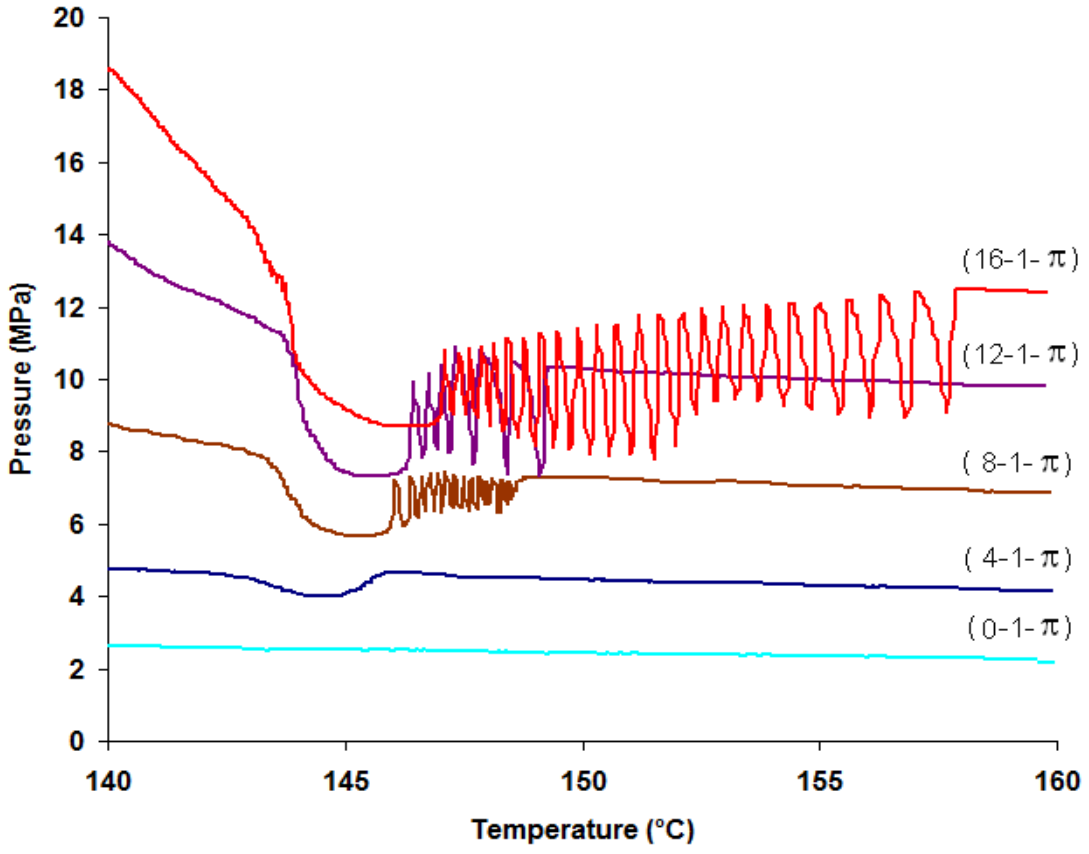

Figure 6.16: Low shear rate, 150s^{-1}, window effects of PE-B with varying the die length (16-1-π, 12-1-π, 8-1-π, 4-1-π and 0-1-π viz. orifice die).

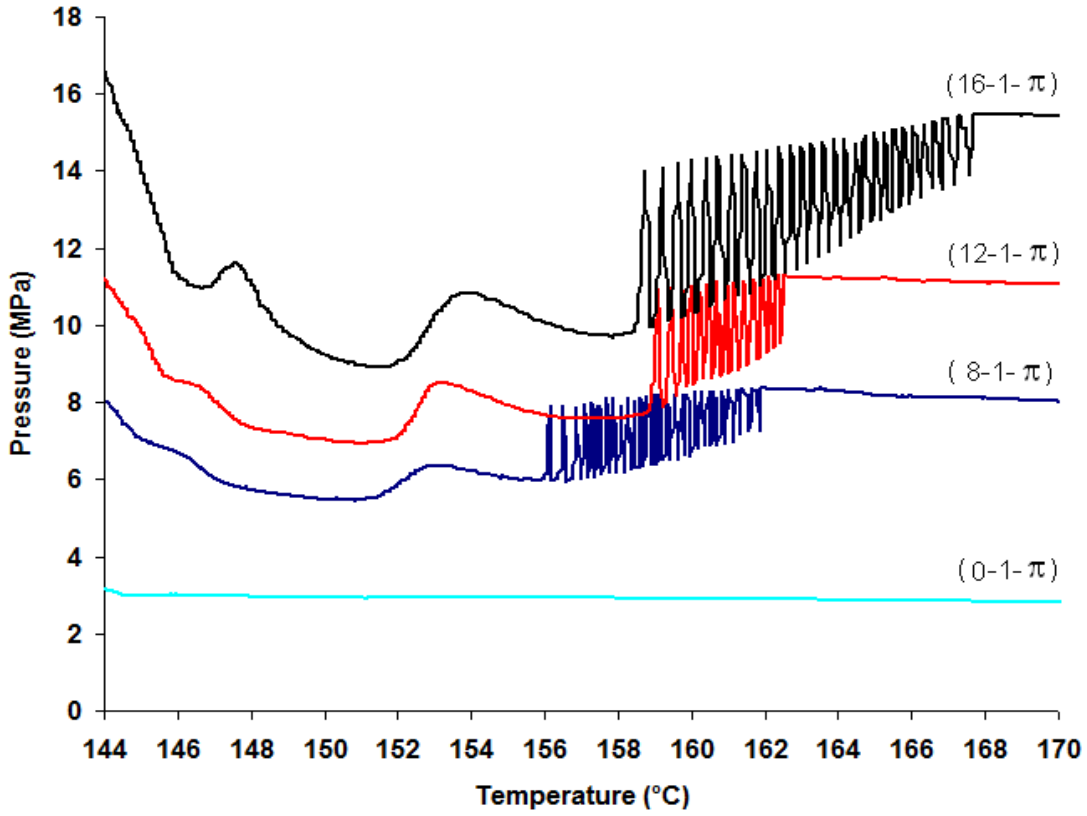

Figure 6.17: High shear rate, 300s^{-1}, window effects of PE-B with varying die length (16-1-π, 12-1-π, 8-1-π and 0-1-π viz. orifice die).

6.2.5.2 Variation of die entry angle:

Elongational flow is not the origin of melt flow singularity. However, it may have an influence on flow criticalities. Varying the die entry angle can adjust the elongational 'strength' during the convergent flow for fixed barrel and capillary diameters. The elongational 'strength' is expected to increase as the entry angle rises on account of ensuing larger convergence at die entry. The $\dot{\gamma}_c^{\,w}$, corresponding to the onset appearance of the window effect at 146°C is plotted against the die entry angle as shown in Figure 6.18(a). It is found that $\dot{\gamma}_c^{\,w}$ corresponding to the low temperature window increases as the die entry angle decreases. On the other hand, for the middle temperature extrusion window, $\dot{\gamma}_c^{\,w}$ is independent of the die entry angle, depicted in Figure 6.18(b).

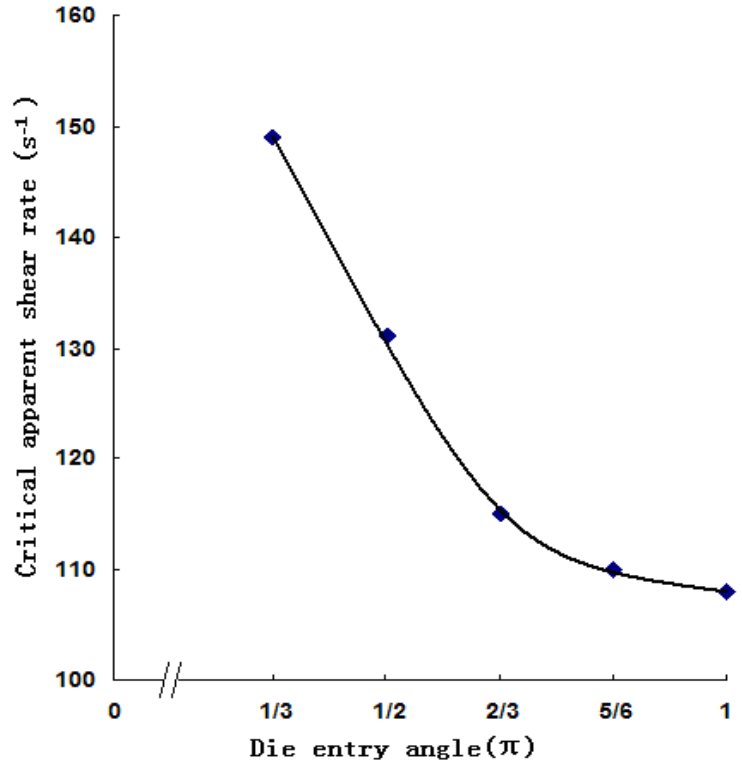

Figure 6.18(a): $\dot{\gamma}_c^{w}$ for low temperature window at 146° with varying entry angle (16-1-π, 16-1-5/6π, 16-1-2/3π, 16-1-1/2π, and 16-1-1/3π)

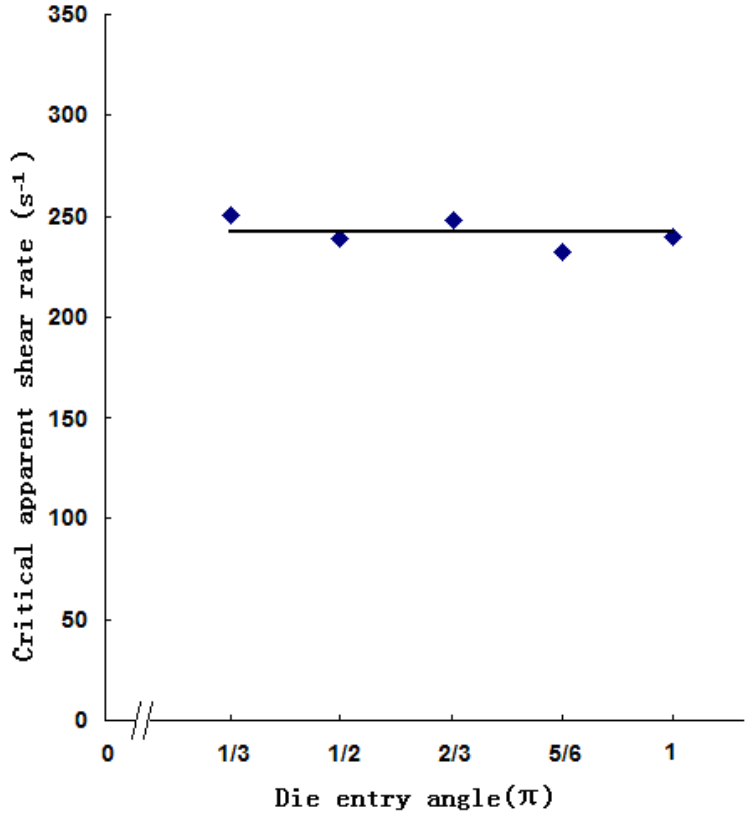

Figure 6.18(b): $\dot{\gamma}_c^{w}$ for middle temperature window at 152°C with varying entry angle with constant capillary length and bore diameter (16-1-π, 16-1-5/6π, 16-1-2/3π, 16-1-1/2π, and 16-1-1/3π)

6.2.6 Slip flow velocity

The slip velocity was determined with a series of dies having different bore diameters, but the L/R ratio of each die is kept constant at 32; hence, the end pressure correction is not required. Slip flow velocities were performed at two characteristic window temperatures, 146°C and 152°C as shown in Figure 6.19(a-b). It is found that slip flow occurs when the imposed $\dot{\gamma}_a$ is above the corresponding $\dot{\gamma}_c^{w}$. Therefore, it gives mutual support to the hydrodynamic condition of extrusion window, viz. slip flow. In addition, the slip flow velocity increases with imposed $\dot{\gamma}_a$ as shown in Table 6.1(a-b).

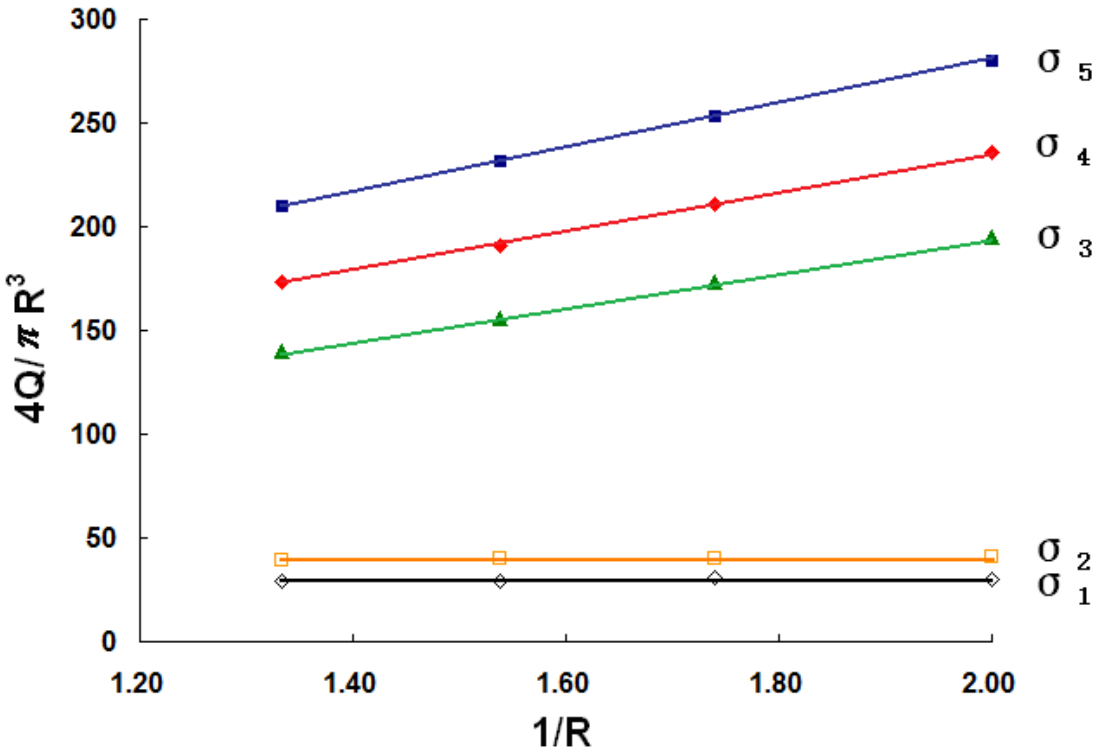

Figure 6.19(a): The volumetric output rate at different wall shear stress plotted as a function of the inverse of die radius at 146°C. Slip velocity is determined from the gradient of each line.

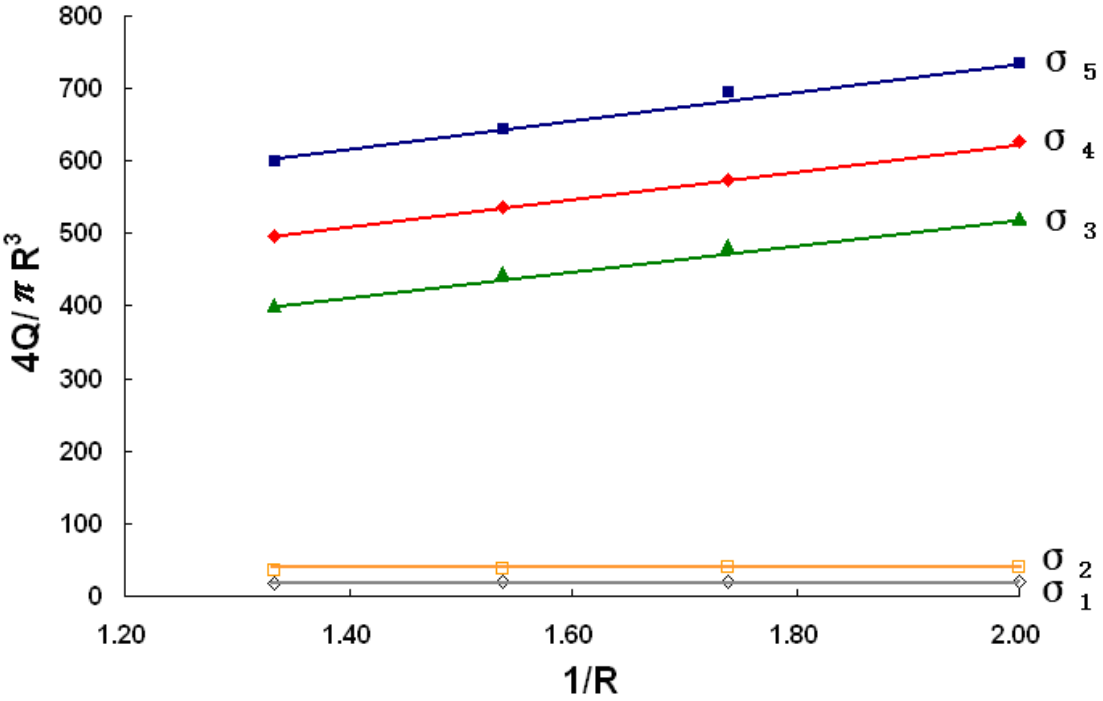

Figure 6.19(b): The volumetric output rate at different wall shear stress plotted as a function of the inverse of die radius at 152°C. Slip velocity is determined from the gradient of each line.

Table 6.1(a): Slip velocity as a function of wall shear stress at 146°C.

Shear stress (MPa)	Slip flow velocity (mm s^{-1})
σ_1=0.148	0
σ_2=0.167	0
σ_3=0.151	20.69
σ_4=0.157	23.76
σ_5=0.164	26.23

Table 6.1(b): Slip velocity as a function of wall shear stress at 152°C.

Shear stress (MPa)	Slip flow velocity (mm s^{-1})
σ_1=0.093	0
σ_2=0.123	0
σ_3=0.170	44.85
σ_4=0.181	48.98
σ_5=0.192	53.14

6.2.7 Study flow induced orientation via ex-situ wide angle X-ray scattering (WAXS)

The effect of temperature on flow induced orientation was studied at a shear rate of $50s^{-1}$ in which there is no appearance of the window effect. As shown in Figure 6.20,

the orientation effect during capillary flow increases as the extrusion temperature decreases. At 150°C there is no 'arc' observed in X-ray diffraction patterns. It indicates that there is no orientation remaining on the surface layer of extrudates. Whereas, with decreasing the extrusion temperature to 148°C, twin saddle shaped X-ray diffraction pattern corresponding to (110) are observed on the equator. It indicates that an oriented structure formed during capillary flow and can be retained after extrusion. This orientation structure is correlated to twisted kebabs[52]. As the extrusion temperature decreases further, to 146°C and 144°C, saddle shaped X-ray diffraction patterns on each side move towards the equator and merge into each other to form two single peaks on the equator. This X-ray diffraction pattern is associated with no twisted kebabs, viz. more highly oriented structure compared to that at 148°C. On the other hand, the calculated Hermans orientation factors of c-axis (Figure 6.21) also indicate that the orientation effect on surface layer of extrudate tends to be more pronounced with decreasing temperature.

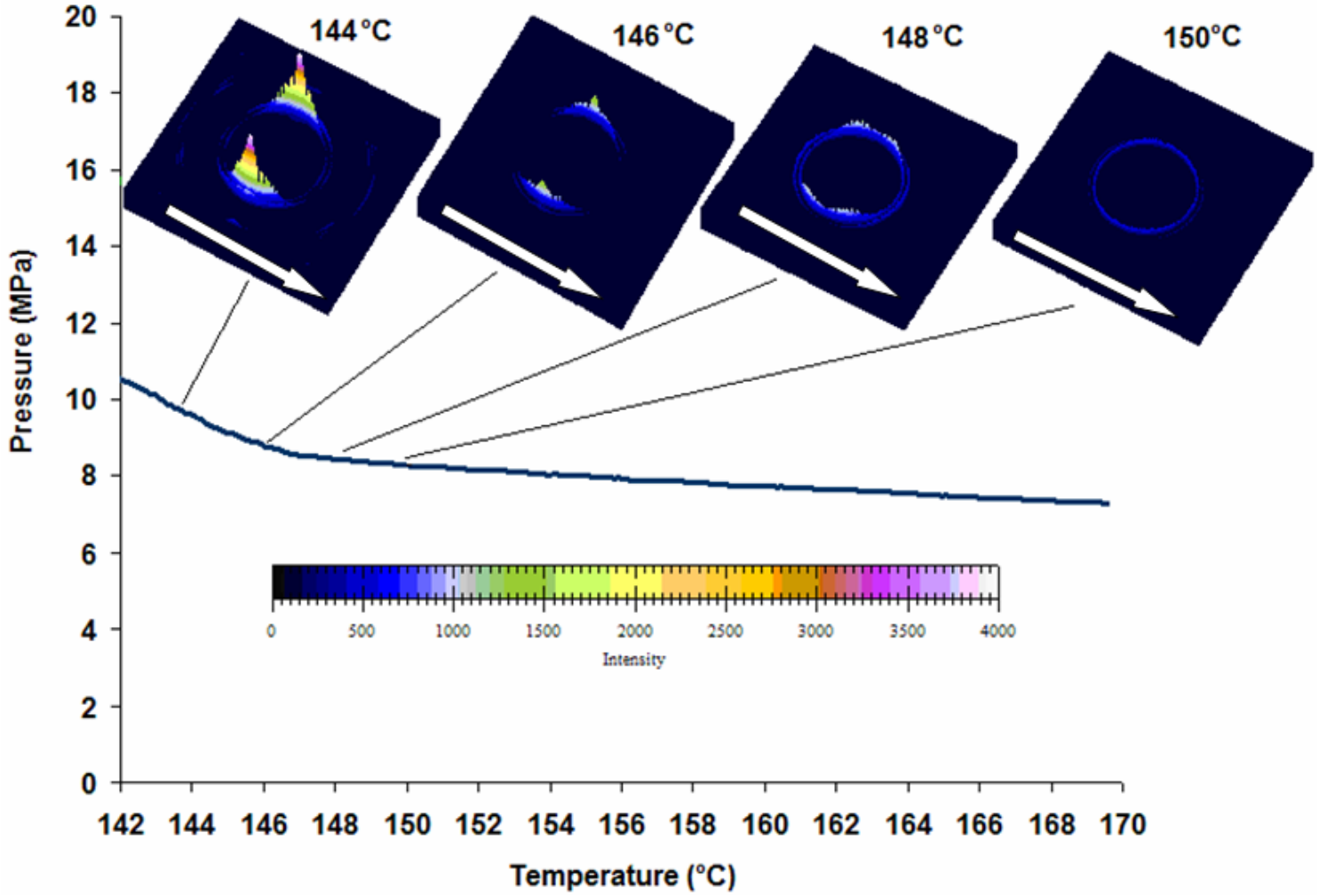

Figure 6.20: X-ray diffraction patterns of extrudate surface at different extrusion temperatures, but at the same apparent shear rate, $50s^{-1}$. White arrows show the flow direction of extrudate.

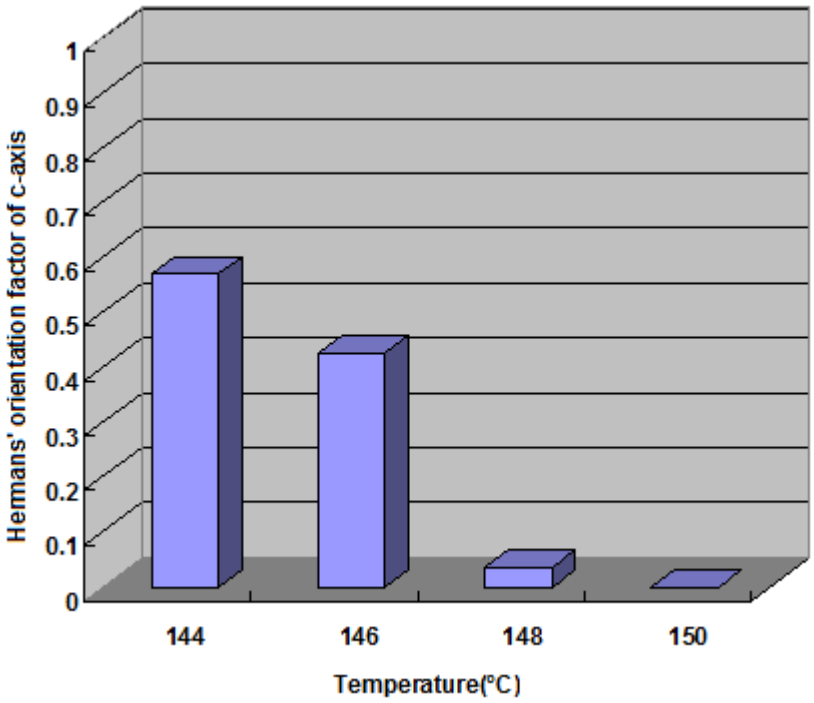

Figure 6.21: Hermans orientation factors as a function of extrusion temperature at the same apparent shear rate, $50s^{-1}$.

Here the orientation degree of PE is quantified via the Hermans orientation factor, f_c which can be calculated from an equation as (6.1) shown below:

$$f_c = \frac{(3 < \cos^2 \beta_c > -1)}{2} \tag{6.1}$$

Where β_c is the angle between the flow direction and the chain direction, viz. the *c*-axis of orthorhombic PE crystal. Generally speaking the orientation factors are calculated based on (200) and (020) reflections. Since the (020) reflection for PE does not exist, the $< \cos^2 \beta_c >$ is calculated via Wilchinsky's method[53] using the (110) and (200).

$$< \cos^2 \beta_c >= 1 - 0.565 < \cos^2 \beta_{200} > -1.435 < \cos^2 \beta_{110} > \tag{6.2}$$

The $< \cos^2 \beta_{hlk} >$ is calculated as follows:

$$\left\langle \cos^2 \beta_{hkl} \right\rangle = \frac{\int_0^{\frac{\pi}{2}} I(\beta) \cos^2 \beta \sin \beta d\beta}{\int_0^{\frac{\pi}{2}} I(\beta) \sin \beta d\beta} \tag{6.3}$$

Where $I(\beta)$ is the diffracted intensity and β is azimuthal angle. $< \cos^2 \beta_{110} >$ and $< \cos^2 \beta_{200} >$ are calculated by Eq 6.3 according to the diffraction intensity at

different azimuthal angles of inner diffraction ring and outer diffraction ring respectively (Appendix D).

According to the slip flow theory corresponding to a high surface energy die, e.g. metal die without coating, slip flow arises from disentanglement of adsorbed chains from free chains. Therefore, the adsorbed chains are likely to keep attaching on the inner capillary wall; on the other hand, the free chains are extruded out of the die after disentanglement from tethered chains, resulting in a less oriented surface layer of extrudate. In order to give support to this theory in practice, an ex-situ WAXS was performed to study the flow induced orientation on the extrudate surface after extrusion. It is apparent that in-situ WAXS cannot be competent to this aim since it is impossible to identify the disengagement interface between adsorbed chains and free chains. Moreover, this interface might not exist for an incompletely developed slip flow, especially for a broad molecular weight distributed polymer or bimodal polymer. [All samples used in ex-situ WAXS experiments are from ISR tests].

To explore the window effect on flow induced orientation, X-ray diffraction patterns of extrudate surface layer are compared at different apparent shear rates, but extruded at an isothermal condition, i.e. window temperature, 146°C, corresponding to the pressure minimum of extrusion window occurring at $150s^{-1}$. It is depicted in Figures 6.22 that there is a highly orientated structure, corresponding to no twisted kebab, observed at low apparent shear rate, $50s^{-1}$. However, an unexpected less orientation is observed at high shear rate of $150s^{-1}$， and the following X-ray diffraction patterns corresponding to higher apparent shear rates also possess less orientation compared with stick flow, at $50s^{-1}$. One of possible reasons for the high shear rate anomaly is due to slip flow. Combining with the results from ISR at 146°C as depicted in Figure 6.7(c), it is found that slip flow is the hydrodynamic origin of window effect, which coincides with the existence of window effect slip flow. In addition, with further increasing the apparent shear rate in the window effect slip flow region, the orientation factors increase slightly; however they are still much less than that obtained in stick flow at a low shear rate of $50s^{-1}$. Moreover, chain relaxation should be taken into account since the orientations are not determined in in-situ experiments

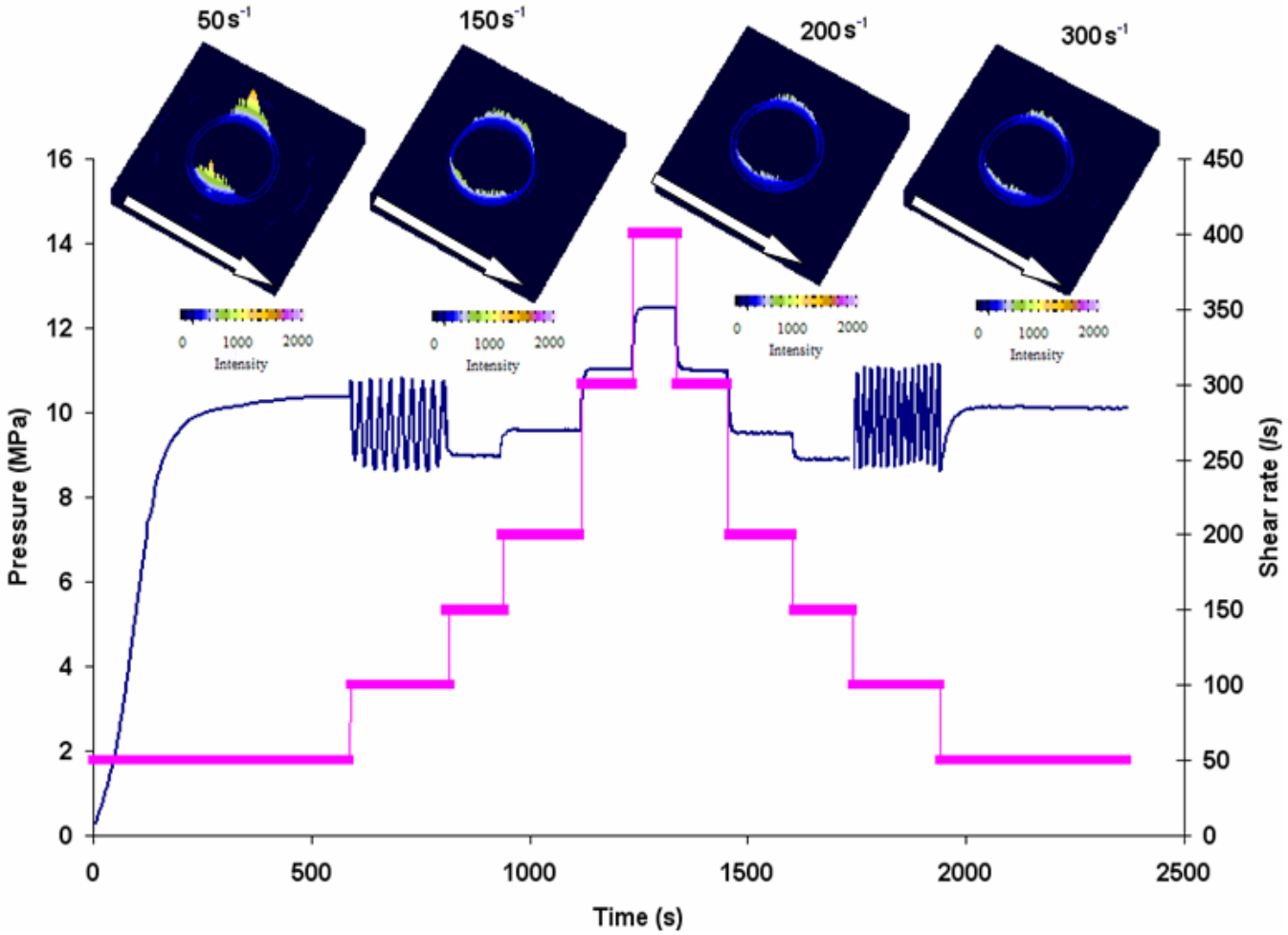

Figure 6.22: X-ray diffraction patterns as a function of apparent shear rate at the same extrusion temperature, 146°C. White arrows show the flow direction of extrudate

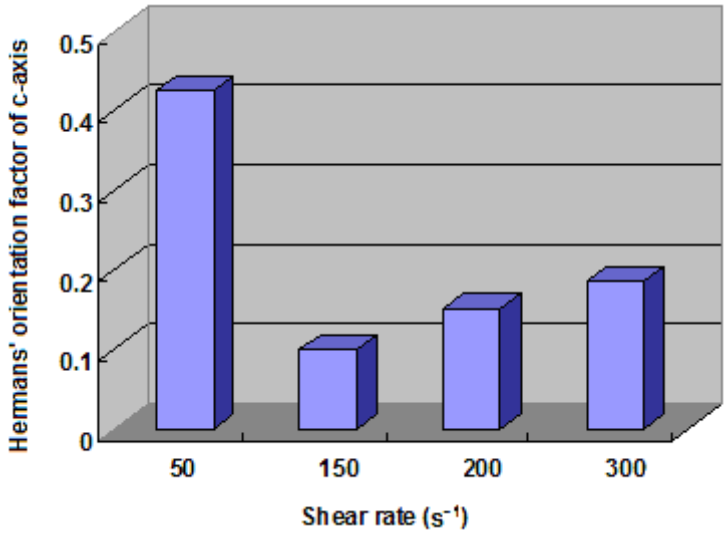

Figure 6.23: Hermans orientation factors as a function of apparent shear rate at the same extrusion temperature, 146°C.

6.3 Discussion

6.3.1 Stick-slip flow

Numerous studies have been devoted to investigate the origin of spurt flow, here referred to as stick-slip flow [26,54]. The general effect of stick-slip flow is pressure oscillation as a function of time, observed in the course of 'rate-controlled' capillary flow. According to Kolnaar's studies[31(c)], the extrudate profiles observed in pressure oscillation consist of three repeating units: (a)surface distortion, also referred to as sharkskin effect, occurring in the discrete stick flow, (b)helical distorted extrudate emerging in the high-shear-rate discrete slip flow after the pressure reaches the maximum value and (c)smooth extrudate obtained in low-shear-rate discrete slip flow.

However, in the capillary flow of PE-B sharkskin does not occur under any flow conditions prior to the appearance of pressure oscillation. This coincides with previous studies by Howells and Benbow [26(c)]. It was found that a broad molecular weight distribution lowers the susceptibility to sharkskin. The disappeared sharkskin effect in stick flow of PE-B is a symptom of distinct extrudate profiles occurring in stick-slip flow of bimodal molecular weight distributed linear polyethylene. It was found that in stick-slip flow of PE-B a smooth extrudate with low die swell ratio yielded in the discrete stick flow.

The hydrodynamic origin of the stick-slip flow in rate controlled rheometer can be elucidated by stick-slip flow theory[39]. Prior to stick-slip flow, a steady state stick flow can be fully developed at low shear rate where no slip flow occurs, and a smooth and glossy extrudate is yielded. With increasing the imposed piston velocity, the apparent shear rate increases. Once the imposed $\dot{\gamma}_a$ reaches the $\dot{\gamma}_c{}^p$, spurt flow occurs. At the beginning of the stick-slip flow, the extrusion pressure builds up gradually in the discrete stick flow due to the difference between the applied flow rate $Q_a = V\pi R_b{}^2$ *(V is piston velocity,* R_b *is radius of barrel)* and the real volumetric output rate Q. When the extrusion pressure/ the wall shear stress reaches the critical value ($\sigma_w = \sigma_w^u$), slip flow occurs and extrusion pressure drops suddenly.

Extrudate profiles in either discrete slip flow or stationary slip flow are dependent on σ_w. When $\sigma_w \geq \sigma_c^h$, helical distortion slip flow occurs. On the other hand, when $\sigma_c^h > \sigma_w \geq \sigma_c^w$, window effect slip flow emerges.

The stick-slip flow observed in the stress controlled capillary flow is signified by a jump in the flow rate at a critical shear stress σ_c. Therefore σ_c indicates the hydrodynamic boundary condition for stick-slip flow. However, neither σ_w nor $\dot{\gamma}_a$ are under control in the rate controlled capillary flow. σ_w periodically increases and decreases with the pressure oscillation. Meanwhile, the real apparent shear rate $\dot{\gamma}_a$ changes as a function of time. It is worth highlighting that the real apparent shear rate, $\dot{\gamma}_a$, is not equal to the applied apparent shear rate, $\langle \dot{\gamma}_a \rangle$, during stick–slip flow since Q is not identical with Q_a. The $\dot{\gamma}_a$ falls into two catalogues: one is associated with the discrete stick flow, named as stick flow apparent wall shear rate $\dot{\gamma}_{a,stick}$, the other corresponds to discrete slip flow, termed as slip flow apparent wall shear rate $\dot{\gamma}_{a,slip}$. During discrete stick flow it is apparent that $\dot{\gamma}_{a,stick}$ starting from $4Q_a / \pi R^3$ and then gradually decreases until σ_w reaches σ_w^u. On the other hand, $\dot{\gamma}_{a,slip}$ starts from a maximum value and reduces to $4Q_a / \pi R^3$.

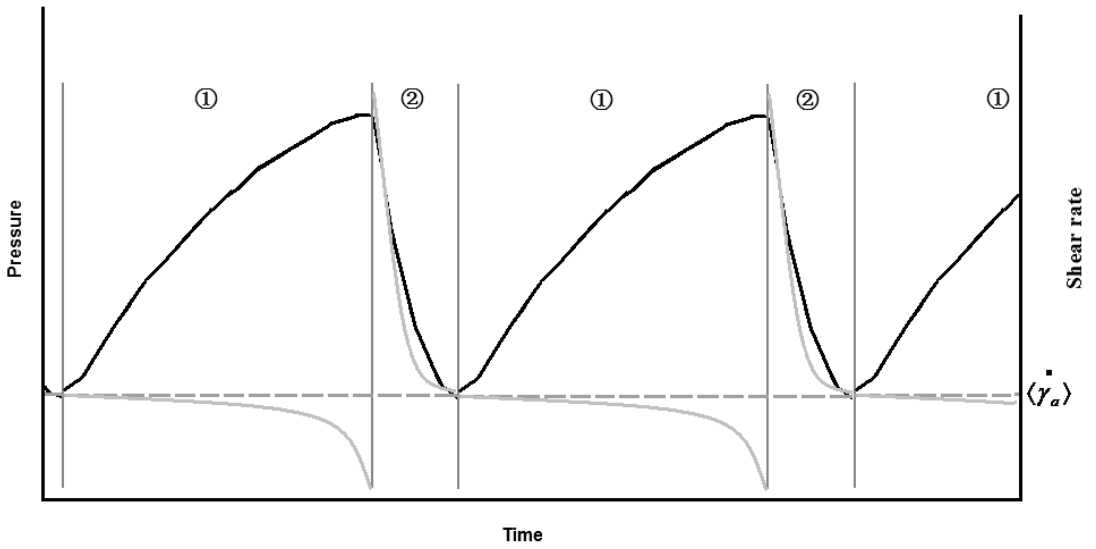

Figure 6.21: A schematic plot of real apparent shear rate as a function of time during stick-slip flow in the rate-controlled capillary rheometer. The black curve denotes the extrusion pressure in melt instability; the dash line shows the applied apparent shear rate, and the gray curves represent the real apparent shear rate, viz. $\dot{\gamma}_{a,slip}$ in region one and $\dot{\gamma}_{a,stick}$ in region two.

6.3.2 Hydrodynamic boundary conditions of window effect

Conventional polymer processing is performed in the steady state stick flow regime. The hydrodynamic boundary condition is governed by a critical shear rate, corresponding to the onset of periodic bulk distortion, or referred to as bamboo effect. Here this critical shear rate is signified by $\dot{\gamma}_c^{\,p}$. Whereas, it was found that the steady state stick flow is not the only polymer processing condition since the smooth extrudate with uniform throughput rate can also be determined in the window effect. The corresponding hydrodynamic condition is window effect slip flow. Compared with stick flow, the window effect slip flow occurs at relatively higher shear rate and low temperature, and the corresponding hydrodynamic boundary conditions are dominated by two critical shear rates, $\dot{\gamma}_c^{\,w}$ and $\dot{\gamma}_c^{\,h}$. The $\dot{\gamma}_c^{\,w}$ is the lower limit shear rate of the window effect slip flow and the $\dot{\gamma}_c^{\,h}$ is the upper limit shear rate.

6.3.3 Molecular origin of the double extrusion windows

Bimodal PE can be considered as a PE-PE blend via chemical route. It consists of two molecular weight components, one is the low molecular weight component M_L, and the other is the high molecular weight component M_H. Prior to exploring the molecular origin of the dual window effect, the nature of single extrusion window of

PE-B at low temperature, occurring at the critical apparent shear rate of PE-B, $108s^{-1}$, need to be revealed. According to the molecular weight dependence of the critical apparent shear rate, M_H is likely to give rise to the onset single extrusion window. However, such a low window temperature does not obey the theoretical prediction regarding the molecular weight dependence of window temperature, Figure 6.5. In order to give a theoretical explanation for this contradiction, the chain dynamics of entangled fluids need to be recalled. The macroscopic shear stress applied in the complex fluids is transferred to each molecular via entanglement constraints. In the molecular scale, according to the reptation model, the entanglement constraints on each polymer chain arise from its neighbouring chains acting as a confining tube along its contour. Regarding the window effect the adsorbed chains need to be stretched by neighbouring chains via entanglement constraints under flow condition. For a broad/bimodal molar mass distributed linear polyethylene, the polymer chains have a wide range of lengths. Some of the entanglement constraints between the short chains and long tethered chains will disappear and unrecoverable under flow condition since short chains, initially entangled with an adsorbed long chain, are likely to coil back on another previously entangled long chain at high-temperature flow condition. Therefore, the short free chain is likely to release the entanglement constraint with the long adsorbed chain resulting in easing constraint release. Consequently, the onset window effect of M_H shifts to low temperature and occurs at high critical shear rate in order to maintain the stretched conformation of long chains via limited entanglement constraints.

With increase in the shear rate the single extrusion window arising from the slip flow of M_H shifts to higher temperature and also broadens, see figure 6.4. Above the critical shear rate the broadened extrusion window of M_H may be attributed to M_L since random coiled short chains can hinder the long chain adsorption on the capillary wall, resulting to a low window termination temperature.

When the applied shear rate rises further to $300s^{-1}$, a duel window effect occurs. The low temperature window is likely to arise from window effect slip flow of M_L. In comparison of pressure minima in the dual extrusion window, the high temperature window has the low pressure minimum. It is coincided with the molecular weight

dependence of critical shear stress, i.e. the higher the molecular weight, the low the critical shear stress. Even though the critical shear stress for the onset of window effect is also dependent on temperature, considering the low temperature anomaly, the low critical shear stress for the high temperature window should be still attributed to M_H. In summary, M_H and M_L give rise to high temperature window and low temperature window respectively.

The molecular origin of high-surface-energy-die slip flow is attributed to the disentanglement of tethered chains on capillary wall from free chains in bulk. However, there is no evidence to support this. In this chapter, ex-situ WAXS results give some support to this theory. At the window temperature, 146°C, orientation factors of C-axis are compared at different apparent shear rate as depicted in Figure 6.23. It was found that the orientation factor of C-axis at $50s^{-1}$ is higher than those at $150s^{-1}$, $200s^{-1}$ and $300s^{-1}$. It can only be elucidated by window effect slip flow, in which the adsorbed chains are stretched during capillary flow and are retained in a stretched chain conformation. Such stretched adsorbed chains form a self lubrication layer on the inner capillary wall and reduce the surface energy of the capillary wall to ease the slip flow. Consequently only free chains with less orientation are extruded through the capillary die.

6.3.4 The influence of die geometry on flow criticalities

6.3.4.1 Change length with diameter and entry angle constant.

Capillary flow gives rise to the melt flow singularity of PE since there was no window effect occurring during melt flow through an orifice alone, viz. capillary free flow. It implies that the appearance of window effect does not rely on convergent flow. Regarding the effect of capillary length on flow criticalities of extrusion, it is found that the window effect is independent of the capillary length.

6.3.4.2 Change entry angle with diameter and length constant.

The influence of convergent flow on the window effect was studied using different entry-angle dies with a fixed capillary diameter and capillary length. Thus the elongational strength can be altered by varying the die entry angle. Though the convergent flow does not give rise to the melt flow singularity, it influences the flow

criticalities regarding the low temperature window. It was found that the $\dot{\gamma}_c^{\,w}$ increases as the die entry angle decreases. However, the $\dot{\gamma}_c^{\,w}$ for the middle temperature window is independent of the die entry angle. It implies that the pre-stretched chain conformation formed in convergent flow is likely to assist the development of the stretched chain conformation at low temperature. However, the pre-stretched chain conformation is unstable at high temperature due to the Brownian fluctuation. Hence, the $\dot{\gamma}_c^{\,w}$ of middle temperature window, at 152°C, is independent of the die entry angle.

6.4 Conclusions

This is the first study to reveal melt flow singularity of bimodal PE in the course of capillary flow. Bimodal PE-B showed a dual window effect in both isothermal and non-isothermal conditions when the T and $\dot{\gamma}_a$ reach critical values. Based on molecular weight dependence of flow criticalities, the low temperature window is attributed to the slip flow of M_L and the high temperature window arises from the slip flow of M_H.

The ex-situ WAXS results strengthen the slip flow theory corresponding to high surface energy die. In the window effect slip flow, less orientation was observed from X-ray diffraction pattern of extrudate surface. This result can be elucidated by slip flow mechanism that only free chains are extruded out of the capillary die after disentanglement from adsorbed chains; however, the adsorbed chains left in the inner capillary wall constitute a self-lubrication layer to ease the slip flow.

The hydrodynamic origin of the extrusion window is attributed to the window effect slip flow, which is set in between the pressure oscillation regime and helical distortion regime. It was found that the hydrodynamic boundary conditions of window effect slip flow are governed by two flow criticalities, viz. $\dot{\gamma}_c^{\,w}$ and $\dot{\gamma}_c^{\,h}$.

The extrudate profiles in the discrete slip flow and the stationary slip flow are dependent on σ_w. Helical distortion occurs when $\sigma_w \geq \sigma_c^h$; whereas if $\sigma_c^h > \sigma_w \geq \sigma_c^w$, window effect slip flow emerges.

Regarding the influence of various die geometries on flow criticalities of the extrusion window, first of all, it was found that the melt flow singularity of PE-B is attributed to capillary flow. Secondly, the window effect is independent of capillary length. Finally, it was proven that the $\dot{\gamma}_c^{\,w}$ corresponding to low temperature window increases with decreasing die entry angle. However, $\dot{\gamma}_c^{\,w}$ for the middle temperature window remains unaffected. It suggests that the pre-stretched chain conformation formed during convergent flow may ease the appearance of window effect slip flow at low temperature, but it has no apparent effect at high temperature.

Chapter 7 Broad extrusion window of linear polyethylene

7.1 Introduction

A bimodal polyethylene, PE-B, showed a dual window effect. According to the molecular weight dependence of flow criticalities and window temperature, the low temperature window arises from low molecular weight component and the high temperature window is attributed to high molecular weight component. It implies that a polyethylene (PE) with extremely broad molecular weight distribution may have a broad extrusion window. Therefore in this chapter a PE, with broad molecular weight distribution (MWD=27) is selected to study the window effect.

7.2 Results

7.2.1 The broad extrusion window of PE-C

A linear PE, PE-C, having characteristics of broad molecular weight distribution, shows a broad pressure drop situated in a low temperature regime, from 150°C to 160°C, in DTS at the shear rate of $50s^{-1}$. Within this broad temperature interval, polymer melt is extruded through the capillary die at a uniform throughput rate. Such a broad extrusion window has remarkable potential in energy-efficient processing for PE. Compared with melt flow behaviour of relatively narrow molecular weight distributed PE, there is an irregular pressure oscillation pattern observed in melt flow instability regime, from 170°C to 165°C during cooling, viz. the extrusion pressure tends to be stabilised and gives a sign of window effect slip flow. However, it finally returns to pressure oscillation. Such an irregular pressure oscillation pattern indicates occurrence of a meta-stable window effect slip flow prior to the broad extrusion window regime. Regarding the window effect during cooling, till 155°C, the extrusion pressure remains at minimum. Below 155°C the pressure increases gradually as the temperature decreases. Once the temperature reaches 150 °C, the flow induced solidification occurs accompanied by a significant upswing in pressure.

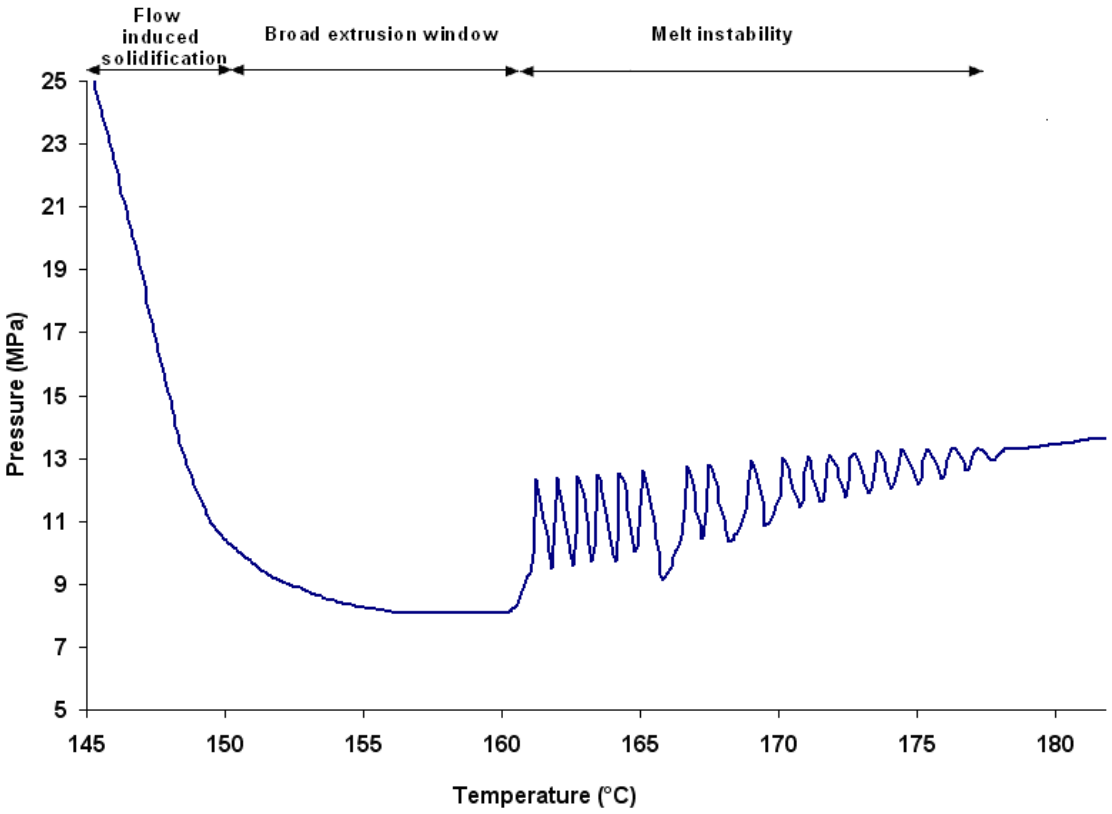

Figure 7.1: A plot of extrusion pressure against temperature showing a broad extrusion window of PE-C at the shear rate of $50s^{-1}$ (Die geometry: L-D-2α: 16-1-π)

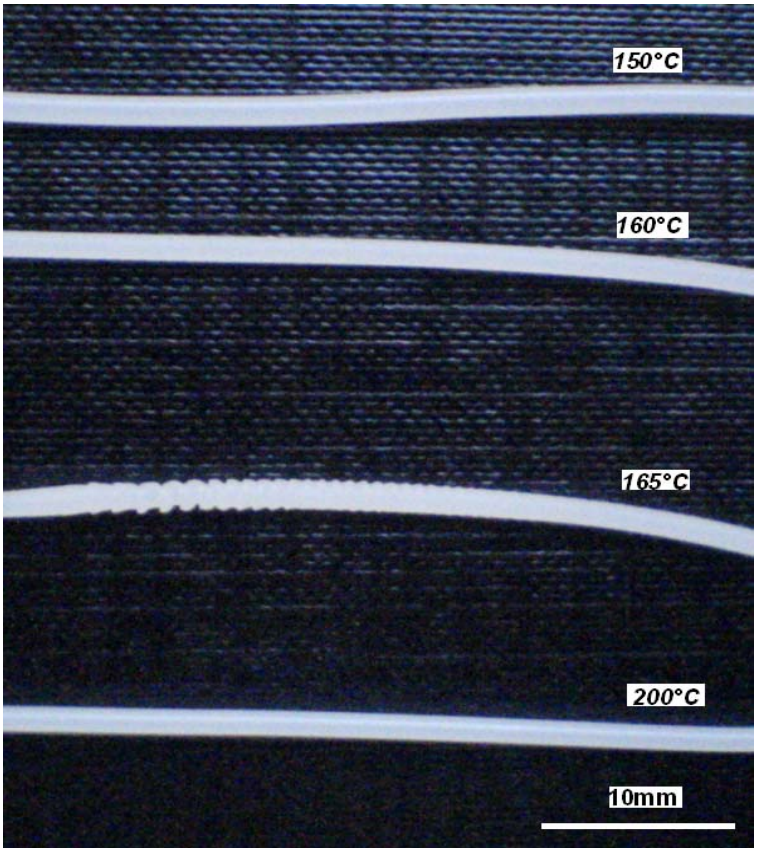

Figure 7.2: Photographs of extrudate obtained in DTS at a fixed shear rate, $50s^{-1}$

7.2.2 The effect of apparent shear rate on melt flow singularity of PE-C

Figure 7.3 gives an overview of window development with increasing the imposed $\dot{\gamma}_a$. At low $\dot{\gamma}_a$, $8s^{-1}$, the extrusion pressure increases steadily as the temperature diminishes and no melt flow singularity occurs during the DTS. The extrudate is smooth and glossy throughout the entire temperature regime (from 180°C to 142°C) at low shear rate ($<10s^{-1}$). With increasing $\dot{\gamma}_a$ to $10s^{-1}$, a pressure drop is observed in a narrow temperature interval located at 150°C. Since it is the onset occurrence of the extrusion window, the critical apparent shear rate, $\dot{\gamma}_c^{\,w}$, for the window effect of PE-C is determined as $10s^{-1}$ for the die geometry of 16-1-π. Surprisingly, it is also found that the flow behaviour at a critical shear rate of $10s^{-1}$ is also free of the melt instability and extrudate distortion. The unexpected extrudate profile at the critical shear rate may arise from the broad molecular weight distribution of the polymer studied. As the shear rate increases to $40s^{-1}$, the single pressure drop turns to multi-pressure drops. In addition, a higher window temperature leads to a lower pressure minimum. The temperature regime from 150°C to 155°C, corresponding to the appearance of multi-windows one by one with increasing the shear rate, is named the *window development regime*.

On further increasing the shear rate to $50s^{-1}$, the multi-windows merge together and eventually form a broad extrusion window. Moreover the broad extrusion window extends from 155°C to 160°C. As $\dot{\gamma}_a$ increases further, to $75s^{-1}$, such a broad window broadens further, to 164°C, as shown in Figure 7.4. The enlargement of broad extrusion window with the further increase in shear rate is referred to as the window broadening effect when the $\dot{\gamma}_a \geq 40s^{-1}$. The corresponding temperature regime, from 155°C to 164°C is named the *window broadening regime*.

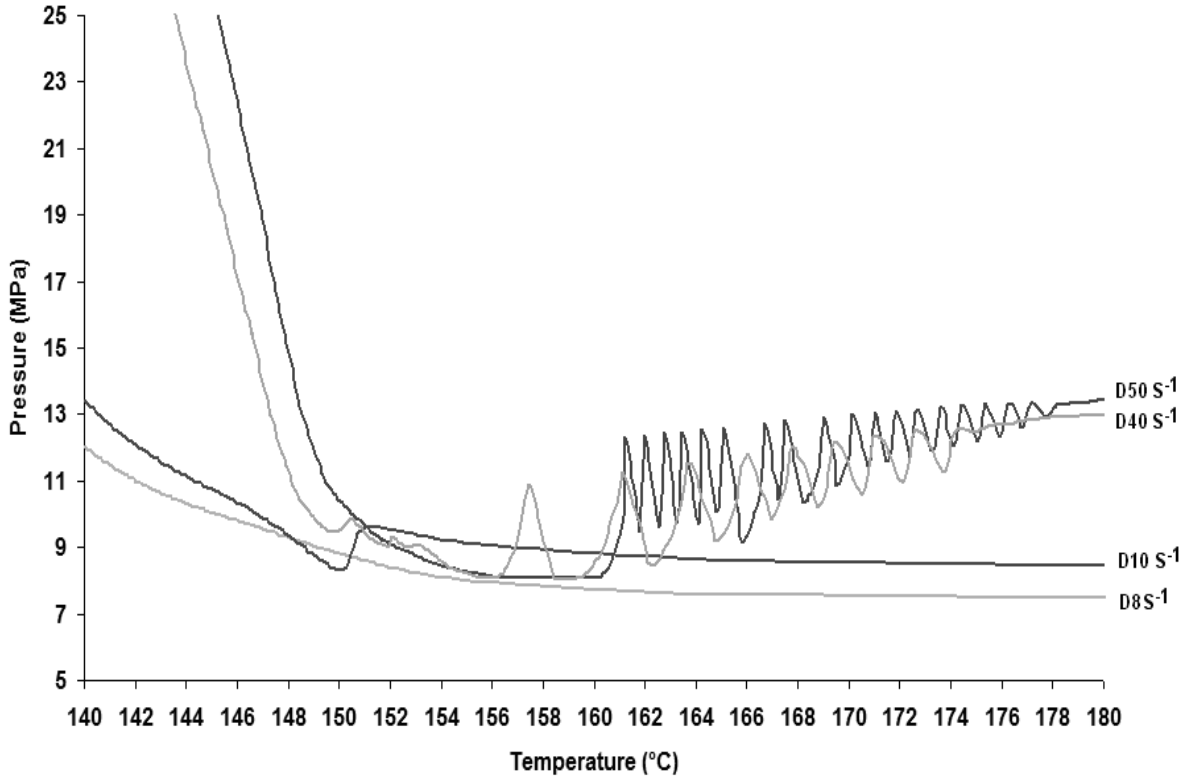

Figure 7.3: A plot of extrusion pressure versus temperature showing the melt flow behaviour at various shear rates, in which the onset appearance of the window effect indicates the critical apparent shear rate, $10s^{-1}$(Die geometry: L-D-2α: 16-1-π)

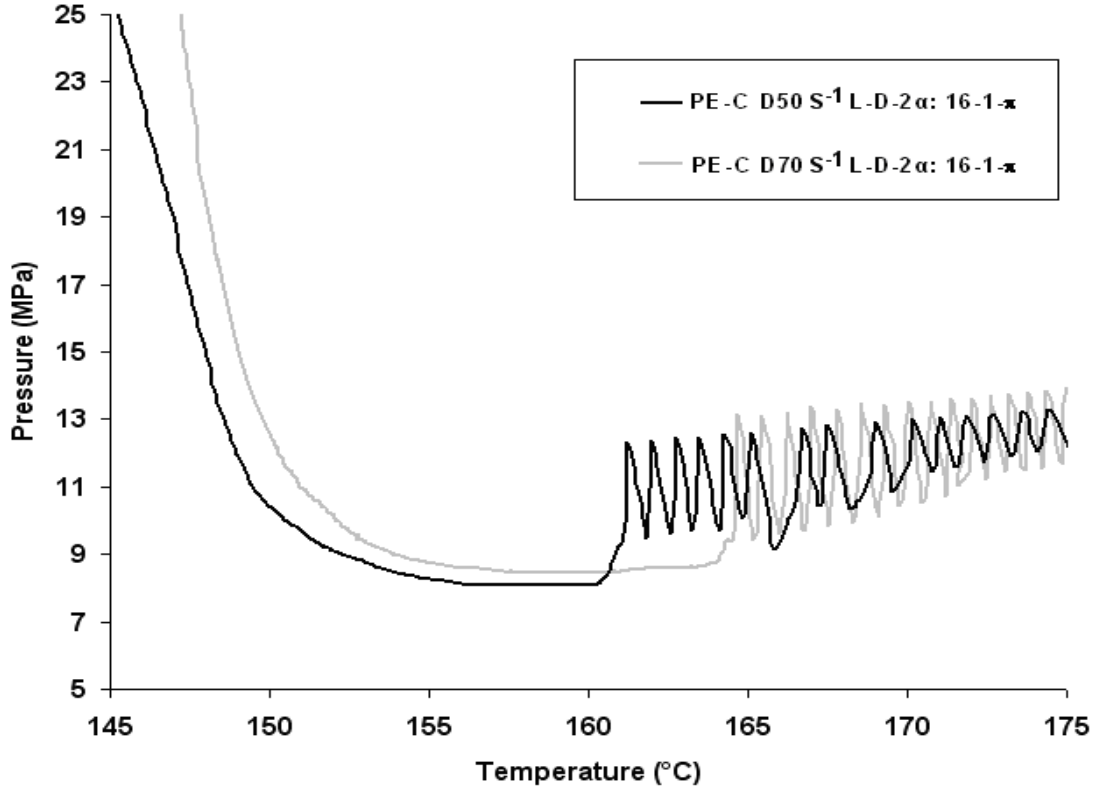

Figure 7.4: The window broadening effect on increasing $\dot{\gamma}_a$ from $50s^{-1}$ to $70s^{-1}$ (Die geometry: L-D-2α: 16-1-π)

7.2.3 Isothermal step rate (ISR) rheological characterisation

A characteristic pressure trace recorded in ISR is shown in Figure 7.5(d) at 165°C. There are three representative melt flow regimes: (a) steady state flow corresponding to the fully developed stick flow, (b) melt instability associated with pressure oscillation and (c) slip flow consisting of window effect slip flow and helical distortion slip flow. Distinctions between the window effect and helical distortion slip flows were described in Chapter 5 of this thesis.

The existence of a broad extrusion window is verified via ISR. Extrusion pressures recorded in ISR at a shear rate, $50s^{-1}$ are plotted as a function of temperature in Figure 7.7. The Figure shows a broad pressure drop situated in between 160°C and 150°C, which coincides with the window temperature interval corresponding to the broad pressure drop observed in DTS at the apparent shear rate of $50s^{-1}$. It is to be noted that the lower-limit temperature for the isothermal experiment is 150°C, at or below this temperature flow induced solidification emerges, resulting in a significant upswing in extrusion pressure. Finally capillary flow ceases. As shown in Figure 7.5(a), flow induced solidification occurs when $\dot{\gamma}_a$ is at or above $50s^{-1}$. Therefore, the critical apparent shear rate, $\dot{\gamma}_s$, corresponding to the onset of the flow induced solidification, at 150°C is $50s^{-1}$. To recall it was determined that the onset temperature of flow induced solidification, T_s, is 150°C in DTS at a shear rate of $50s^{-1}$. Therefore both DTS and ISR results give mutual support to each other regarding the flow criticalities of flow induced solidification.

To reveal the hydrodynamic origin of the broad window effect, melt flow behaviour of PE-C and corresponding extrudate profiles were studied via ISR. The stable pressure traces after the oscillations in Figure 7.5 can only be attributed to the slip flow mechanism. Therefore, it is concluded that slip flow occurs at the broad extrusion window flow conditions. For instance, in ISR tests at a given apparent shear rate of $50s^{-1}$, slip flows occur at 150°C, 155°C and 160°C. With further increasing the ISR temperature, pressure oscillations emerge. Thus slip flow is the hydrodynamic condition of the broad extrusion window. Additional evidence to prove the appearance of slip flow in the broad extrusion window flow conditions will be shown later in the slip flow velocity measurements, Figures 7.14 and 7.15.

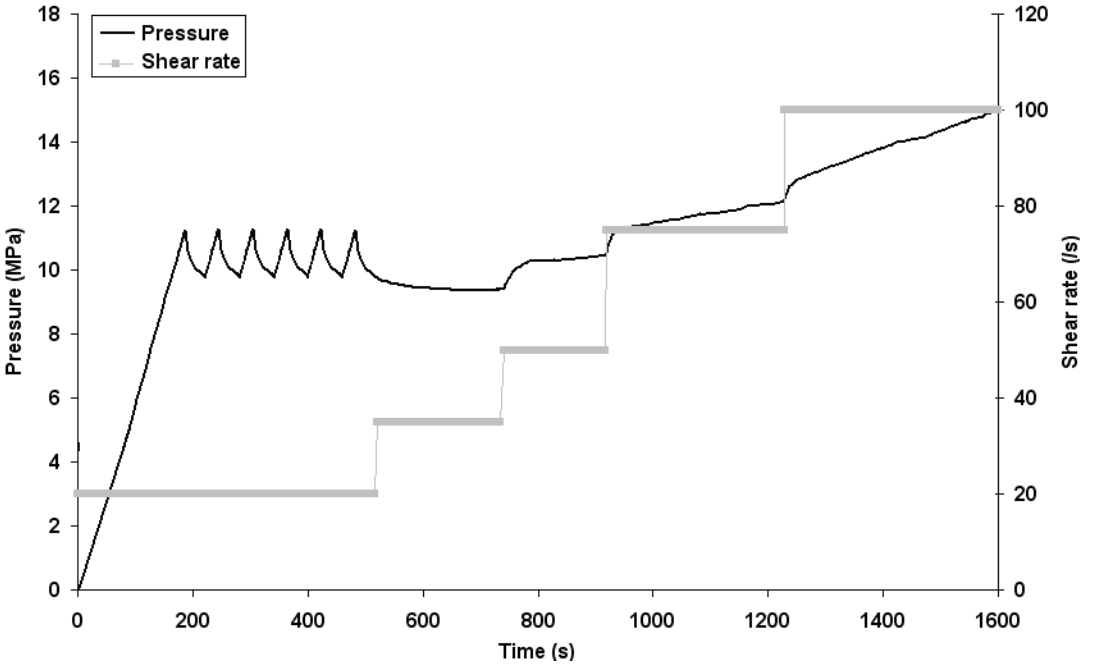

Figure 7.5(a): A plot of pressure vs. time at different shear rate, $20s^{-1}$, $35s^{-1}$, $50s^{-1}$, $75s^{-1}$ and $100s^{-1}$, recorded in a static experiment at 150°C (Die geometry: L-D-2α: 16-1-π)

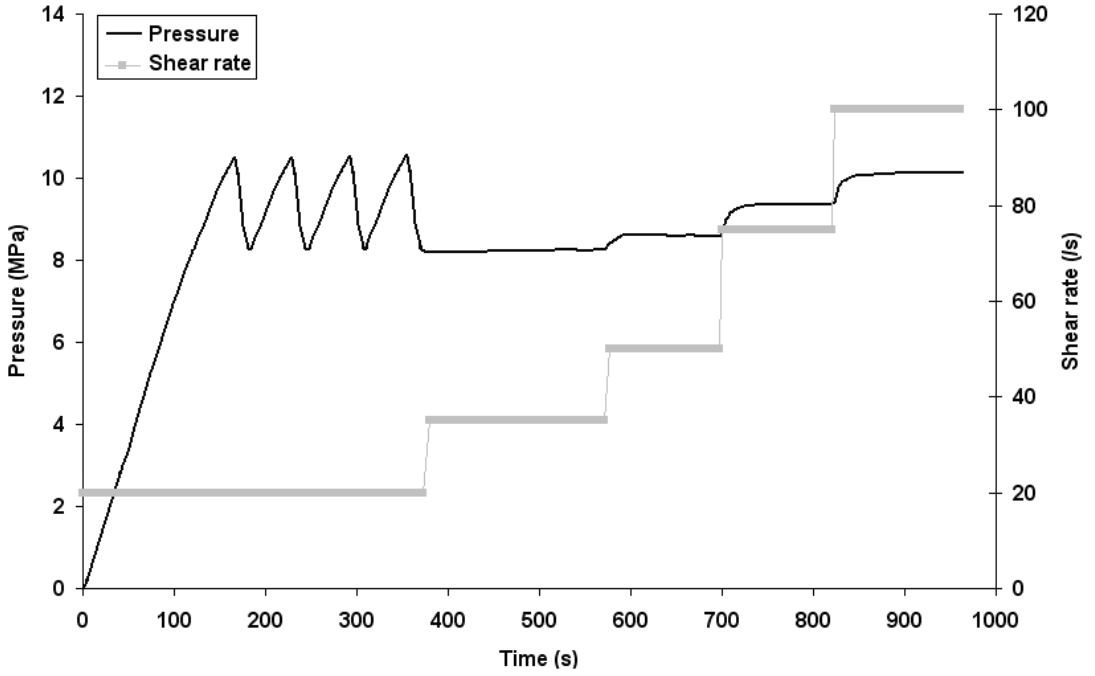

Figure 7.5(b): A plot of pressure vs. time at different shear rate, $20s^{-1}$, $35s^{-1}$, $50s^{-1}$, $75s^{-1}$ and $100s^{-1}$, recorded in a static experiment at 155°C (Die geometry: L-D-2α: 16-1-π)

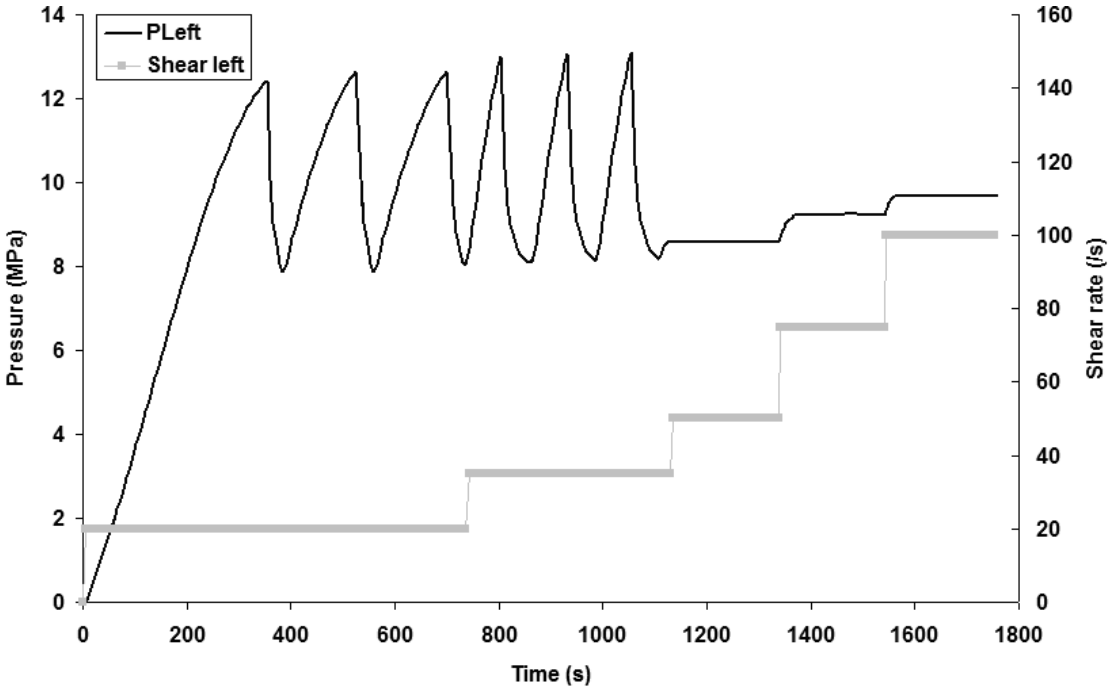

Figure 7.5(c): A plot of pressure vs. time at different shear rate, $20s^{-1}$, $35s^{-1}$, $50s^{-1}$, $75s^{-1}$ and $100s^{-1}$, recorded in a static experiment at 160°C (Die geometry: L-D-2α: 16-1-π)

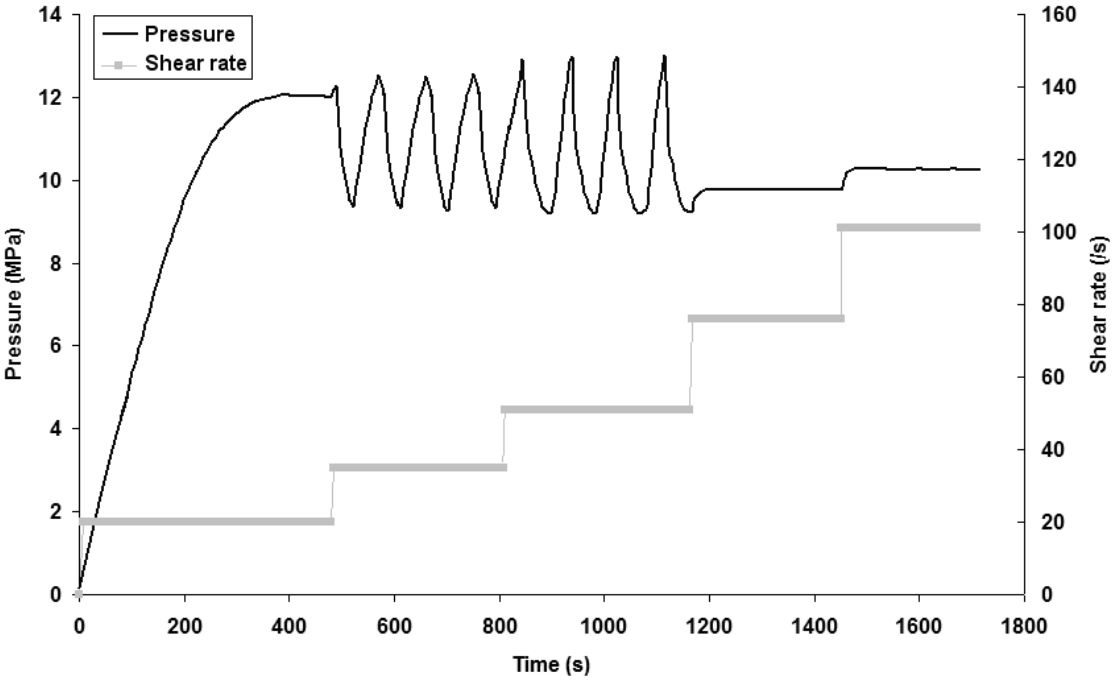

Figure 7.5(d): A plot of pressure vs. time at different shear rate, $20s^{-1}$, $35s^{-1}$, $50s^{-1}$, $75s^{-1}$ and $100s^{-1}$, recorded in a static experiment at 165°C (Die geometry: L-D-2α: 16-1-π)

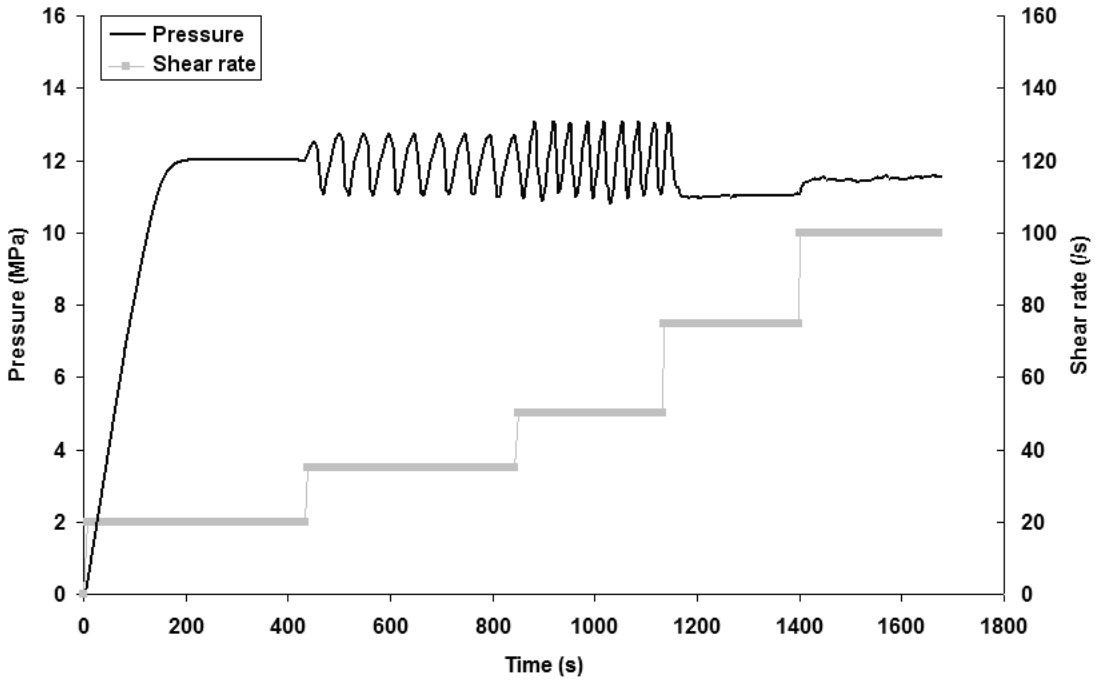

Figure 7.5(e) A plot of pressure vs. time at different shear rate, $20s^{-1}$, $35s^{-1}$, $50s^{-1}$, $75s^{-1}$ and $100s^{-1}$ recorded in a static experiment at 170°C (Die geometry: L-D-2α: 16-1-π)

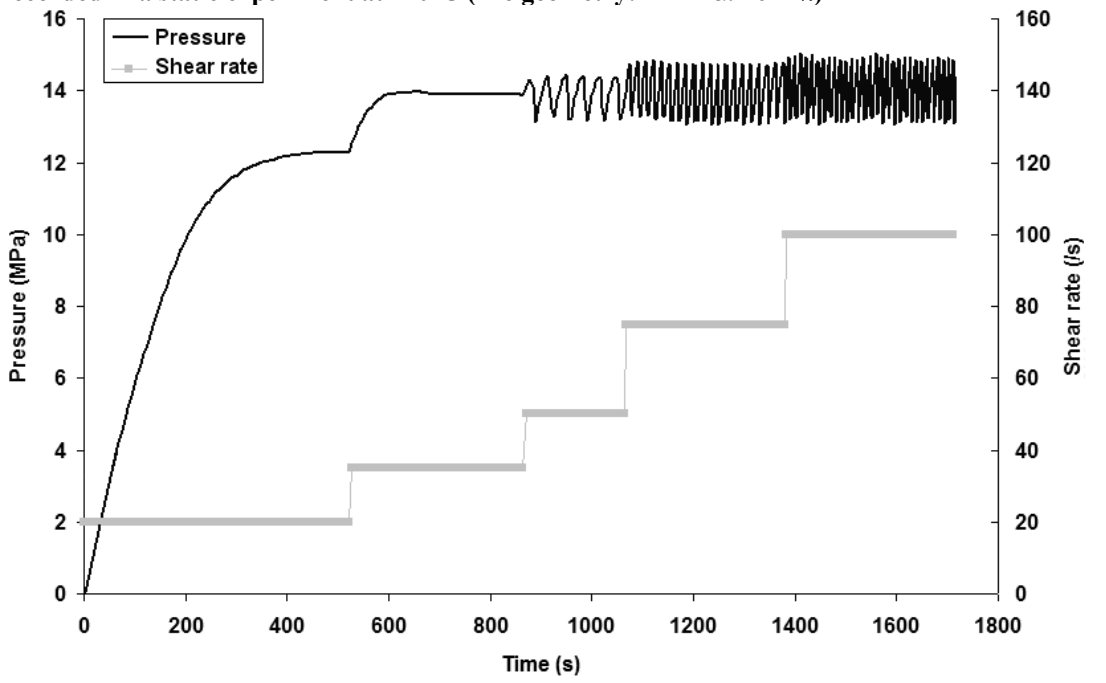

Figure 7.5(f): A plot of pressure vs. time at different shear rate, $20s^{-1}$, $35s^{-1}$, $50s^{-1}$, $75\ s^{-1}$ and $100s^{-1}$ recorded in a static experiment at 180°C (Die geometry: L-D-2α: 16-1-π)

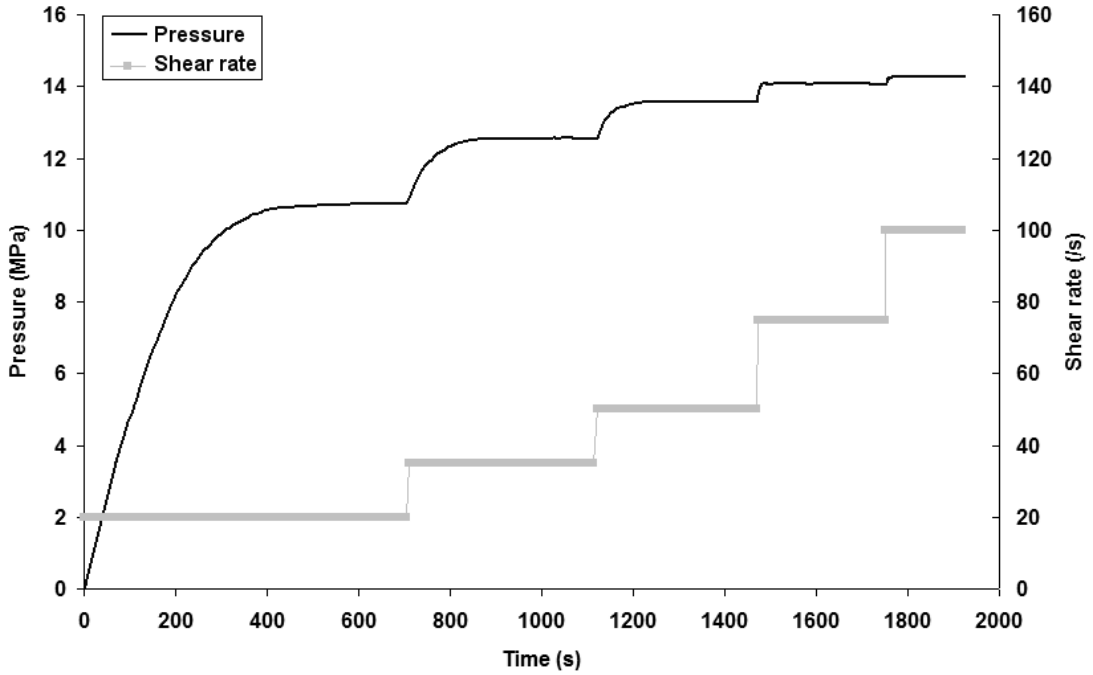

Figure 7.5(g): A plot of pressure vs. time at different shear rate, $20s^{-1}$, $35s^{-1}$, $50s^{-1}$, $75\ s^{-1}$ and $100s^{-1}$ recorded in a static experiment at 190°C (Die geometry: L-D-2α: 16-1-π)

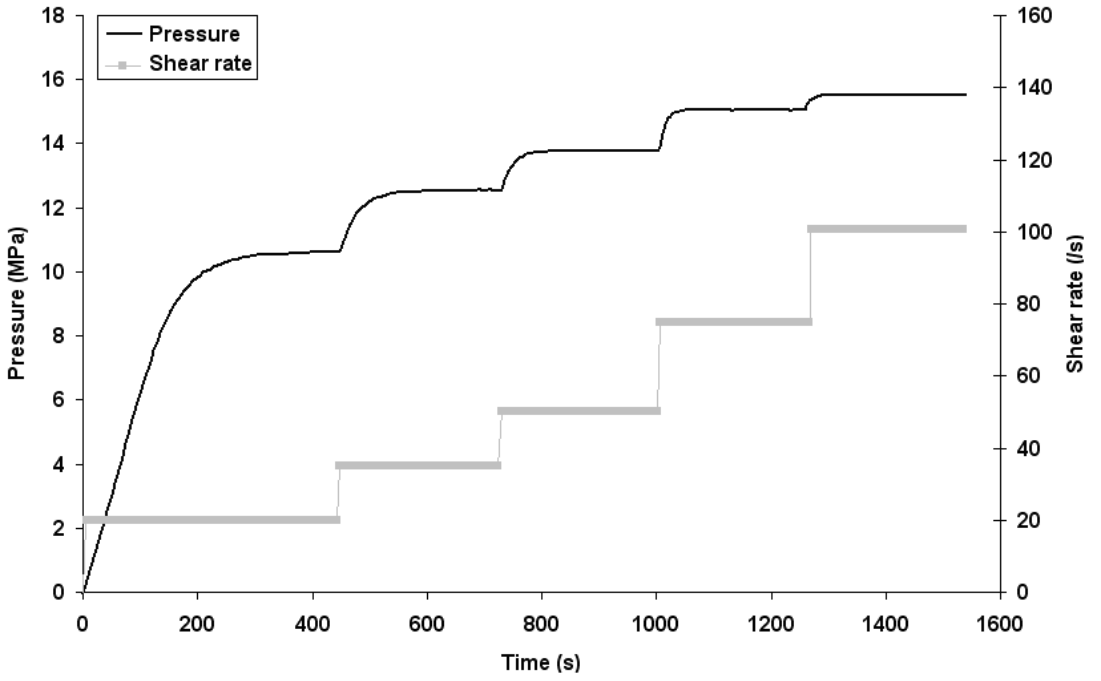

Figure 7.5(h) A plot of pressure vs. time at different shear rate, $20s^{-1}$, $35s^{-1}$, $50s^{-1}$, $75s^{-1}$, $100s^{-1}$ and $150s^{-1}$ recorded in a static experiment at 200°C (Die geometry: L-D-2α: 16-1-π)

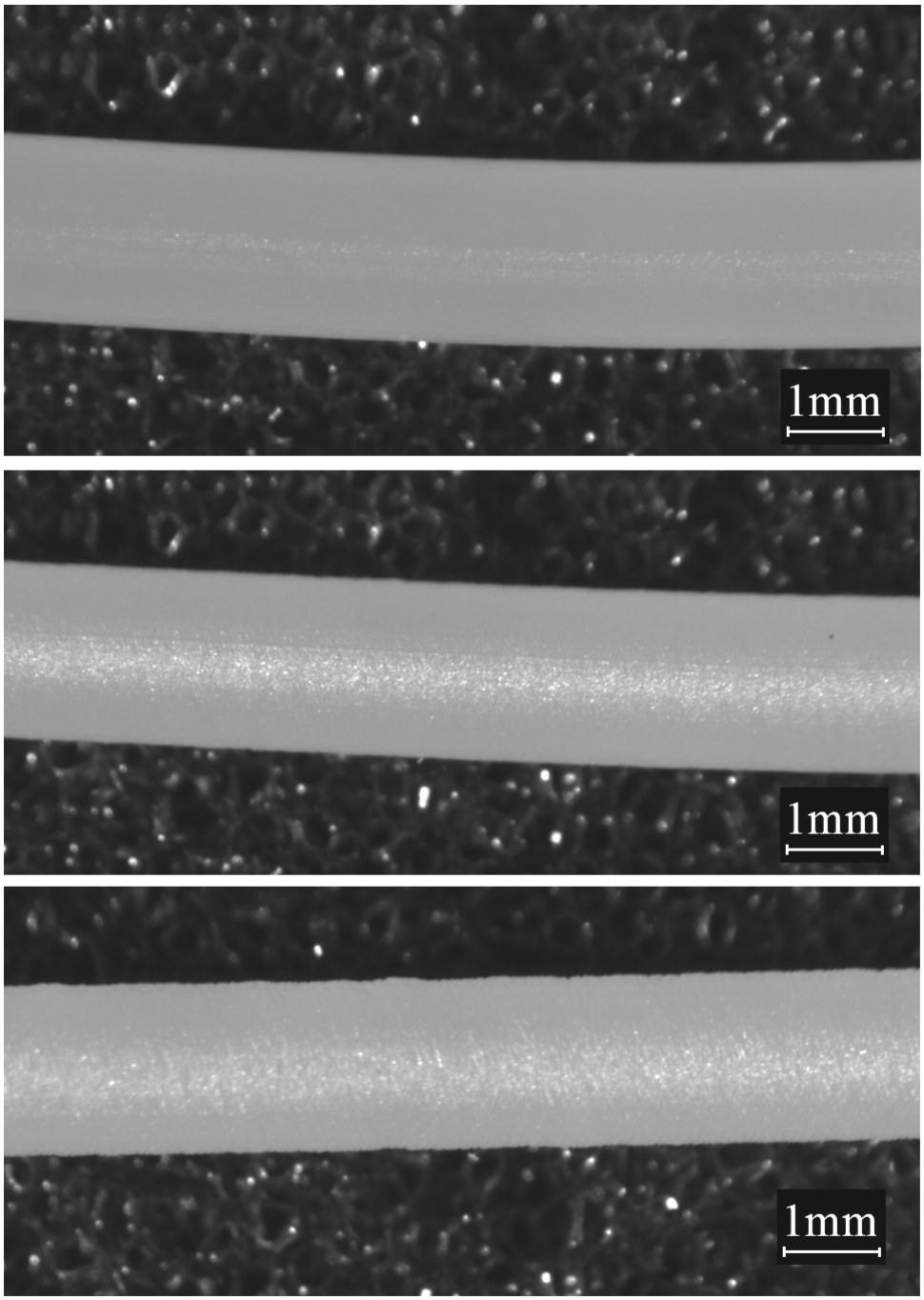

Figure 7.6: Microscope observations of three extrudates obtained in ISR with shear rate, $50s^{-1}$, at 150°C, 155°C and 160°C from top to bottom.

It can be observed from Figure 7.6 that extrudate profiles corresponding to the broad extrusion window, at the shear rate of $50s^{-1}$, show different surface morphologies at different temperatures. Starting from high temperature at 160°C, the corresponding flow condition is situated in window broadening regime. The resultant extrudate shows an expected fine-scale surface distortion. This kind of rough extrudate with fine scale surface distortion was reported in the literature[25(a)]. Regarding the effect of window temperature on the extrudate profile, it is observed that the fine-scale surface

distortion emerging in the window broadening regime gradually weakens as the temperature diminishes; finally it disappears when the extrusion temperature is below 155°C. Below 155°C, a glossy and smooth extrudate is observed in window development regime as shown in Figure 7.6 at temperature 150°C. This implies that the window effect can minimise and final eliminate surface distortion on decreasing the temperature.

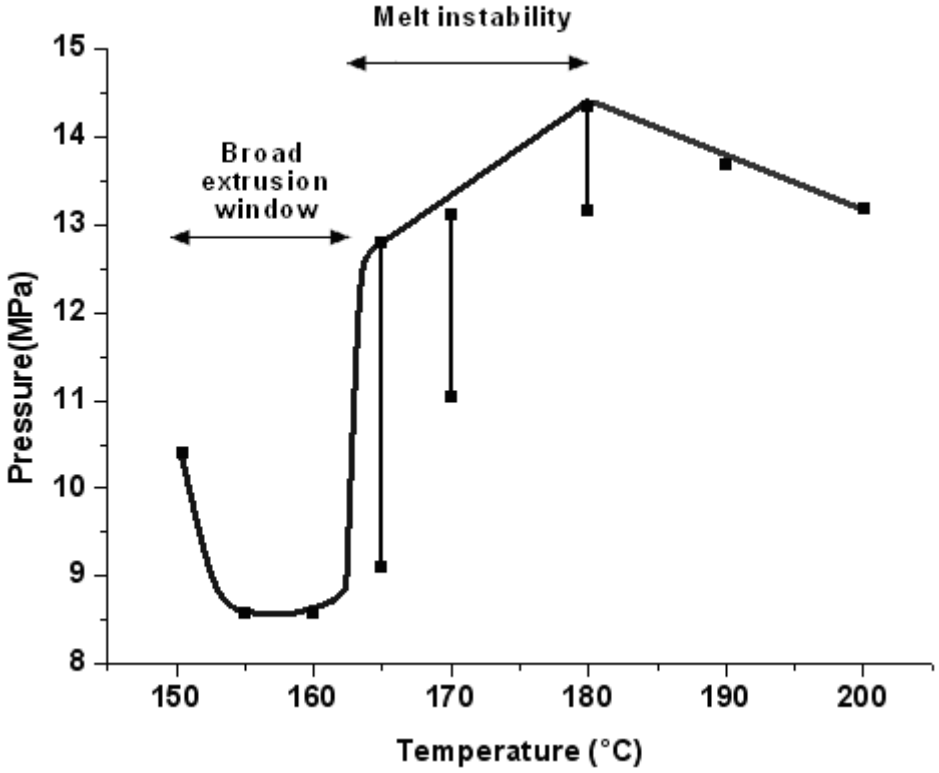

Figure 7.7: A plot of extrusion pressure against temperature at shear rate $50s^{-1}$, in which each data point is recorded from isothermal conditions in the static experiment. The vertical bars denote oscillations in the pressure (Die geometry: L-D-2α: 16-1-π).

7.2.4 The impact of extrusion window on die swell

The die swell ratios recorded in ISR are plotted against temperature as shown in Figure 7.8. It is found that the swelling ratio at shear rate, $8s^{-1}$, increases gradually as temperature decreases and eventually increases rapidly when flow induced solidification occurs at 150°C. When the imposed $\dot{\gamma}_a$ reaches the critical value, $10s^{-1}$, it is observed that a minimum swelling ratio emerges at 150°C, which is consistent with the window temperature observed in DTS and ISR at $10s^{-1}$. At the shear rate of $50s^{-1}$, a considerable drop of die swell ratio is also observed within the temperature interval of the broad extrusion window, see Figure 7.9. Moreover at $50s^{-1}$, the die-swell ratio of the extrudate obtained at the window temperature, 158°C, is identical to

the die-swell ratio at 200°C. The similarity in die-swell ratio at the two distinct extrusion temperatures cannot be explained simply by the continuum rheology of polymer melts and requires the consideration of molecular origin of the window effect. In addition, the minimum die swell ratio emerging at window temperature offers a special advantage in polymer processing, viz. an accurate product dimension control.

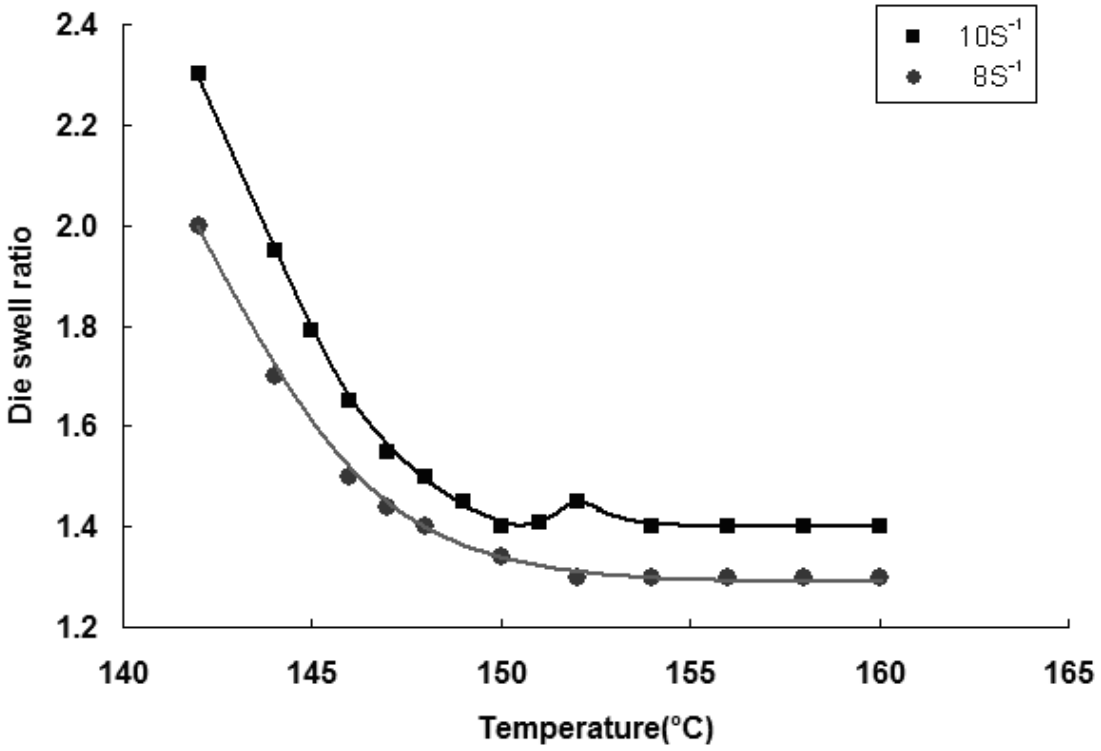

Figure 7.8: Swelling ratio as a function of temperature recorded in ISR at fixed shear rates of $8s^{-1}$ and $10s^{-1}$ (Die geometry: L-D-2α: 16-1- π)

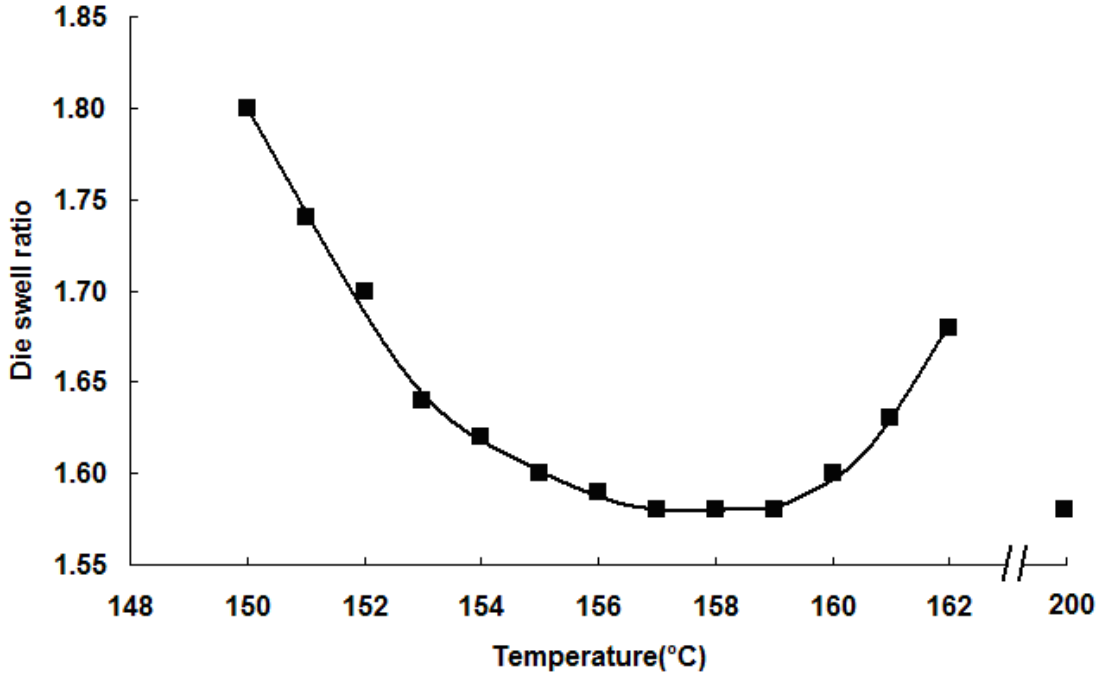

Figure 7.9: Swelling ratio as a function of temperature in ISR at a fixed shear rate of $50s^{-1}$ (Die geometry: L-D-2α: 16-1- π)

7.2.5 The effect of die geometry on extrusion window

7.2.5.1 Variation of capillary length

The $\dot{\gamma}_c^{\,w}$ values for various capillary lengths with the fixed bore diameter (1mm) and entrance angle(π) are determined in the DTS experiments, where the onset appearance of the window effect for a 16mm length capillary die occurs when the $\dot{\gamma}_a$ reaches $10s^{-1}$ as shown in Figure 7.3. From Figure 7.10 it is found that the $\dot{\gamma}_c^{\,w}$ almost remains unaffected by varying the capillary lengths. The unchanged critical shear rate suggests that the $\dot{\gamma}_c^{\,w}$ is independent of capillary length.

Figures 7.11 and 7.12 show the extrusion pressure vs. temperature traces recorded in both capillary flow and capillary free flow (0-1-π). In the course of capillary free flow the extrusion pressure increases gradually with decreasing temperature. The sudden increase in pressure arises from the flow induced solidification. However, the absence of window effect in the capillary free flow confirms that the origin of the extrusion window of broad molar mass distributed polyethylene does not arise from convergent flow.

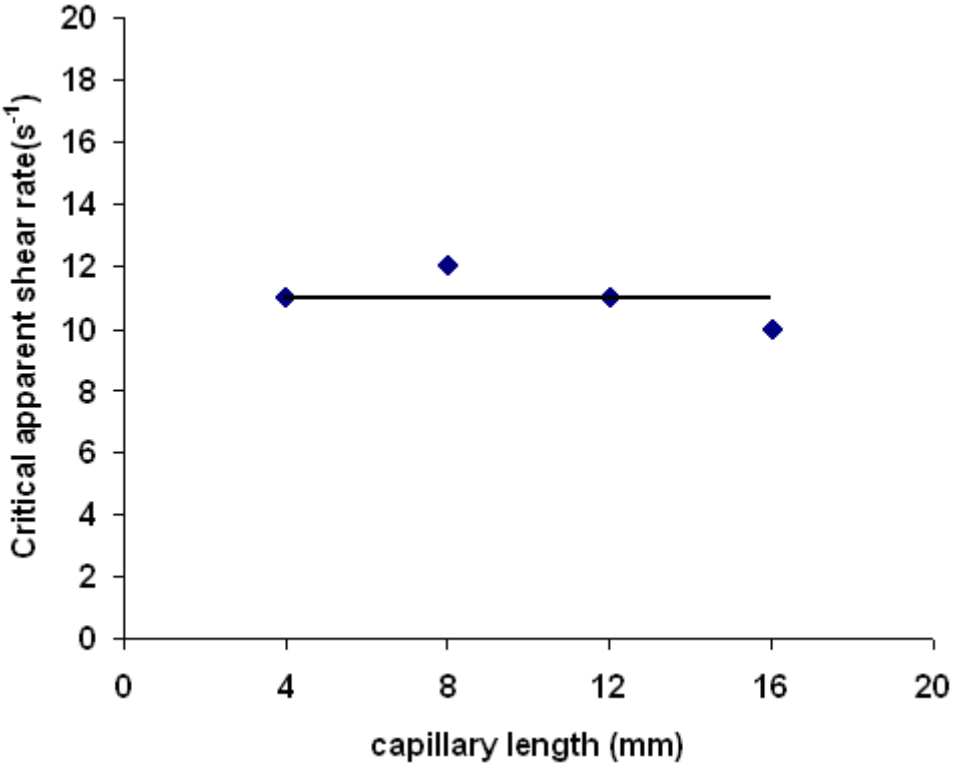

Figure 7.10: Critical shear rate, γ_c as a function of *L (capillary die geometry: D=1mm, $2\alpha = \pi$)*

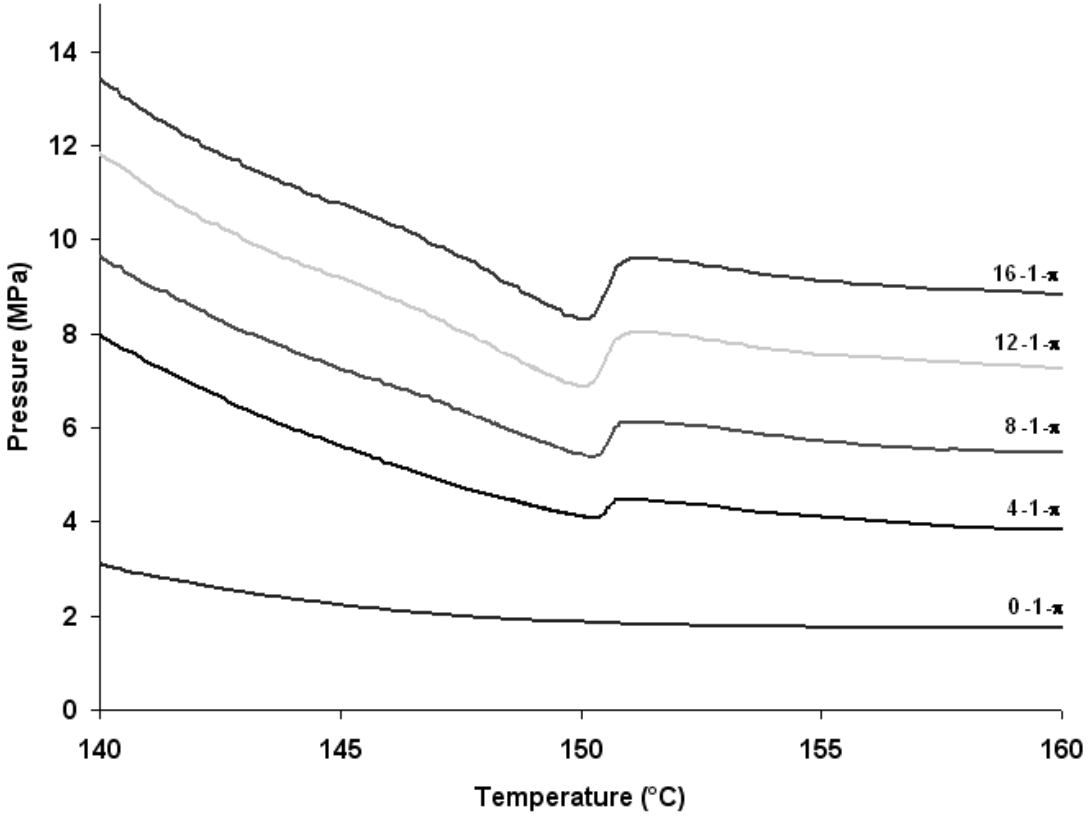

Figure 7.11: Extrusion pressure vs. temperature traces recorded in dynamic experiment, $12s^{-1}$, using a series capillary die with various die length.

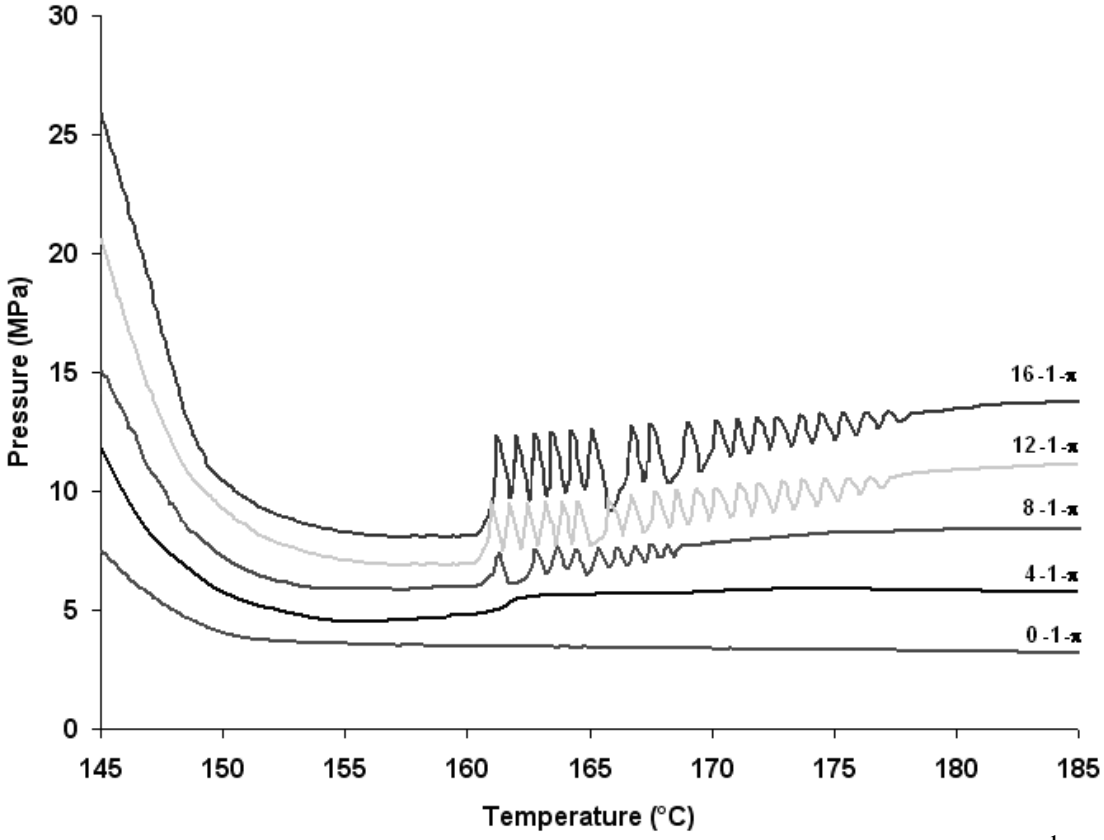

Figure 7.12: Extrusion pressure vs. temperature traces recorded in dynamic experiment, 50s^{-1}, using a series capillary die with various die lengths.

7.2.5.2 Variation of die entry angle

It is well known that the strength of elongational flow can be altered by varying die entry angle since convergent flow promotes elongational flow. Regarding the broad extrusion window, the effect of varying entry angles on $\dot{\gamma}_c^{\,w}$ is studied in a flow system with various die entry angles with the fixed barrel and capillary diameters. It is revealed that the $\dot{\gamma}_c^{\,w}$ remains independent of the die entry angle (Figure 7.13). These experimental findings strongly suggest that the convergent flow has non-effect on the extrusion window of PE-C.

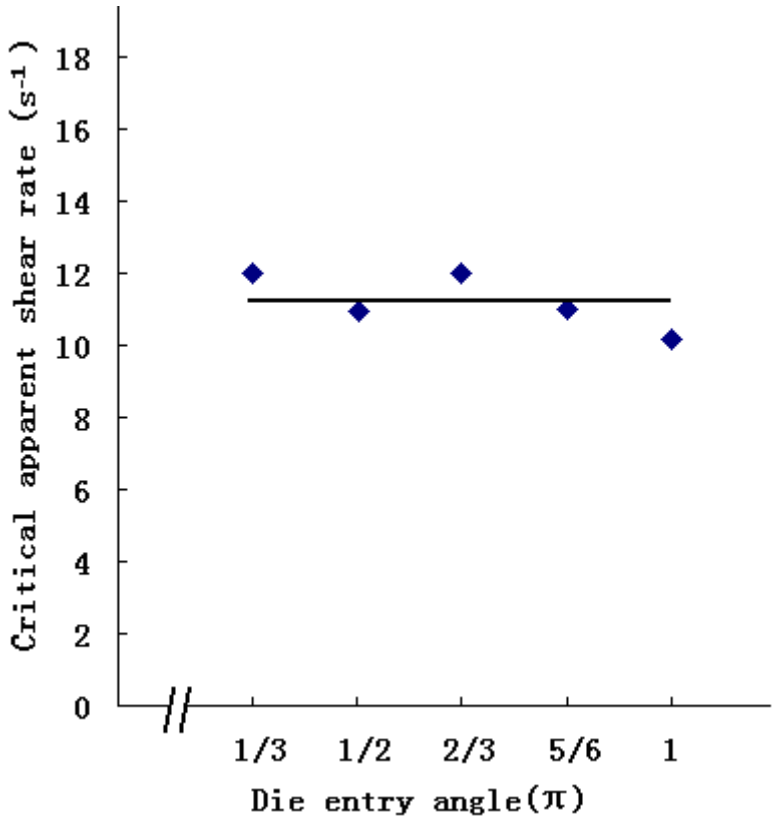

Figure 7.13: Critical apparent shear rate of PE-C vs. die entry angle (die length, L=16mm; capillary diameter D=1mm).

7.2.6 Slip flow velocity

A slip flow characterisation was performed to verify the appearance of slip flow in the extrusion window of PE-C. According to the plots of $\dot{\gamma}_a$ vs. *1/R, where R is the capillary radius,* from Figure 7.14 and 7.15, it can be observed that $\dot{\gamma}_a$ remains unaffected within the stick flow regime at low shear rate, whereas slip flow occurs when the corresponding $\dot{\gamma}_a$ is above the $\dot{\gamma}_c^{\,w}$ for the capillary die with a bore radius of 0.5mm. It suggests that the slip flow occurs at the flow conditions corresponding to the window effect. These results confirm that the window effect slip flow is the hydrodynamic condition of the broad extrusion window. Moreover, it is also found from Table 7.1 that slip velocity increases with the σ_c^w, within the slip flow regime.

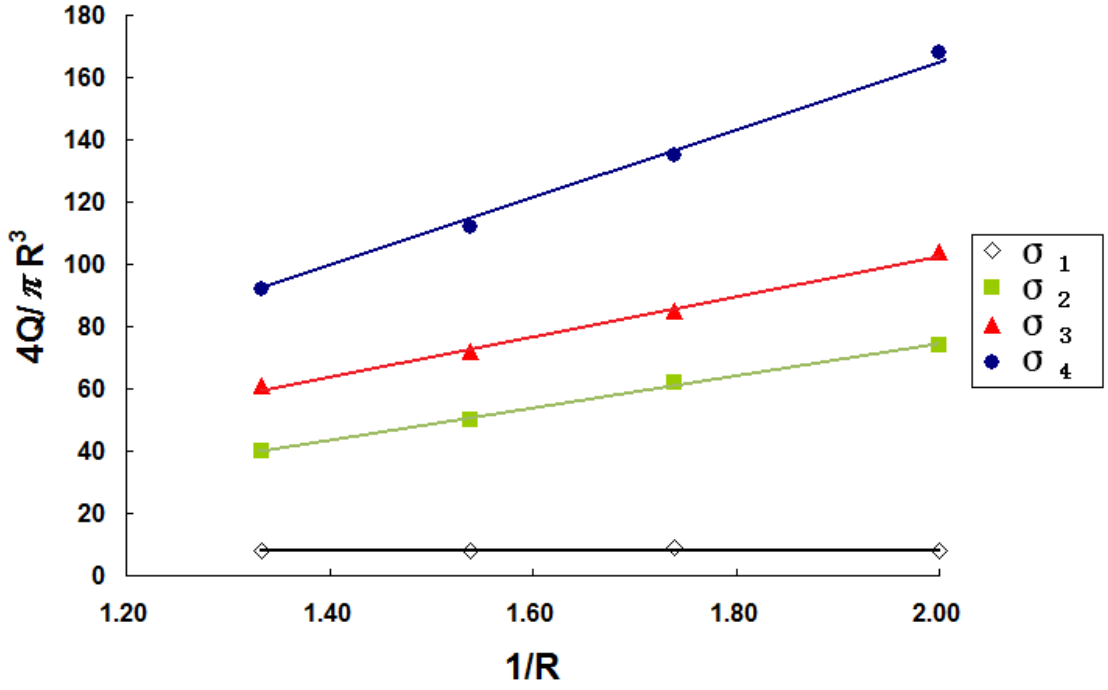

Figure 7.14:The volumetric output rate at different wall shear stress plotted as a function of the inverse of die radius at 150°C. Slip velocity is determined from the gradient of each line.

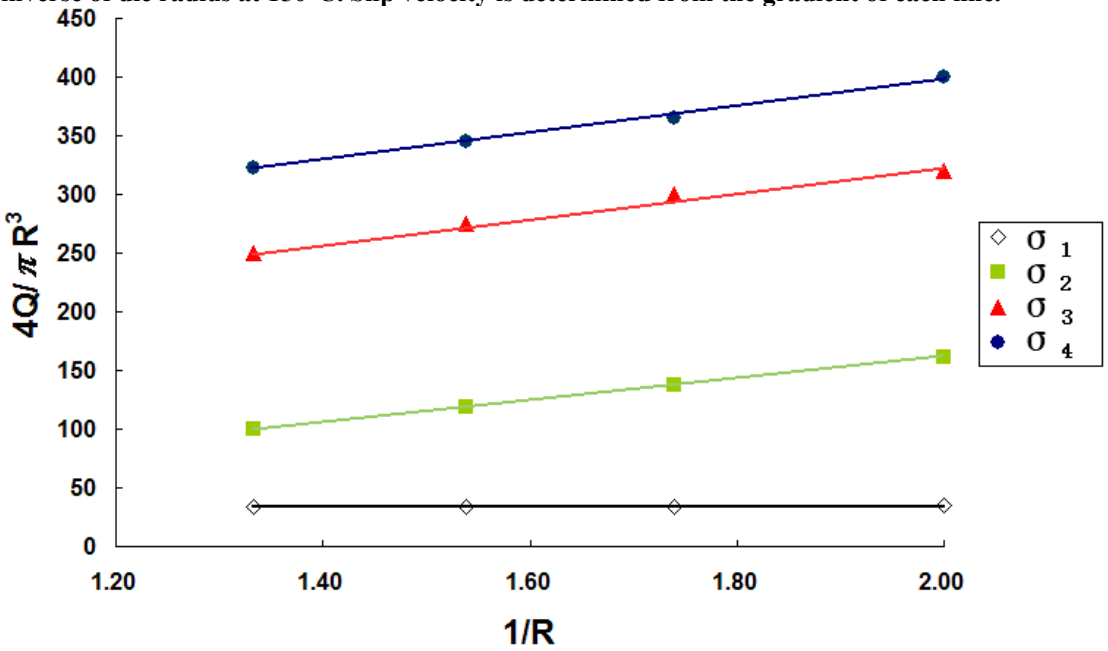

Figure 7.15:The volumetric output rate at different wall shear stress plotted as a function of the inverse of die radius at 155°C. Slip velocity is determined from the gradient of each line.

Table 7.1(a): The slip velocity determined at 150°C according to the gradient of volumetric output rate vs. the inverse of capillary diameter.

Shear stress (MPa)	Slip flow velocity (mm s^{-1})
σ_1=0.14	0
σ_2 =0.18	12.92
σ_3 =0.20	16.19
σ_4 =0.22	28.61

Table 7.1(b): The slip velocity determined at 155°C according to the gradient of volumetric output rate vs. the inverse of capillary diameter.

Shear stress (MPa)	Slip flow velocity (mm s^{-1})
σ_1=0.13	0
σ_2 =0.17	22.93
σ_3 =0.22	26.50
σ_4 =0.25	28.97

7.3 Discussion

7.3.1 The molecular origin of broad extrusion window

This is the first study of melt flow singularity of linear PE with a broad molecular weight distribution. From Figure 7.4, it was observed that the broad extrusion window occurs at an appropriate shear rate, $50s^{-1}$, which should be higher than the critical shear rate for the lowest molecular weight component. In contrast to the narrow extrusion window of linear PEs characterised by a relatively narrow molecular weight distribution (PDI<7), the broad extrusion window can offer an energy-efficient processing route since it can be tolerant thermal fluctuations during polymer processing.

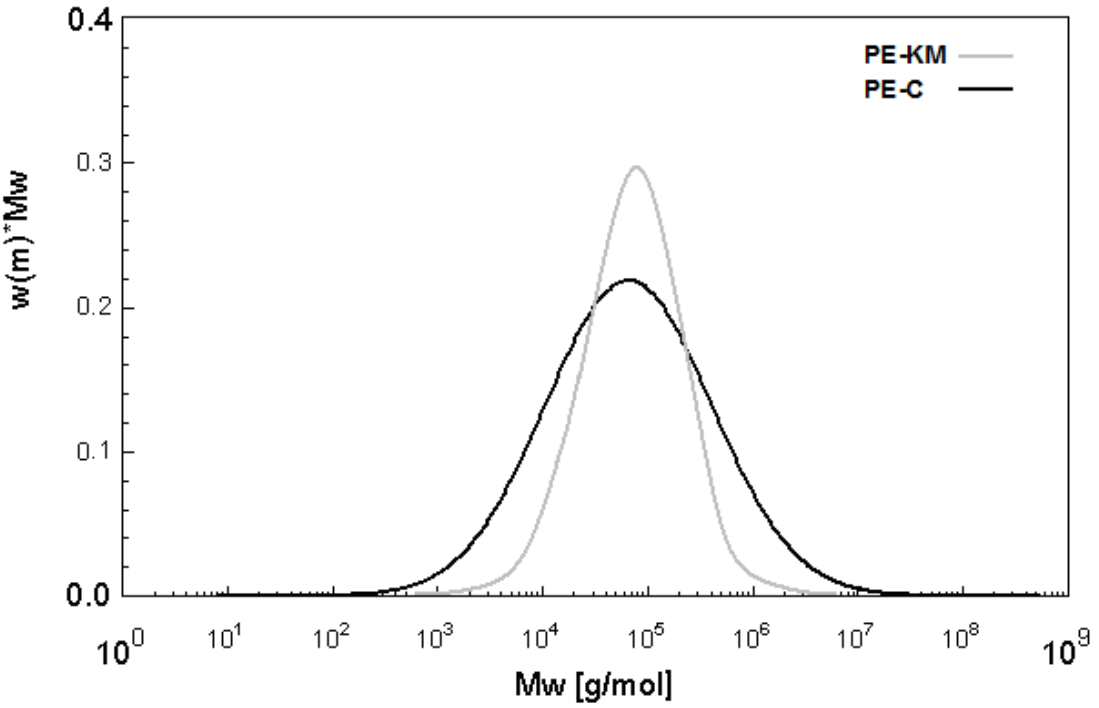

Figure 7.16 Synthesised molecular weight distribution traces of PE-C and PE-KM.

Table 7.2 the melt flow criticalities for PE-KM[31] and PE-C.

Samples	Critical onset apparent shear rate (s^{-1})	Temperature minimum at the critical shear rate (°C)
PE-KM	8	149.5
PE-C	10	150.0

In order to study the effect of molecular weight distribution on the narrow extrusion window of PE-C occurring at the critical onset apparent shear rate, $\dot{\gamma}_c^{\,w}$=10s^{-1}, one of Kolnaar's samples, PE-KM, is selected to compare with PE-C. Regarding the molecular characteristics, PE-C and PE-KM have distinct weight average molecular weight, M_w, and molecular weight distribution, MWD, (i.e. PE-C: M_w=349,100 g mol^{-1} MWD=27.8 [c]; PE-KM: M_w =280,000 g mol^{-1} MWD=7.5 see Table 7.2). According to the molecular weight dependence on flow criticalities, the high molecular weight linear PE should exhibit onset of the window effect at lower shear rate compared to the low molecular weight linear PE. However $\dot{\gamma}_c^{\,w}$ of PE-C is greater than that of PE-KM. One of the possible reasons may be attributed to the low molecular weight PE components in PE-C. The synthesised molecular weight distribution curves of PE-KM and PE-C are shown in Figure 7.16. It can be seen that PE-C consists of high percentage of low molar mass PEs, where the low end molar mass is even lower than that of PE-KM. These low molar mass agile chains, with short relaxation time, have a significant impact on the window effect arising from the acting molecular weight component in PE-C. First of all, the short chains can reduce the effective adsorbed chain density which is defined as a number of adsorbed chains per unit area on capillary wall. Secondly, the presence of short chains can interrupt the adsorption of long chains on the capillary wall and perturb the stretched chain conformation of long chains at window temperature due to Brownian fluctuation. Consequently, the onset of the window effect of PE-C occurs above the predicted critical shear rate (~4s^{-1}) based on the molecular weight dependence of flow criticality. In summary, the presence of low molar mass component shifts the critical shear rate

[c] characterised via rheology route

for window effect to the higher values. This negative effect is likely to be even worse at the higher temperature.

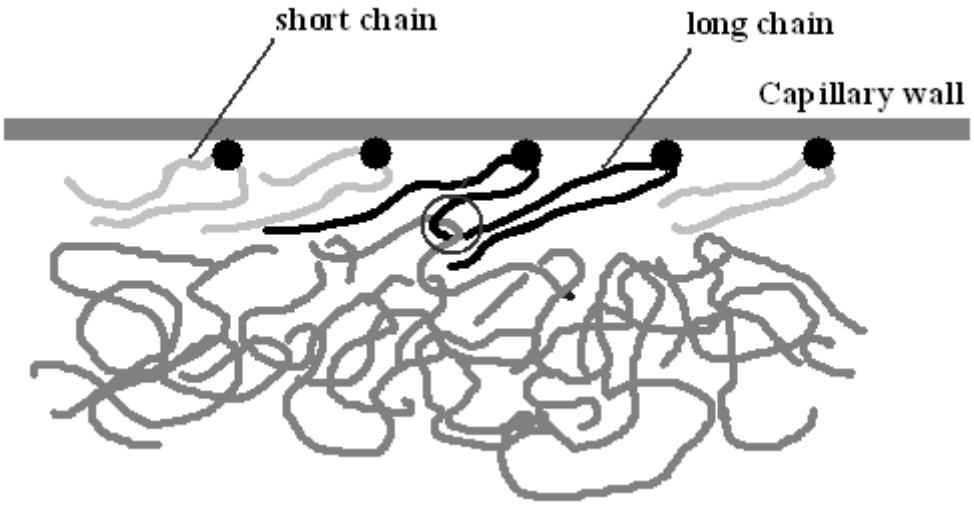

Figure 7.17: A schematic diagram showing the effect of hindered disentanglement process of long chains, occurring at low temperature, resulting in the termination of the entire disentanglement of adsorbed chains from free chains, even though adsorbed short chains are fully disentangled from free chains in bulk.

PE-C can be considered as a blend of linear PEs with different molecular weight components. Each molecular weight component has a characteristic window temperature. Accompanied with each window effect arising from different molecular weight components, a broad temperature window occurs at an appropriate shear rate ($50s^{-1}$). The appropriate shear rate is higher than the critical shear rates of different molar mass components presenting in the PE-C. The lowest window temperature of PE-C is 150°C as shown in Figure 7.3. It implies that there is no trace of any lower temperature extrusion windows, corresponding to the lower molar mass linear polyethylenes (<100,000 g mol^{-1}), even if the apparent shear rate increases. The disappearance of all the low temperature windows (<150°C) is attributed to the terminated slip flow hydrodynamic condition of short chains with presence of long chains. Considering two key factors in the window effect slip flow, one is the maintained stretched chain conformation, and the other is the disentanglement of adsorbed chains from free chains. At high temperature, long chains possessing longer relaxation time can enhance the stretched chain conformation of shorter chains under flow condition. At lower temperature, however, it can also cease the disentanglement of adsorbed chains from the free chains due to the increase in the entanglement density with bulk chains resulting from dual/multi adsorption points of each long

chain as shown in Figure 7.17. Therefore, the window effect associated with low molar mass component fails to exist in the broad extrusion window.

There are two distinct types of flow behaviour found in the broad extrusion window of PE-C. One is named as the window development regime, and the other is termed as the window broadening regime. Within the window development regime, extrusion windows emerge at different temperatures one by one, up to 155°C, as the applied apparent shear rate increases (from $10s^{-1}$ to $40s^{-1}$). It is found that the subsequent windows occur at higher temperatures with even lower pressure minima. According to the window temperature dependence on molecular weight and flow criticalities, those high temperature windows are attributed to the higher molecular weight components. If the window temperature still obeys the molecular weight dependence at 155°C, the window effect at 155°C should arise from a linear polyethylene with M_w above but near 1,000,000 g mol^{-1} according to the extrapolation plot of the window temperature vs. molecular weight depicted in Figure 5.5. Generally speaking, PE with M_w above 1,000,000 g mol^{-1} is an intractable material by conventional polymer processing routes like extrusion and injection moulding. Kolnaar also pointed out that the upper limit molecular weight for the narrow window effect[31(a)] was around 1,000,000g mol^{-1}. However the existence of high temperature window at 155°C suggests a possible route to process the intractable PE with assistance of agile short chains within extrusion window flow conditions.

With regards to the window broadening regime, it was found that the pressure minimum remains unaffected during cooling until the temperature reaches 155°C. It is apparent that the molecular origin of window broadening cannot be attributed to slip flow of M_Z since the constant pressure minimum contradicts molecular weight dependence of flow criticalities. One of possible reasons for window broadening is attributed to the slip flow of acting molecular weight components (~1,000,000 g mol^{-1}) with assistance of the UHMWPE component (~3,000,000 g mol^{-1}) in PE-C. From rheological characterisation, PE-C contains UHMWPE component which is situated at the far end of molecular weight distribution curve ($>M_Z$). Such extremely long chains have no window effect themselves. Whereas they can facilitate the orientation of long chains and maintain the stretched chain conformation at even high

temperatures. In addition, it was also found that the window broadening effect extends to high temperature on increasing apparent shear rate further from $50s^{-1}$ to $70s^{-1}$. According to coil-stretch transition theory, the higher the apparent shear rate, the higher the onset temperature of the window effect. As $\dot{\gamma}_a$ increases, the stretched chain conformation of long chains can be maintained at even higher temperature with aid of extremely long polymer chains, M_Z, to counteract the negative effect of Brownian fluctuation of short chains and maintain the unstable stretched chain conformation of long chains as the temperature increases. Consequently, the extrusion window at $70s^{-1}$ is broader than that at $50s^{-1}$, even though the T_s at $70s^{-1}$ is higher than that at $50s^{-1}$.

Looking back to the melt flow singularity of a bimodal polyethylene, PE-B, there are three pressure drops observed in the course of capillary flow of PE-B at an apparent shear rate of $300s^{-1}$. In fact the high temperature pressure drop arises from window broadening effect.

7.3.2 The effect of extrusion window on die swell

It is well known that the die swell arises from the elastic recovery of stretched chains. According to slip flow theory corresponding to high surface energy die, most of the adsorbed chains remain tethered on the capillary wall and free chains are extruded out of the capillary die. The disentanglement degree of the free chains during the window effect slip flow governs the die swell ratio of extrudate. Window effect slip flow occurs at certain flow criticalities. When the extrusion temperature is close to the window temperature, ±1°C, slip flow occurs at an appropriate apparent shear rate. However, the slip flow hydrodynamic condition is not fully developed until the temperature reaches the critical window temperature. Therefore, the minimum die swell ratio occurs at the very extrusion temperature corresponding to the pressure minimum within the extrusion window, where the window effect slip flow is fully developed.

It was also found that the die swell ratios recorded at 158°C and 200°C for PE-C are identical at a shear rate of $50s^{-1}$. One of the possible reasons is due to the distinct hydrodynamic conditions. At 158°C it is slip flow, however, at 200°C it is stick flow. High temperature stick flow, at 200°C, has low die swell ratio, arising from short

relaxation time of polymer chains at high temperature. However, low temperature slip flow shows the low die swell ratio that is attributed to disentangled free chains occurring within window effect slip flow.

7.3.3 The influence of die geometry on flow criticalities

7.3.3.1 Change length with diameter and entry angle constant.

With regards to the broad extrusion window, pure orifice flow does not give rise to the broad window effect. According to slip flow theory associated with high surface energy die, polymer chains should attach and adsorb on the capillary wall first, and then adsorbed chains are oriented to a certain stretched chain conformation, finally such tethered chains can disentangle from free chains and slip flow occurs. Therefore, the capillary flow is a prerequisite for the appearance of slip flow since cylindrical capillary wall provides a high surface energy substrate for chain attachment. Whereas the $\dot{\gamma}_c^{\,w}$ is independent of the capillary length.

7.3.3.2 Change entry angle with diameter and length constant.

It was known that window effect is not attributed to convergent flow; however, it may have an effect on $\dot{\gamma}_c^{\,w}$. It was revealed that the $\dot{\gamma}_c^{\,w}$ of PE-B increases as the die entry angle reduces for low temperature extrusion window. By contrast, the $\dot{\gamma}_c^{\,w}$ of PE-C and the middle temperature window of PE-B are independent of the die entry angle. It implies that pre-stretched chains only have an effect on $\dot{\gamma}_c^{\,w}$ at low temperature, since such pre-aligned chains can only be maintained at low temperature and reduce the critical strain rate for the onset of stretched chain conformation for slip flow. However, pre-aligned chains are likely to be unstable at high temperature, e.g.150°C. Therefore, variation of die entry angle has no effect on $\dot{\gamma}_c^{\,w}$ of PE-C.

7.4 Conclusion

Linear PE with broad molecular weight distribution exhibits a broad extrusion window. Subsequent to a narrow extrusion window occurring at $10s^{-1}$, intriguing multi-windows emerged as the shear rate increases to $40s^{-1}$. Eventually all the extrusion windows merged with each other forming a broad extrusion window at a shear rate of $50s^{-1}$.

It was found that the $\dot{\gamma}_c^{w}$ of PE-C is higher than the predicted value based on molecular weight dependence since the presence of agile short chains reduces the effective adsorbed chain density and also perturbs the stretched chain conformation of the acting molecular weight components.

The multi-windows observed in the window development regime are attributed to window effect slip flows corresponding to diverse molecular weight components in PE-C. Each molecular weight component in PE-C has a window effect at or around the characteristic window temperature, obeying the molecular weight dependence. In the window development regime, extrusion windows emerge at different temperatures, up to 155°C, with increasing applied apparent shear rate from $10s^{-1}$ to $40s^{-1}$. Higher temperature windows have an even lower pressure minimum, obeying the dependence of rescaled wall shear stress on molecular weight.

Prior to the window development regime, the window broadening regime occurs at a shear rate of $50s^{-1}$ or above. This effect is attributed to the UHMWPE component in PE-C. According to the coil-stretch theory, UHMWPE with longer relaxation time can maintain the stretched chain conformation of long chains at even higher temperatures. As a consequence, the window effect can extend to 160°C or even higher temperatures with further increasing of the shear rate. It is also implies that the intractable UHMWPE can be processed, with the assistance of certain loading of inner 'lubricant', i.e. agile short chains.

Regarding the effect of die geometry on flow criticalities, it was found that the capillary flow is a mechanism responsible for the broad extrusion window. However, flow criticalities of the extrusion window are independent of capillary length. On the other hand, it is found that the variation of die entry angle has no effect on $\dot{\gamma}_c^{w}$ of PE-C since the pre-aligned chain conformation occurring in convergent flow cannot be maintained at higher temperature, 150°C.

Chapter 8: The influence of nanofillers on the melt flow singularity of linear polyethylene

8.1 Introduction

The similar molecular composition of carbon nanotubes and polyethylene (PE) gives rise to the favourable epitaxial matching between the two. Moreover, it is well known that the presence of nanofillers can influence the chain dynamics[55] and thus is likely to influence the window effect. Considering the relatively high relaxation times of the several-micrometer length nanotubes compared to the low molar mass flexible linear PE molecules, the nanotubes are likely to maintain the stretched state – thus favouring the window effect. However, by changing the aspect ratio of the filler from nanotubes to spherical particles such as carbon black, the anticipated chain orientation near the capillary wall can be influenced negatively – opposing the appearance of window effect.

Considering the above thoughts, in this chapter two carbon-based nanofillers, multi-walled carbon nanotubes (MWCNTs) and carbon black (CB), were used to modify the melt flow behaviour of linear PE. Prior to the study of flow behaviour of PE nanocomposites, the studies have been performed on the neat sample, as shown in chapter 4.

8.2 Results

In this chapter PE-A, with narrow molecular weight distribution, was selected as a reference material to study the effect of carbon based nanofillers on window effect of linear PE.

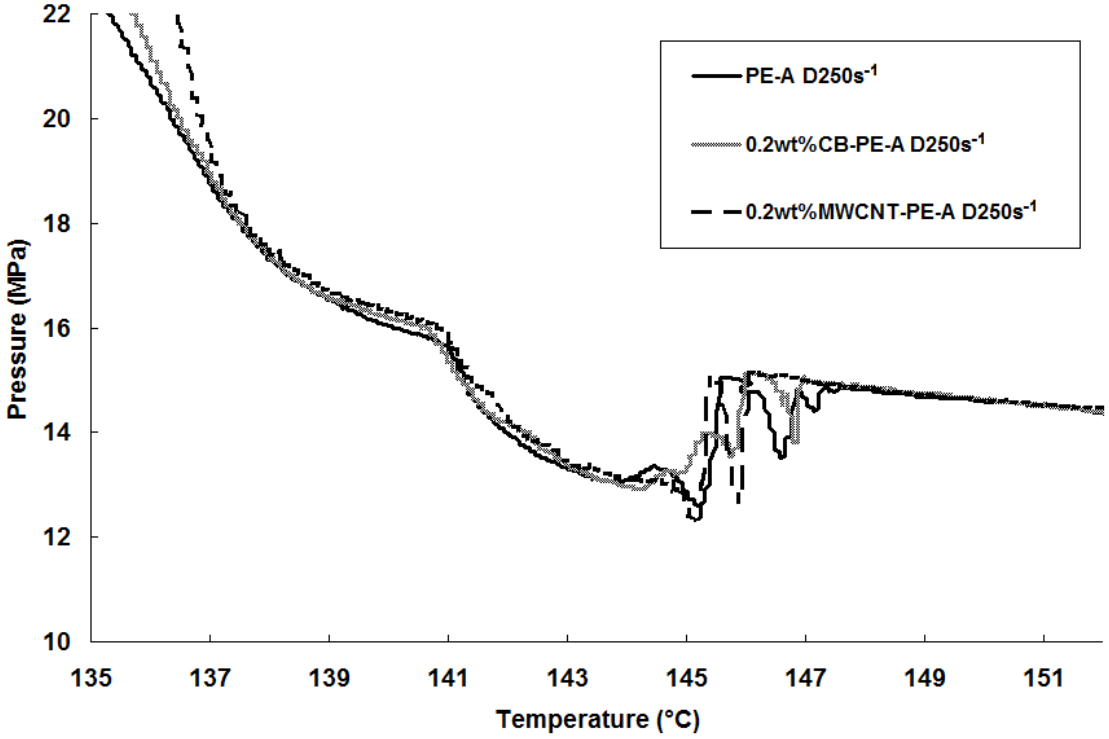

Figure 8.1: A plot of extrusion pressures as a function of temperature recorded during dynamic cooling experiments with a constant shear rate at 250s^{-1} (L-D-2α: 16-1-π) showing the melt flow behaviour of neat PE-A and PE-A with 0.2wt%MWCNTs and PE-A 0.2wt%CB.

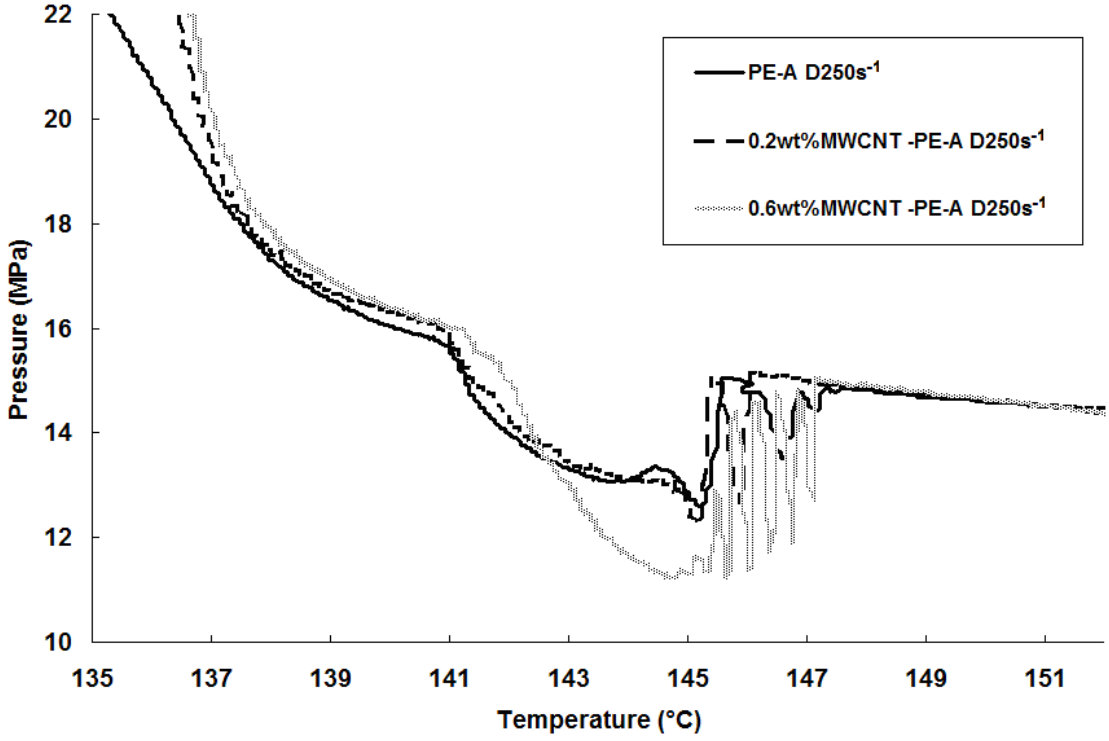

Figure 8.2: A plot of corrected pressures as a function of temperature recorded during dynamic cooling experiments with a constant shear rate at 250s^{-1} (L-D-2α: 16-1-π) showing the melt flow behaviour of neat PE-A and PE-A with 0.2wt%MWCNTs and PE-A with 0.6wt%MWCNTs.

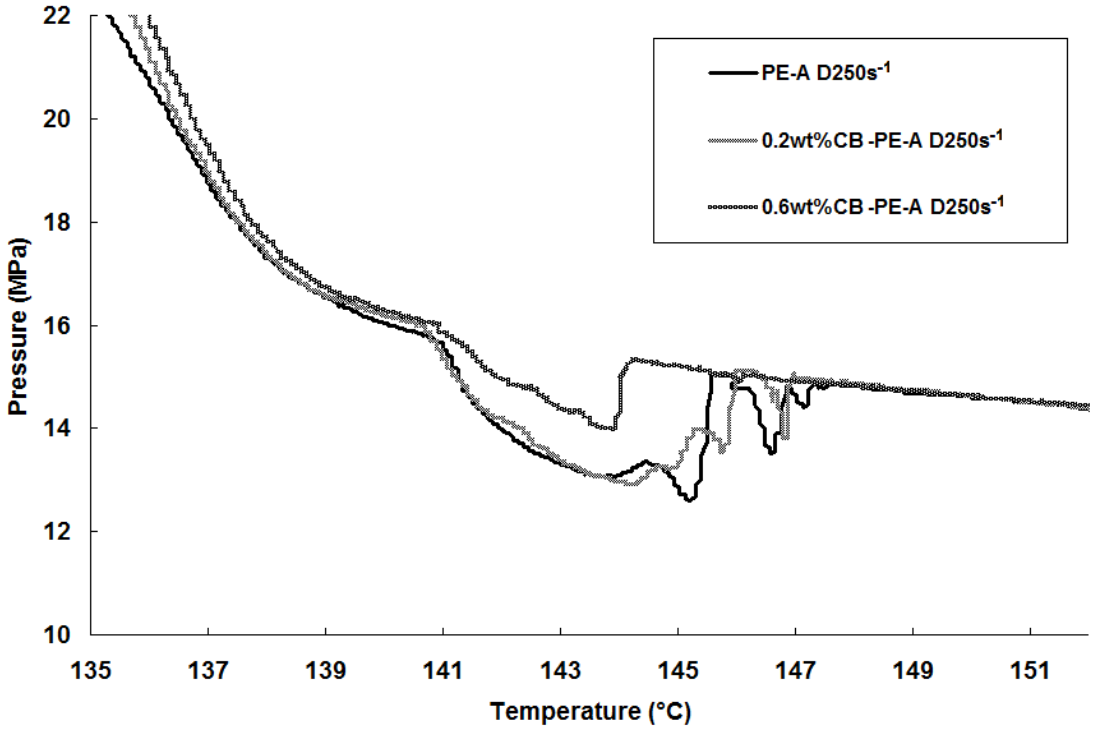

Figure 8.3: A plot of corrected pressures as a function of temperature recorded during dynamic cooling experiments with a constant shear rate at 250s^{-1} (L-D-2α: 16-1-π) showing the melt flow behaviour of neat PE-A and 0.2wt%CB-PE-A and 0.6wt%CB-PE-A.

Figure 8.1 shows that the window effect remains unaffected on the addition of 0.2wt% of the two carbon-based nanofillers respectively. However, apparent differences are observed in the flow induced solidification region. Within this region, the extrusion pressure of 0.2wt% MWCNTs-PE-A and 0.2wt%CB-PE-A increases steeply. A closer comparison between the two carbon nanofillers suggests that the building-up rate is more pronounced in PE-MWCNTs composites.

The effect of various loadings of MWCNTs on the melt flow behaviour of the linear PE is depicted in Figure 8.2. On increasing the loading of MWCNTs to 0.6wt%, a distinct decrease in the pressure minimum is observed, though the width of the temperature window does not change. The drop in pressure minimum of 0.6wt%MWCNTs-PE-A is circa 2 MPa lower than that of the neat PE-A. This indicates a significant impact of MWCNTs on the flow criticalities of the window effect of linear polyethylene. In addition, without any sign of window broadening, the temperature window of 0.6wt%MWCNTs-PE-A shifts to a higher temperature (145°C).

In the contrast to the nanotubes, the 0.6wt% CB reinforced PE-A has the opposite effect on melt flow behaviour, see Figure 8.3. Compared to the neat polymer, PE-A, in the presence of the carbon black (a) the onset temperature of the extrusion window shifts to a lower temperature (b) and the drop in pressure is reduced. The contradicting observations between 0.6wt%CB-PE-A and 0.6wt%MWCNTs-PE-A, implies that the filler morphology has a significant impact on flow criticalities.

8.3 Discussion

8.3.1 The impact of the CB/MWCNTs on the extrusion window of PE-A

The extrusion window remains unaffected on addition of 0.2wt%CB or 0.2wt%MWCNTs into PE-A matrix. However, with further increase in the weight percentage of the nanofillers, from 0.2wt% to 0.6wt%, different aspect-ratio nanofillers have distinct impacts on the extrusion window. Regarding the window effect of the 0.6wt%MWCNTs-PE-A, it is found that, in Figure 8.2, the pressure minimum is circa 2MPa lower than that of neat PE-A or 0.2wt%MWCNTs-PE-A. The drop in pressure suggests a lower wall shear stress for the slip flow. According to Brochard and de Gennes' theory[41], the critical wall shear stress for stick-slip transition can be quantified as in the equation (1.26). The wall shear stress for slip flow is dependent on the adsorbed chain density ν and entanglement distance D^* at a given temperature. The adsorbed chain densities, ν, remain less unaffected on addition of the MWCNTs since there is a only small amount of MWCNTs present in the PE-A matrix. Therefore the lower wall shear stress for slip flow is attributed to the increasing entanglement distance with addition of 0.6wt%MWCNTs in the PE-A matrix. In fact, high-aspect-ratio MWCNTs with longer relaxation time can ease the alignment of molecular chains in the flow direction. Moreover, the presence of MWCNTs along the wall-melt interface can maintain the stretched chain conformation at higher temperature as shown in Figure 8.4. Hence, the aligned adsorbed chains attached to the nanotubes will possess less entanglement. Consequently, the effective entanglement distance of 0.6wt%MWCNTs-PE-A is greater than that in the neat PE-A, resulting in a deeper pressure drop observed in extrusion window.

On the other hand, CB, however, have an opposite effect on pressure minimum of the extrusion window, depicted in Figure 8.3. Spherical shaped CB can inhibit chain alignments as shown in Figure 8.5. At the molecular length scale the spherical shaped CB can induce the stretched polymer chain to coil back. As a consequence, presence of the CB can hinder the chain disengagement and maintain the entanglement density between the adsorbed chains and free chains, resulting in a higher critical shear stress for the onset of slip flow compared with the neat polymer, PE-A. The effect of CB on the extrusion window is referred to as 'bowling ball' effect.

Besides the distinct impact on the pressure minima, the presences of two different aspect-ratio nanofillers in PE-A matrix also has different effects on window temperature interval. According to the slip flow-hydrodynamic boundary conditions, SL - HBC , MWCNTs have potential to broaden the extrusion window since they can maintain the stretched chain conformation of agile PE chains at even higher temperature due to epitaxial growth of PE on MWCNTs[55,56]. In practice, it is found that the onset temperature, T_{onset} , of window effect increases from 144°C to 145°C on addition of the 0.6wt%MWCNTs in PE-A. However, it is also observed that the presence of the MWCNTs rises the termination temperature, T_{ter} , of the window effect. It implies that the presence of the MWCNTs may also cease the disentanglement of adsorbed chains from the free chains due to the increased melt viscosity at higher temperature compared to the neat polymer, PE-A. In summary, the MWCNTs can only shift the window to a higher temperature rather than broadening the extrusion window. In contrast, CB shows an opposite impact on window temperature interval. Due to the bowling ball effect, the unstable stretched chain conformation cannot be maintained in the presence of the spherical CB at high temperatures. Therefore, the addition of 0.6wt% CB decreases the T_{onset} of window effect. Consequently, considering an almost unchanged T_{ter} of 0.6wt% CB-PE-A, it is concluded that the spherical CB cannot broaden the extrusion window either.

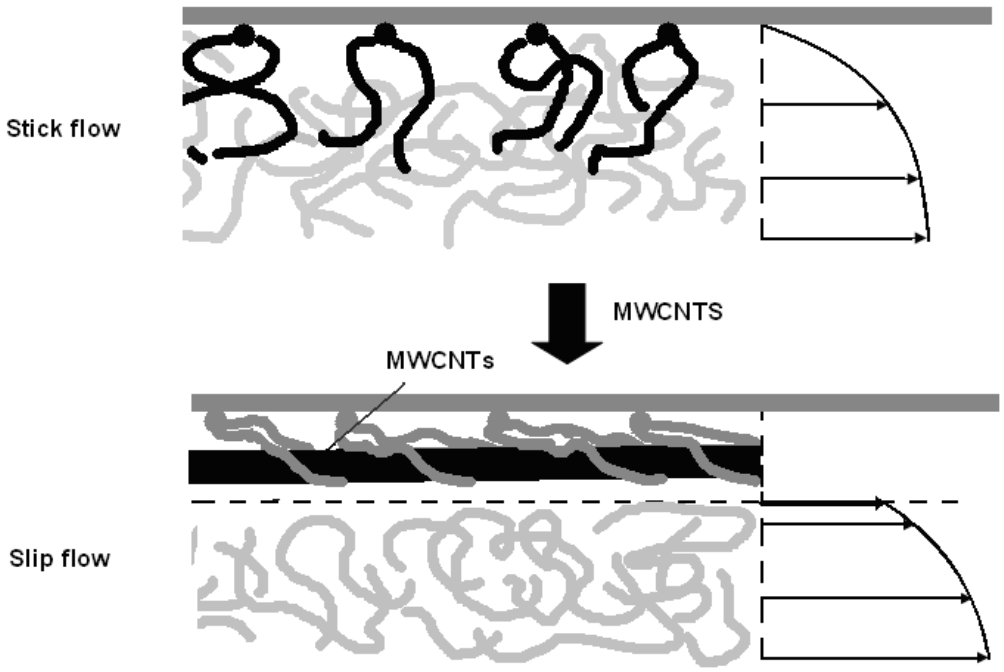

Figure 8.4: The effect of MWCNTs on the onset temperature of extrusion window. Compared to the neat polymer the presence of MWCNTs in polymer matrix promotes the chain alignment along the flow direction and maintains the stretched chain conformation at higher temperature, 145ºC, where the neat polymer does show window effect.

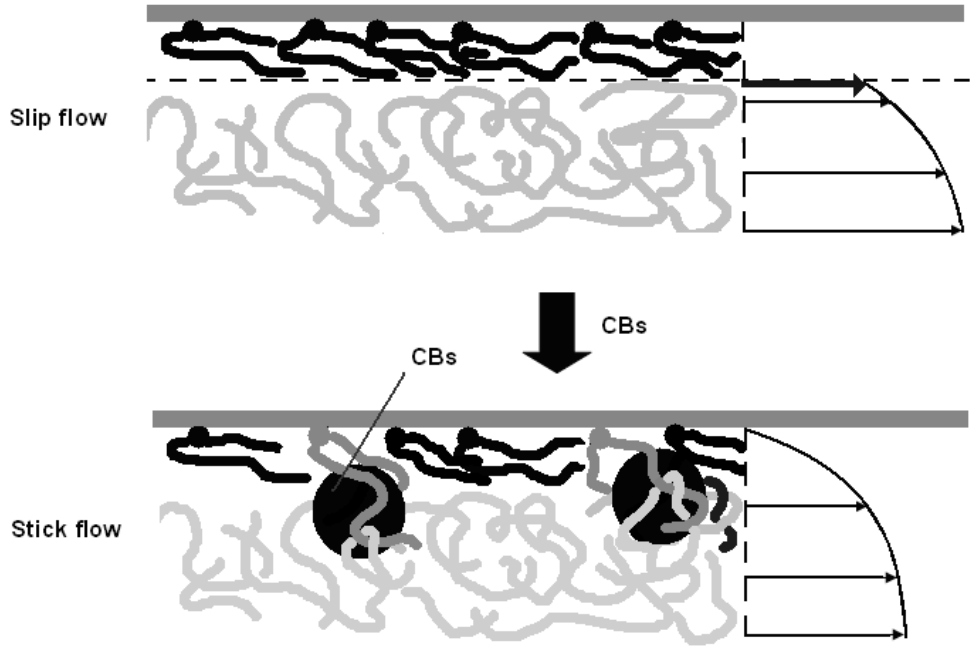

Figure 8.5: The effect of CBs on the onset temperature of extrusion window. In the presence of CBs the stretched chain conformation of some of the adsorbed chains, denoted by darker gray chains, cannot be maintained at 144ºC, the onset temperature of window effect for the neat polymer. Thus compared to the neat polymer, the orientation and adsorption is perturbed in the presence of CBs.

8.3.2 The effect of the CB/MWCNTs on flow induced solidification of PE-A

Regarding the effect of nanofillers on flow induced solidification, it is found that both T_s and crystallisation rate are enhanced on addition of CB and MWCNTs. As shown in Table 8.1, T_s increase with weight percentage of the two nanofillers and the effect of MWCNTs on T_s is more pronounced than that of CB. Due to the epitaxial growth of PEs on MWCNTs and CB [55,56], two carbon-based nanofillers can act as stable nucleus precursors to induce crystallisation. Therefore, under flow conditions the onset crystallisation temperatures in such heterogeneous systems are higher than homogeneous crystallisation. On the other hand, it is also found that extrusion pressure build-up rates for PE-nanocomposites are higher than that of PE-A as shown in Figure 8.1. It implies that both MWCNTs and CB can enhance the crystallisation rate. The effect is more pronounced in the present of MWCNTs.

Table 8.1 the onset temperature of flow induced solidification of PE-A and PE-nanocomposites at a constant apparent shear rate at 250s^{-1}.

Samples	T_s (°C)
PE-A	139.6
0.2wt%CB-PE-A	139.7
0.6wt%CB-PE-A	140.0
0.2wt%MWCNTs-PE-A	139.7
0.6wt%MWCNTs-PE-A	140.2

8.4 Conclusions

1) PE-A is an ideal reference sample to study the influence of carbon-based nanofillers on extrusion window since there is no interference of flow induced solidification ina narrow extrusion window region.
2) The extrusion window remains unaffected on addition of 0.2wt% CB or MWCNTs in a PE-A matrix.
3) MWCNTs can reduce the wall shear stress of window effect slip flow, resulting in a lower pressure minimum observed in extrusion window of 0.6wt% MWCNTs-PE-A. The lowered wall shear stress is attributed to the enlarged entanglement distances since MWCNTs can enhance chain alignment during capillary flow. Regarding the window temperature interval, it was found that MWCNTs cannot broaden the extrusion window but they can shift the window effect to a relatively higher temperature. High-aspect-ratio MWCNTs with longer relaxation time can

maintain the unstable stretched chain conformation at even higher temperature due to the epitaxial matching with PEs. Therefore, the T_{onset} increases to high temperature in the presence of MWCNTs. On the other hand, it was also observed that the disentanglement of tethered chain from free chains ceases at higher temperature, compared to the neat polymer, with the presence of MWCNTs. The increased T_{ter} is owing to the higher melt viscosity on addition of the MWCNTs.

4) Spherical CB with aspect ratio of one showed an opposite effect on extrusion window compared with MWCNTs. The presence of CB can induce the stretched chains to coil back due to the 'bowling ball' effect. Consequently, the entanglement distance between the adsorbed chains and free chains decreases, resulting in a higher wall shear stress observed in window effect slip flow compared with neat polymer. On the other hand, CB can also decrease T_{onset} since stretched chain conformation cannot be maintained in the presence of CB. In summary, CB decreases the pressure drop in the extrusion window and narrow the width of the window temperature interval.
5) Both MWCNTs and CB can enhance the T_s and crystallisation rate since the PEs can epitaxial growth on both nanofillers and these heterogeneous nucleus (CB and MWCNTs) are stable with increasing temperature.

Chapter 9 Conclusions and Future Work

In this thesis we addressed the molecular origin of the extrusion window of linear PE, and uncovered the hydrodynamic boundary condition for window effect. The extrusion window occurs at certain flow criticalities depending on molecular architecture. Some of the salient observations are summarised below.

1. Based on simple molecular weight dependence of flow criticalities the melt flow singularity observed in rate-controlled rheology can be linked with stick-slip transition theory that is based on stress controlled rheology. It is found that, even though the two effects emerge from two distinct rheological approaches, their molecular origin is the same; that is, slip flow occurs due to the disentanglement of tethered chains on the capillary wall from the free chains in the bulk. In detail the rescaled critical apparent shear rate, $a_T \dot{\gamma}_c^{w}$, corresponding to the onset of the window effect of a relatively narrow molar mass distributed linear PE (PDI<7) follows the power law relationship with molecular weight, that scales with -3.75±0.2. According to Wang's systematic study reported in the literature, the critical wall shear stress, σ_c, for stick-slip transition scales with -0.5 power of the molecular weight. Therefore, the two effects, extrusion window and stick-slip transition, can be linked with respective molecular weight dependence via a universal power law relationship between apparent viscosity and weight average molecular weight.

2. The hydrodynamic origin of the window effect can be elucidated by the window effect slip flow theory. At a critical apparent shear rate, polymer chains situated at wall-melt interface are tethered on the capillary wall. Subsequent to the chain attachment, the adsorbed chains are initially oriented along the flow direction. Since such a stretched chain conformation of adsorbed chains can be maintained at or above the critical apparent shear rate, free chains in the bulk can disentangle from the adsorbed chains resulting in window effect slip flow. The ex-situ WAXS results strengthen the window effect slip flow theory corresponding to a high surface energy die. To recall, the X-ray diffraction pattern of the extrudate obtained in the window effect slip flow conditions has less surface orientation compared to the polymer extruded at the lower shear rate, within the stick flow conditions. It implies that free

chains are extruded out of the capillary die after disentanglement from adsorbed chains and most of the adsorbed chains remain attached on the inner capillary wall. Moreover, the slip flow velocity experiments also verify that slip flow occurs in the extrusion window.

3. The revealed hydrodynamic origin of the extrusion window implies that the window effect occurs at a certain stretched chain conformation where the time required for disengagement of adsorbed chains from free chains should be shorter than the relaxation of the stretched chains. Therefore, at the same apparent shear rate high molecular weight linear PE should exhibit window effect at higher onset temperature compared to the low molecular weight linear PE. The experimental results coincide with theoretical prediction, viz. it was found that the onset temperature of window effect, T_{onset} ,increases with molecular weight. Whereas, the termination temperature of window effect, T_{ter} , shows dependence on two effects: (1) hindered disentanglement (2) flow induced solidification of the melt.

4. Bimodal PE, PE-B, showed a dual window effect at an apparent shear rate of $300s^{-1}$. According to molecular weight dependence of $\dot{\gamma}_c^{\,w}$ and σ_c , low molecular weight component, M_L , gives rise to the low temperature window and the high temperature window arise from the high molecular weight component, M_H .

5. An extraordinary broad extrusion window was observed in the capillary flow of a unimodal linear PE having high polydispersity, PDI=27.8. The molecular origin of such a broad extrusion window arises from this broad molecular weight distribution. The broad molar mass distributed polyethylene, PE-C, can be considered as PE blends with different molecular weight components where each molecular weight component has a characteristic window temperature. According to the dependence of window temperature and flow criticalities on the molecular weight, the low molecular weight components should have window effect at low temperature with higher pressure minimum, but by contrast the high molecular weight components have window effect at higher temperature and lower pressure minimum. The theoretical predications are in agreement with experimental observations, where multi-windows occur at the shear

rate of $40s^{-1}$ and the higher the window temperature the lower the pressure minimum. The corresponding multi windows temperature interval, from 150°C to 155°C, is referred to as window development regime. With further increasing the applied shear rate to $50s^{-1}$ multi windows merge into each other to form a broad extrusion window. Moreover, it was observed that the broadened extrusion window extends to higher temperature with applied shear rate. The enlarged extrusion window is due to the window broadening effect. The molecular origin of this effect is attributed to the window effect slip flow of the acting PE component($\sim 10^6$ g mol^{-1}) with assistance of ultra-high molecular weight PE, UHMWPE, components ($>10^6$ g mol^{-1}). Although UHMWPE is an intractable polymer, it can ease and maintain the alignment of long chains so that window effect slip flow can extend to even higher temperature. Looking back the highest temperature window (158°C) of PE-B occurring at $300s^{-1}$, the molecular origin of the third window is most likely to arise from the window effect slip flow of M_H with assistance of highest molecular weight component corresponding to the end tail of molecular weight distribution curve.

6. The hydrodynamic origin of the extrusion window is attributed to the window effect slip flow, which is situated in between pressure oscillation regime and helical distortion regime. The hydrodynamic boundary conditions (*HBC*) for window effect slip flow are governed by two critical apparent shear rates associated with the onset of window effect slip flow and helical distortion, $\dot{\gamma}_c^{\,w}$ and $\dot{\gamma}_c^{\,h}$ respectively. In addition, two flow criticalities shift to higher values with increasing temperature.

7. The hydrodynamic origin of stick-slip flow has been a less well understood rheological property of PE. In spurt flow neither the apparent shear rate nor the apparent shear stress is under control. In addition, it was found that two melt flow behaviours, viz. (1) discrete stick flow and (2) discrete slip flow, occur periodically during pressure oscillation. The hydrodynamic origin of the two flow behaviours are elucidated below:

1) Discrete stick flow: above the critical shear rate corresponding to the onset of pressure oscillation, $\dot{\gamma}_c^{\,p}$, stick flow cannot achieve an equilibrium flow condition. Consequently the applied flow rate Q_a, is greater than the real volumetric output rate,

Q. The differences between Q_a and Q, viz. Q_a-Q, lead to the increase in pressure. The resultant flow condition is referred to as discrete stick flow. Regarding the extrudate profiles obtained in the discrete stick flow, linear PE with different molar mass distribution showed distinct surface morphologies. For a narrow molar mass distributed linear polyethylene, reported in the Kolnaar's study, surface distortion was observed in the discrete stick flow. However, for a broad molar mass distributed or bimodal PE in this study smooth extrudate was attained in the discrete stick flow. This result coincides with Howells and Benbow[26(c)], that the higher polydispersity lowers the susceptibility to sharkskin.

2) Discrete slip flow: as mentioned above the extrusion pressure increases in the discrete stick flow. Once the resultant wall shear stress, σ_w, reaches the upper limit wall shear stress of pressure oscillation, σ_w^u, discrete slip flow occurs. Owing to discrete slip flow, the real volumetric output rate is much higher than the applied flow rate, viz. $Q > Q_a$. Consequently polymer decompression occurs accompanied with rapid pressure drop. The discrete slip flow falls into two categories: one is the discrete window effect slip flow; the other is the discrete helical distortion slip flow. A critical apparent wall shear stress, σ_c^h, draws a clean break between them. During the pressure drop in the discrete slip flow, if the $\sigma_w^u \geqslant \sigma_w \geqslant \sigma_c^h$, the discrete helical distortion slip flow occurs; whereas, if the $\sigma_c^h > \sigma_w \geqslant \sigma_w^l$, the discrete window effect slip flow emerges.

8. According to the window effect slip flow theory, multi-walled carbon nanotubes (MWCNTs) with relatively longer relaxation time have potential to maintain the stretched chain conformation at even higher temperature, resulting to shift the onset of the window effect to a higher temperature. In practice, the presence of 0.6wt% MWCNTs in PE-A matrix does increase the onset temperature of the window effect. However, it also raises the termination temperature. Finally, it fails to broaden the extrusion window. To study the influence of filler morphology on extrusion window, another carbon based nanofiller, carbon black (CB), was introduced into flow system of linear PE. It is found that the extrusion window is narrowed owing to the decrease

in the onset temperature of window effect on the addition of 0.6wt%CB in PE-A matrix. Consequently, neither MWCNTs nor CB can broaden the window effect.

In detail, the window effect of a linear polymer, PE-A, with relatively narrow molar mass distribution, PDI=3.7, remains unaffected on the addition of 0.2wt% CB or MWCNTs in PE-A matrix. However, on the addition of 0.6wt% CB or MWCNTs different aspect-ratio nanofillers showed distinct impacts on the extrusion window. With respect to 0.6wt%MWCNTs-PE-A, MWCNTs reduce the $\sigma_{\min} / T_{\min}$ for the window effect slip flow, resulting in a lower pressure minimum observed in extrusion window. The lowered rescaled wall shear stress arises from the enlarged entanglement distances between adsorbed chains and free chains since MWCNTs can enhance chain alignment during capillary flow. Regarding the window temperature interval, MWCNTs can shift the window effect to a relatively higher temperature, rather than broadening the extrusion window. High-aspect-ratio MWCNTs with longer relaxation time can maintain the stretched chain conformation at even higher temperature due to the epitaxial matching of PEs on MWCNTs. On the other hand, it was also observed that, in the presence of MWCNTs, the T_{ter} shifted to higher temperature owing to the increase in melt viscosity on the addition of the MWCNTs.

Spherical CB have an opposite influence on extrusion window compared with MWCNTs. The presence of CB can induce the stretched chains to coil back due to the bowling ball effect. As a consequence, the entanglement distance of the adsorbed chains decreases, resulting in a higher wall shear stress for slip flow occurring in extrusion window compared with neat polymer. On the other hand, CB can also decrease T_{onset} since the stretched chain conformation cannot be maintained due to the Brownian motion of CB. In summary, CB minimise the pressure drop in the extrusion window and narrow the window temperature interval.

In the flow induced solidification region, Both CB and MWCNTs enhance the onset temperature of flow induced solidification, T_s, and crystallisation rate. This strongly supports the epitaxial matching of PE on both nanofillers (CB and MWCNTs).

9. Regarding the effect of various die geometries on flow criticalities of extrusion window of bimodal PE and unimodal PE with broad molecular weight distribution, it was found that the melt flow singularity is attributed to capillary flow since convergent flow cannot give rise to window effect. Secondly, the window effect is independent of capillary length. Finally, it is proven that the $\dot{\gamma}_c^{\ w}$ remains unaffected by die entry angle, suggesting the elongational flow has no effect on flow criticalities of the extrusion window. However, there is a low temperature anomaly for low temperature window of PE-B. It suggests that the pre-stretched long chain, M_H, occurring during elongational flow may assist the low molar mass polymer chains to attain the stretched chain conformation. Moreover it also indicates that such a pre-stretched chain conformation can only be maintained and has effect on extrusion window at low temperature, <150°C.

In this thesis the objective of broadening the extrusion window has been achieved, i.e. such a broad extrusion window is found in the rate-controlled capillary flow of a unimodal linear PE with broad molecular weight distribution (PDI~27). Some future work may be suggested:

a) Broad extrusion window opens a gate to energy efficient processing of linear PE. It has all the advantages of narrow extrusion window and also overcomes a challenge with regard to temperature fluctuation during industry processing. A systematic study on industrial scale application is recommended, viz. a continuous processing test via industrial scale extruder is suggested.

b) It was found that an intractable UHMWPE could be processed by a conventional route with assistance of short chains. However, it requests a systematic study to find out an ideal 'recipe', viz. the loading of short chains and its M_w and MWD.

c) PE resins processed in extrusion window possess less orientation on the surface, resulting in poor mechanical properties. Therefore post-drawing is essential to enhance the orientation to improve the mechanical properties of the final products, such as cling films or fibres. In summary, the window effect can offer a route to

process PE with less energy cost and post drawing can compensate the ‘side effect‘ of extrusion window and enhance the mechanical properties of final products. The ideal post drawing speed and temperature needs further investigation. In addition, according to current knowledge of post drawing, the ideal post drawing temperature should be higher than, but close to, the melting point. This means that the post drawing may be applicable, just following up the extrusion at window temperature, since the window temperature is more close to the solidification temperature compared to the conventional processing temperature.

d) According to hydrodynamic origin of window effect, extrusion window may exist in the other polymers. Therefore, melt flow singularities of other thermoplastics should be studied in future.

References

[1] PlasticsEurope, *The compelling facts about plastics: an analysis of plastics production, demand and recovery for 2006 in Europe*, **2008**.

[2] Fawcett, E. W.; Gibson, R. Q.; Perrin, M. H.; Patton J. G.; Williams E. G. *Brit. Pat. 2816883*, **1937** (Imperial Chemical Industries).

[3] Ziegler, K. *Belgium Patent 533*, **1955**.

[4] Natta, G.; Pino, P.; Corradini, P.; Danusso, F.; Mantica, E.; Mazzanti, G.; Moraglio, G. *J. Am. Chem. Soc.* **1955**, 77, 1708.

[5] (a) Li, S.; Burstein, A.H. *J. Bone Joint Surg.* **1994**, 76A, 1080.
(b) Kurtz, S. M.; Muratoglu, O.K.; Evans, M.; Edidin, A.A. *Biomaterials* **1999**, 20, 1659.

[6] (a) Smith, P.; Lemstra, P.J. *UK Patent 2051661*, **1979**.
(b) Smith, P.; Lemstra, P.J. *Makrom. Chem.* **1979**, 180, 2983.

[7] Cahn, R.W.; Haasen, P.; Kramer, E.J. *Processing of Polymers*, VCH: Weinheim, **1997**.

[8] (a) de Gennes, *J. Chem. Phys.* **1971**, 55, 572.
(b) Dealy, J. M.; Larson, R. G. *Structure and Rheology of Molten Polymers*. Hanser Gardner Pubns: Cincinnati, **2006**.
(c) Rubinstein, M.; Colby, R. H. *Polymer Physics*. Oxford University Press: **2003**.
(d) de Gennes, P. J. *Scaling concepts in polymer physics*. Cornell University Press:Ithaca, NY, **1979**.
(e)Doi, M.; Edwards, S. F. *The theory of polymer dynamics*. Clarendon Press: Oxford,**1986**.

[9] (a) Smith, P.; Lemstra, P.J.; Booij, H.C. *J. Polym. Sci., Phys.* **1982**, 20, 2229.
(b) Smith, P.; Lemstra, P.J. *J. Mater. Sci*. **1980**, 15, 505.

[10] van der Vegt, A. K.; Smit, P.P. A. *Adv. Polym. Sci. Technol. Soc. Chem. Ind.* **1967**, 26, 313.

[11] (a) Devaux, N.; Monasse, B.; Haudin, J. M.; Moldenaers, P.; Vermant, J. *Rheol. Acta* **2004**, 43, 210.
(b) Heeley, E. L.; Maidens, A. V.; Olmsted, P. D.; Bras, W.; Dolbnya, I. P.; Fairclough, J. P. A.; Terril, N. J.; Ryan, A. J. *Macromolecules* **2003**, 36, 3656.
(c) Kumaraswamy, G.; Issaian, A. M.; Kornfield, J. A. *Macromolecules* **1999**, 32, 7537.
(d) McHugh, A. *J. Polym. Eng. Sci*. **1982**, 22, 15.
(e) Muthukumar, M. *Adv. chem. Phy*.**2004**, 128.

[12] (a) Pennings, J.; Kiel , A. M. Kolloid-Z. Z. *Polym*. **1965**, 205, 160.
(b) Binsbergen, F. L. *Nature* **1966**, 211, 516.
(c) Hill, M. J.; Barham, P. J.; Keller, A. *Coll. & Polym. Sci.* **1980**, 258, 1023.

[13] Brydson, J. A. *Flow Properties of Polymer Melts* 2nd ed., George Godwin Limited, London, **1995**.

[14] Cook, J. A.; Gilbert, M. Presented at Third International PRI Conference PVC, 87, Brighton, **1987**.

[15] Skelland, A. H. P. *Non-Newtonian Flow and Heat Transfer*, Wiley-VCH, NY, **1961**.

[16] Reiner, M. *Deformation, Fracture and Flow*; H. K. Lewis, **1960**.

[17] (a) Sutera, S. P.; Skalak, R. *The history of Poiseuille's law*, Annual Review of Fluid Mechanics, **1993**.
(b)Whorlow, R. W. *Rheology Techniques*; Ellis Horwood, **1979**.

[18] Macosko, C. W. *Rheology:principles, measurements, and applications*; Wiley-VCH,USA, **1994**.

[19] Bagley, E. B. *J. Appl. phy*. **1957**, 28, 624.

[20] Cogswell, F. N. *Polymer Melt Rheology, a guide for industry practice*; Woodhead, Cambridge, England, **1994**.

[21] (a) Arai, T.; Aoyama, H. *Trans. Soc. Rheo.***1963,** 7, 333.
(b) Bagley, E. B.; Duffey, H. J. *Trans. Soc. Rheo*.**1970,** 14, 545.
(c) Bagley, E. B.; Storey, S. H.; West, D. C. *J. Appl. Polym. Sci*., **1963**, 7, 1661.
(d) Beynon, D. L. T.; Glyde, B.S. *British Plastics*, **1960,** 33, 414.
(e) Han, C. D.; Kim, K. U. *Polym. Eng. Sci.*, **1971**, 11, 395.
(f) Locati, G. Rheologica Acta, **1976**, 15,525.
(g) Metzger, A. P.; Matlack, J. D. *Polym. Eng. Sci.*, **1968**, 8, 10.
(h) Nakajima, N.; Shida, M. *Trans. Soc. Rheo.*, **1966**, 10, 299.
(j) Rogers, M. G. *J. Appl. Polym. Sci.* **1970**, 14, 1679.
(k) Tanner, R. I. *J. Appl. Polym. Sci.* **1970**, 8, 2067.
(l) Metzger, A. P.; Matlack, J. D. *Polym. Eng. Sci.* **1968**, 8, 110.

[22] Lodge, A. S. *Elastic Liquids*; Academic Press, London, **1964**.

[23] Nason, H. K. *J. Appl. Phy.* **1945**, 16, 338.

[24] (a) Tordella, J. P. *J. Appl. Phy*.**1956**, 27, 454.
(b) Tordella, J. P. *Trans. Soc. Rheo.* **1957**, 1, 203.
(c) Tordella, J. P. *Rheologica Acta* **1958**, 1, 216.
(d) Tordella, J. P. *J. Appl. Polym. Sci.*. **1963**, 7, 215.
(e) Tordella, J. P. *Trans. Soc. Rheo.* **1963**, 7, 231.

[25] (a) Bagley, E. B.; Cabott, I. M. *J. Appl. Phy*. **1958**, 29, 109.
(b) Bagley, E. B.; Birks, A. M. *J. Appl. Phy*. **1960**, 31, 556.
(c) Bagley, E. B.; Schreiber, H. P. *Trans. Soc. Rheo.*, **1961**, 5, 341.

[26] (a) Spencer, R. S.; Dillon, R. E. *J. Coll. Sci*.**1948**, 3, 163.
(b) Spencer, R. S.; Dillon, R. E. *J. Coll. Sci*. **1949**, 4, 214.
(c) Howells. E. R.; Benbow, J. J. *Trans. o plast. Instit*. **1962**, 30, 240.
(d) Vinogradov, G. V.; Ivanova, L. I. *Rheologica Acta* **1967**, 6, 209.
(e) Vinogradov, G. V.; Ivanova, L. I. *Rheologica Acta* **1968**, 7, 243.
(f) Benbow, J. J.; Lamb, P. *Soc. Plast. Eng. Trans.* **1963**, 3, 7.
(g) Clegg, P. L. *Rheology of Elastomers*, Pergamon, London, **1958**.
(h) Cogswell, F. N.; Lamb, P. *Trans. plast. Instit*. **1967**, 35, 803.
(i) Cogswell, F. N. *Plast. And Polym*. **1973**, 41, 39.
(j) Howells, E. R.; Benbow, J. J., *Trans. plast. Instit*. **1962**, 30, 240.
(k) Hanson, D. E. *Polym. Eng. Sci.*, **1969**, 9, 405.

[27] (a) Kalika, D. S.; Denn, M. M. *J. Rheol*. **1987**, 31,815.
(b)Ramamurthy, A. V. *J. Rheol*. **1986**, 30, 337.

[28] (a) Drda, P. P.; Wang, S. Q. *Phys. Rev. Lett*. **1995**, 75, 2698.
(b) Brochard, F.; de Gennes, P. G. *Langmuir* **1992**, 8, 3033.

[29] Agassant, J. F. *Polymer processing: principles and modelling*; Hanser Publishers, NY **1991.**

[30] (a) Waddon, A. J.; Keller, A. *J. Polym. Sci.* **1990**, 28, 1063.
(b) Narh, K. A.; Keller, A. *Polymer*, **1991**, 32, 2512.
(c) Narh, K. A.; Keller, A. *J. Mater. Sci.* **1991**, 10 ,1301.
(d)Waddon, A. J.; Keller, A. *J. Polym. Sci.* Polym. Phy. **1992**, 30, 923.

[31] (a) Kolnaar, J. W. H.; Keller, A. *Polymer* **1994**, 35, 3863.
(b) Kolnaar, J. W. H.; Keller, A. *Polymer* **1995**, 36, 821.
(c) Kolnaar, J. W. H.; Keller, A. *Polymer* **1997**, 38, 1817.

[32] A. K. van der Vegt; P. P. A. ,Smith, *Polym. Sci. Technol. Soc. Chem. Ind.* **1967**, 26, 313.

[33] Kolnaar, J. W. H.; Keller, A.; Seifert, S.; Zschunke, C.; Zachmann, H.G. *Polymer* **1995**, 36, 3969.

[34] van Bilsen, H. M. M.; Fischer, H.; Kolnaar, J. W. H.; Keller, A. *Macromolecules* **1995**; 28, 8523.

[35] (a) Pennings, A.J.; Zwijnenburg, A. *J. Polym. Sci.* Polym. Phy. **1979**, 17, 1011.
(b) van Aerle, N.A.J.M.; Lemstra, P.J.; Braam, A.W.M. *Polym. Commun.*. **1989**, 30, 7.
(c) Rastogi, S.; Odell, J.A. *Polym. Commun.* **1993**, 34,1523.

[36] (a) Clough, S.B. *Polym. Lett.* **1970**, 8, 519.
(b) Clough, S.B. *J. Macro. Sci. p. B* **1970**, 4,199.
(c) Hikmet, R.M.; Lemstra, P.J. ; Keller, A. *Coll. Polym. Sci.* **1987,** 265 , 185.

[37] Kolnaar, J. W. H. Ph.D. Thesis, University of Bristol, **1987.**

[38] (a)Rudin, A.; Chang, R.-J. *J. Appl. Polym. Sci*. **1978**, 22, 781.
(b)Kataoka, T.; Ueda, Sh. *Rheologica Acta* **1971**, 10, 446.

[39] (a)Wang, S.-Q.; Drda, P. A. *Macromolecules* **1996**, 29, 2627.
(b)Wang, S.-Q.; Drda, P. A. *Macromolecules* **1996**, 29, 4115.
(c)Wang, S.-Q.; Drda, P. A. *Rheol. Acta* **1997**, 36, 128.

[40] Hill, D. A.; Denn, M.; Salmeron, M. Q. *Chem.Eng. Sci.* **1994**, 49, 655.

[41] Brochard, F.; de Gennes, P. G. *Langmuir* **1992**, 8, 3033.

[42] de Gennes P. G., *Scaling Concepts in Polymer Physics*; Cornell University Press, Ithaca, NY, **1979**.

[43] (a)Berry, G. C.; Fox. T. G. *Adv. Polym. Sci.* **1968**, 5, 261.
(b)Colby, R. H.; Fetters, L. J.; Graessley, W. W. *Macromolecules* **1987**, 20, 2226.

[44] Fox, T.G.; Flory, P. J. *J. Phys. Coll. Chem.* **1951**, 55, 221.

[45] (a)Bersted, B. H. *J. Appl. Polym. Sc*i. **1975**,19, 2167.
(b)Bersted, B. H.; Slee, J. D. *J. Appl. Polym. Sc*i. **1977**,21, 2631.
(c)Colby, R.H.; Fetters, L.J.; Graessley, W.W. *Macromolecules*, **1987**, 20, 2226.
(d)Malkin, A. Y.; Teishev, A. E. *Polym. Eng. Sci.* **1991**, 31, 1590.
(e)Tuminello, W. H. *Polym. Eng. Sci.* **1991**, 31, 1496.
(f)Nichetti, D.; Manas-Zloczower I., *J. Rheo.* **1998**, 42, 951.

[46] (a)Doi, M.; Edwards, S.F. *The Theory of Polymer Dynamics*; Clarendon Oxford, **1986**.
(b)Rubinstein M.; Colby R.H. *J. Chem. Phys.* **1988**, 89, 5291.
(c)des Cloizeaux J. *Europhys. Lett.* **1998**, 5, 417.
(d)Tsenoglou C. *J. Polym. Sci. Polym. Phy.* **1988**, 26, 2329.

[47] (a)Marrucci, G. *J. Polym. Sci.* **1985**,23, 159.
(b)Rubinstein, M.; Helfand, E.; Pearson, D.S. *Macromolecules*, **1987**, 20, 822.
(c)van Ruymbeke, E.; Keunings, R.; Stéphenne, V. Hagenaars, A.; Bailly C. *Macromolecules* **2002**, 35, 2689.
(d)van Ruymbeke, E.; Keunings, R.; Bailly, C. *J. Non-Newtonian Fluid Mech.* **2002**, 105, 153.

[48] (a) Mead, D. W. *J. Rheo.* **1994**, 38, 1739.
(b) Mead, D. W. *J. Rheo.* **1994**, 38, 1797.

[49] Carreau, P.J.; de Kee, D. C.R.; Chhabra, R.P. *Rheology of Polymeric Systems, Principles and Applications;* Hanser, Munich, Vienna, NY, **1997**.

[50] (a) Keller, A.; Odell, J. A. *J. Polym. Sci., Polym. Syrup.* **1978**, 63, 155.
(b) Odell, J. A.; Grubb, D. T.; Keller, A. *Polymer* **1978**, 19, 617.
(c) Bashir, Z.; Odell, J. A.; Keller, A. *J. Mater. Sci.* **1984**,19, 3713.
(d) Bashir, Z., Odell, J. A. and Keller, A. *J. Mater. Sci.* **1986**, 21, 3993.
(e) Bashir, Z.; Keller, A. *Coll. Polym. Sci.* **1989**, 267, 116.

[51] Bird, R. B.; Armstrong, R. C.; Hassager, O. *Dynamics of Polymeric Liquids*, Wiley Interscience, NY, **1987**.

[52] Haggenmueller, R.; Fischer, J. E.; Winey, K. I. *Macromolecules* **2006**, 39, 2964.

[53] Wilchinsky, Z. W. *J. Appl. Phys*.**1960**, 31, 1969.

[54] (a)Petrie, C. J. S.; Denn, M. M. AIChE J. **1976**, 22, 209.
(b)Pearson, J. R. A. *Mechanics of Polymer Processing*; Elsevier: London, **1985**.
(c) Lupton, J. M.; Regester, R. W. *Polym. Eng. Sci.* **1965**, 5, 235.
(d) Denn, M. M. *Annu. Rev. Fluid Mech.* **1990**, 22, 13.
(e) Hatzikiriakos, S. G.; Dealy, J. M. *J. Rheol.* **1992**, 36, 845.

[55] (a)Zhang, Q.; Lippits, D.R.; Rastogi, S. *Macromolecules* **2006**, 39, 658.
(b)Zhang, Q.; Rastogi, S.; Chen, D.; Lippits, D.R.; Lemstra, P.J. *Carbon* **2006**, 44, 778.
(c) Vega, J. F.; Martinez-Salazar, J. *Macromolecules* **2009**, 42, 4719.
(d) Jain, S.; Goossens, J. G. P.; Peters, G. W. M.; Lemstra, P.J. *Softmatter* **2008**, 4, 1848.

[56] (a) Li, C. Y.; Li, L. Y.; Cai, W.; Kodjie, S. L.; Tenneti, K. K. *Adv. Mater.* **2005**,17,1198.
(b) Li, L. Y.; Yang, Y.; Yang, G. L.; Chen, X. *Nano Letter* **2006**, 6 , 1007.

[57] Patil, N.; Balzano, L.; Portale, G.; Rastogi, S., 'a study on the interaction and aspect ratio of nanoparticles on structure development of a linear polymer.' *Macromolecules* (due to be published)

Appendices

Appendix A. Material data sheet

a) PE-A and PE-C are confidential products supplied by SABIC Europe.

b) PE-B is a commercial polymer, BS2581, supplied by Borealis.

24.04.2008 Ed.8

Polyethylene

BS2581

High Density Polyethylene for Blow Moulding

Description

BS2581 is a high density polyethylene intended for blow moulding products with high stiffness and very good environmental stress crack resistance (ESCR)

Applications

Industrial chemicals
Household and chemical containers such as detergents, cleaners, motor oils

Bottles and containers up to 10 litres

Special features

Good stress crack resistance
High stiffness

Physical Properties

Property	Typical Value Data should not be used for specification work	Test Method
Density	958 kg/m3	ISO 1183
Melt Flow Rate (190 °C/2,16 kg)	0,3 g/10min	ISO 1133
Melt Flow Rate (190 °C/5 kg)	1,3 g/10min	ISO 1133
Melt Flow Rate (190 °C/21,6 kg)	28 g/10min	ISO 1133
Flexural Modulus (1 mm/min)	1.400 MPa	ISO 178
Tensile Modulus (1 mm/min)	1.300 MPa	ISO 527-2
Tensile Strain at Yield (50 mm/min)	8 %	ISO 527-2
Tensile Stress at Yield (50 mm/min)	29 MPa	ISO 527-2
Heat Deflection Temperature (0,45 MPa)	80 °C	ISO 75-2
Environmental Stress Crack Resistance (Antarox 10 %), (F50),	100 h	ASTM D 1693-A
Hardness, Shore D	65	ISO 868

Processing Techniques

Following parameters should be used as guidelines:

BS2581 is easy to extrude and can be used in all conventional blow-moulding machines

Barrel	170 - 190 °C
Die	175 - 190 °C
Melt temperature	170 - 200 °C

Borealis AG | Wagramerstrasse 17-19 | 1220 Vienna | Austria
Telephone +43 1 224 00 0 | Fax +43 1 22 400 333
FN 269858a | CCC Commercial Court of Vienna | Website www.borealisgroup.com

BOREALIS

Page 1 of 2

Polyethylene
BS2581

Storage
BS2581 should be stored in dry conditions at temperatures below 50 °C and protected from UV-light. Improper storage can initiate degradation, which results in odour generation and colour changes and can have negative effects on the physical properties of this product.

Safety
The product is not classified as a dangerous preparation.

Recycling
The product is suitable for recycling using modern methods of shredding and cleaning. In-house production waste should be kept clean to facilitate direct recycling.

Please see our Safety Data Sheet for details on various aspects of safety, recovery and disposal of the product, for more information contact your Borealis representative.

Related Documents
The following related documents are available on request, and represent various aspects on the usability, safety, recovery and disposal of the product.

Safety Data Sheet
Statement on compliance to food contact regulations

Disclaimer

The product(s) mentioned herein are not intended to be used for medical, pharmaceutical or healthcare applications and we do not support their use for such applications.

To the best of our knowledge, the information contained herein is accurate and reliable as of the date of publication, however we do not assume any liability whatsoever for the accuracy and completeness of such information.

Borealis makes no warranties which extend beyond the description contained herein. Nothing herein shall constitute any warranty of merchantability or fitness for a particular purpose.

It is the customer's responsibility to inspect and test our products in order to satisfy itself as to the suitability of the products for the customer's particular purpose. The customer is responsible for the appropriate, safe and legal use, processing and handling of our products.

No liability can be accepted in respect of the use of Borealis' products in conjunction with other materials. The information contained herein relates exclusively to our products when not used in conjunction with any third party materials.

Borealis AG | Wagramerstrasse 17-19 | 1220 Vienna | Austria
Telephone +43 1 224 00 0 | Fax +43 1 22 400 333
FN 269858a | CCC Commercial Court of Vienna | Website www.borealisgroup.com

Appendix B. ARES plate-plate rheometer data

Table a: dynamic strain sweep results of PE-A

γ (%)	*G′ (Pa)*	*G″ (Pa)*	*tan (δ)*
0.134	1.74E+05	1.38E+05	0.789
0.240	1.75E+05	1.32E+05	0.755
0.424	1.79E+05	1.32E+05	0.741
0.776	1.80E+05	1.33E+05	0.738
1.341	1.80E+05	1.31E+05	0.728
2.201	1.80E+05	1.30E+05	0.722
3.568	1.80E+05	1.30E+05	0.718
5.733	1.80E+05	1.29E+05	0.715
9.160	1.80E+05	1.29E+05	0.714

Table b: dynamic strain sweep results of PE-C

γ (%)	*G′ (Pa)*	*G″ (Pa)*	*Tan (δ)*
0.161	2.34E+05	1.17E+05	0.501
0.264	2.36E+05	1.14E+05	0.483
0.433	2.38E+05	1.15E+05	0.484
0.692	2.38E+05	1.16E+05	0.485
1.093	2.38E+05	1.15E+05	0.483
1.717	2.38E+05	1.14E+05	0.481
2.705	2.38E+05	1.14E+05	0.480
4.268	2.38E+05	1.14E+05	0.479
6.735	2.38E+05	1.14E+05	0.479

Table c: dynamic frequency sweep results of PE-A

ω (rad/s)	*G′ (Pa)*	*G″ (Pa)*	*tan (δ)*	*η* (Pa s)*
500.000	1.806E+05	1.296E+05	0.718	4.445E+02
315.479	1.492E+05	1.342E+05	0.900	6.360E+02
199.054	1.087E+05	1.183E+05	1.088	8.071E+02
125.594	7.695E+04	9.772E+04	1.270	9.903E+02
79.245	5.301E+04	7.783E+04	1.468	1.188E+03
50.000	3.544E+04	6.027E+04	1.700	1.398E+03
31.548	2.298E+04	4.545E+04	1.978	1.614E+03
19.905	1.446E+04	3.339E+04	2.309	1.828E+03
12.559	8.854E+03	2.398E+04	2.708	2.035E+03
7.924	5.265E+03	1.685E+04	3.200	2.228E+03
5.000	3.059E+03	1.163E+04	3.801	2.405E+03
3.155	1.741E+03	7.905E+03	4.541	2.566E+03
1.991	9.727E+02	5.296E+03	5.445	2.705E+03
1.256	5.329E+02	3.508E+03	6.583	2.825E+03
0.792	2.912E+02	2.303E+03	7.908	2.929E+03
0.500	1.565E+02	1.499E+03	9.576	3.015E+03

Table d. dynamic frequency sweep results of PE-C

ω *(rad/s)*	*G′* *(Pa)*	*G″* *(Pa)*	*tan* *(δ)*	*η** *(Pa s)*
100.000	2.386E+05	1.142E+05	0.479	2.645E+03
63.096	2.052E+05	1.058E+05	0.515	3.659E+03
39.811	1.751E+05	9.655E+04	0.551	5.022E+03
25.119	1.481E+05	8.710E+04	0.588	6.838E+03
15.849	1.241E+05	7.765E+04	0.626	9.235E+03
10.000	1.031E+05	6.849E+04	0.665	1.237E+04
6.310	8.488E+04	5.972E+04	0.704	1.645E+04
3.981	6.931E+04	5.154E+04	0.744	2.170E+04
2.512	5.614E+04	4.404E+04	0.785	2.840E+04
1.585	4.511E+04	3.728E+04	0.826	3.692E+04
1.000	3.594E+04	3.127E+04	0.870	4.764E+04
0.631	2.838E+04	2.599E+04	0.916	6.100E+04
0.398	2.226E+04	2.142E+04	0.962	7.759E+04
0.251	1.731E+04	1.751E+04	1.011	9.801E+04
0.158	1.338E+04	1.420E+04	1.061	1.231E+05
0.100	1.029E+04	1.140E+04	1.109	1.536E+05
0.063	7.858E+03	9.096E+03	1.158	1.905E+05
0.040	5.979E+03	7.226E+03	1.209	2.356E+05
0.025	4.539E+03	5.690E+03	1.254	2.898E+05
0.016	3.452E+03	4.460E+03	1.292	3.559E+05
0.010	2.611E+03	3.471E+03	1.329	4.343E+05
0.006	1.970E+03	2.691E+03	1.366	5.285E+05
0.004	1.495E+03	2.081E+03	1.392	6.436E+05
0.003	1.133E+03	1.607E+03	1.419	7.827E+05
0.002	8.546E+02	1.237E+03	1.448	9.487E+05
0.001	6.437E+02	9.523E+02	1.479	1.149E+06

Appendix C. Capillary rheology data

a) Extrusion pressure vs. Temperature

One typical example of capillary rheology data is shown below. Due to the massive amount of data points, only one example of capillary rheology results, i.e. dynamic temperature sweep of PE-A at $300s^{-1}$, is depicted here.

Table e. dynamic temperature sweep results of PE-A at the apparent shear rate of $300s^{-1}$

Sample No.	*T (°C)*	*P (MPa)*	*Sample No.*	*T (°C)*	*P (MPa)*	*Sample No.*	*T (°C)*	*P (MPa)*
1	152.01	15.42	417	146.06	12.09	833	140.29	17.19
2	152.01	15.46	418	145.98	12.23	834	140.29	17.19
3	152.01	15.46	419	145.98	12.33	835	140.29	17.19
4	152.01	15.46	420	145.98	12.46	836	140.29	17.19
5	152.01	15.46	421	145.98	12.56	837	140.23	17.19
6	151.93	15.46	422	145.98	12.66	838	140.23	17.22
7	151.93	15.46	423	145.9	12.76	839	140.23	17.22
8	151.93	15.46	424	145.9	12.86	840	140.23	17.26
9	151.93	15.46	425	145.9	13.03	841	140.23	17.26
10	151.93	15.46	426	145.9	13.13	842	140.23	17.26
11	151.93	15.46	427	145.9	13.29	843	140.23	17.22
12	151.84	15.46	428	145.9	13.39	844	140.14	17.26
13	151.84	15.46	429	145.81	13.46	845	140.14	17.26
14	151.84	15.46	430	145.81	13.59	846	140.14	17.29
15	151.84	15.46	431	145.81	13.66	847	140.14	17.29
16	151.84	15.46	432	145.81	13.73	848	140.14	17.29
17	151.75	15.46	433	145.81	13.79	849	140.14	17.29
18	151.75	15.46	434	145.81	13.83	850	140.14	17.29
19	151.75	15.46	435	145.71	13.93	851	140.06	17.29
20	151.75	15.46	436	145.71	13.96	852	140.06	17.32
21	151.75	15.46	437	145.71	13.96	853	140.06	17.32
22	151.75	15.49	438	145.71	13.99	854	140.06	17.32
23	151.67	15.49	439	145.71	13.99	855	140.06	17.32
24	151.67	15.49	440	145.71	13.99	856	140.06	17.32
25	151.67	15.49	441	145.64	13.89	857	139.98	17.36
26	151.67	15.49	442	145.64	13.79	858	139.98	17.36
27	151.67	15.49	443	145.64	13.69	859	139.98	17.36
28	151.67	15.49	444	145.64	13.56	860	139.98	17.39
29	151.58	15.49	445	145.64	13.36	861	139.98	17.39
30	151.58	15.49	446	145.64	13.19	862	139.98	17.39
31	151.58	15.49	447	145.64	12.99	863	139.9	17.39
32	151.58	15.49	448	145.56	12.69	864	139.9	17.42
33	151.58	15.52	449	145.56	12.36	865	139.9	17.42
34	151.58	15.52	450	145.56	12.26	866	139.9	17.46
35	151.58	15.52	451	145.56	12.19	867	139.9	17.46
36	151.48	15.52	452	145.56	12.16	868	139.9	17.46
37	151.48	15.52	453	145.48	12.09	869	139.83	17.46

38	151.48	15.52	454	145.48	12.09	870	139.83	17.46
39	151.48	15.52	455	145.48	12.16	871	139.83	17.46
40	151.48	15.52	456	145.48	12.19	872	139.83	17.49
41	151.48	15.52	457	145.48	12.29	873	139.83	17.52
42	151.48	15.52	458	145.48	12.33	874	139.75	17.52
43	151.4	15.52	459	145.48	12.36	875	139.75	17.52
44	151.4	15.52	460	145.39	12.53	876	139.75	17.52
45	151.4	15.52	461	145.39	12.63	877	139.75	17.52
46	151.4	15.52	462	145.39	12.69	878	139.75	17.56
47	151.4	15.52	463	145.39	12.76	879	139.75	17.56
48	151.4	15.52	464	145.39	12.83	880	139.66	17.56
49	151.3	15.52	465	145.39	12.86	881	139.66	17.56
50	151.3	15.52	466	145.3	12.93	882	139.66	17.59
51	151.3	15.52	467	145.3	12.96	883	139.66	17.59
52	151.3	15.52	468	145.3	13.06	884	139.66	17.62
53	151.3	15.56	469	145.3	13.13	885	139.66	17.62
54	151.3	15.56	470	145.22	13.16	886	139.66	17.62
55	151.3	15.56	471	145.22	13.19	887	139.58	17.62
56	151.21	15.56	472	145.22	13.19	888	139.58	17.62
57	151.21	15.56	473	145.22	13.26	889	139.58	17.66
58	151.21	15.56	474	145.22	13.26	890	139.58	17.66
59	151.21	15.56	475	145.22	13.29	891	139.58	17.66
60	151.21	15.56	476	145.13	13.33	892	139.58	17.66
61	151.11	15.56	477	145.13	13.33	893	139.58	17.66
62	151.11	15.56	478	145.13	13.36	894	139.5	17.69
63	151.11	15.56	479	145.13	13.36	895	139.5	17.72
64	151.11	15.56	480	145.13	13.36	896	139.5	17.72
65	151.11	15.59	481	145.13	13.36	897	139.5	17.72
66	151.11	15.56	482	145.13	13.33	898	139.5	17.72
67	151.11	15.56	483	145.05	13.29	899	139.5	17.72
68	151.02	15.59	484	145.05	13.26	900	139.42	17.72
69	151.02	15.59	485	145.05	13.23	901	139.42	17.72
70	151.02	15.59	486	145.05	13.19	902	139.42	17.76
71	151.02	15.59	487	145.05	13.13	903	139.42	17.76
72	151.02	15.59	488	145.05	13.09	904	139.42	17.79
73	151.02	15.59	489	145.05	13.06	905	139.42	17.79
74	150.93	15.59	490	145.05	13.03	906	139.35	17.79
75	150.93	15.59	491	144.96	12.96	907	139.35	17.82
76	150.93	15.59	492	144.96	12.93	908	139.35	17.82
77	150.93	15.59	493	144.96	12.89	909	139.35	17.82
78	150.93	15.59	494	144.96	12.86	910	139.35	17.82
79	150.93	15.59	495	144.96	12.86	911	139.35	17.82
80	150.93	15.59	496	144.88	12.83	912	139.35	17.86
81	150.93	15.59	497	144.88	12.83	913	139.26	17.86
82	150.86	15.59	498	144.88	12.79	914	139.26	17.86
83	150.86	15.59	499	144.88	12.79	915	139.26	17.86
84	150.86	15.59	500	144.88	12.79	916	139.26	17.92
85	150.86	15.59	501	144.88	12.79	917	139.26	17.96
86	150.86	15.59	502	144.79	12.79	918	139.26	17.96
87	150.76	15.59	503	144.79	12.79	919	139.2	17.96

88	150.76	15.62	504	144.79	12.79	920	139.2	17.96
89	150.76	15.62	505	144.79	12.83	921	139.2	17.99
90	150.76	15.62	506	144.79	12.83	922	139.2	17.99
91	150.76	15.62	507	144.79	12.86	923	139.2	17.99
92	150.76	15.62	508	144.79	12.86	924	139.11	18.02
93	150.67	15.62	509	144.7	12.86	925	139.11	18.02
94	150.67	15.62	510	144.7	12.86	926	139.11	18.02
95	150.67	15.62	511	144.7	12.86	927	139.11	18.02
96	150.67	15.62	512	144.7	12.86	928	139.11	18.06
97	150.67	15.62	513	144.62	12.89	929	139.11	18.06
98	150.67	15.62	514	144.62	12.89	930	139.03	18.06
99	150.57	15.62	515	144.62	12.89	931	139.03	18.06
100	150.57	15.62	516	144.62	12.89	932	139.03	18.09
101	150.57	15.66	517	144.62	12.89	933	139.03	18.12
102	150.57	15.66	518	144.62	12.89	934	139.03	18.12
103	150.57	15.66	519	144.53	12.89	935	139.03	18.12
104	150.57	15.66	520	144.53	12.89	936	139.03	18.12
105	150.48	15.66	521	144.53	12.89	937	138.96	18.16
106	150.48	15.66	522	144.53	12.89	938	138.96	18.16
107	150.48	15.66	523	144.53	12.89	939	138.96	18.16
108	150.48	15.66	524	144.53	12.89	940	138.96	18.16
109	150.48	15.66	525	144.53	12.89	941	138.96	18.19
110	150.48	15.66	526	144.46	12.89	942	138.96	18.19
111	150.41	15.66	527	144.46	12.86	943	138.87	18.19
112	150.41	15.66	528	144.46	12.86	944	138.87	18.22
113	150.41	15.66	529	144.46	12.86	945	138.87	18.22
114	150.41	15.66	530	144.46	12.86	946	138.87	18.22
115	150.41	15.69	531	144.46	12.86	947	138.87	18.26
116	150.41	15.69	532	144.46	12.86	948	138.87	18.26
117	150.31	15.69	533	144.37	12.86	949	138.81	18.29
118	150.31	15.69	534	144.37	12.86	950	138.81	18.29
119	150.31	15.69	535	144.37	12.86	951	138.81	18.32
120	150.31	15.69	536	144.37	12.86	952	138.81	18.36
121	150.31	15.69	537	144.37	12.86	953	138.81	18.39
122	150.31	15.69	538	144.37	12.86	954	138.72	18.39
123	150.31	15.69	539	144.28	12.89	955	138.72	18.42
124	150.31	15.69	540	144.28	12.89	956	138.72	18.42
125	150.21	15.69	541	144.28	12.89	957	138.72	18.46
126	150.21	15.69	542	144.28	12.89	958	138.72	18.52
127	150.21	15.69	543	144.28	12.89	959	138.72	18.52
128	150.21	15.69	544	144.28	12.89	960	138.64	18.56
129	150.21	15.69	545	144.19	12.89	961	138.64	18.56
130	150.21	15.69	546	144.19	12.89	962	138.64	18.59
131	150.14	15.69	547	144.19	12.89	963	138.64	18.59
132	150.14	15.69	548	144.19	12.89	964	138.64	18.59
133	150.14	15.69	549	144.19	12.89	965	138.56	18.66
134	150.14	15.69	550	144.19	12.89	966	138.56	18.66
135	150.14	15.69	551	144.11	12.93	967	138.56	18.66
136	150.14	15.69	552	144.11	12.93	968	138.56	18.66
137	150.05	15.69	553	144.11	12.96	969	138.56	18.66

138	150.05	15.69	554	144.11	12.96	970	138.56	18.66
139	150.05	15.72	555	144.11	12.96	971	138.56	18.69
140	150.05	15.72	556	144.11	12.96	972	138.56	18.69
141	150.05	15.72	557	144.03	12.96	973	138.49	18.72
142	150.05	15.72	558	144.03	12.96	974	138.49	18.72
143	149.95	15.72	559	144.03	12.96	975	138.49	18.76
144	149.95	15.72	560	144.03	12.96	976	138.49	18.76
145	149.95	15.72	561	144.03	12.96	977	138.49	18.79
146	149.95	15.72	562	143.96	12.96	978	138.49	18.79
147	149.95	15.72	563	143.96	12.96	979	138.41	18.79
148	149.86	15.72	564	143.96	12.96	980	138.41	18.79
149	149.86	15.72	565	143.96	12.96	981	138.41	18.82
150	149.86	15.72	566	143.96	12.96	982	138.41	18.82
151	149.86	15.72	567	143.96	12.96	983	138.41	18.86
152	149.86	15.72	568	143.96	12.96	984	138.41	18.89
153	149.86	15.72	569	143.96	12.96	985	138.33	18.89
154	149.77	15.72	570	143.86	12.96	986	138.33	18.92
155	149.77	15.72	571	143.86	12.96	987	138.33	18.92
156	149.77	15.72	572	143.86	12.96	988	138.33	18.92
157	149.77	15.72	573	143.86	12.96	989	138.33	18.92
158	149.77	15.72	574	143.86	12.96	990	138.33	18.96
159	149.77	15.72	575	143.86	12.96	991	138.33	18.96
160	149.77	15.72	576	143.86	12.96	992	138.25	18.96
161	149.69	15.72	577	143.78	12.99	993	138.25	18.99
162	149.69	15.76	578	143.78	12.99	994	138.25	19.06
163	149.69	15.76	579	143.78	12.99	995	138.25	19.06
164	149.69	15.76	580	143.78	13.03	996	138.25	19.09
165	149.69	15.76	581	143.78	13.03	997	138.18	19.12
166	149.69	15.76	582	143.69	13.03	998	138.18	19.12
167	149.69	15.76	583	143.69	13.03	999	138.18	19.16
168	149.59	15.76	584	143.69	13.03	1000	138.18	19.16
169	149.59	15.76	585	143.69	13.03	1001	138.18	19.19
170	149.59	15.76	586	143.69	13.03	1002	138.1	19.22
171	149.59	15.76	587	143.62	13.03	1003	138.1	19.22
172	149.59	15.76	588	143.62	13.03	1004	138.1	19.22
173	149.59	15.76	589	143.62	13.03	1005	138.1	19.26
174	149.59	15.76	590	143.62	13.03	1006	138.1	19.29
175	149.58	15.76	591	143.62	13.03	1007	138.1	19.29
176	149.58	15.76	592	143.54	13.03	1008	138.1	19.29
177	149.58	15.76	593	143.54	13.03	1009	138.02	19.32
178	149.58	15.76	594	143.54	13.03	1010	138.02	19.36
179	149.58	15.76	595	143.54	13.03	1011	138.02	19.36
180	149.46	15.76	596	143.54	13.06	1012	138.02	19.39
181	149.46	15.76	597	143.54	13.06	1013	138.02	19.39
182	149.46	15.76	598	143.44	13.09	1014	138.02	19.39
183	149.46	15.76	599	143.44	13.09	1015	138.02	19.42
184	149.46	15.76	600	143.44	13.09	1016	137.95	19.46
185	149.46	15.76	601	143.44	13.13	1017	137.95	19.46
186	149.46	15.76	602	143.44	13.13	1018	137.95	19.46
187	149.28	15.76	603	143.44	13.13	1019	137.95	19.46

188	149.28	15.76	604	143.44	13.16	1020	137.95	19.49
189	149.28	15.76	605	143.37	13.16	1021	137.95	19.52
190	149.28	15.79	606	143.37	13.16	1022	137.87	19.52
191	149.28	15.79	607	143.37	13.19	1023	137.87	19.56
192	148.98	15.79	608	143.37	13.19	1024	137.87	19.56
193	148.98	15.79	609	143.37	13.19	1025	137.87	19.59
194	148.98	15.79	610	143.37	13.19	1026	137.87	19.62
195	148.98	15.79	611	143.37	13.19	1027	137.87	19.62
196	148.98	15.79	612	143.27	13.23	1028	137.78	19.62
197	148.98	15.79	613	143.27	13.23	1029	137.78	19.66
198	148.98	15.79	614	143.27	13.23	1030	137.78	19.69
199	148.96	15.79	615	143.27	13.26	1031	137.78	19.69
200	148.96	15.79	616	143.2	13.26	1032	137.78	19.72
201	148.96	15.79	617	143.2	13.29	1033	137.78	19.72
202	148.96	15.79	618	143.2	13.29	1034	137.78	19.76
203	148.96	15.79	619	143.2	13.29	1035	137.7	19.76
204	148.96	15.79	620	143.2	13.29	1036	137.7	19.76
205	149.07	15.79	621	143.2	13.29	1037	137.7	19.79
206	149.07	15.76	622	143.2	13.29	1038	137.7	19.82
207	149.07	15.79	623	142.95	13.33	1039	137.7	19.85
208	149.07	15.79	624	142.95	13.33	1040	137.63	19.89
209	149.07	15.79	625	142.95	13.33	1041	137.63	19.92
210	149.07	15.79	626	142.95	13.39	1042	137.63	19.92
211	149.07	15.79	627	142.95	13.39	1043	137.63	19.92
212	148.98	15.82	628	143.11	13.36	1044	137.63	19.92
213	148.98	15.79	629	143.11	13.39	1045	137.63	19.99
214	148.98	15.79	630	143.11	13.43	1046	137.58	20.02
215	148.98	15.79	631	143.11	13.43	1047	137.58	20.05
216	148.98	15.79	632	143.11	13.43	1048	137.58	20.05
217	148.98	15.79	633	143.11	13.43	1049	137.58	20.09
218	148.87	15.79	634	142.95	13.43	1050	137.58	20.12
219	148.87	15.82	635	142.95	13.43	1051	137.58	20.12
220	148.87	15.82	636	142.95	13.46	1052	137.58	20.15
221	148.87	15.82	637	142.95	13.46	1053	137.5	20.15
222	148.87	15.82	638	142.95	13.46	1054	137.5	20.19
223	148.87	15.82	639	142.95	13.46	1055	137.5	20.19
224	148.78	15.82	640	142.94	13.46	1056	137.5	20.22
225	148.78	15.82	641	142.94	13.49	1057	137.5	20.25
226	148.78	15.82	642	142.94	13.49	1058	137.5	20.25
227	148.78	15.82	643	142.94	13.49	1059	137.42	20.29
228	148.78	15.82	644	142.94	13.49	1060	137.42	20.32
229	148.72	15.82	645	142.94	13.53	1061	137.42	20.35
230	148.72	15.82	646	142.81	13.53	1062	137.42	20.39
231	148.72	15.82	647	142.81	13.53	1063	137.42	20.42
232	148.72	15.82	648	142.81	13.56	1064	137.42	20.42
233	148.72	15.82	649	142.81	13.56	1065	137.33	20.45
234	148.59	15.82	650	142.81	13.56	1066	137.33	20.45
235	148.59	15.82	651	142.81	13.56	1067	137.33	20.49
236	148.59	15.82	652	142.81	13.59	1068	137.33	20.49
237	148.59	15.82	653	142.71	13.59	1069	137.33	20.52

238	148.59	15.82	654	142.71	13.59	1070	137.33	20.55
239	148.59	15.82	655	142.71	13.59	1071	137.33	20.55
240	148.52	15.82	656	142.71	13.63	1072	137.24	20.59
241	148.52	15.82	657	142.71	13.63	1073	137.24	20.65
242	148.52	15.82	658	142.71	13.66	1074	137.24	20.69
243	148.52	15.82	659	142.63	13.66	1075	137.24	20.72
244	148.52	15.82	660	142.63	13.66	1076	137.24	20.75
245	148.52	15.82	661	142.63	13.69	1077	137.18	20.75
246	148.52	15.82	662	142.63	13.73	1078	137.18	20.79
247	148.52	15.82	663	142.63	13.73	1079	137.18	20.79
248	148.42	15.82	664	142.63	13.79	1080	137.18	20.82
249	148.42	15.82	665	142.54	13.79	1081	137.18	20.85
250	148.42	15.86	666	142.54	13.79	1082	137.18	20.85
251	148.42	15.86	667	142.54	13.83	1083	137.1	20.95
252	148.42	15.86	668	142.54	13.86	1084	137.1	21.02
253	148.42	15.86	669	142.54	13.89	1085	137.1	21.02
254	148.42	15.86	670	142.47	13.89	1086	137.1	21.02
255	148.32	15.86	671	142.47	13.89	1087	137.1	21.05
256	148.32	15.86	672	142.47	13.89	1088	137.03	21.09
257	148.32	15.86	673	142.47	13.93	1089	137.03	21.15
258	148.32	15.86	674	142.47	13.93	1090	137.03	21.15
259	148.32	15.86	675	142.47	13.96	1091	137.03	21.19
260	148.24	15.86	676	142.37	13.96	1092	137.03	21.19
261	148.24	15.86	677	142.37	13.99	1093	137.03	21.22
262	148.24	15.86	678	142.37	14.03	1094	137.03	21.25
263	148.24	15.86	679	142.37	14.03	1095	136.94	21.29
264	148.24	15.86	680	142.37	14.03	1096	136.94	21.29
265	148.24	15.89	681	142.37	14.03	1097	136.94	21.35
266	148.24	15.89	682	142.31	14.09	1098	136.94	21.35
267	148.15	15.89	683	142.31	14.09	1099	136.94	21.39
268	148.15	15.89	684	142.31	14.09	1100	136.94	21.39
269	148.15	15.89	685	142.31	14.13	1101	136.87	21.42
270	148.15	15.89	686	142.31	14.13	1102	136.87	21.45
271	148.15	15.86	687	142.23	14.19	1103	136.87	21.45
272	148.15	15.86	688	142.23	14.22	1104	136.87	21.55
273	148.15	15.86	689	142.23	14.26	1105	136.87	21.55
274	148.05	15.86	690	142.23	14.29	1106	136.87	21.59
275	148.05	15.86	691	142.23	14.32	1107	136.79	21.62
276	148.05	15.86	692	142.23	14.36	1108	136.79	21.65
277	148.05	15.86	693	142.23	14.39	1109	136.79	21.65
278	148.05	15.86	694	142.15	14.42	1110	136.79	21.72
279	147.97	15.86	695	142.15	14.42	1111	136.79	21.75
280	147.97	15.86	696	142.15	14.49	1112	136.79	21.82
281	147.97	15.86	697	142.15	14.52	1113	136.71	21.85
282	147.97	15.86	698	142.15	14.56	1114	136.71	21.85
283	147.97	15.86	699	142.15	14.59	1115	136.71	21.89
284	147.97	15.89	700	142.07	14.59	1116	136.71	21.95
285	147.88	15.89	701	142.07	14.66	1117	136.71	21.95
286	147.88	15.89	702	142.07	14.69	1118	136.71	21.99
287	147.88	15.89	703	142.07	14.69	1119	136.63	22.05

288	147.88	15.89	704	142.07	14.72	1120	136.63	22.05
289	147.88	15.89	705	142.07	14.72	1121	136.63	22.09
290	147.88	15.89	706	141.99	14.76	1122	136.63	22.09
291	147.79	15.89	707	141.99	14.76	1123	136.63	22.12
292	147.79	15.89	708	141.99	14.76	1124	136.63	22.12
293	147.79	15.89	709	141.99	14.79	1125	136.55	22.19
294	147.79	15.89	710	141.99	14.79	1126	136.55	22.22
295	147.79	15.89	711	141.99	14.82	1127	136.55	22.22
296	147.79	15.89	712	141.99	14.82	1128	136.55	22.22
297	147.79	15.89	713	141.91	14.82	1129	136.55	22.25
298	147.71	15.89	714	141.91	14.86	1130	136.55	22.25
299	147.71	15.89	715	141.91	14.86	1131	136.48	22.29
300	147.71	15.89	716	141.91	14.86	1132	136.48	22.32
301	147.71	15.89	717	141.91	14.86	1133	136.48	22.32
302	147.71	15.89	718	141.83	14.89	1134	136.48	22.32
303	147.71	15.89	719	141.83	14.89	1135	136.48	22.39
304	147.62	15.89	720	141.83	14.92	1136	136.48	22.39
305	147.62	15.89	721	141.83	14.92	1137	136.48	22.39
306	147.62	15.89	722	141.83	14.96	1138	136.39	22.39
307	147.62	15.89	723	141.83	14.96	1139	136.39	22.42
308	147.62	15.89	724	141.74	14.99	1140	136.39	22.45
309	147.54	15.92	725	141.74	14.99	1141	136.39	22.52
310	147.54	15.89	726	141.74	14.99	1142	136.39	22.52
311	147.54	15.82	727	141.74	15.02	1143	136.39	22.52
312	147.54	15.79	728	141.74	15.02	1144	136.32	22.55
313	147.54	15.76	729	141.74	15.06	1145	136.32	22.62
314	147.54	15.69	730	141.68	15.06	1146	136.32	22.62
315	147.45	15.69	731	141.68	15.09	1147	136.32	22.65
316	147.45	15.69	732	141.68	15.12	1148	136.32	22.69
317	147.45	15.66	733	141.68	15.16	1149	136.32	22.72
318	147.45	15.59	734	141.68	15.19	1150	136.32	22.75
319	147.45	15.56	735	141.68	15.22	1151	136.24	22.79
320	147.36	15.46	736	141.58	15.22	1152	136.24	22.82
321	147.36	15.42	737	141.58	15.32	1153	136.24	22.82
322	147.36	15.39	738	141.58	15.32	1154	136.24	22.85
323	147.36	15.36	739	141.58	15.36	1155	136.24	22.85
324	147.36	15.29	740	141.58	15.42	1156	136.24	22.95
325	147.36	15.09	741	141.58	15.46	1157	136.17	22.95
326	147.28	14.96	742	141.5	15.49	1158	136.17	22.95
327	147.28	14.92	743	141.5	15.56	1159	136.17	22.95
328	147.28	14.92	744	141.5	15.59	1160	136.17	23.02
329	147.28	14.92	745	141.5	15.66	1161	136.17	23.05
330	147.28	14.92	746	141.5	15.66	1162	136.17	23.09
331	147.28	14.92	747	141.5	15.69	1163	136.09	23.12
332	147.19	14.96	748	141.43	15.72	1164	136.09	23.15
333	147.19	15.02	749	141.43	15.76	1165	136.09	23.19
334	147.19	15.06	750	141.43	15.79	1166	136.09	23.22
335	147.19	15.06	751	141.43	15.82	1167	136.09	23.22
336	147.19	15.06	752	141.43	15.86	1168	136.09	23.25
337	147.19	15.06	753	141.43	15.89	1169	136.01	23.29

338	147.19	15.06	754	141.43	15.92	1170	136.01	23.32
339	147.09	15.02	755	141.35	15.99	1171	136.01	23.35
340	147.09	15.02	756	141.35	15.99	1172	136.01	23.39
341	147.09	15.02	757	141.35	16.06	1173	136.01	23.42
342	147.09	15.02	758	141.35	16.09	1174	136.01	23.45
343	147.09	15.06	759	141.35	16.16	1175	135.93	23.52
344	147.09	15.06	760	141.35	16.19	1176	135.93	23.55
345	147.03	15.06	761	141.35	16.29	1177	135.93	23.62
346	147.03	15.06	762	141.26	16.29	1178	135.93	23.65
347	147.03	15.06	763	141.26	16.32	1179	135.93	23.65
348	147.03	15.06	764	141.26	16.36	1180	135.93	23.69
349	147.03	15.02	765	141.26	16.42	1181	135.93	23.72
350	147.03	14.99	766	141.26	16.46	1182	135.85	23.75
351	146.93	14.99	767	141.18	16.52	1183	135.85	23.75
352	146.93	14.99	768	141.18	16.56	1184	135.85	23.82
353	146.93	14.96	769	141.18	16.56	1185	135.85	23.82
354	146.93	14.96	770	141.18	16.59	1186	135.85	23.89
355	146.93	14.92	771	141.18	16.62	1187	135.78	23.89
356	146.93	14.89	772	141.11	16.66	1188	135.78	23.92
357	146.84	14.79	773	141.11	16.69	1189	135.78	23.92
358	146.84	14.69	774	141.11	16.69	1190	135.78	23.99
359	146.84	14.49	775	141.11	16.72	1191	135.78	23.99
360	146.84	14.36	776	141.11	16.76	1192	135.78	24.02
361	146.84	14.16	777	141.11	16.76	1193	135.69	24.05
362	146.84	13.89	778	141.03	16.76	1194	135.69	24.09
363	146.75	13.66	779	141.03	16.76	1195	135.69	24.09
364	146.75	13.39	780	141.03	16.79	1196	135.69	24.12
365	146.75	13.26	781	141.03	16.79	1197	135.69	24.15
366	146.75	13.16	782	141.03	16.79	1198	135.69	24.22
367	146.75	13.06	783	141.03	16.82	1199	135.69	24.22
368	146.68	12.93	784	140.95	16.86	1200	135.63	24.25
369	146.68	12.93	785	140.95	16.86	1201	135.63	24.25
370	146.68	12.96	786	140.95	16.86	1202	135.63	24.32
371	146.68	13.03	787	140.95	16.86	1203	135.63	24.32
372	146.68	13.06	788	140.95	16.86	1204	135.63	24.35
373	146.68	13.09	789	140.86	16.89	1205	135.63	24.39
374	146.59	13.19	790	140.86	16.89	1206	135.63	24.42
375	146.59	13.33	791	140.86	16.89	1207	135.56	24.45
376	146.59	13.39	792	140.86	16.89	1208	135.56	24.49
377	146.59	13.56	793	140.86	16.92	1209	135.56	24.49
378	146.59	13.66	794	140.86	16.92	1210	135.56	24.52
379	146.59	13.76	795	140.78	16.92	1211	135.56	24.52
380	146.59	13.89	796	140.78	16.92	1212	135.56	24.55
381	146.51	14.03	797	140.78	16.92	1213	135.56	24.59
382	146.51	14.13	798	140.78	16.92	1214	135.49	24.65
383	146.51	14.36	799	140.78	16.92	1215	135.49	24.69
384	146.51	14.46	800	140.78	16.96	1216	135.49	24.69
385	146.51	14.56	801	140.78	16.96	1217	135.49	24.72
386	146.51	14.72	802	140.7	16.99	1218	135.49	24.75
387	146.41	14.79	803	140.7	16.99	1219	135.41	24.79

388	146.41	14.86	804	140.7	16.99	1220	135.41	24.82
389	146.41	14.96	805	140.7	16.99	1221	135.41	24.85
390	146.41	15.06	806	140.7	16.99	1222	135.41	24.92
391	146.41	15.12	807	140.7	16.99	1223	135.41	24.92
392	146.41	15.22	808	140.63	16.99	1224	135.33	24.95
393	146.32	15.29	809	140.63	17.02	1225	135.33	24.95
394	146.32	15.36	810	140.63	17.02	1226	135.33	25.05
395	146.32	15.39	811	140.63	17.02	1227	135.33	25.05
396	146.32	15.46	812	140.63	17.02	1228	135.33	25.09
397	146.32	15.49	813	140.54	17.06	1229	135.33	25.15
398	146.32	15.52	814	140.54	17.06	1230	135.33	25.19
399	146.32	15.59	815	140.54	17.06	1231	135.25	25.22
400	146.26	15.62	816	140.54	17.06	1232	135.25	25.22
401	146.26	15.66	817	140.54	17.09	1233	135.25	25.29
402	146.26	15.66	818	140.54	17.09	1234	135.25	25.35
403	146.26	15.59	819	140.46	17.09	1235	135.25	25.42
404	146.26	15.09	820	140.46	17.09	1236	135.25	25.49
405	146.26	14.49	821	140.46	17.09	1237	135.17	25.52
406	146.06	13.43	822	140.46	17.09	1238	135.17	25.55
407	146.06	12.79	823	140.46	17.12	1239	135.17	25.62
408	146.06	12.49	824	140.46	17.12	1240	135.17	25.62
409	146.06	12.29	825	140.46	17.12	1241	135.17	25.68
410	146.06	12.13	826	140.15	17.16	1242	135.17	25.72
411	146.06	11.89	827	140.15	17.16	1243	135.14	25.75
412	146.06	11.86	828	140.15	17.16	1244	135.14	25.75
413	146.06	11.86	829	140.15	17.16	1245	135.14	25.78
414	146.06	11.93	830	140.15	17.16	1246	135.14	25.82
415	146.06	11.99	831	140.29	17.16	1247	135.14	25.85
416	146.06	12.03	832	140.29	17.19	1248	135.14	25.85

b) Die swell ratio

The die swell ratios were measured and compared at different extrusion temperatures, but at the same apparent shear rate, during the isothermal step rate capillary flow.

Table f: Die swell ratios of PE-B at an apparent shear rate of 150s^{-1} as a function of extrusion temperature

***T* (°C)**	***Dc* (mm)**	***De* (mm)**	***De/Dc* (mm)**
140.0	1	3.568	3.568
141.0	1	3.102	3.102
143.0	1	2.125	2.125
144.0	1	1.748	1.748
145.0	1	1.658	1.658
145.5	1	1.643	1.643
146.0	1	1.639	1.639
146.5	1	1.656	1.656
147.0	1	1.723	1.723

Table g: Die swell ratios of PE-B at an apparent shear rate of $300s^{-1}$ as a function of extrusion temperature

T (°C)	*Dc (mm)*	*De (mm)*	*De/Dc*
144.0	1	2.202	2.202
144.0	1	2.202	2.202
145.0	1	1.958	1.958
145.5	1	1.885	1.885
146.0	1	1.840	1.840
146.5	1	1.834	1.834
147.0	1	1.830	1.830
147.5	1	1.896	1.896
148.0	1	1.786	1.786
149.0	1	1.694	1.694
150.0	1	1.648	1.648
151.0	1	1.621	1.621
152.0	1	1.572	1.572
153.0	1	1.691	1.691
154.0	1	1.756	1.756
155.0	1	1.724	1.724
156.0	1	1.702	1.702
157.0	1	1.685	1.685
158.0	1	1.668	1.668

Table h: Die swell ratios of PE-C at an apparent shear rate of $8s^{-1}$ as a function of extrusion temperature

T (°C)	*Dc (mm)*	*De (mm)*	*De/Dc*
142	1	2.00	2.00
144	1	1.70	1.70
146	1	1.50	1.5
147	1	1.44	1.44
148	1	1.40	1.40
150	1	1.34	1.34
152	1	1.30	1.30
154	1	1.30	1.30
156	1	1.30	1.30
158	1	1.30	1.30
160	1	1.30	1.30

Table i: Die swell ratios of PE-C at an apparent shear rate of $10s^{-1}$ as a function of extrusion temperature

T (°C)	*Dc (mm)*	*De (mm)*	*De/Dc*
142	1	2.30	2.30
144	1	1.95	1.95
145	1	1.79	1.79

146	1	1.65	1.65
147	1	1.55	1.55
148	1	1.50	1.50
149	1	1.45	1.45
150	1	1.40	1.40
151	1	1.41	1.41
152	1	1.45	1.45
154	1	1.40	1.40
156	1	1.40	1.40
158	1	1.40	1.40
160	1	1.40	1.40

c) Slip flow velocity measurement

Slip flow velocities were determined in the isothermal mono-rate time sweep experiments. A series of capillary dies with a constant L/R ratio, but different 1/R, was used to determine the slip flow velocity. For each given die an apparent shear rate corresponding to a given shear stress was recorded. Following that the recorded apparent shear rates for different 1/R dies were plotted against the 1/R. Finally the slope of the plot of the apparent shear rate vs. 1/R is equal to $4V_s$.

Table j: Apparent shear rates of PE-B at 146ºC corresponding to a fixed shear stress for different 1/R dies with a constant L/R ratio

R	*1/R*	$\dot{\gamma}_a^1(\sigma_w=0.148)$	$\dot{\gamma}_a^2(\sigma_w=0.167)$	$\dot{\gamma}_a^3(\sigma_w=0.151)$	$\dot{\gamma}_a^4(\sigma_w=0.157)$	$\dot{\gamma}_a^5(\sigma_w=0.164)$
1.00	2.00	30	41	195	236	280
1.15	1.74	31	40	173	211	253
1.30	1.54	29	40	156	191	232
1.50	1.33	29	39	140	173	210

Table k: Apparent shear rates of PE-B at 152 ºC corresponding to a fixed shear stress for different 1/R dies with a constant L/R ratio

R	*1/R*	$\dot{\gamma}_a^1(\sigma_w=0.093)$	$\dot{\gamma}_a^2(\sigma_w=0.123)$	$\dot{\gamma}_a^3(\sigma_w=0.170)$	$\dot{\gamma}_a^4(\sigma_w=0.181)$	$\dot{\gamma}_a^5(\sigma_w=0.192)$
1.00	2.00	20	40	520	626	740
1.15	1.74	21	39	482	574	695
1.30	1.54	19	37	445	536	645
1.50	1.33	18	36	400	495	600

Table l: Apparent shear rates of PE-C at 150 ºC corresponding to a fixed shear stress for different 1/R dies with a constant L/R ratio

R	*1/R*	$\dot{\gamma}_a^1$ *(*σ_w *=0.140)*	$\dot{\gamma}_a^2$ *(*σ_w *=0.180)*	$\dot{\gamma}_a^3$ *(*σ_w *=0.200)*	$\dot{\gamma}_a^4$ *(*σ_w *=0.220)*
1.00	2.00	8	74	104	168
1.15	1.74	9	62	85	135
1.30	1.54	8	50	72	112
1.50	1.33	8	40	61	92

Table m: Apparent shear rates of PE-C at 155ºC corresponding to a fixed shear stress for different 1/R dies with a constant L/R ratio

R	*1/R*	$\dot{\gamma}_a^1$ *(*σ_w *=0.130)*	$\dot{\gamma}_a^2$ *(*σ_w *=0.170)*	$\dot{\gamma}_a^3$ *(*σ_w *=0.220)*	$\dot{\gamma}_a^4$ *(*σ_w *=0.250)*
1.00	2.00	35	161	320	400
1.15	1.74	34	138	300	365
1.30	1.54	34	119	275	345
1.50	1.33	34	100	250	322

Appendix D. Herman's Orientation factors

Some x-ray diffraction data, i.e. diffraction intensities of (110) plane at different azimuthal angles, is shown in Table n. The tested sample, PE-B, was extruded at a shear rate of $50s^{-1}$ at 150 ºC.

Table n: X-ray diffraction intensities (I) at different azimuthal angles (A_z) corresponding to the diffraction of (110) plane

A_z (°)	I (a.u.)	A_z (°)	I (a.u.)	A_z (°)	I (a.u.)	A_z (°)	I (a.u.)
0.50	197.61	90.50	224.66	180.50	197.61	270.50	243.04
1.50	202.83	91.50	230.90	181.50	202.83	271.50	240.60
2.50	191.67	92.50	227.58	182.50	191.67	272.50	228.58
3.50	182.73	93.50	236.41	183.50	182.73	273.50	232.41
4.50	190.00	94.50	239.03	184.50	190.00	274.50	239.25
5.50	197.25	95.50	243.36	185.50	197.25	275.50	244.63
6.50	188.47	96.50	251.26	186.50	188.47	276.50	245.77
7.50	188.66	97.50	240.53	187.50	188.66	277.50	240.86
8.50	188.34	98.50	260.66	188.50	188.34	278.50	249.03
9.50	190.76	99.50	246.46	189.50	190.76	279.50	245.40
10.50	189.17	100.50	245.86	190.50	189.17	280.50	247.93
11.50	192.38	101.50	254.90	191.50	192.38	281.50	242.47
12.50	199.22	102.50	250.88	192.50	199.22	282.50	248.19
13.50	190.33	103.50	251.39	193.50	190.33	283.50	252.88
14.50	188.33	104.50	253.42	194.50	188.33	284.50	260.91
15.50	188.94	105.50	249.36	195.50	188.94	285.50	250.71
16.50	189.96	106.50	259.08	196.50	189.96	286.50	255.53
17.50	190.58	107.50	261.96	197.50	190.58	287.50	250.95
18.50	187.67	108.50	271.60	198.50	187.67	288.50	259.00
19.50	190.58	109.50	279.60	199.50	190.58	289.50	261.26
20.50	193.52	110.50	274.63	200.50	193.52	290.50	255.64
21.50	188.26	111.50	266.56	201.50	188.26	291.50	268.94
22.50	193.47	112.50	270.00	202.50	193.47	292.50	266.88
23.50	200.52	113.50	258.92	203.50	200.52	293.50	263.09
24.50	189.18	114.50	259.83	204.50	189.18	294.50	251.31
25.50	201.29	115.50	262.71	205.50	201.29	295.50	257.23
26.50	199.14	116.50	266.69	206.50	199.14	296.50	265.99
27.50	199.39	117.50	273.74	207.50	199.39	297.50	254.93
28.50	199.06	118.50	269.23	208.50	199.06	298.50	263.64
29.50	195.60	119.50	262.83	209.50	195.60	299.50	267.28
30.50	196.20	120.50	253.37	210.50	196.20	300.50	253.99
31.50	205.12	121.50	249.01	211.50	205.12	301.50	256.97
32.50	195.56	122.50	257.31	212.50	195.56	302.50	255.58
33.50	207.07	123.50	250.75	213.50	207.07	303.50	247.55
34.50	212.56	124.50	257.55	214.50	212.56	304.50	252.17
35.50	213.27	125.50	257.29	215.50	213.27	305.50	253.02
36.50	208.49	126.50	259.54	216.50	208.49	306.50	253.23

37.50	203.81	127.50	250.96	217.50	203.81	307.50	251.01
38.50	202.04	128.50	251.01	218.50	202.04	308.50	246.60
39.50	207.67	129.50	244.56	219.50	207.67	309.50	252.47
40.50	213.83	130.50	238.40	220.50	213.83	310.50	241.12
41.50	215.94	131.50	247.78	221.50	215.94	311.50	240.95
42.50	226.76	132.50	242.88	222.50	226.76	312.50	236.77
43.50	220.74	133.50	231.28	223.50	220.74	313.50	237.89
44.50	215.48	134.50	238.80	224.50	215.48	314.50	237.78
45.50	222.54	135.50	239.46	225.50	222.54	315.50	237.34
46.50	221.14	136.50	237.90	226.50	221.14	316.50	231.35
47.50	231.02	137.50	236.26	227.50	231.02	317.50	238.80
48.50	226.85	138.50	221.95	228.50	226.85	318.50	226.11
49.50	224.12	139.50	229.33	229.50	224.12	319.50	226.27
50.50	227.82	140.50	225.94	230.50	227.82	320.50	221.98
51.50	231.60	141.50	221.18	231.50	231.60	321.50	228.79
52.50	236.49	142.50	218.94	232.50	236.49	322.50	222.92
53.50	239.79	143.50	220.57	233.50	239.79	323.50	212.10
54.50	245.45	144.50	211.97	234.50	245.45	324.50	219.12
55.50	234.16	145.50	205.33	235.50	234.16	325.50	222.93
56.50	241.66	146.50	209.12	236.50	241.66	326.50	209.58
57.50	243.00	147.50	206.21	237.50	243.00	327.50	215.63
58.50	243.24	148.50	209.59	238.50	243.24	328.50	215.82
59.50	247.64	149.50	204.49	239.50	247.64	329.50	210.15
60.50	246.82	150.50	206.77	240.50	246.82	330.50	203.61
61.50	251.96	151.50	206.58	241.50	251.96	331.50	214.60
62.50	257.53	152.50	200.76	242.50	257.53	332.50	205.36
63.50	252.52	153.50	202.84	243.50	252.52	333.50	204.16
64.50	252.50	154.50	199.22	244.50	252.50	334.50	198.94
65.50	249.66	155.50	194.74	245.50	249.66	335.50	197.27
66.50	247.10	156.50	196.88	246.50	247.10	336.50	199.97
67.50	250.13	157.50	203.18	247.50	250.13	337.50	204.31
68.50	251.55	158.50	200.75	248.50	251.55	338.50	198.09
69.50	254.15	159.50	193.06	249.50	254.15	339.50	197.81
70.50	249.78	160.50	189.79	250.50	249.78	340.50	201.13
71.50	256.90	161.50	187.31	251.50	256.90	341.50	197.30
72.50	247.06	162.50	188.73	252.50	247.06	342.50	194.88
73.50	245.18	163.50	199.85	253.50	245.18	343.50	195.74
74.50	244.73	164.50	196.61	254.50	244.73	344.50	198.11
75.50	252.65	165.50	196.08	255.50	252.65	345.50	204.65
76.50	250.61	166.50	197.65	256.50	250.61	346.50	194.83
77.50	240.67	167.50	194.27	257.50	240.67	347.50	196.48
78.50	237.23	168.50	193.29	258.50	237.23	348.50	198.24
79.50	247.25	169.50	186.88	259.50	247.25	349.50	197.91
80.50	245.35	170.50	189.00	260.50	245.35	350.50	190.90
81.50	243.10	171.50	190.12	261.50	243.10	351.50	191.91
82.50	235.67	172.50	184.73	262.50	235.67	352.50	191.62
83.50	241.15	173.50	191.14	263.50	241.15	353.50	200.84

84.50	238.82	174.50	191.02	264.50	238.82	354.50	191.99
85.50	234.16	175.50	193.78	265.50	234.16	355.50	196.57
86.50	234.83	176.50	193.66	266.50	234.83	356.50	192.67
87.50	227.20	177.50	191.73	267.50	227.20	357.50	199.96
88.50	244.68	178.50	195.78	268.50	244.68	358.50	202.48
89.50	228.99	179.50	197.74	269.50	228.99	359.50	196.82

Appendix E. DSC

The crystallinity of each sample is determined by DSC, viz. the enthalpy of fusion measured in the first melting of each sample divided by the enthalpy of fusion of 100% crystallised polyethylene, i.e. 295J g^{-1}.

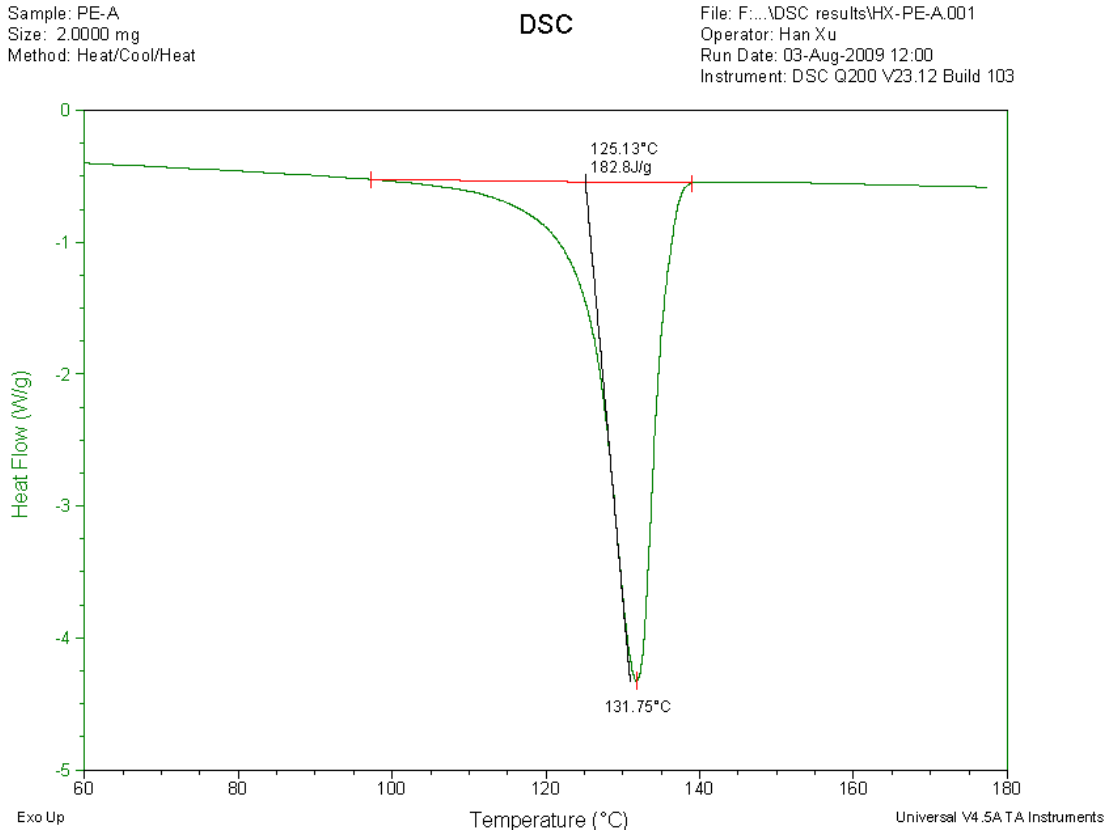

Figure a: DSC curve of PE-A in the first heating run.

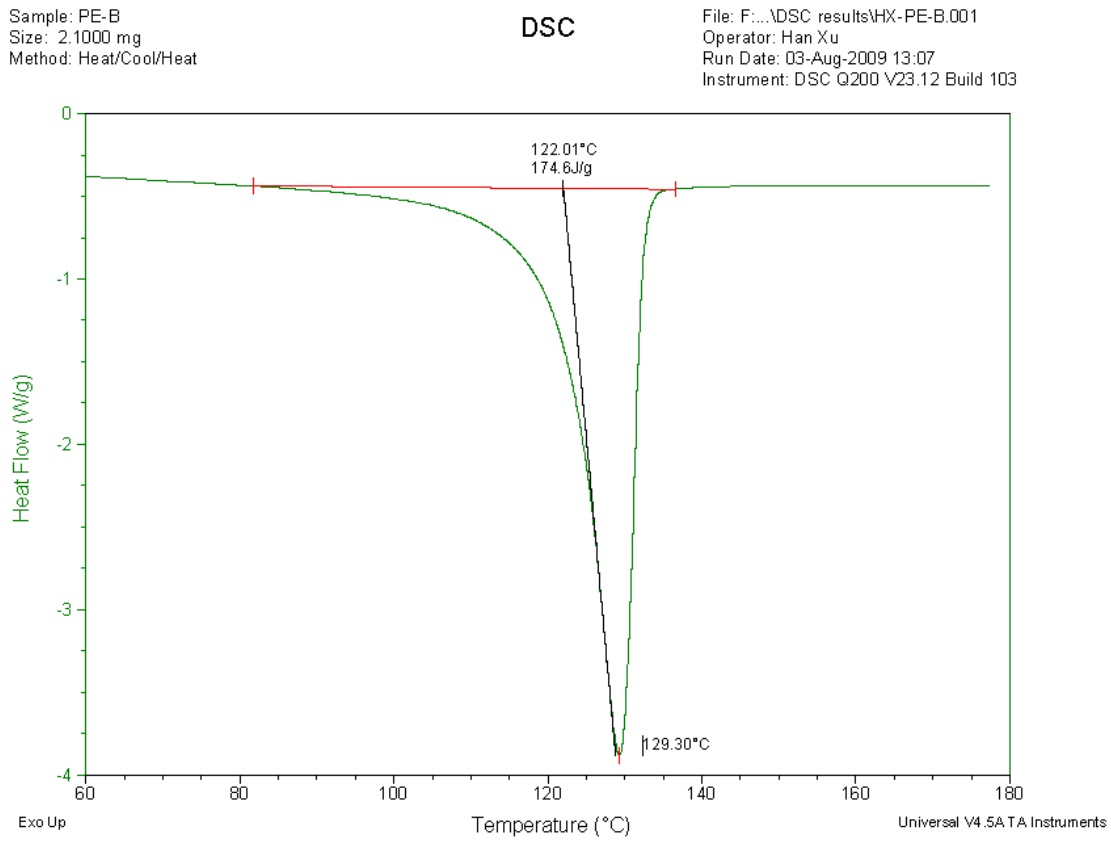

Figure b: DSC curve of PE-B in the first heating run.

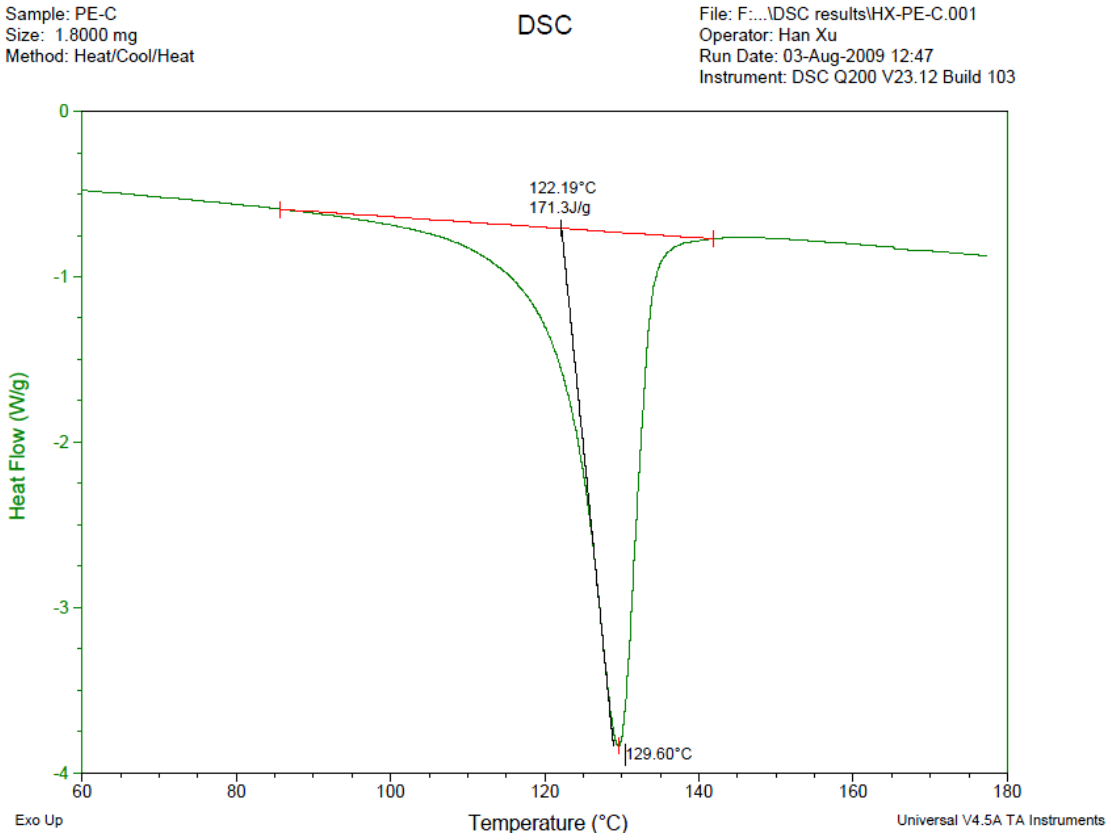

Figure c: DSC curve of PE-C in the first heating run.